The role of the complete Coriolis force in cross-equatorial transport of abyssal ocean currents

Andrew L. Stewart

Corpus Christi College

University of Oxford

A thesis submitted for the degree of

Doctor of Philosophy

Hilary Term 2011

To my wife, Usha

Acknowledgements

I would like to acknowledge the Engineering and Physical Sciences Research Council (EPSRC) for funding my DPhil. via a Doctoral Training Account award. All of the research described herein has been carried out with the support of the Oxford Centre for Industrial and Applied Mathematics (OCIAM), the Mathematical Institute, and Corpus Christi College at the University of Oxford.

I would like to thank my supervisor, Dr Paul Dellar, for his patience and attention over the last four years. Paul first suggested that I apply for a DPhil at Oxford, which I believe has considerably improved my experience of postgraduate study and offered me many more opportunities than I might otherwise have been afforded.

I would like to thank Professors David Marshall of AOPP and Robb McDonald of UCL for agreeing to serve as my examiners, and for constructive recommendations that have improved this work. I would like to thank Professor Ted Johnson of UCL for useful discussions that have contributed significantly to my research. I would also like to thank the staff and students of the 2009 Program in Geophysical Fluid Dynamics at Woods Hole Oceanographic Institution for an inspiring and enjoyable summer.

I would like to thank the staff and students of OCIAM for providing a pleasant and stimulating research environment. In particular I would like to thank my office-mates — Xiaodong Luo, Ian Hewitt, Gemma Fay, Emma Warneford, and the elusive Timothy Squires — for enduring my company with good humour.

On a more personal level, I would like to thank my friends in Oxford for their support. My time here has been improved considerably by the company of Nick Rounthwaite, Richard Johnson, Franchesca Richards, Fabian Grabenhorst and Anna Sproul. My involvement with the Oxford Judo Club has left me with many happy, albeit painful, memories, and has been a refreshing distraction from my pursuit of mathematics.

I would like to thank my family, particularly my parents Neil and Linda, and my brothers Ian and Alex, for their interest in my work and for their continuing support. Finally, I would like to thank my wife, Usha, for her patience, understanding and companionship throughout.

The role of the complete Coriolis force in cross-equatorial transport of abyssal ocean currents

Andrew L. Stewart

Corpus Christi College

A thesis submitted for the degree of

Doctor of Philosophy

Hilary Term 2011

In studies of the ocean it has become conventional to retain only the component of the Coriolis force associated with the radial component of the Earth's rotation vector, the so-called "traditional approximation". We investigate the role of the "non-traditional" component of the Coriolis force, corresponding to the non-radial component of the rotation vector, in transporting abyssal waters across the equator.

We first derive a non-traditional generalisation of the multi-layer shallow water equations, which describe the flow of multiple superposed layers of inviscid, incompressible fluid with constant densities over prescribed topography in a rotating frame. We derive these equations both by averaging the three-dimensional governing equations over each layer, and via Hamilton's principle. The latter derivation guarantees that conservation laws for mass, momentum, energy and potential vorticity are preserved. Within geophysically realistic parameters, including the complete Coriolis force modifies the domain of hyperbolicity of the multi-layer equations by no more than 5%. By contrast, long linear plane waves exhibit dramatic structural changes due to reconnection of the surface and internal wave modes in the long-wave limit.

We use our non-traditional shallow water equations as an idealised model of an abyssal current flowing beneath a less dense upper ocean. We focus on the Antarctic Bottom Water, which crosses the equator in the western Atlantic ocean, where the bathymetry forms an almost-westward channel. Cross-equatorial flow is strongly constrained by potential vorticity conservation, which requires fluid to acquire a large relative vorticity in order to move between hemispheres. Including the complete Coriolis force accounts for the fact that fluid crossing the equator in an eastward/westward channel experiences a smaller change in angular momentum, and therefore acquires less relative vorticity. Our analytical and numerical solutions for shallow water flow over idealised channel topography show that the non-traditional component of the Coriolis force facilitates cross-equatorial flow through an almost-westward channel.

Statement of Originality

I confirm that this thesis is wholly my own original work, and that no part of this thesis has been accepted or is currently being submitted for any degree, diploma, certificate, or other qualification at the University of Oxford or elsewhere. All methods and techniques used in this thesis that have been developed by other authors have been acknowledged by citation of the relevant publications.

Contents

List of Figures

Chapter 1

Introduction

The large-scale dynamics of the Earth's oceans and atmosphere are dominated by the interaction of the Coriolis force and stratification, and involve complex phenomena over wide ranges of length and time scales. Simplifications and approximations are thus widely used in the attempt to formulate more tractable descriptions of particular phenomena. In particular, it has become conventional to neglect the component of the Coriolis force associated with the locally horizontal component of the Earth's rotation vector $\mathbf{\Omega}$. The rotation vector is directed parallel to the Earth's rotation axis, so at a typical point on the Earth's surface $\mathbf{\Omega}$ has components in both the locally vertical and locally horizontal directions. The exceptions are the poles, where $\mathbf{\Omega}$ is purely vertical, and the equator, where $\mathbf{\Omega}$ is purely horizontal. However, the contribution to the Coriolis force due to the locally horizontal component of $\mathbf{\Omega}$ is widely neglected. This approximation was named the "traditional approximation" by Eckart (1960), on the grounds that it was widely used, but seemed to lack theoretical justification. In Figure 1.1 we illustrate the Earth's rotation vector and the neglect of its locally horizontal component under the traditional approximation.

The traditional approximation may be formally derived using a shallow layer approximation, *i.e.* that vertical lengthscales are small compared with horizontal lengthscales (*e.g.* White and Bromley, 1995). Some of the recent interest in re-evaluating the traditional approximation is driven by the increasing resolutions of numerical simulations, which now reach horizontal lengthscales for which the traditional approximation becomes questionable. For example, in 1992 the UK Meteorological Office abandoned the traditional approximation in their unified model for the atmosphere (Cullen, 1993). Similarly, the traditional approximation is sometimes justified as being valid in the dispersion relation for internal waves when the buoyancy or Brunt–Väisälä frequency N is much larger than the inertial frequency f (Phillips, 1968, 1973; Hendershott, 1981). However, the oceans contain substantial wave activity at or near inertial frequencies (Munk and Phillips, 1968; Fu, 1981), and

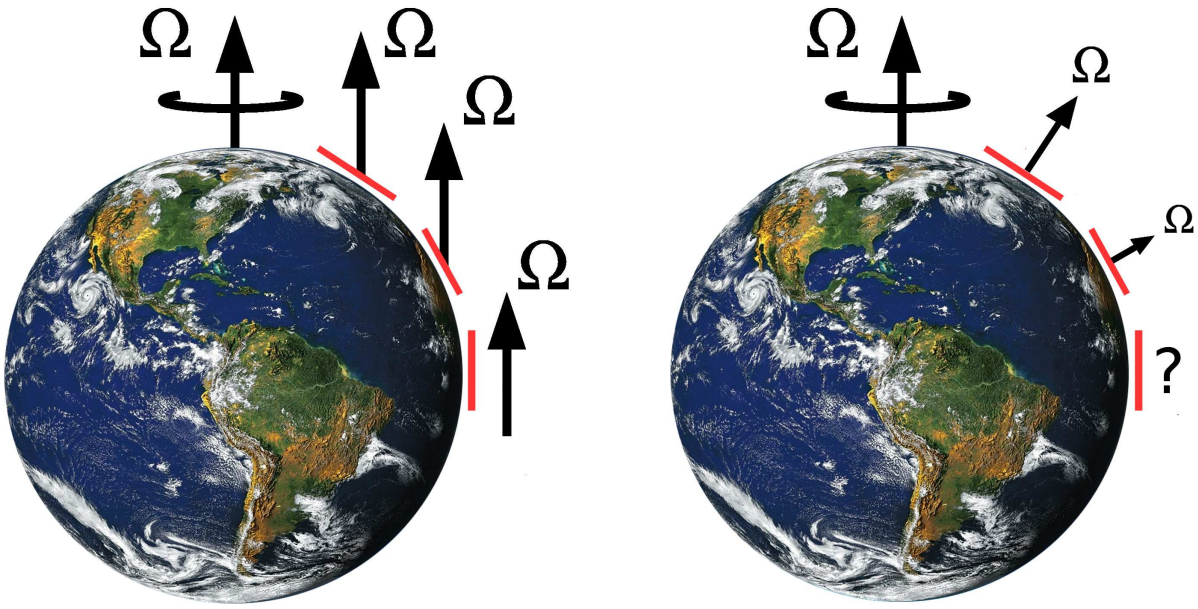

Figure 1.1: Illustration of the Earth's rotation vector, which is everywhere aligned with the planet's axis (left image). In the local plane of the Earth's surface the rotation vector changes direction with latitude, but its magnitude is uniform. Under the traditional approximation the locally horizontal component of the rotation vector is neglected (right image). The rotation vector is always aligned with the locally vertical axis, but decreases in magnitude towards the equator. *(Earth photograph courtesy of NASA)*

regions of very weak stratification where the Brunt–Väisälä or buoyancy frequency N is less than ten times the inertial frequency (Munk, 1981). In fact, the observed peak of wave activity with near-inertial frequencies ω tends to be even more pronounced than the $(\omega^2 - f^2)^{-1/2}$ factor included in the widely-used Garrett and Munk (1972, 1979) models for the energy spectrum. van Haren and Millot (2005) found areas of the Mediterranean with little or no stratification ($N = 0 \pm 0.4f$) to within the uncertainty of their measurements.

A recent review by Gerkema et al. (2008) explored the material that is available on the topic of the traditional approximation. The effect of including the non-traditional components of the Coriolis force is sometimes quite pronounced, particularly in mesoscale flows such as Ekman spirals (Leibovich and Lele, 1985) and deep convection (Marshall and Schott, 1999). Its role has been studied in settings as diverse as the circulation of deep lakes (Botte and Kay, 2002), and the formation of zonal jets (Fruman et al., 2009). Many previous investigations have focused on internal waves, where the weak stratification permits large amplitudes and makes non-traditional effects more prominent. Long, large-amplitude waves also carry the most energy, making them dynamically important for the circulation of the global ocean. For example Thuburn et al. (2002b) and Gerkema and Shrira (2005b,a) found new linear wave modes associated with the non-traditional component

of the Coriolis force, and Kasahara (2003) began an extended and continuing investigation (see Kasahara, 2007; Kasahara and Gary, 2010) into non-traditional waves in continuously-stratified fluids. These works are discussed further in connection with our analysis of linear plane waves in Chapter 3. By contrast, there has been very little previous work on the role of the complete Coriolis force in cross-equatorial flows, which we study extensively in Chapters 4–6. Colin de Verdière and Schopp (1994) and Schopp and Colin de Verdière (1997) obtained analytical solutions for flow in a spherical shell, and Raymond (2000) examined linear meridional/vertical oscillations of the near-equatorial atmosphere.

This thesis is concerned with the derivation and application of shallow water equations that include the complete Coriolis force. Shallow water equations are widely used as conceptual models in geophysical fluid dynamics because they capture the interaction between rotation and stratification, and between waves and vortices evolving on disparate timescales. The simplest shallow water equations describe the motion of a single layer of fluid with a free surface. They may be derived by averaging the three-dimensional equations of motion across the layer, under the assumption that the layer's depth is small compared with its horizontal dimensions. Many more phenomena may be described by shallow water models with two or more distinct layers of different densities. These models capture some of the baroclinic effects that arise in continuously stratified fluids, such as internal waves (*e.g.* LeBlond and Mysak, 1978) and baroclinic instability (*e.g.* Phillips, 1954; Boss, Paldor, and Thompson, 1996; Vallis, 2006). They describe the troposphere and the stratosphere (*e.g.* Vallis, 2006), the upper mixed layer and the lower ocean (*e.g.* LeBlond and Mysak, 1978; Salmon, 1982b), and deep ocean currents flowing beneath relatively quiescent fluid (*e.g.* Nof and Olson, 1993). They also form the basis of many three-dimensional numerical models that use a Lagrangian discretisation in the vertical, such as the Miami Isopycnal Coordinate Ocean Model (MICOM) described by Bleck et al. (1992) and Bleck and Chassignet (1994). All of these models are conventionally derived using the traditional approximation. A schematic of the multi-layer shallow water model of the ocean is shown in Figure 1.2.

The core material of this thesis may be broadly divided into two parts. The first, comprised of Chapters 2 and 3, concerns the derivation and analysis of multi-layer shallow water equations that include the complete Coriolis force. Dellar and Salmon (2005) showed that the complete Coriolis force could be included in shallow water equations for a single fluid layer flowing over prescribed bottom topography. In Chapter 2 we extend these equations to the case of arbitrarily many superposed layers, and correct the treatment of the spatially-varying rotation vector $\mathbf{\Omega}$. Our multi-layer shallow water equations thereby capture the interaction between the complete Coriolis force and density stratification. The small density difference between adjacent layers means that

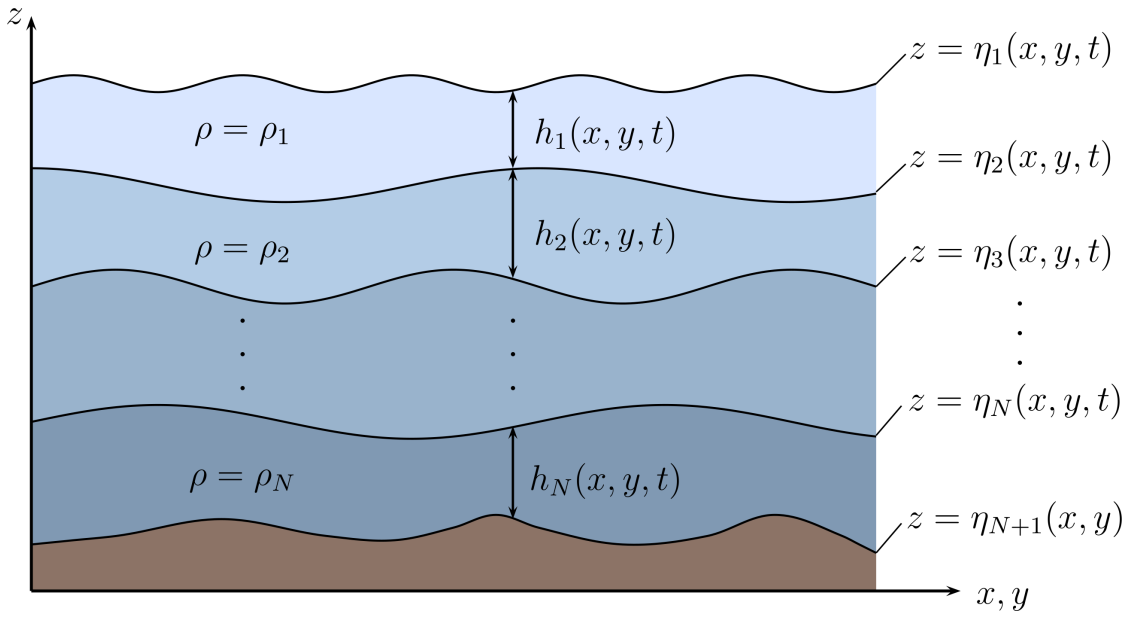

Figure 1.2: A schematic of the multi-layer shallow water model, in which N superposed layers of constant densities flow over a prescribed bottom topography. The upper surface of each layer is given by $z = \eta_i(x, y, t)$, $i = 1, \ldots, N$, and the bottom topography is prescribed as $z = \eta_{N+1}(x, y) = h_b(x, y)$. We also denote the layer thickness as $h_i(x, y, t)$, depth-averaged horizontal velocities as $\boldsymbol{u}_i(x, y, t)$ and densities as ρ_i.

Coriolis and buoyancy forces become comparable over a much smaller lengthscale than they do at the ocean surface, and so non-traditional effects should be much more pronounced. We explore this possibility in Chapter 3, where we investigate hyperbolicity and linear plane waves in the non-traditional multi-layer shallow water equations. Another extended set of shallow water equations, the multi-layer Green-Naghdi equations (Green and Naghdi, 1976), are ill-posed for solving initial-value problems (Liska et al., 1995; Liska and Wendroff, 1997). The traditional two-layer shallow water equations lose their hyperbolicity, and thus become ill-posed for solving initial-value problems, when the velocity difference between the two layers exceeds a critical threshold. For more details, see Chapter 3. While the hyperbolicity of the equations is not substantially modified by the inclusion of the complete Coriolis force, linear plane waves exhibit dramatic and unexpected changes in their structure at long wavelengths.

The second part of this thesis, comprised of Chapters 4–6, concerns the role of the complete Coriolis force in cross-equatorial abyssal ocean currents. Being denser than their surrounding fluid, abyssal currents are largely driven by gravity and steered by their local bathymetry. Over large scales they are also strongly influenced by the Coriolis force, which tends to push northward/southward-flowing currents against the western/eastern continental slope in the southern hemisphere, and vice versa in the northern hemisphere (Stommel and Arons, 1960a). The dynamics of these currents

becomes complicated close to the equator, where geostrophic balance breaks down as the locally vertical component of the Earth's rotation vector changes sign (Nof and Olson, 1993). Direct measurement of abyssal equatorial currents requires flowmeters to be set up at depths of thousands of metres, and years of measurement may be necessary to capture the slow variation of the flow (*e.g.* Hall et al., 1997).

Although most of our results apply generally to cross-equatorial abyssal currents, the Antarctic Bottom Water (AABW) serves as the focus for much of this work. The AABW originates from ice melting in the Weddell Sea near Antarctica, which forms a particularly cold, fresh body of water that sinks and flows north as a deep western boundary current in the south Atlantic (McCartney and Curry, 1993). The ocean bed steers the AABW to the east as it approaches the equator (Durrieu de Madron and Weatherly, 1994), in agreement with the classical geostrophic theory of Stommel and Arons (1960a). However, a portion of the AABW has been observed to cross the equator, and penetrates far into the northern hemisphere (Friedrichs and Hall, 1993; Rhein et al., 1998). To cross the equator through the Ceara abyssal plain, a deep, almost-westward bathymetric channel formed between the continental rise of South America and the mid-Atlantic ridge. Hall et al. (1994, 1997) measured the flow of the AABW through this channel, and estimated its transport at around 2 Sv ($1\ \mathrm{Sv} = 10^6\,\mathrm{m}^3\,\mathrm{s}^{-1}$). In Figure 1.3 we plot the bathymetry around the Ceara abyssal plane, and indicate the paths of the AABW as predicted by our numerical solutions of the shallow water equations, described in Chapter 6.

From the perspective of inviscid, ideal fluid dynamics, it is surprising that any current is able to travel far across the equator. As the fluid crosses the equator, the locally vertical component of the rotation vector changes sign. To conserve potential vorticity, the fluid must acquire an increasingly large relative vorticity as it moves further north. Killworth (1991) showed that this generation of relative vorticity prevents fluid moving more than approximately two deformation radii beyond the equator via geostrophic adjustment. The potential vorticity must therefore be modified by dissipative processes to permit cross-equatorial flow (Edwards and Pedlosky, 1998). However, conservation of potential vorticity remains a strong constraint on a cross-equatorial current, and a series of investigations have attempted to explain why such a large portion of the AABW is able to reach the northern hemisphere. Nof (1990) first highlighted the importance of the channel-like equatorial bathymetry using a reduced-gravity shallow water model, showing that a northward-flowing western boundary current with an unrestricted eastern front would be blocked by the equator. Nof and Olson (1993) then showed that the current could cross the equator in the presence of an opposing vertical wall to the east, by switching from the western to the eastern wall of the channel as it crossed the equator. Nof and Borisov (1998) later conducted some numerical simulations in an idealised

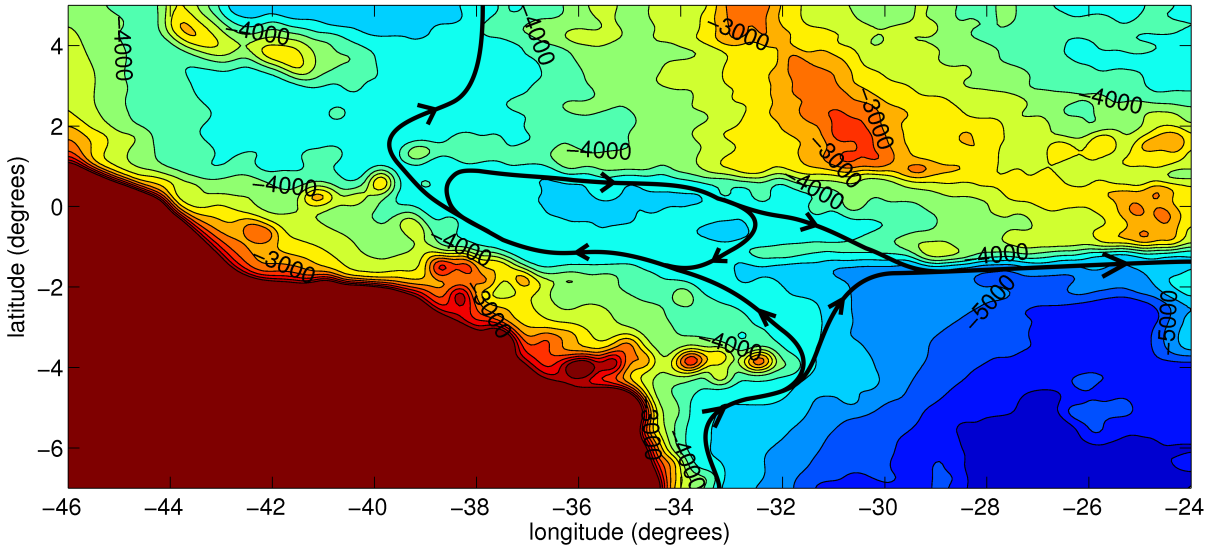

Figure 1.3: Contours of the bathymetry around the Ceara abyssal plane, where the AABW crosses the equator. The labels indicate the depths of the contours, which are shaded at intervals of 250 m. The data has been taken from Amante and Eakins (2009), interpolated onto a grid of 331 by 181 points, and smoothed via ten applications of a nine-gridpoint average (c.f Choboter and Swaters, 2004) to remove small-scale features and highlight the large-scale structure. The arrows indicate the major paths of the AABW as predicted by our numerical solutions of the shallow water equations, as described in Chapter 6.

channel, and showed that flow across the equator was dominated by inertial effects and the channel geometry. Stephens and Marshall (2000) represented the AABW using the frictional-geostrophic shallow water equations, which they integrated numerically over almost the entire Atlantic ocean. Despite neglecting the advection terms that Nof and Borisov (1998) found to be necessary for an accurate representation of the AABW's equatorial dynamics, they obtained a reasonable estimate for the cross-equatorial transport in the western Atlantic. Choboter and Swaters (2000, 2004) compared the frictional-geostrophic and shallow water equations in numerical simulations of the AABW through idealised and realistic topography. They found that it was necessary to include advection to reproduce the cross-equatorial transport measurements of Hall et al. (1997).

All of the studies mentioned above employ the traditional approximation. Non-traditional effects have received little attention in connection with abyssal currents, perhaps due to a lack of useful idealised models that account for the complete Coriolis force. Exceptions include Raymond (2000), who showed that the non-traditional component of the Coriolis force substantially affects atmospheric cross-equatorial flow described by the two-dimensional, linear, inviscid governing equations on an equatorial β-plane. Colin de Verdière and Schopp (1994) obtained two-dimensional analytical solutions for simple inviscid cross-equatorial flows, and later Schopp and Colin de Verdière (1997)

showed that inviscid, rotationally-dominated fluid could cross the equator in Taylor columns, but could not pass beyond a cylinder parallel to the planet's rotation axis and tangent to the equator. Hua et al. (1997) showed that the potential vorticity of equator-crossing fluid must be zero, accounting for the complete Coriolis force, as otherwise it will be subject to inertial instability. Measurements by Firing (1987) indicate that deep water tends to adhere to a state of zero potential vorticity within approximately 3° of the equator, and Hua et al. (1997) conclude that this should facilitate angular momentum exchanges between hemispheres.

It is surprising that more previous studies of abyssal cross-equatorial flow have not seriously considered the influence of the non-traditional component of the Coriolis force. Non-traditional effects should be particularly pronounced at the equator, because the size of the horizontal component of the rotation vector is $\Omega \cos\phi$, where ϕ is latitude. Meanwhile the vertical component of the rotation vector is $\Omega \sin\phi$, which vanishes at the equator. This is compounded by the weak stratification of the abyssal ocean, where the Brünt–Väisälä or buoyancy frequency N is closer to the inertial frequency Ω (*e.g.* van Haren and Millot, 2004). Additionally, the large variations in the abyssal bathymetry, such as that shown in Figure 1.3, may induce large vertical velocities, which in turn induce a zonal acceleration via the non-traditional component of the Coriolis force. We therefore expect non-traditional effects to play a prominent role in the equatorial dynamics of the AABW and other abyssal currents.

In Chapter 4 we idealise the cross-equatorial flow of the AABW to steady, one-dimensional flow across a zonal channel straddling the equator. This model problem provides an intuition for the action of the non-traditional component of the Coriolis force, and our results suggest that non-traditional effects in a zonal equatorial channel should facilitate cross-equatorial flow of an abyssal current. In Chapter 5 we obtain steady two-dimensional asymptotic solutions for a current flowing through an idealised cross-equatorial channel, oriented at an arbitrary angle to the equator. Our analysis exploits the scale separation for a current that is much longer than it is wide, and much wider than it is deep. The case of an almost-westward (or almost-eastward) channel is a special case that is best considered under a modified asymptotic regime. We find that the current must cross the channel as it crosses the equator, and that including the complete Coriolis force may substantially increase the transport in an almost-westward channel. In Chapter 6 we derive an energy- and potential enstrophy-conserving finite-difference scheme for the non-traditional single-layer shallow water equations, and obtain numerical solutions for cross-equatorial flow through an idealised channel. The behaviour of the current depends strongly on the orientation of the channel, and is substantially modified by the inclusion of the complete Coriolis force when the channel is almost-westward.

The chapters of this thesis have been written such that they are more-or-less self-contained, for the convenience of both the author and the reader. As of the time of writing, Chapters 2–5 have been submitted for publication in a state close to their present form. Chapter 2 appeared in the *Journal of Fluid Mechanics* in 2010, and Chapter 3 is under consideration for publication in the same journal. Chapter 4 has been accepted for publication in *Ocean Modelling*, and Chapter 5 is under consideration for publication in the same journal. Portions of Chapter 6 are being prepared for submission to the *Journal of Computational Physics* and the *Journal of Physical Oceanography*.

Chapter 2

Derivation of the non-traditional multi-layer shallow water equations

This chapter is based upon Stewart and Dellar (2010).

2.1 Introduction

In this chapter we derive multilayer shallow water equations that include the complete Coriolis force, in contrast to the conventional shallow water equations that rely upon the traditional approximation in their derivation. We thus extend the derivation of single layer shallow water equations by Dellar and Salmon (2005) to encompass several superposed layers of inviscid fluid of different, constant densities flowing over topography, as illustrated in Figure 1.2. Dellar and Salmon (2005) corrected an earlier attempt by Bazdenkov, Morozov, and Pogutse (1987) whose equations failed to conserve either energy or potential vorticity in the presence of topography. Our multilayer equations provide a useful idealised setting for studying the interaction between density stratification and rotation, and the resulting sets of two-dimensional equations are practical for numerical studies of some of the phenomena described in Chapter 1.

The three-dimensional Euler equations for a rotating, stratified, ideal fluid possess conservation laws for energy, momentum, and potential vorticity. Attention in geophysical fluid dynamics has been focused on model equations that share the same conservation laws, which are easily destroyed by making approximations directly in the equations. In addition to a derivation by averaging the three-dimensional Euler equations, we derive our multilayer shallow water equations by making approximations in a variational principle, Hamilton's principle of least action, as formulated for a three-dimensional ideal fluid. The previously mentioned conservation laws are related to symmetries in the variational principle by Noether's theorem (see §2.5) and any equations derived by making

approximations that preserve these symmetries will possess equivalent conservation laws. The single layer shallow water equations may be readily derived from Hamilton's principle by integrating a three-dimensional Lagrangian across the layer (Salmon, 1983, 1988, 1998). However, the extension to two or more layers is considerably more involved, because the derivation relies upon introducing Lagrangian particle labels within each layer. The transmission of pressures between layers requires some means to synchronise the positions of particles in the different layers. Our first derivation is equivalent to Salmon's (1982b) derivation of the two-layer traditional shallow water equations from Hamilton's principle. Salmon (1982b) coupled the two layers using a double integral of a delta function across both layers in the Lagrangian (see §2.7). This approach does not readily extend to many layers, because one would need integrals across all N layers. We avoid the integrals across multiple layers by transforming each of the integrals into an integral over layer i when deriving the equations of motion for layer i. However, the calculation is still sufficiently involved that we present a second derivation that explicitly includes the work done by the pressure exerted by other layers in the Lagrangian.

The non-traditional components of the Coriolis force appear through terms involving the half-layer heights $\overline{z}_i = \frac{1}{2}(\eta_i + \eta_{i+1})$, where $z = \eta_i(x, y, t)$ is the upper surface of the i^{th} layer, as in Figure 1.2. This is because the non-traditional terms are linear in z when the fluid moves approximately in columns, and layer-averaging a function that is linear in z is equivalent to evaluating the function at the midpoint of the layer. In particular, the potential vorticity within each layer involves the component of the planetary rotation vector $\mathbf{\Omega}$ that is normal to the half-layer surface (as in Dellar and Salmon, 2005) rather than the vertical component as found under the traditional approximation.

The equations derived in this chapter are also relevant for the development of large scale numerical ocean models. Due to the large disparity in the horizontal and vertical lengthscales, many three-dimensional numerical ocean models use different discretisations in the horizontal and vertical coordinates. In particular, it is common to use an isopycnal coordinate, a constant density surface, which is also a Lagrangian coordinate, in the vertical to prevent excessive diffusion across tilted isopycnal surfaces. One may think of a layered model with many layers, as illustrated in Figure 1.2, as arising from a Lagrangian finite difference discretisation in the vertical. The most well-known model in this class is the Miami Isopycnal Coordinate Ocean Model (MICOM) as described in Bleck et al. (1992) and Bleck and Chassignet (1994). The multilayer equations derived in this chapter could be used to extend a layered ocean model like MICOM to include the complete Coriolis force.

2.2 Three-dimensional equations and coordinates

We model each layer as an inviscid, incompressible, fluid of constant density ρ_i in a frame rotating with angular velocity $\mathbf{\Omega}$. The fluid's motion is thus governed by the Euler equations,

$$\frac{\partial \boldsymbol{u}_i}{\partial t} + (\boldsymbol{u}_i \cdot \nabla)\, \boldsymbol{u}_i + 2\,\mathbf{\Omega} \times \boldsymbol{u}_i + \frac{1}{\rho_i}\nabla p_i + \nabla\Phi = 0, \quad \nabla \cdot \boldsymbol{u}_i = 0, \tag{2.1}$$

in conjunction with boundary conditions at the interfaces between layers (see below). Here $\boldsymbol{u}_i$ and p_i are the velocity and pressure within the i^{th} layer. The geopotential Φ is the combined potential for the gravitational acceleration and the centrifugal acceleration due to rotation.

The geopotential gradient is much larger than the inertial and Coriolis terms in geophysically reasonable parameter regimes, so it must be balanced primarily by the pressure gradient. We therefore set up a coordinate system in which $\nabla\Phi = g\hat{\mathbf{z}}$, with g being the gravitational acceleration (which by convention includes the centrifugal force). The vector $\hat{\mathbf{z}}$ is a unit vector in the direction that is locally upward as defined by $\nabla\Phi$, and the horizontal directions are tangent to the surfaces of constant geopotential.

In theoretical studies of geophysical fluid dynamics it is common to use Cartesian, or pseudo-Cartesian, coordinates (Pedlosky, 1987; Salmon, 1998; Vallis, 2006). By pseudo-Cartesian coordinates we mean the use of curvilinear coordinates under an approximation that allows the curvilinear metric to be neglected in the equations of motion. Curvilinear coordinates are necessary because the "horizontal" coordinates should lie within, rather than merely be tangent to, the surfaces of constant geopotential. This is the correct interpretation of the so-called β-plane approximation to spherical geometry (Phillips, 1973).

The Earth's angular velocity vector $\mathbf{\Omega}$ is directed parallel to the line from South pole to North pole. However, the direction of $\mathbf{\Omega}$ relative to local coordinates with $\hat{\mathbf{z}}$ vertical changes with latitude, so $\mathbf{\Omega}$ must be spatially varying in the pseudo-Cartesian coordinates of the ocean model presented in Figure 1.2. This approximation, retaining only the latitude-dependence of the rotation vector from spherical geometry in an otherwise pseudo-Cartesian formulation, is known as the β-plane approximation. The simpler f-plane approximation arises from taking $\mathbf{\Omega}$ constant, and becomes valid on lengthscales much smaller than the planetary radius.

We allow for arbitrary orientation of the x- and y-axes, generalising the conventional axes in which the y-axis points North and the x-axis points East. We write $\mathbf{\Omega} = (\Omega_x, \Omega_y, \Omega_z)$, and allow Ω_x, Ω_y, and Ω_z to be arbitrary functions of x and y. The three-dimensional vector field $\mathbf{\Omega}$ must be non-divergent, $\nabla \cdot \mathbf{\Omega} = 0$, to ensure conservation of potential vorticity (Grimshaw, 1975). To allow for spatial variation of Ω_x and Ω_y, we must therefore allow Ω_z to depend on z. We take $\Omega_z = \Omega_z(x, y, z)$ while $\Omega_x = \Omega_x(x, y)$, $\Omega_y = \Omega_y(x, y)$. This is sufficiently flexible to capture a variety

of β-plane approximations in which Ω_x and Ω_y, as well as Ω_z, depend on latitude. Integrating $\nabla \cdot \boldsymbol{\Omega} = 0$ with respect to z yields the following expression for Ω_z,

$$\Omega_z(x, y, z) = \Omega_{z0}(x, y) - \left(\frac{\partial \Omega_x}{\partial x} + \frac{\partial \Omega_y}{\partial y} \right) z, \tag{2.2}$$

where $\Omega_{z0} = \Omega_z|_{z=0}$.

Dellar (2011) showed that one may derive (2.1) in a pseudo-Cartesian form, together with (2.2) and expressions for Ω_x and Ω_y, by introducing suitable curvilinear coordinates into Hamilton's principle on a sphere, and then approximating for motions on lengthscales that are small compared with the planetary radius. In this derivation, the z-dependence of Ω_z arises as a pseudo-Cartesian approximation to the dependence of the angular momentum of a particle rotating with the planetary angular velocity $\boldsymbol{\Omega}$ on spherical radius.

2.3 Derivation by layer averaging

One route to deriving our extended shallow water equations is via an extension of the standard derivation of the traditional approximation shallow water equations by averaging across layers. We obtain two-dimensional equations for the depth-averaged horizontal velocities and the layer depths by integrating the three-dimensional equations of motion over each fluid layer. Our approach follows the derivation of the nonrotating and weakly nonlinear "great lake" equations by Camassa et al. (1996), as adapted by Dellar and Salmon (2005) to include the Coriolis force. Our treatment of multiple layers is similar to Liska and Wendroff's (1997) derivation of multilayer Green–Naghdi equations, and to Choi and Camassa's (1996) derivation of two-layer equations for weakly nonlinear internal waves.

2.3.1 Formulation and nondimensionalisation

Within each layer we write the three-dimensional velocity vector as $(\boldsymbol{u}_i, w_i)$, where $\boldsymbol{u}_i = (u_i, v_i)$ is now a two-dimensional vector for the horizontal velocity. Separating the Euler equations (2.1) into horizontal and vertical components, we obtain

$$\frac{\partial \boldsymbol{u}_i}{\partial t} + (\boldsymbol{u}_i \cdot \nabla)\, \boldsymbol{u}_i + w_i \frac{\partial \boldsymbol{u}_i}{\partial z} + 2\Omega_z \boldsymbol{z} \times \boldsymbol{u}_i + 2\boldsymbol{\Omega} \times \hat{\boldsymbol{z}} w_i + \frac{1}{\rho_i} \nabla p_i = 0, \tag{2.3a}$$

$$\frac{\partial w_i}{\partial t} + \boldsymbol{u}_i \cdot \nabla w_i + w_i \frac{\partial w_i}{\partial z} + 2(v_i \Omega_x - u_i \Omega_y) + \frac{1}{\rho_i} \frac{\partial p_i}{\partial z} + g = 0, \tag{2.3b}$$

$$\nabla \cdot \boldsymbol{u}_i + \frac{\partial w_i}{\partial z} = 0, \tag{2.3c}$$

for $i = 1, \ldots, N$. The quantities appearing in the three-dimensional Euler equations are all functions of x, y, z, and t, and henceforth $\nabla \equiv (\partial/\partial x, \partial/\partial y)$ is the two-dimensional gradient vector.

We assume that each layer of fluid is bounded by an upper surface $z = \eta_i(x, y, t)$, and a lower surface $z = \eta_{i+1}(x, y, t)$. The exception is the lowest layer, the N^{th} layer, that flows over a fixed topography $z = \eta_{N+1}(x, y) = h_b(x, y)$. For future use, we also define the layer heights $h_i = \eta_i - \eta_{i+1}$, as shown in Figure 1.2. We assume that the upper surface of the uppermost layer is stress-free, and that the pressure is continuous across each internal surface. This leads to the following boundary conditions for the pressures,

$$p_1 = 0 \quad \text{on} \quad z = \eta_1, \qquad p_i = p_{i+1} \quad \text{on} \quad z = \eta_{i+1}. \tag{2.4}$$

By considering $(D/Dt)(z - \eta_i) = 0$ at $z = \eta_i$ in each of the two layers bounded by η_i, we obtain the kinematic boundary conditions,

$$\begin{aligned} w_i &= \frac{\partial \eta_i^{(-)}}{\partial t} + \boldsymbol{u}_i \cdot \nabla \eta_i^{(-)} \qquad \text{on} \quad z = \eta_i^{(-)}, \\ w_i &= \frac{\partial \eta_{i+1}^{(+)}}{\partial t} + \boldsymbol{u}_i \cdot \nabla \eta_{i+1}^{(+)} \qquad \text{on} \quad z = \eta_{i+1}^{(+)}. \end{aligned} \tag{2.5}$$

The superscripts $^{(+)}$ and $^{(-)}$ denote that these conditions should be evaluated just above and just below the boundary, respectively, due to the discontinuity of the tangential velocity across the interfaces. Compatibility of the different expressions for $\partial_t \eta_i$ from each side of the layer is equivalent to continuity of the normal velocity across each interface.

We now apply a nondimensionalisation similar to that used by Camassa et al. (1996), but adapted to a rotating system. We write

$$\begin{gathered} \boldsymbol{x} = L\tilde{x}, \quad z = \varepsilon L \tilde{z}, \quad \boldsymbol{u}_i = U \tilde{\boldsymbol{u}}_i, \quad w_i = \varepsilon U \tilde{w}_i, \quad p_i = 2\Omega L U \rho_i \, \tilde{p}_i, \\ t = L/U \tilde{t}, \quad \boldsymbol{\Omega} = \Omega \tilde{\boldsymbol{\Omega}}, \quad \Omega_z = \Omega \tilde{\Omega}_z, \quad \eta_i = \varepsilon L \tilde{\eta}_i, \end{gathered} \tag{2.6}$$

where U is the velocity scale, $H = \varepsilon L$ is the vertical length scale, L is the horizontal length scale, $\Omega = |(\boldsymbol{\Omega}, \Omega_z)|$ is the magnitude of the Earth's angular velocity. The aspect ratio $\varepsilon = H/L \ll 1$ is assumed to be small, enforcing the assumption of a shallow layer. We choose the nondimensionalisation for w_i so that the small parameter ε does not enter the dimensionless incompressibility condition. The dimensionless versions of equations (2.3a)–(2.3c) are thus

$$\mathrm{Ro}\left(\frac{\partial \tilde{\boldsymbol{u}}_i}{\partial \tilde{t}} + \left(\tilde{\boldsymbol{u}}_i \cdot \tilde{\nabla}\right) \tilde{\boldsymbol{u}}_i + \tilde{w}_i \frac{\partial \tilde{\boldsymbol{u}}_i}{\partial \tilde{z}}\right) + \tilde{\Omega}_z \hat{\boldsymbol{z}} \times \tilde{\boldsymbol{u}}_i + \varepsilon \, \tilde{\boldsymbol{\Omega}} \times \hat{\boldsymbol{z}} \tilde{w}_i + \tilde{\nabla} \tilde{p}_i = 0, \tag{2.7a}$$

$$\varepsilon^2 \mathrm{Ro}\left(\frac{\partial \tilde{w}_i}{\partial \tilde{t}} + \tilde{\boldsymbol{u}}_i \cdot \tilde{\nabla} \tilde{w}_i + \tilde{w}_i \frac{\partial \tilde{w}_i}{\partial \tilde{z}}\right) + \varepsilon(\tilde{v}_i \tilde{\Omega}_x - \tilde{u}_i \tilde{\Omega}_y) + \frac{\partial \tilde{p}_i}{\partial \tilde{z}} + \mathrm{Bu} = 0, \tag{2.7b}$$

$$\nabla \cdot \tilde{\boldsymbol{u}}_i + \frac{\partial \tilde{w}_i}{\partial \tilde{z}} = 0, \tag{2.7c}$$

where $\mathrm{Ro} = U/(2\Omega L)$ and $\mathrm{Bu} = gH/(2\Omega U L)$ are the Rossby and Burger numbers respectively. We assume Ro and Bu are both O(1). Hereafter we will drop the tilde ($\tilde{}$) notation, with the understanding that all variables are dimensionless.

2.3.2 Asymptotic expansion

We wish to obtain averaged momentum equations that are accurate up to first order in the small parameter ε. We therefore pose asymptotic expansions in ε of the dependent variables $\boldsymbol{u}_i$, w_i and p_i,

$$\boldsymbol{u}_i = \boldsymbol{u}_i^{(0)} + \varepsilon \boldsymbol{u}_i^{(1)} + \cdots, \quad w_i = w_i^{(0)} + \varepsilon w_i^{(1)} + \cdots, \quad p_i = p_i^{(0)} + \varepsilon p_i^{(1)} + \cdots, \tag{2.8}$$

for $i = 1, \ldots, N$.

Substituting this expansion into (2.7b), we find that the leading order pressure in each layer is just the hydrostatic pressure,

$$p_i^{(0)} = p_i^{(0)}\Big|_{z=\eta_i} + \mathrm{Bu}(\eta_i - z). \tag{2.9}$$

The leading order horizontal pressure gradient $\nabla p_i^{(0)}$ is thus independent of z within each layer. Additionally, nondimensionalising (2.2) leads to

$$\Omega_z = \Omega_{z0} - \varepsilon \left(\nabla \cdot \boldsymbol{\Omega}\right) z, \tag{2.10}$$

so Ω_z is independent of z at leading order. Equation (2.7a) may therefore be satisfied at leading order by a z-independent horizontal velocity $\boldsymbol{u}_i^{(0)} = \boldsymbol{u}_i^{(0)}(x, y, t)$. In other words, columnar motion is consistent with the leading order horizontal momentum equation.

We now use the vertical momentum equation (2.7b) again to evaluate the first correction pressure terms,

$$p_i^{(1)} = p_i^{(1)}\Big|_{z=\eta_i} + (\eta_i - z)\left(v_i^{(0)}\Omega_x - u_i^{(0)}\Omega_y\right). \tag{2.11}$$

The combination $p_i^{(0)} + \varepsilon p_i^{(1)}$, being the result of balancing the vertical pressure gradient with the gravitational term and the vertical components of the Coriolis acceleration, is known as the 'quasi-hydrostatic' pressure (White and Bromley, 1995; White et al., 2005). The pressure contributions from the layers above may be evaluated using the dimensionless form of the pressure boundary condition (2.4), $p_1^{(0)} + \varepsilon p_1^{(1)} = 0$ on $z = \eta_1$ and $\rho_i\left(p_i^{(0)} + \varepsilon p_i^{(1)}\right) = \rho_{i-1}\left(p_{i-1}^{(0)} + \varepsilon p_{i-1}^{(1)}\right)$ on $z = \eta_i$ for $2 \le i \le N$. This leads to the following expression for the pressure in each layer,

$$\begin{aligned} p_i &= p_i^{(0)} + \varepsilon p_i^{(1)} + \mathrm{O}(\varepsilon^2) \\ &= (\eta_i - z)\left(\mathrm{Bu} + \varepsilon v_i^{(0)}\Omega_x - \varepsilon u_i^{(0)}\Omega_y\right) \\ &\quad + \sum_{j=1}^{i-1} \frac{\rho_j}{\rho_i} h_j \left(\mathrm{Bu} + \varepsilon v_j^{(0)}\Omega_x - \varepsilon u_j^{(0)}\Omega_y\right) + \mathrm{O}(\varepsilon^2). \end{aligned} \tag{2.12}$$

Similarly, we may determine the leading order vertical velocity using (2.7c),

$$w_i^{(0)} = w_i^{(0)}\Big|_{z=\eta_{i+1}} + (\eta_{i+1} - z)\,\nabla \cdot \boldsymbol{u}_i^{(0)}. \tag{2.13}$$

The vertical velocity in each layer acquires a contribution from those in the layers below, which may be evaluated using (2.5) in the form

$$w_i^{(0)} = w_{i+1}^{(0)} + \left(\boldsymbol{u}_i^{(0)} - \boldsymbol{u}_{i+1}^{(0)}\right) \cdot \nabla \eta_{i+1} \quad \text{on} \quad z = \eta_{i+1}. \tag{2.14}$$

Repeated application of (2.13) and (2.14) leads to a complete expression for the leading order vertical velocities:

$$w_i^{(0)} = \nabla \cdot \left(\eta_{i+1} \boldsymbol{u}_i^{(0)}\right) - z \nabla \cdot \boldsymbol{u}_i^{(0)} - \sum_{j=i+1}^{N} \nabla \cdot \left(h_j \boldsymbol{u}_j^{(0)}\right). \tag{2.15}$$

2.3.3 Averaged momentum equations

We now derive two-dimensional equations governing the dynamics of the depth-averaged horizontal velocity in each layer. To perform averaging of (2.7a)–(2.7c), we require a result from Wu (1981) for the average of the material derivative $\mathrm{D}F/\mathrm{D}t$ across a layer of incompressible fluid bounded by the material surfaces $z = \eta_i$ and $z = \eta_{i+1}$,

$$h_i \int_{\eta_{i+1}}^{\eta_i} \left\{ \frac{\partial F}{\partial t} + \boldsymbol{u}_i \cdot \nabla F + w_i \frac{\partial F}{\partial z} \right\} \mathrm{d}z = \frac{\partial}{\partial t}(h_i \overline{F}) + \nabla \cdot (h_i \overline{\boldsymbol{u}_i F}). \tag{2.16}$$

Here an overbar ($\overline{\ }$) denotes a layer-averaged quantity. For example,

$$\overline{\boldsymbol{u}}_i = \frac{1}{h_i} \int_{\eta_{i+1}}^{\eta_i} \boldsymbol{u}_i \, \mathrm{d}z. \tag{2.17}$$

Setting $F = 1$ in (2.16) leads to an exact evolution equation for the layer height h_i,

$$\frac{\partial h_i}{\partial t} + \nabla \cdot (h_i \, \overline{\boldsymbol{u}}_i) = 0. \tag{2.18}$$

Similarly, setting $F = u_i$ and $F = v_i$ allows us to integrate (2.7a) over each layer, as described in Camassa et al. (1996) and Dellar and Salmon (2005), to obtain

$$\begin{aligned} \mathrm{Ro} \left(\frac{\partial}{\partial t} \left(h_i \overline{\boldsymbol{u}}_i \right) + \nabla \cdot \left(h_i \overline{\boldsymbol{u}_i \, \boldsymbol{u}_i} \right) \right) + h_i \hat{\boldsymbol{z}} \times \overline{\Omega_z \boldsymbol{u}_i} \\ + \varepsilon \boldsymbol{\Omega} \times \hat{\boldsymbol{z}} \int_{\eta_{i+1}}^{\eta_i} w_i^{(0)} \mathrm{d}z + \int_{\eta_{i+1}}^{\eta_i} \nabla \left(p_i^{(0)} + \varepsilon p_i^{(1)} \right) \mathrm{d}z = \mathrm{O}(\varepsilon^2). \end{aligned} \tag{2.19}$$

To obtain evolution equations for the averaged velocities $\overline{\boldsymbol{u}}_i$, we note that $\boldsymbol{u}_i$ and Ω_z are z-independent at leading order, and so averages of their products may be factorised to sufficient accuracy (Camassa et al., 1996; Su and Gardner, 1969) as $\overline{\boldsymbol{u}_i \boldsymbol{u}_i} = \overline{\boldsymbol{u}}_i \overline{\boldsymbol{u}}_i + \mathrm{O}(\varepsilon^2)$, $\overline{\Omega_z \boldsymbol{u}_i} = \overline{\Omega}_z \overline{\boldsymbol{u}}_i + \mathrm{O}(\varepsilon^2)$.

We may also determine the averaged pressure gradient using (2.12),

$$\begin{aligned}\int_{\eta_{i+1}}^{\eta_i} \nabla\left(p_i^{(0)}+\varepsilon p_i^{(1)}\right)\mathrm{d}z &= \tfrac{1}{2}\varepsilon h_i\left(v_i^{(0)}\Omega_x - u_i^{(0)}\Omega_y\right)\nabla\left(\eta_{i+1}+\eta_i\right)\\ &+ h_i\nabla\left\{\mathrm{Bu}\,\eta_i + \tfrac{1}{2}\varepsilon h_i\left(v_i^{(0)}\Omega_x - u_i^{(0)}\Omega_y\right)\right.\\ &\left.+\sum_{j=1}^{i-1}\frac{\rho_j}{\rho_i}h_j\left(\mathrm{Bu}+\varepsilon v_j^{(0)}\Omega_x - \varepsilon u_j^{(0)}\Omega_y\right)\right\},\end{aligned} \tag{2.20}$$

and the averaged vertical velocity using (2.15),

$$\int_{\eta_{i+1}}^{\eta_i} w_i^{(0)}\mathrm{d}z = h_i\left[\boldsymbol{u}_i^{(0)}\cdot\nabla\eta_{i+1} - \tfrac{1}{2}h_i\nabla\cdot\boldsymbol{u}_i^{(0)} - \sum_{j=i+1}^{N}\nabla\cdot\left(h_j\boldsymbol{u}_j^{(0)}\right)\right]. \tag{2.21}$$

Substituting these expressions into (2.19) yields

$$\begin{aligned}&\mathrm{Ro}\left(\frac{\partial}{\partial t}\left(h_i\overline{\boldsymbol{u}}_i\right)+\nabla\cdot\left(h_i\overline{\boldsymbol{u}}_i\overline{\boldsymbol{u}}_i\right)\right)+h_i\hat{\boldsymbol{z}}\times\overline{\Omega}_z\overline{\boldsymbol{u}}_i\\ &+\tfrac{1}{2}\varepsilon h_i\left(v_i^{(0)}\Omega_x-u_i^{(0)}\Omega_y\right)\nabla\left(\eta_{i+1}+\eta_i\right)\\ &+h_i\nabla\left\{\mathrm{Bu}\,\eta_i+\tfrac{1}{2}\varepsilon h_i\left(v_i^{(0)}\Omega_x-u_i^{(0)}\Omega_y\right)\right.\\ &\qquad\left.+\sum_{j=1}^{i-1}\frac{\rho_j}{\rho_i}h_j\left(\mathrm{Bu}+\varepsilon v_j^{(0)}\Omega_x-\varepsilon u_j^{(0)}\Omega_y\right)\right\}\\ &+\varepsilon\boldsymbol{\Omega}\times\hat{\boldsymbol{z}}h_i\left[\boldsymbol{u}_i^{(0)}\cdot\nabla\eta_{i+1}-\tfrac{1}{2}h_i\nabla\cdot\boldsymbol{u}_i^{(0)}-\sum_{j=i+1}^{N}\nabla\cdot\left(h_j\boldsymbol{u}_j^{(0)}\right)\right]=\mathrm{O}(\varepsilon^2).\end{aligned} \tag{2.22}$$

To complete the derivation, we note that $\boldsymbol{u}_i^{(0)} = \overline{\boldsymbol{u}}_i + \mathrm{O}(\varepsilon)$ and that the advection terms may be simplified using (2.18). Additionally, integrating (2.10) yields an expression for $\overline{\Omega}_z$,

$$\overline{\Omega}_z = \Omega_{z0} - \varepsilon\,\overline{z}_i\,\nabla\cdot\boldsymbol{\Omega}, \tag{2.23}$$

where $\overline{z}_i = \frac{1}{2}\left(\eta_i+\eta_{i+1}\right)$ is the vertical position of the midsurface of the layer. The linear dependence of Ω_z on z makes the average of Ω_z across the layer equal to the value of Ω_z at the midsurface.

Neglecting terms of $\mathrm{O}(\varepsilon^2)$ and above, and dropping the overbars on averaged velocities, we rearrange (2.22) to obtain

$$\begin{aligned}&\mathrm{Ro}\left(\frac{\partial\boldsymbol{u}_i}{\partial t}+(\boldsymbol{u}_i\cdot\nabla)\boldsymbol{u}_i\right)+\left(\Omega_{z0}-\tfrac{1}{2}\varepsilon\nabla\cdot\left(\left(\eta_i+\eta_{i+1}\right)\boldsymbol{\Omega}\right)\right)\hat{\boldsymbol{z}}\times\boldsymbol{u}_i\\ &+\nabla\left\{\mathrm{Bu}\,\eta_i+\tfrac{1}{2}\varepsilon h_i(v_i\Omega_x-u_i\Omega_y)+\frac{1}{\rho_i}\sum_{j=1}^{i-1}\rho_j h_j\big(\mathrm{Bu}+\varepsilon\left(v_j\Omega_x-u_j\Omega_y\right)\big)\right\}\\ &\qquad-\varepsilon\,\boldsymbol{\Omega}\times\hat{\boldsymbol{z}}\,\nabla\cdot\left[\tfrac{1}{2}h_i\boldsymbol{u}_i+\sum_{j=i+1}^{N}h_j\boldsymbol{u}_j\right]=0.\end{aligned} \tag{2.24}$$

We thus obtain shallow water momentum equations governing the averaged horizontal fluid velocities and layer heights. We may recover the traditional multilayer shallow water equations by setting $\Omega_x = \Omega_y = 0$, or equivalently by letting ε tend to zero. The terms proportional to Ω_x and Ω_y are the corrections to the traditional shallow water equations that arise from the non-traditional components of the Coriolis force.

The final term in (2.24) may be rewritten as a time derivative using the continuity equations for the layer heights,

$$-\boldsymbol{\Omega} \times \hat{\boldsymbol{z}} \, \nabla \cdot \left[\tfrac{1}{2} h_i \boldsymbol{u}_i + \sum_{j=i+1}^{N} h_j \boldsymbol{u}_j \right] = \frac{\partial}{\partial t} \left[\boldsymbol{\Omega} \times \hat{\boldsymbol{z}} \left(\tfrac{1}{2} h_i + \sum_{j=i+1}^{N} h_j \right) \right] = \frac{\partial}{\partial t} \left(\boldsymbol{\Omega} \times \hat{\boldsymbol{z}} \, \overline{z}_i \right), \tag{2.25}$$

where $\overline{z}_i(x, y, t)$ is the vertical coordinate of the midsurface of the i^{th} layer. This term combines with the time derivative of the velocity to form the time derivative of what turns out to be the canonical momentum, as shown in §2.5.2 below. Similarly, the quantity whose gradient appears in $\nabla\{\cdot\}$ is the pressure, given by (2.12), evaluated at the midsurface $\overline{z}_i$.

2.4 Derivation from a variational principle

We may also derive our extended shallow water equations (2.24) and (2.18) from the application of Hamilton's principle of least action. Hamilton's principle gives the equations of motion for a mechanical system as being those that make the action

$$\mathcal{S} = \int_{t_0}^{t_1} \mathcal{L} \, \mathrm{d}t \tag{2.26}$$

stationary over variations that vanish at the endpoints t_0 and t_1. For example, the three-dimensional Euler equations for an incompressible, inviscid fluid may be obtained from Hamilton's principle and the Lagrangian (Eckart, 1960)

$$\mathcal{L} = \iiint \mathrm{d}a \, \mathrm{d}b \, \mathrm{d}c \, \frac{1}{2} \left| \frac{\partial \boldsymbol{x}}{\partial \tau} \right|^2 - p(\boldsymbol{a}, \tau) \left(\frac{\partial(x, y, z)}{\partial(a, b, c)} - \frac{1}{\rho_0} \right). \tag{2.27}$$

In this formulation, the most natural extension of Lagrange's formulation of particle mechanics (as in Goldstein, 1980) to hydrodynamics, fluid elements are described by their positions $\boldsymbol{x}(\boldsymbol{a}, \tau)$ as functions of a set of labels $\boldsymbol{a}$ and time τ. We have returned to using $\boldsymbol{x}$ and $\boldsymbol{a}$ to denote three-dimensional vectors. A detailed description is given in the next subsection. The first term in (2.27) is identifiable as the kinetic energy of a fluid element. The second term introduces a Lagrange multiplier $p(\boldsymbol{a}, \tau)$ to enforce incompressibility, expressed using the Jacobian of the label-to-particle map and a reference density ρ_0. By restricting the dependence of $\boldsymbol{x}$ on $\boldsymbol{a}$ so as to enforce columnar motion, one may derive various two-dimensional Lagrangians that lead to shallow water equations (Salmon, 1982b, 1988; Miles and Salmon, 1985).

2.4.1 Particle labels

Within each layer we let the positions of the fluid elements be $\boldsymbol{x}$, which we treat as functions of some particle labels $\boldsymbol{a}_i = (a_i, b_i, c_i)$ and time τ. In the i^{th} layer, $\boldsymbol{x}$ denotes the position at time τ of the particle whose label is $\boldsymbol{a}_i$. To clarify, we write

$$\boldsymbol{x} = \boldsymbol{x}_i = (x_i(\boldsymbol{a}_i, \tau), y_i(\boldsymbol{a}_i, \tau), z_i(\boldsymbol{a}_i, \tau)), \tag{2.28}$$

to reflect the dependence of $\boldsymbol{x}$ on the particle labels in each layer. We use τ for time to emphasise that $\partial/\partial\tau$ means a partial derivative at fixed labels $\boldsymbol{a}_i$ rather than at fixed position $\boldsymbol{x}_i$. Thus $\partial/\partial\tau = \partial/\partial t + \boldsymbol{u}_i \cdot \nabla$ corresponds to an advective or material derivative with the velocity field defined by $\boldsymbol{u}_i(\boldsymbol{x}_i, \tau) = \partial\boldsymbol{x}_i/\partial\tau$.

We choose the particle labels $\boldsymbol{a}_i$ to be mass-weighted coordinates that satisfy

$$\mathrm{d}a_i\mathrm{d}b_i\mathrm{d}c_i = \rho_i \, \mathrm{d}x_i\mathrm{d}y_i\mathrm{d}z_i, \tag{2.29}$$

for $i = 1, \ldots, N$. This means that the density and velocity may both be expressed in terms of the label-to-particle map $\boldsymbol{x}_i(\boldsymbol{a}_i, \tau)$. Varying this map induces coordinated variations of the density and velocity, which is what distinguishes the variational principle for a fluid from the variational principle for a cloud of non-interacting particles. In particular, the density within each layer is related to the Jacobian of the map by

$$\frac{\partial(x_i, y_i, z_i)}{\partial(a_i, b_i, c_i)} = \frac{1}{\rho_i}. \tag{2.30}$$

Differentiating this relation with respect to τ leads to the incompressibility condition (2.3c), as in Miles and Salmon (1985). Thus the continuity equation (kinematics) is incorporated in the label-to-particle map, while the momentum equation (dynamics) will come from Hamilton's principle.

2.4.2 Formulation of the multilayer Lagrangian

We formulate a Lagrangian for the multilayered system from the kinetic energies $\mathcal{T}_i$, potential energies $\mathcal{U}_i$, and pressure constraints $\mathcal{P}_i$ in each layer,

$$\begin{aligned} \mathcal{L} &= \sum_{i=1}^{N} \mathcal{T}_i - \mathcal{U}_i + \mathcal{P}_i, \qquad (2.31) \\ &= \sum_{i=1}^{N} \iiint \mathrm{d}a_i\mathrm{d}b_i\mathrm{d}c_i \, \left\{ \tfrac{1}{2} \left| \frac{\partial \boldsymbol{x}_i}{\partial \tau} + \boldsymbol{R} \right|^2 - \tfrac{1}{2} |\boldsymbol{R}|^2 - g z_i + p_i(\boldsymbol{a}_i, \tau) \left(\frac{\partial(x_i, y_i, z_i)}{\partial(a_i, b_i, c_i)} - \frac{1}{\rho_i} \right) \right\}. \end{aligned}$$

The $\boldsymbol{R}$ terms arise from the Coriolis and centrifugal forces in a rotating frame, and gz_i is the gravitational potential energy.

The Coriolis force is mathematically identical to the Lorentz force experienced by a charged particle in a magnetic field. We may therefore include the Coriolis force in Hamilton's principle by introducing a vector potential $\boldsymbol{R}$ such that

$$\boldsymbol{\nabla} \times \boldsymbol{R} = 2\,\boldsymbol{\Omega}. \tag{2.32}$$

Here $\boldsymbol{R} = (R_x, R_y, R_z)$ and $\boldsymbol{\Omega} = (\Omega_x, \Omega_y, \Omega_z)$ are both three-dimensional vectors. The $\boldsymbol{R}$ notation was introduced by Holm, Marsden, and Ratiu (1986), by analogy with the introduction of a vector potential $\boldsymbol{A}$ for the magnetic field $\boldsymbol{B} = \nabla \times \boldsymbol{A}$ when formulating the Lagrangian for a charged particle in a magnetic field (*e.g.* Goldstein, 1980). However, various special cases for particular forms of $\boldsymbol{\Omega}$ appeared earlier (*e.g.* Salmon, 1982b, 1983). Pursuing the analogy with magnetic fields, $\nabla \times \boldsymbol{R}$ is left unchanged by the gauge transformations $\boldsymbol{R} \to \boldsymbol{R} + \nabla\varphi$, which gives us some freedom in our choice of $\boldsymbol{R}$. Although $\boldsymbol{R}$ appears explicitly in the Lagrangian (2.31), the contribution from $\nabla\varphi$ to the Lagrangian reduces to a surface integral, which is readily shown to vanish at rigid boundaries. In addition, Dellar and Salmon (2005) showed that the integral over a free surface may be transformed into an exact time derivative, which gives no contribution to the action defined by (2.26). If $\boldsymbol{\Omega}$ is spatially uniform, $\boldsymbol{R} = \boldsymbol{\Omega} \times \boldsymbol{x}$ is a suitable vector potential. The combination $\frac{1}{2}|\partial \boldsymbol{x}_i/\partial\tau + \boldsymbol{R}|^2$ in (2.31) then corresponds to the kinetic energy calculated in an inertial frame. The $-\frac{1}{2}|\boldsymbol{R}|^2$ term in (2.31) subtracts out the effect of the centrifugal force, which we take to have been included in the gravitational acceleration, as explained in the Introduction.

More generally, our assumption that Ω_x and Ω_y are independent of z allows us to find a suitable $\boldsymbol{R}$ by imposing $R_z = 0$. We may then integrate the x- and y-components of (2.32) to obtain

$$\boldsymbol{R} = 2\,(F(x,y) + z\,\Omega_y, G(x,y) - z\,\Omega_x, 0) \tag{2.33}$$

where F and G are arbitrary functions arising from the integration of R_x and R_y with respect to z. We obtain a relation between F and G by substituting (2.33) and (2.2) for Ω_z into the z-component of (2.32),

$$\frac{\partial G}{\partial x} - \frac{\partial F}{\partial y} = \Omega_{z0}(x,y). \tag{2.34}$$

This construction involving F and G is identical to that used under the traditional approximation by Salmon (1982b, 1983). The remaining arbitrariness in F and G is a consequence of being able to make gauge transformations in $\boldsymbol{R}$ as described above.

2.4.3 Dimensionless variables

As before, we introduce dimensionless variables using (2.6), and also

$$F = \Omega L \tilde{F}, \quad G = \Omega L \tilde{G}, \quad \tau = L/U\tilde{\tau}, \quad \mathcal{L} = \frac{\tilde{\mathcal{L}}}{2\rho_1 \varepsilon L^4 \Omega U}. \tag{2.35}$$

We also introduce the dimensionless particle labels defined by

$$a_i = \rho_i^{1/3} L\tilde{a}_i, \quad b_i = \rho_i^{1/3} L\tilde{b}_i, \quad c_i = \rho_i^{1/3} \varepsilon L\tilde{c}_i, \tag{2.36}$$

so that the incompressibility condition (2.30) becomes

$$\frac{\partial(\tilde{x}_i, \tilde{y}_i, \tilde{z}_i)}{\partial(\tilde{a}_i, \tilde{b}_i, \tilde{c}_i)} = 1. \tag{2.37}$$

Here $\varepsilon \ll 1$ is introduced again to enforce the assumption that the layers of fluid are shallow.

We thus obtain the dimensionless Lagrangian

$$\begin{aligned}\tilde{\mathcal{L}} = \sum_{i=1}^{N} \frac{\rho_i}{\rho_1} \iiint \mathrm{d}\tilde{a}_i \mathrm{d}\tilde{b}_i \mathrm{d}\tilde{c}_i \Bigg\{ &\tfrac{1}{2}\mathrm{Ro}\left(\left(\frac{\partial \tilde{x}_i}{\partial \tilde{\tau}}\right)^2 + \left(\frac{\partial \tilde{y}_i}{\partial \tilde{\tau}}\right)^2 + \varepsilon^2 \left(\frac{\partial \tilde{z}_i}{\partial \tilde{\tau}}\right)^2\right) \\ &- \mathrm{Bu}\, \tilde{z}_i + \varepsilon\left(\frac{\partial \tilde{x}_i}{\partial \tilde{\tau}}\tilde{\Omega}_y - \frac{\partial \tilde{y}_i}{\partial \tilde{\tau}}\tilde{\Omega}_x\right)\tilde{z}_i + \left(\frac{\partial \tilde{x}_i}{\partial \tilde{\tau}}\tilde{F} + \frac{\partial \tilde{y}_i}{\partial \tilde{\tau}}\tilde{G}\right) \\ &+ \tilde{p}_i(\tilde{\boldsymbol{a}}_i, \tau)\left(\frac{\partial(\tilde{x}_i, \tilde{y}_i, \tilde{z}_i)}{\partial(\tilde{a}_i, \tilde{b}_i, \tilde{c}_i)} - 1\right)\Bigg\}. \end{aligned} \tag{2.38}$$

We now drop the tilde ˜ notation, with the understanding that all variables used henceforth are dimensionless.

2.4.4 Restriction to columnar motion

In §2.3, we demonstrated that z-independent horizontal velocity satisfies the governing equations at leading order in ε. We will therefore follow Salmon (1983, 1988) and Miles and Salmon (1985) and restrict the fluid to columnar motion by assuming that $x_i = x_i(a_i, b_i, \tau)$ and $y_i = y_i(a_i, b_i, \tau)$ are independent of the vertical particle label c_i. Equation (2.37) then simplifies to

$$\frac{\partial z_i}{\partial c_i} = \frac{\partial(a_i, b_i)}{\partial(x_i, y_i)}. \tag{2.39}$$

Choosing $c_i = 0$ at the bottom of each layer, and $c_i = 1$ at the top, we may integrate (2.39) with respect to c_i to determine z_i,

$$z_i = h_i c_i + \eta_{i+1}. \tag{2.40}$$

This defines h_i as the reciprocal of the Jacobian of the horizontal particle positions and labels,

$$h_i = \left(\frac{\partial(x_i, y_i)}{\partial(a_i, b_i)}\right)^{-1}. \tag{2.41}$$

We write the expression this way to emphasise that h_i is more naturally treated as a function of the particle labels a_i and b_i, rather than the particle positions x_i and y_i. Differentiating $h_i(a_i, b_i, \tau)$ with respect to τ leads to the layer-averaged continuity equation (2.18), as in Miles and Salmon (1985). Substituting (2.41) into (2.40) gives

$$z_i = h_i c_i + \eta_{i+1} = h_i c_i + h_b + \sum_{j=i+1}^{N} h_j = h_i c_i + h_b + \sum_{j=i+1}^{N} \frac{\partial(a_j, b_j)}{\partial(x_j, y_j)}, \tag{2.42}$$

where $h_b(x,y) = \eta_{N+1}(x,y)$ is the height of the bottom topography. The vertical coordinate in each layer therefore acquires a dependence on the particle labels in all of the layers below. It is this dependence that allows each layer to respond to the motion of the layers above and below it.

Substituting these expressions into the Lagrangian (2.38) we obtain

$$\mathcal{L} = \sum_{i=1}^{N} \frac{\rho_i}{\rho_1} \iint \mathrm{d}a_i \mathrm{d}b_i \int_0^1 \mathrm{d}c_i \left\{ \tfrac{1}{2}\mathrm{Ro}\left(\frac{\partial x_i}{\partial \tau}\right)^2 + \tfrac{1}{2}\mathrm{Ro}\left(\frac{\partial y_i}{\partial \tau}\right)^2 + \left(\frac{\partial x_i}{\partial \tau}F + \frac{\partial y_i}{\partial \tau}G\right) - \left(\mathrm{Bu} + \varepsilon\frac{\partial y_i}{\partial \tau}\Omega_x - \varepsilon\frac{\partial x_i}{\partial \tau}\Omega_y\right)(h_i c_i + \eta_{i+1}) \right\}. \tag{2.43}$$

The pressure terms involving the Lagrange multipliers $\tilde{p}_i(\tilde{\boldsymbol{a}}_i, \tau)$ have been discarded because our c_i to z_i map has been explicitly constructed to enforce incompressibility. We have also discarded terms $O(\varepsilon^2)$ and above, as in §2.3, so we have also dropped the $(\partial z_i/\partial\tau)^2$ term from (2.38) to obtain (2.43). Miles and Salmon (1985) showed that retaining this term in a single layer leads to the equations derived by Green and Naghdi (1976) using Cosserat surfaces.

We may now complete the integration over c_i in (2.43) to obtain the two-dimensional "shallow water" Lagrangian

$$\mathcal{L} = \sum_{i=1}^{N} \frac{\rho_i}{\rho_1} \iint \mathrm{d}a_i \mathrm{d}b_i \left\{ \tfrac{1}{2}\mathrm{Ro}\left(\frac{\partial x_i}{\partial \tau}\right)^2 + \tfrac{1}{2}\mathrm{Ro}\left(\frac{\partial y_i}{\partial \tau}\right)^2 + \left(\frac{\partial x_i}{\partial \tau}F + \frac{\partial y_i}{\partial \tau}G\right) - \left(\mathrm{Bu} + \varepsilon\frac{\partial y_i}{\partial \tau}\Omega_x - \varepsilon\frac{\partial x_i}{\partial \tau}\Omega_y\right)(\tfrac{1}{2}h_i + \eta_{i+1}) \right\}. \tag{2.44}$$

The integration over c_i leads to the appearance of $(\frac{1}{2}h_i + \eta_{i+1})$ in the last term in the integrand. Since z_i depends linearly on c_i through (2.42), the average of any quantity that varies linearly in z_i across a layer is equal to the quantity evaluated at the mid-point of the layer.

2.4.5 Derivation of momentum equations

The most straightforward route to the shallow water equations is to require that the variations of $\mathcal{L}$ with respect to $\boldsymbol{x}_i(\boldsymbol{a}_i, \tau)$ vanish, in accordance with Hamilton's principle of least action. Having integrated over the third direction, we now return to two-dimensional vector notation and set $\boldsymbol{x}_i = (x_i, y_i)$ and $\boldsymbol{a}_i = (a_i, b_i)$. We first note that we may transform between integrals over particle labels $\mathrm{d}a_j\mathrm{d}b_j$ and $\mathrm{d}a_i\mathrm{d}b_i$ using (2.41) in the form

$$\iint \mathrm{d}a_j\mathrm{d}b_j \; A = \iint \mathrm{d}x_j\mathrm{d}y_j \; h_j A = \iint \mathrm{d}x_i\mathrm{d}y_i \; h_j A = \iint \mathrm{d}a_i\mathrm{d}b_i \; \frac{h_j A}{h_i}, \tag{2.45}$$

for any A and $j \neq i$. We see that when varying $\boldsymbol{x}_i(\boldsymbol{a}_i, \tau)$, we must transform all integrals $\mathrm{d}a_j\mathrm{d}b_j$ to determine their contribution to the variation. We therefore apply (2.45) to transform the Lagrangian

in (2.44) into an integral over the labels in the i^{th} layer,

$$\mathcal{L} = \iint \mathrm{d}a_i \mathrm{d}b_i \sum_{j=1}^{N} \frac{\rho_j h_j}{\rho_1 h_i} \left\{ \tfrac{1}{2}\mathrm{Ro}\left(\frac{\partial x_j}{\partial \tau}\right)^2 + \tfrac{1}{2}\mathrm{Ro}\left(\frac{\partial y_j}{\partial \tau}\right)^2 + \left(\frac{\partial x_j}{\partial \tau}F + \frac{\partial y_j}{\partial \tau}G\right) \right.$$
$$\left. - \left(\mathrm{Bu} + \varepsilon\frac{\partial y_j}{\partial \tau}\Omega_x - \varepsilon\frac{\partial x_j}{\partial \tau}\Omega_y\right)\left(\tfrac{1}{2}h_j + B + \sum_{k=j+1}^{N} h_k\right)\right\}. \tag{2.46}$$

A more explicit approach to the transformation of integrals between layers was used by Salmon (1982b) and is described briefly in an Appendix. A different approach that avoids this technicality completely is described in §2.4.6 below.

When taking variations of $\boldsymbol{x}_i$, we assume that $\partial \boldsymbol{x}_j/\partial\tau$ and h_j for all $j \neq i$ are prescribed functions of $\boldsymbol{x}$ evaluated at $\boldsymbol{x}_i$. For this we use the (nonvarying) label-to-particle maps in the layers $j \neq i$, and their inverses. Similarly, h_b, F, G, Ω_x and Ω_y are all treated as prescribed functions of $\boldsymbol{x}$ evaluated at $\boldsymbol{x}_i$. The variation of any prescribed function $A(\boldsymbol{x})$ with respect to $\boldsymbol{x}_i$ is (Miles and Salmon, 1985)

$$\delta A = \nabla A \cdot \boldsymbol{\delta x}_i. \tag{2.47}$$

To resolve the implicit dependence of h_i on $\boldsymbol{x}_i$ we rewrite (2.41) as

$$h_i \frac{\partial(x_i, y_i)}{\partial(a_i, b_i)} = 1, \tag{2.48}$$

and take variations

$$\begin{aligned} 0 = \delta\left(h_i \frac{\partial(x_i, y_i)}{\partial(a_i, b_i)}\right) &= \delta h_i \frac{\partial(x_i, y_i)}{\partial(a_i, b_i)} + h_i \frac{\partial(\delta x_i, y_i)}{\partial(a_i, b_i)} + h_i \frac{\partial(x_i, \delta y_i)}{\partial(a_i, b_i)} \\ &= \frac{\delta h_i}{h_i} + h_i \frac{\partial(x_i, y_i)}{\partial(a_i, b_i)}\left[\frac{\partial(\delta x_i, y_i)}{\partial(x_i, y_i)} + \frac{\partial(x_i, \delta y_i)}{\partial(x_i, x_i)}\right] \\ &= \frac{\delta h_i}{h_i} + \frac{\partial \delta x_i}{\partial x_i} + \frac{\partial \delta y_i}{\partial y_i}, \end{aligned} \tag{2.49}$$

to obtain (Miles and Salmon, 1985)

$$\delta h_i = -h_i \nabla \cdot \boldsymbol{\delta x}_i. \tag{2.50}$$

For an arbitrary quantity Q multiplying the variation δh_i, we obtain (Miles and Salmon, 1985)

$$\iint \mathrm{d}a_i \mathrm{d}b_i \, Q \delta h_i = -\iint \mathrm{d}a_i \mathrm{d}b_i \, Q h_i \nabla \cdot \boldsymbol{\delta x}_i = \iint \mathrm{d}a_i \mathrm{d}b_i \, \frac{1}{h_i} \nabla\left(h_i^2 Q\right) \cdot \boldsymbol{\delta x}_i. \tag{2.51}$$

The second step follows from a transformation to an integral with respect to $\mathrm{d}x\mathrm{d}y$, integration by parts, and then a transformation back to an integral in $\mathrm{d}a_i\mathrm{d}b_i$.

We now show that the majority of the terms in the integrand in (2.46) make no contribution when we vary $\boldsymbol{x}_i$. For any prescribed function $A(\boldsymbol{x})$, the variation of the functional $\mathcal{L}_A$ defined by

$$\mathcal{L}_A = \iint \mathrm{d}a_i \mathrm{d}b_i \, \frac{A}{h_i}, \tag{2.52}$$

is given by

$$\delta\mathcal{L}_A = \iint \mathrm{d}a_i\mathrm{d}b_i\ \frac{1}{h_i}\delta A - \frac{A}{h_i^2}\delta h_i = \iint \mathrm{d}a_i\mathrm{d}b_i\ \frac{1}{h_i}\nabla A\cdot\boldsymbol{\delta x}_i - \frac{1}{h_i}\nabla\left(\frac{h_i^2 A}{h_i^2}\right)\cdot\boldsymbol{\delta x}_i = 0. \tag{2.53}$$

As we treat $\partial\boldsymbol{x}_j/\partial\tau$ and h_j as prescribed functions of $\boldsymbol{x}$ when varying $\boldsymbol{x}_i$ with $i\neq j$, many of the terms in (2.46) are of the form (2.53), and therefore make no contribution under variations of $\boldsymbol{x}_i$. Thus, when we take variations of $\mathcal{L}$ with respect to $\boldsymbol{x}_i$, we may drop all such terms, leaving

$$\begin{aligned}\delta\int \mathrm{d}\tau\mathcal{L} = \delta\int \mathrm{d}\tau\iint \mathrm{d}a_i\mathrm{d}b_i\frac{\rho_i}{\rho_1}\Bigg\{&-\sum_{j=1}^{i-1}\frac{\rho_j}{\rho_i}h_j\left(\mathrm{Bu}+\varepsilon\frac{\partial y_j}{\partial\tau}\Omega_x-\varepsilon\frac{\partial x_j}{\partial\tau}\Omega_y\right)\\ &+\tfrac{1}{2}\mathrm{Ro}\left(\frac{\partial x_i}{\partial\tau}\right)^2+\tfrac{1}{2}\mathrm{Ro}\left(\frac{\partial y_i}{\partial\tau}\right)^2+\left(\frac{\partial x_i}{\partial\tau}F+\frac{\partial y_i}{\partial\tau}G\right)\\ &-\left(\mathrm{Bu}+\varepsilon\frac{\partial y_i}{\partial\tau}\Omega_x-\varepsilon\frac{\partial x_i}{\partial\tau}\Omega_y\right)\left(\tfrac{1}{2}h_i+\eta_{i+1}\right)\Bigg\}.\end{aligned} \tag{2.54}$$

Thus, we are essentially taking variations of the Lagrangian for a single layer of shallow water flowing over a prescribed lower surface $\eta_{i+1}(\boldsymbol{x},t)$, as in Dellar and Salmon (2005), but with additional contributions due to the pressure inherited from each of the layers above (2.12).

Using (2.47) and (2.51) to compute the variation of (2.44) with respect to $\boldsymbol{x}_i$ gives

$$\begin{aligned}\delta\int \mathrm{d}\tau\mathcal{L} = \int \mathrm{d}\tau\iint \mathrm{d}a_i\mathrm{d}b_i\frac{\rho_i}{\rho_1}\Bigg\{&-\mathrm{Ro}\,\frac{\partial^2\boldsymbol{x}_i}{\partial\tau^2}-\mathrm{Bu}\,\nabla\eta_i\\ &-\nabla\left[\sum_{j=1}^{i-1}\frac{\rho_j}{\rho_i}h_j\left(\mathrm{Bu}+\varepsilon\frac{\partial y_j}{\partial\tau}\Omega_x-\varepsilon\frac{\partial x_j}{\partial\tau}\Omega_y\right)\right]\\ &+\frac{\partial x_i}{\partial\tau}\nabla F_i+\frac{\partial y_i}{\partial\tau}\nabla G_i-\frac{\partial}{\partial\tau}(F_i,G_i)\\ &+\varepsilon\left(\tfrac{1}{2}h_i+\eta_{i+1}\right)\left(\frac{\partial x_i}{\partial\tau}\nabla\Omega_y-\frac{\partial y_i}{\partial\tau}\nabla\Omega_x\right)\\ &+\varepsilon\left(\frac{\partial x_i}{\partial\tau}\Omega_y-\frac{\partial y_i}{\partial\tau}\Omega_x\right)\nabla\left(\tfrac{1}{2}h_i+\eta_{i+1}\right)\\ &+\varepsilon\frac{\partial}{\partial\tau}\left(\left(\tfrac{1}{2}h_i+\eta_{i+1}\right)(-\Omega_y,\Omega_x)\right)\\ &+\tfrac{1}{2}\varepsilon\nabla\left[h_i\left(\frac{\partial x_i}{\partial\tau}\Omega_y-\frac{\partial y_i}{\partial\tau}\Omega_x\right)\right]\Bigg\}\cdot\boldsymbol{\delta x}_i,\end{aligned} \tag{2.55}$$

for $i=1,\ldots,N$. Rewriting the material time derivatives as $\partial/\partial\tau=\partial/\partial t+\boldsymbol{u}_i\cdot\nabla$, the terms involving F_i and G_i combine to give

$$u_i\nabla F_i+v_i\nabla G_i-(\boldsymbol{u}_i\cdot\nabla F_i,\boldsymbol{u}_i\cdot\nabla G_i)=(G_{ix}-F_{iy})(v_i,-u_i), \tag{2.56}$$

and $G_{ix}-F_{iy}=\Omega_{z0}$ using (2.34). Hamilton's principle, setting the integrand of (2.55) equal to zero, thus gives the same equations of motion (2.24) as before.

2.4.6 Alternative formulation using a separate Lagrangian for each layer

In the previous approach the different layers were coupled together through the label-to-particle map. The map from the label c_i to the vertical position z_i depended upon the heights of every layer underneath. Varying the map from c_i to z_i would raise or lower every layer above, and thus change these layers' contributions to the gravitational potential energy. This is the natural way to include the pressure exerted by the layers above, but taking variations is complicated by the need to transform integrals over the upper layers into integrals with respect to a_i, b_i, c_i.

In this section we describe a different derivation that uses a separate Lagrangian $\mathcal{L}_i$ for each layer of fluid. The label-to-particle map in each layer may be varied independently, making the derivation of the equations of motion much simpler. In particular, this approach would be much more attractive for deriving multilayer analogues of the Green and Naghdi (1976) equations that retain the vertical kinetic energy $\frac{1}{2}\dot{z}_i^2$ in each layer.

We begin with a three-dimensional Lagrangian, as before, and decompose it into the sum of contributions from each of the different layers. This leads to a Lagrangian for the multilayer system that is the sum of separate Lagrangians for each layer. The layers are coupled through an additional term representing the work done by the pressure in the layers above, analogous to the treatment of external pressure in Miles and Salmon (1985).

Returning to three-dimensional notation, we may formulate a Lagrangian for the i^{th} layer as

$$\mathcal{L}_i = \mathcal{T}_i - \mathcal{U}_i + \mathcal{P}_i + \mathcal{W}_i, \tag{2.57}$$

where $\mathcal{T}_i$ and $\mathcal{U}_i$ are the kinetic and potential energies given in (2.31), and $\mathcal{P}_i$ is a incompressibility constraint that contains the pressure p_i as a Lagrange multiplier p_i. So far this is exactly the same as in Eckart (1960) and §2.4.2 above. The extra contribution $\mathcal{W}_i$ is the work done on the upper surface of each layer by the layers above,

$$\mathcal{W}_i = \iiint \mathrm{d}a_i \mathrm{d}b_i \mathrm{d}c_i \, \Big\{ -\frac{1}{\rho_i} P_i(x_i, y_i, \tau) \Big\}, \tag{2.58}$$

treated analogously to the imposed external pressure on a single fluid layer in Miles and Salmon (1985). Thus $P_i(x_i, y_i, \tau)$ is the pressure exerted on layer i by the layers above.

We may therefore write the complete three-dimensional Lagrangian as

$$\begin{aligned} \mathcal{L}_i = \iiint \mathrm{d}a_i \mathrm{d}b_i \mathrm{d}c_i \, \Bigg\{ & \tfrac{1}{2} \left| \frac{\partial \boldsymbol{x}_i}{\partial \tau} + \boldsymbol{R} \right|^2 - \tfrac{1}{2} |\boldsymbol{R}|^2 - g z_i \\ & + p_i(\boldsymbol{a}_i, \tau) \left(\frac{\partial(x_i, y_i, z_i)}{\partial(a_i, b_i, c_i)} - \frac{1}{\rho_i} \right) - \frac{1}{\rho_i} P_i(\boldsymbol{x}_i, \tau) \Bigg\}. \end{aligned} \tag{2.59}$$

Taking variations of (2.59) with respect to x_i, y_i z_i, and p_i, and invoking Hamilton's principle of least action, we recover (2.3a), (2.3b), and (2.30), respectively. In (2.3a), p_i is replaced by $p_i + P_i$

and the pressure boundary condition is modified to $p_i = 0$ on $z = \eta_i$. The inclusion of P_i thereby accounts for the pressure imposed in layer i by the fluid in the layers above.

We now apply the nondimensionalisations in (2.6), (2.35) and (2.36) to the Lagrangian in (2.59), dropping the tilde ($\tilde{}$) notation for dimensionless variables,

$$\begin{aligned}\mathcal{L}_i = \iiint \mathrm{d}a_i \mathrm{d}b_i \mathrm{d}c_i \; \Bigg\{ & \tfrac{1}{2}\mathrm{Ro}\left(\frac{\partial x_i}{\partial \tau}\right)^2 + \tfrac{1}{2}\mathrm{Ro}\left(\frac{\partial y_i}{\partial \tau}\right)^2 - \mathrm{Bu}\, z_i \\ & + \; \varepsilon\left(\frac{\partial x_i}{\partial \tau}\Omega_y - \frac{\partial y_i}{\partial \tau}\Omega_x\right) z_i + \left(\frac{\partial x_i}{\partial \tau}F + \frac{\partial y_i}{\partial \tau}G\right) \\ & + \; p_i(\boldsymbol{a}_i, \tau)\left(\frac{\partial(x_i, y_i)}{\partial(a_i, b_i)}\frac{\partial z_i}{\partial c_i} - 1\right) - P_i(x_i, y_i, \tau)\Bigg\}. \end{aligned} \tag{2.60}$$

Here we have introduced the shallow water assumptions, restricting x_i and y_i to be independent of c_i, and neglecting terms of $\mathrm{O}(\varepsilon^2)$. To determine $P_i(x_i, y_i, \tau)$, the unknown pressures exerted on the upper surface of each layer, we consider variations of (2.60) with respect to z_i alone,

$$\begin{aligned}\delta \int \mathrm{d}\tau \mathcal{L}_i = \int \mathrm{d}\tau \iiint \mathrm{d}a_i \mathrm{d}b_i \mathrm{d}c_i \Bigg\{ & -\mathrm{Bu} \\ & - \frac{\partial(x_i, y_i)}{\partial(a_i, b_i)}\frac{\partial p_i}{\partial c_i} - \varepsilon\left(\frac{\partial y_i}{\partial \tau}\Omega_x - \frac{\partial x_i}{\partial \tau}\Omega_y\right)\Bigg\}\delta z_i. \end{aligned} \tag{2.61}$$

Hamilton's principle states that leading order variations of the action with respect to z_i must vanish, so it follows that the integrand in (2.61) must be uniformly equal to zero. Using (2.41) to evaluate the Jacobian multiplying $\partial p_i/\partial c_i$, this yields

$$\frac{\partial p_i}{\partial c_i} = h_i\left(\mathrm{Bu} + \varepsilon\, v_i\Omega_x - \varepsilon\, u_i\Omega_y\right). \tag{2.62}$$

This is equivalent to what White and Bromley (1995) call quasihydrostatic balance in the vertical momentum equation. We may thus determine p_i by integrating with respect to c_i,

$$p_i = p_i|_{c_i=1} + (1 - c_i)h_i\left(\mathrm{Bu} + \varepsilon\, v_i\Omega_x - \varepsilon\, u_i\Omega_y\right). \tag{2.63}$$

The Lagrangian pressure boundary condition is

$$\rho_i p_i\Big|_{c_i=1} = \rho_{i-1}p_{i-1}\Big|_{c_{i-1}=0}, \tag{2.64}$$

which corresponds to continuity of the dimensional pressure at the interface. We let $P_1 = 0$, corresponding to the stress-free boundary condition on the upper surface of the top layer, and let

$$P_i = \frac{\rho_{i-1}}{\rho_i}p_{i-1}\Big|_{c_i=1} = \sum_{j=1}^{i-1}\frac{\rho_j}{\rho_i}P_j = \sum_{j=1}^{i-1}\frac{\rho_j}{\rho_i}h_j\left(\mathrm{Bu} + \varepsilon\, v_j\Omega_x - \varepsilon\, u_j\Omega_y\right), \tag{2.65}$$

for $i = 2, \ldots, N$. This expression for the pressure acting on the upper surface of each layer is the same as the expression calculated by layer averaging in (2.12).

We now simplify (2.60) using the assumption of columnar motion, as in §2.4.2 above. The definitions (2.40) and (2.41) mean that (2.30) is satisfied automatically, so we may drop the terms multiplied by p_i in the Lagrangian. We may then integrate with respect to c_i by substituting in (2.40), leading to a two-dimensional 'shallow water' Lagrangian,

$$\begin{aligned}
\mathcal{L}_i \;=\; & \iint \mathrm{d}a_i \mathrm{d}b_i \int_0^1 \mathrm{d}c_i \; \left\{ \tfrac{1}{2}\mathrm{Ro}\left(\frac{\partial x_i}{\partial \tau}\right)^2 + \tfrac{1}{2}\mathrm{Ro}\left(\frac{\partial y_i}{\partial \tau}\right)^2 - P_i \right. \\
& \left. - \left(\mathrm{Bu} + \varepsilon \frac{\partial y_i}{\partial \tau}\Omega_x - \varepsilon \frac{\partial x_i}{\partial \tau}\Omega_y\right)(h_i c_i + \eta_{i+1}) + \left(\frac{\partial x_i}{\partial \tau}F + \frac{\partial y_i}{\partial \tau}G\right)\right\} \\
=\; & \iint \mathrm{d}a_i \mathrm{d}b_i \left\{ \tfrac{1}{2}\mathrm{Ro}\left(\frac{\partial x_i}{\partial \tau}\right)^2 + \tfrac{1}{2}\mathrm{Ro}\left(\frac{\partial y_i}{\partial \tau}\right)^2 - \mathrm{Bu}\left(\tfrac{1}{2}h_i + \eta_{i+1}\right) - P_i \right. \\
& \left. + \varepsilon\left(\frac{\partial x_i}{\partial \tau}\Omega_y - \frac{\partial y_i}{\partial \tau}\Omega_x\right)\left(\tfrac{1}{2}h_i + \eta_{i+1}\right) + \left(\frac{\partial x_i}{\partial \tau}F + \frac{\partial y_i}{\partial \tau}G\right)\right\}. \qquad (2.66)
\end{aligned}$$

Thus, we recover the effective Lagrangian (2.54) used to take variations with respect to $\boldsymbol{x}_i$ in §2.4.5.

2.5 Conservation properties

We now show that our non-traditional multilayer shallow water equations inherit the expected conservation laws for energy, momentum, and potential vorticity from the underlying three-dimensional equations. The existence of these conservation laws is guaranteed by our variational formulation in §2.4, and Noether's theorem that relates symmetries in a variational principle to conservation laws (*e.g.* Goldstein, 1980). Conservation of energy and momentum are consequences of symmetries under translations in time and space, while material conservation of potential vorticity follows from a more subtle symmetry under relabelling of the particles (Ripa, 1981; Salmon, 1982a, 1988, 1998).

2.5.1 Energy conservation

An equation expressing conservation of energy may be obtained either by manipulating the extended shallow water equations (2.24), or by a Legendre transformation of the Lagrangian (2.44). The latter approach corresponds to finding the quantity that is conserved under time translation, as required by Noether's theorem (*e.g.* Goldstein, 1980; Salmon, 1998) since the Lagrangian does not depend explicitly upon τ. We present the energy conservation law in dimensional form for ease of

interpretation,

$$\frac{\partial}{\partial t}\left\{\sum_{i=1}^{N}\tfrac{1}{2}\rho_i h_i\left|\boldsymbol{u}_i\right|^2+\tfrac{1}{2}\rho_i g h_i\left(\eta_i+\eta_{i+1}\right)\right\}$$
$$+\nabla\cdot\left\{\sum_{i=1}^{N}h_i\boldsymbol{u}_i\left(\tfrac{1}{2}\rho_i\left|\boldsymbol{u}_i\right|^2+\rho_i g\eta_i+\rho_i h_i\left(v_i\Omega_x-u_i\Omega_y\right)\right.\right. \tag{2.67}$$
$$\left.\left.+\sum_{j=1}^{i-1}\rho_j g h_j+2\rho_j h_j\left(v_j\Omega_x-u_j\Omega_y\right)\right)\right\}=0.$$

As usual, the energy density is unaffected by the Coriolis force, and is simply the sum of the integrals of the three-dimensional energy density $\frac{1}{2}\rho_i\left|\boldsymbol{u}_i\right|^2+\rho_i g z$ over each layer. However, the energy flux differs from the standard shallow water form by terms proportional to Ω_x and Ω_y. These extra terms represent the work done by the quasihydrostatic (as opposed to purely hydrostatic) pressure.

2.5.2 Canonical momenta

The canonical momenta are best considered using the standard axes of geophysical fluid dynamics. We take the x-axis pointing East, and the y-axis pointing North, so that $\Omega_x=0$, $\Omega_y=\Omega_y(y)$ and $\Omega_{z0}=\Omega_{z0}(y)$. We first turn our attention to the zonal momentum, which we expect to be conserved when the Lagrangian contains no explicit dependence on x. We therefore choose $G=0$ and $F(y)=-\int\Omega_{z0}(y)\mathrm{d}y$, as in Salmon (1982b). We also assume a zonally symmetric topography $\eta_{N+1}(y)$ with no x-dependence. The shallow water Lagrangian (2.44) then becomes

$$\mathcal{L}=\sum_{i=1}^{N}\frac{\rho_i}{\rho_1}\iint\mathrm{d}a_i\mathrm{d}b_i\left\{\tfrac{1}{2}\mathrm{Ro}\left|\dot{\boldsymbol{x}}_i\right|^2+\dot{x}_i F+\left(\varepsilon\dot{x}_i\Omega_y-\mathrm{Bu}\right)\left(\tfrac{1}{2}h_i+\eta_{i+1}\right)\right\}, \tag{2.68}$$

where $\dot{\boldsymbol{x}}_i=(\dot{x}_i,\dot{y}_i)=(\partial x/\partial\tau,\partial y/\partial\tau)$. The canonical momenta in the x direction are given by

$$p_{ix}=\frac{\delta\mathcal{L}}{\delta\dot{x}_i}=\mathrm{Ro}\,u_i+F+\varepsilon\,\Omega_y\left(\tfrac{1}{2}h_i+\eta_{i+1}\right). \tag{2.69}$$

We do not expect any individual canonical momentum p_{ix} to be conserved. When we take variations with respect to x_i, the $\boldsymbol{x}_j$ and h_j in the other layers ($j\neq i$) are treated as prescribed functions of x_i, so there is no symmetry associated with translations in x_i alone. In other words, the form drag due to tilted interfaces between layers transfers momentum between layers.

However, there is a symmetry if we translate all of the x_i simultaneously by the same amount, letting $x_i\to x_i+\delta x$ with the same variation δx for each $i=1,\ldots,N$. The resulting variation of

the Lagrangian (2.68) is

$$\delta\int \mathrm{d}\tau\mathcal{L} = \int \mathrm{d}\tau \sum_{i=1}^{N} \frac{\rho_i}{\rho_1} \iint \mathrm{d}a_i\mathrm{d}b_i \left\{ \left(\mathrm{Ro}\,\dot{x}_i + F + \varepsilon\,\Omega_y\left(\tfrac{1}{2}h_i + \eta_{i+1}\right)\right) \frac{\partial(\delta x)}{\partial\tau} \right.$$
$$\left. +\ (\varepsilon\dot{x}_i\Omega_y - \mathrm{Bu}) \left(\tfrac{1}{2}\delta h_i + \sum_{j=i+1}^{N} \delta h_j\right) \right\}. \tag{2.70}$$

Using $\delta h_i = -h_i\partial(\delta x)/\partial x$ for variations in x_i, we find that

$$\iint \mathrm{d}a_i\mathrm{d}b_i\, A\,\delta h_j = -\iint \mathrm{d}a_i\mathrm{d}b_i\, Ah_j\frac{\partial(\delta x)}{\partial x} = \iint \mathrm{d}a_i\mathrm{d}b_i\,\frac{1}{h_i}\frac{\partial}{\partial x}\left(h_ih_jA\right)\delta x \tag{2.71}$$

for an arbitrary function A and any i and j. This result is very similar to (2.51), in that the second equality follows from a transformation to an integral over $\mathrm{d}x\mathrm{d}y$, integration by parts, and then transformation back to an integral over $\mathrm{d}a_i\mathrm{d}b_i$. It allows us to simplify (2.70) into

$$\delta\int \mathrm{d}\tau\mathcal{L} = \iint \mathrm{d}a_1\mathrm{d}b_1 \int \mathrm{d}\tau \sum_{i=1}^{N} \frac{\rho_i}{\rho_1}\frac{h_i}{h_1} \left\{ -\frac{\partial}{\partial\tau_i}\left(\mathrm{Ro}\,\dot{x}_i + F + \varepsilon\,\Omega_y\left(\tfrac{1}{2}h_i + \eta_{i+1}\right)\right) \right.$$
$$\left. +\ \frac{1}{h_i}\frac{\partial}{\partial x}\left[h_i\left(\varepsilon\dot{x}_i\Omega_y - \mathrm{Bu}\right)\left(\tfrac{1}{2}h_i + \sum_{j=i+1}^{N} h_j\right)\right]\right\}\delta x, \tag{2.72}$$

where we have used (2.45) to transform each of the integrals $\mathrm{d}a_i\mathrm{d}b_i$ for $i = 2,\ldots N$ into an integral $\mathrm{d}a_1\mathrm{d}b_1$. We write $\partial/\partial\tau_i = \partial/\partial t + \boldsymbol{u}_i\cdot\nabla$ for the material time derivative in layer i.

By Hamilton's principle of least action, the integrand in (2.72) must be equal to zero. Redimensionalising and using (2.18), we obtain the momentum conservation equation

$$\frac{\partial}{\partial t}\left(\sum_{i=1}^{N}\rho_ih_ip_{ix}\right) + \nabla\cdot\left\{\rho_ih_ip_{ix}\boldsymbol{u}_i + \rho_ih_i\left(g - 2\Omega_yu_i\right)\left(\tfrac{1}{2}h_i + \sum_{j=i+1}^{N}h_j\right)\hat{\boldsymbol{x}}\right\} = 0. \tag{2.73}$$

Thus, the conserved total zonal momentum is a weighted sum of the canonical momenta over the layers.

If Ω_y, Ω_{z0}, and η_{N+1} are all constants, we may find a similar conservation law for the meridional momentum by choosing $F = 0$ and $G = x\Omega_{z0}$. The shallow water Lagrangian now takes the form

$$\mathcal{L} = \sum_{i=1}^{N}\frac{\rho_i}{\rho_1}\iint \mathrm{d}a_i\mathrm{d}b_i\left\{\tfrac{1}{2}\mathrm{Ro}\,|\dot{\boldsymbol{x}}_i|^2 + \dot{y}_iG + (\varepsilon\dot{x}_i\Omega_y - \mathrm{Bu})\left(\tfrac{1}{2}h_i + \eta_{i+1}\right)\right\}, \tag{2.74}$$

and the canonical y-momenta are now given by

$$p_{iy} = \frac{\delta\mathcal{L}}{\delta\dot{y}_i} = \mathrm{Ro}\,v_i + x\Omega_{z0}. \tag{2.75}$$

We thus obtain a conservation law for the y-momentum by a process similar to that described above,

$$\frac{\partial}{\partial t}\left(\sum_{i=1}^{N}\rho_ih_ip_{iy}\right) + \nabla\cdot\left\{\rho_ih_ip_{iy}\boldsymbol{u}_i + \rho_ih_i\left(g - 2\Omega_yu_i\right)\left(\tfrac{1}{2}h_i + \sum_{j=i+1}^{N}h_j\right)\hat{\boldsymbol{y}}\right\} = 0. \tag{2.76}$$

There is no one choice for F and G that allows us to express conservation of x- and y-momentum simultaneously, but there are two conserved components of momentum when the rotation vector and the bottom topography are constants. On a beta-plane, for example, we would not expect a conserved meridional momentum because Ω_z depends explicitly on latitude y. We also see that the conserved zonal momentum contains terms proportional to Ω_y, whilst the conserved meridional momentum does not depend upon Ω_y. In these standard axes the non-traditional components of the Coriolis force act vertically and zonally, but not meridionally, see (2.3a-c).

2.5.3 Potential vorticity

Material conservation of potential vorticity is even more important in geophysical fluid dynamics than conservation of energy and momentum. Both the latter quantities may be transported over large distances by waves, while potential vorticity remains tied to fluid particles. Each layer of our equations possesses a potential vorticity q_i that obeys the conservation law $\partial_t q_i + \boldsymbol{u}_i \cdot \nabla q_i = 0$, with

$$q_i = \frac{1}{h_i}\left\{\left[\Omega_{z0} - \tfrac{1}{2}\varepsilon\nabla\cdot\left(\left(\eta_i+\eta_{i+1}\right)\boldsymbol{\Omega}\right)\right] + \mathrm{Ro}\left(\frac{\partial v_i}{\partial x} - \frac{\partial u_i}{\partial y}\right)\right\}. \tag{2.77}$$

This expression for q_i differs from the standard shallow water potential vorticity by the term $-\frac{1}{2}\varepsilon\nabla\cdot\left(\left(\eta_i+\eta_{i+1}\right)\boldsymbol{\Omega}\right)$ that contains the horizontal components Ω_x and Ω_y of the rotation vector. Equivalently, if we expand the divergence into two terms, we obtain

$$\Omega_{z0} - \overline{z}_i\nabla\cdot\boldsymbol{\Omega} - \boldsymbol{\Omega}\cdot\nabla\overline{z}_i = \Omega_z - \boldsymbol{\Omega}\cdot\nabla\overline{z}_i = (\boldsymbol{\Omega},\Omega_z)\cdot\nabla(z-\overline{z}_i(x,y,t)) \tag{2.78}$$

where $\overline{z}_i = \frac{1}{2}\left(\eta_i+\eta_{i+1}\right)$ is the z-coordinate of the midsurface of the i^{th} layer. The non-traditional effects therefore replace the vertical component of rotation vector, as found in the standard shallow water potential vorticity, by the component perpendicular to the layer's midsurface $z=\overline{z}_i(x,y,t)$.

The potential vorticity conservation law with the expression (2.77) for q_i may be obtained from the curl of (2.24), or we may find q_i directly from the canonical momenta. The particle relabelling symmetry (*e.g.* Ripa, 1981; Salmon, 1982a, 1988, 1998) implies material conservation of

$$q_i = \frac{1}{h_i}\left(\frac{\partial p_{iy}}{\partial x_i} - \frac{\partial p_{ix}}{\partial y_i}\right) \tag{2.79}$$

for any Lagrangian that depends on the particle labels a_i and b_i only through the height h_i formed from the Jacobian $\partial(x_i,y_i)/\partial(a_i,b_i)$. Moreover, the combination of p_{ix} and p_{iy} appearing in q_i is invariant under changes of gauge in $\boldsymbol{R}$, *i.e.* it is the same for all possible choices of F and G, even though p_{ix} and p_{iy} themselves are gauge-dependent.

2.6 Non-canonical Hamiltonian structure

Our equations may also be expressed using the non-canonical Hamiltonian structure for multilayered shallow water equations formulated by Ripa (1993). The non-canonical Hamiltonian formalism is convenient for fluid systems expressed using Eulerian (space-fixed) variables, as described in Shepherd (1990); Morrison (1998); Salmon (1988, 1998). It specifies the evolution of any functional $\mathcal{F}$ as being given by $\mathcal{F}_t = \{\mathcal{F}, \mathcal{H}\}$ in terms of a Hamiltonian functional $\mathcal{H}$ and a Poisson bracket $\{\cdot, \cdot\}$ that satisfies certain geometrical properties.

Using dimensional variables for simplicity, and writing the fluid velocity as $\mathbf{u}_i = (u_{ix}, u_{iy})$, the evolution of the density-weighted canonical momenta

$$v_{ix} = \rho_i p_{ix} = \rho_i \left(u_{ix} + F + \Omega_y \left(\tfrac{1}{2}h_i + \eta_{i+1}\right)\right), \quad v_{iy} = \rho_i p_{iy} = \rho_i u_{iy}, \tag{2.80}$$

and the layer depth h_i under our non-traditional multilayer shallow water equations is given by

$$\frac{\partial}{\partial t}\begin{pmatrix} v_{ix} \\ v_{iy} \\ h_i \end{pmatrix} = -\begin{pmatrix} 0 & -q_i & \partial_x \\ q_i & 0 & \partial_y \\ \partial_x & \partial_y & 0 \end{pmatrix}\begin{pmatrix} \delta\mathcal{H}/\delta v_{ix} \\ \delta\mathcal{H}/\delta v_{iy} \\ \delta\mathcal{H}/\delta h_i \end{pmatrix}. \tag{2.81}$$

The Hamiltonian is the energy density from §2.5.1, but expressed in terms of the v_{ix}, v_{iy}, and h_i,

$$\mathcal{H} = \sum_{k=1}^{N} \frac{h_k}{2\rho_k}\left\{\left[v_{kx} - \rho_k\left(F + \Omega_y\left(\tfrac{1}{2}h_k + \eta_{k+1}\right)\right)\right]^2 + v_{ky}^2\right\} + g\rho_k h_k\left(\tfrac{1}{2}h_k + \eta_{k+1}\right). \tag{2.82}$$

Calculation of the variational derivative $\delta\mathcal{H}/\delta h_i$ is complicated by the hidden dependence of η_k on $h_k, \ldots, h_N$ through the relation

$$\eta_k = \eta_{N+1} + \sum_{j=k}^{N} h_j, \tag{2.83}$$

where $\eta_{N+1}(x, y)$ is the fixed bottom topography. The calculations are essentially the same as those computing the variation in the potential energy part of the Lagrangian in §2.4. The combination $\frac{1}{2}h_k + \eta_{k+1}$ appearing in (2.82) is the mid-point of layer k, denoted $\tilde{h}_k$ by Ripa (1993).

All the coupling between layers is thus expressed through the Hamiltonian. The Poisson bracket that generates (2.81) may be written as a sum of standard shallow water Poisson brackets (*e.g.* Shepherd, 1990) for each layer, as in Ripa (1993),

$$\{F, G\} = \sum_{i=1}^{N} \iint \mathrm{d}x\mathrm{d}y\ \rho_i q_i \hat{\mathbf{z}} \cdot \left(\frac{\delta F}{\delta \boldsymbol{v}_i} \times \frac{\delta G}{\delta \boldsymbol{v}_i}\right) + \frac{\delta G}{\delta h_i}\nabla \cdot \left(\frac{\delta F}{\delta \boldsymbol{v}_i}\right) - \frac{\delta F}{\delta h_i}\nabla \cdot \left(\frac{\delta G}{\delta \boldsymbol{v}_i}\right). \tag{2.84}$$

This definition holds for any functionals $\mathcal{F}$ and $\mathcal{G}$ satisfying suitable boundary conditions that allow integrations by parts in (2.84) without generating surface terms. The Poisson bracket may be shown to be bilinear, antisymmetric, and to satisfy the Jacobi identity $\{\mathcal{F}, \{\mathcal{G}, \mathcal{K}\}\} + \{\mathcal{G}, \{\mathcal{K}, \mathcal{F}\}\} +$

$\{\mathcal{K},\{\mathcal{F},\mathcal{G}\}\}=0$ for all functionals $\mathcal{F}$, $\mathcal{G}$, and $\mathcal{K}$. Equation (2.81) then follows from (2.84) and the evolution equation $\mathcal{F}_t=\{\mathcal{F},\mathcal{H}\}$ by setting $\mathcal{F}$ equal to v_{ix}, v_{iy}, and h_i in turn. Conservation laws like those listed in §2.5 may be derived from properties of the Poisson bracket, especially the existence of so-called Casimir functionals $\mathcal{C}$ that satisfy $\{\mathcal{C},\mathcal{F}\}=0$ for all functionals $\mathcal{F}$. A full description may be found in Ripa (1993) and survey articles such as Shepherd (1990); Morrison (1998); Salmon (1988, 1998).

2.7 Connection with Salmon's two-layer variational formulation

The two-layer version of our derivation in §2.4.5 is equivalent to Salmon's (1982b) derivation of the two-layer shallow water equations from the Lagrangian

$$\mathcal{L}=\rho_1\iint \mathrm{d}a_1\mathrm{d}b_1\,L_1+\rho_2\iint \mathrm{d}a_2\mathrm{d}b_2\,L_2+\rho_1\iint \mathrm{d}a_1\mathrm{d}b_1\iint \mathrm{d}a_2\mathrm{d}b_2\,L_{12}, \tag{2.85}$$

which we write as $\mathcal{L}=\mathcal{L}_1+\mathcal{L}_2+\mathcal{L}_{12}$. The Lagrangian densities for $i=1,2$ are

$$L_i=\frac{1}{2}\left(\frac{\partial x_i}{\partial\tau}\right)^2+\frac{1}{2}\left(\frac{\partial y_i}{\partial\tau}\right)^2-\frac{1}{2}g\frac{\partial(a_i,b_i)}{\partial(x_i,y_i)} \tag{2.86}$$

in dimensional variables, and we have excluded rotation for simplicity. The two layers are coupled through $\mathcal{L}_{12}$, which is expressed as a simultaneous integral over both layers of a delta function density,

$$L_{12}=-g\delta(\boldsymbol{x}_1-\boldsymbol{x}_2), \tag{2.87}$$

that ties together the particle positions $\boldsymbol{x}_1$ and $\boldsymbol{x}_2$ in the two layers.

Using $\mathrm{d}a_1\mathrm{d}b_1=h_1(\boldsymbol{x}_1,t)\,\mathrm{d}x_1\mathrm{d}y_1$ we transform $\mathcal{L}_{12}$ into

$$\mathcal{L}_{12}=-\rho_1\iint \mathrm{d}x_1\mathrm{d}y_1\iint \mathrm{d}a_2\mathrm{d}b_2\;gh_1(\boldsymbol{x}_1,t)\;\delta(\boldsymbol{x}_1-\boldsymbol{x}_2), \tag{2.88}$$

and then perform the integrations over x_1 and $y_1$to obtain

$$\mathcal{L}_{12}=-\rho_1\iint \mathrm{d}a_2\mathrm{d}b_2\;gh_1(\boldsymbol{x}_2,t). \tag{2.89}$$

The total Lagrangian (2.85) thus becomes

$$\mathcal{L}=\rho_1\iint \mathrm{d}a_1\mathrm{d}b_1\left\{\tfrac{1}{2}|\dot{\boldsymbol{x}}_1|^2-\tfrac{1}{2}gh_1\right\}+\rho_2\int \mathrm{d}a_2\mathrm{d}b_2\left\{\tfrac{1}{2}|\dot{\boldsymbol{x}}_2|^2-\tfrac{1}{2}gh_2-\frac{\rho_1}{\rho_2}gh_1(\boldsymbol{x}_2,t)\right\}, \tag{2.90}$$

which is the same as (2.54) above with $N=2$ and $i=2$. Varying the map $(\boldsymbol{a}_2,\tau)\mapsto\boldsymbol{x}_2(\boldsymbol{a}_2,\tau)$ gives the lower layer equation of motion.

Conversely, using $\mathrm{d}a_2\mathrm{d}b_2=h_2(\boldsymbol{x}_2,t)\mathrm{d}x_2\mathrm{d}y_2$ we transform $\mathcal{L}_{12}$ into

$$\mathcal{L}_{12}=-\rho_1\iint \mathrm{d}a_1\mathrm{d}b_1\iint \mathrm{d}x_2\mathrm{d}y_2\;gh_2(\boldsymbol{x}_2,t)\;\delta(\boldsymbol{x}_1-\boldsymbol{x}_2), \tag{2.91}$$

and then perform the integration over x_2 to obtain

$$\mathcal{L}_{12} = -\rho_1 \iint \mathrm{d}a_1 \mathrm{d}b_1 \; g h_2(\boldsymbol{x}_1, t). \tag{2.92}$$

The total Lagrangian (2.85) then becomes

$$\mathcal{L} = \rho_1 \iint \mathrm{d}a_1 \mathrm{d}b_1 \left\{ \tfrac{1}{2}|\dot{\boldsymbol{x}}_1|^2 - \tfrac{1}{2} g h_1 - g h_2(\boldsymbol{x}_1, t) \right\} + \rho_2 \iint \mathrm{d}a_2 \mathrm{d}b_2 \left\{ \tfrac{1}{2}|\dot{\boldsymbol{x}}_2|^2 - \tfrac{1}{2} g h_2 \right\}, \tag{2.93}$$

which is the same as (2.54) above with $N = 2$ and $i = 1$. Varying the map $(\boldsymbol{a}_1, \tau) \mapsto \boldsymbol{x}_1(\boldsymbol{a}_1, \tau)$ gives the upper layer equation of motion.

Salmon's (1982b) expression of $\mathcal{L}_{12}$ as an integral over both layers explicitly indicates that it contributes to the equations of motion in both layers, as found by varying $\boldsymbol{x}_1$ and $\boldsymbol{x}_2$ independently. However, extending this approach to n layers would require writing the coupling terms as integrals over all n layers. This is avoided by the approaches we presented in §2.4. Our first approach is mathematically equivalent to Salmon's, but we transform directly from (2.89) to (2.92) without the intermediate multiple integral. Our second approach avoids this issue completely by expressing the coupling using explicit $\mathcal{W}_i$ terms in the Lagrangians.

2.8 Discussion

We have derived multilayer shallow water equations that include a complete treatment of the Coriolis force, thus extending the single-layer equations of Dellar and Salmon (2005) to multiple layers. We have presented a derivation of our equations by direct averaging of the three-dimensional Euler equations across layers, and two derivations by averaging three-dimensional Lagrangians in Hamilton's variational principle. Our two variational derivations differ in their treatment of the coupling between layers. The latter derivations guarantee the existence of conservation laws for energy, momentum, and potential vorticity in our equations. These laws are related to symmetries of the variational principle by Noether's theorem, and the symmetries are preserved by our averaging procedure. Our construction of a vector potential for a wide class of spatially varying $\boldsymbol{\Omega}$ extends the variational formulation of Dellar and Salmon (2005), which relied upon constant $\boldsymbol{\Omega}$, and corrects an error in their derivation by averaging the three-dimensional equations when $\partial_x \Omega_x + \partial_y \Omega_y \neq 0$.

This coupling between layers makes our derivations, especially the derivations from Hamilton's principle, much more involved than for a single layer. Our three-dimensional variational formulation is expressed using Lagrangian particle labels. This gives a formulation very close to Hamilton's principle for particle mechanics, and avoids the need to introduce extraneous variables such as Lin constraints or Clebsch potentials (see *e.g.* Salmon, 1988). Lagrangian particle labels are also very convenient for representing the interfaces between different fluid layers, which are themselves

Lagrangian surfaces. However, the reconstruction of particle positions from the labels introduces a hidden coupling between layers. The vertical position of a particle in layer i depends on the vertical position of the lower boundary of the layer, η_{i+1} in our notation, which in turn depends upon the labels in the layers $i+1, \ldots, N$ below.

Our first variational derivation uses the natural Lagrangian of kinetic energy minus gravitational potential energy, plus an incompressibility constraint multiplied by a pressure as a Lagrange multiplier. This is the Lagrangian that may be found in Eckart (1960) for a homogeneous fluid. However, the derivation of the equations of motion in a layered setting requires a very intricate exchange of integration variables between the different layers. This is because the coupling between layers is exerted by particles in adjacent positions on either side of a layer, not by particles with adjacent labels. This coupling was made explicit in an two-layer formulation by Salmon (1982b) that contained a double integral of a delta-function to tie the particle positions in the two layers together. This formulation is equivalent to ours (see §2.7), but does not scale up easily to three or more layers. One would need to include triple and higher integrals across all the layers in the system. As an alternative, we made the coupling between layers explicit by introducing additional terms the Lagrangian. These term represent the work done on each layer by the pressure exerted by the layers above (*c.f.* Miles and Salmon, 1985). With these extra terms to make the previously hidden coupling explicit, we derived the same equations of motion from independent variations of the label-to-particle map within each layer.

The momentum equations we have derived are, in dimensionless form,

$$\begin{aligned}
&\mathrm{Ro}\left(\frac{\partial \boldsymbol{u}_i}{\partial t} + (\boldsymbol{u}_i \cdot \nabla)\boldsymbol{u}_i\right) + \Big(\Omega_{z0} - \tfrac{1}{2}\varepsilon \nabla \cdot \big((\eta_i + \eta_{i+1})\, \boldsymbol{\Omega}\big)\Big)\hat{\boldsymbol{z}} \times \boldsymbol{u}_i \\
&\quad + \nabla \left\{ \mathrm{Bu}\, \eta_i + \tfrac{1}{2}\varepsilon h_i (v_i \Omega_x - u_i \Omega_y) + \frac{1}{\rho_i} \sum_{j=1}^{i-1} \rho_j h_j \big(\mathrm{Bu} + \varepsilon\, (v_j \Omega_x - u_j \Omega_y)\,\big) \right\} \\
&\qquad\qquad - \varepsilon\, \boldsymbol{\Omega} \times \hat{\boldsymbol{z}}\, \nabla \cdot \left\{ \tfrac{1}{2} h_i \boldsymbol{u}_i + \sum_{j=i+1}^{N} h_j \boldsymbol{u}_j \right\} = 0, \qquad (2.24)
\end{aligned}$$

together with the usual continuity equations $\partial_t h_i + \nabla \cdot (h_i \boldsymbol{u}_i) = 0$. They contain several non-traditional corrections to the standard multilayer shallow water equations, as derived under the traditional approximation. The traditional Coriolis term $2\Omega_z \hat{\mathbf{z}} \times \boldsymbol{u}_i$ is modified by replacing the vertical component Ω_z with the component of the full rotation vector $\boldsymbol{\Omega}$ that is perpendicular to each layer's midsurface. Secondly, the pressure changes from the hydrostatic pressure to the quasihydrostatic pressure (White and Bromley, 1995; White et al., 2005), due to the non-traditional Coriolis term $v_i \Omega_x - u_i \Omega_y$ in the vertical momentum equation. The last term in (2.24) has no analogue under the traditional approximation. It arises from the non-traditional Coriolis force

due to the vertical velocity, as reconstructed from the divergence of the horizontal velocity under the assumption of columnar motion, and may be rewritten as the time derivative $\partial_t (\varepsilon \, \mathbf{\Omega} \times \hat{\boldsymbol{z}} \, \overline{z}_i)$, where $\overline{z}_i(x, y, t)$ is the vertical coordinate of the midsurface of the i^{th} layer. This time derivative then combines with the time derivative of the velocity to form the time derivative of the canonical momentum, as shown in §2.5.2.

We have shown that these equations inherit conservation laws for energy, momentum, and potential vorticity from the underlying three-dimensional equations, as is guaranteed by our derivations from Hamilton's principle. The conserved components of momentum include additional non-traditional terms proportional to $\overline{z}_i$, as explained above. These terms represent the angular momentum gained or lost as fluid elements change their vertical position, and hence their distance from the rotation axis. This effect is absent in the traditional approximation, since a fluid element displaced vertically is also displaced parallel to the rotation axis. The conserved energy density is unchanged by non-traditional effects, just as it is unchanged by rotation about a vertical axis, but the energy flux gains additional terms reflecting the work done by the quasihydrostatic (as opposed to purely hydrostatic) pressure on the boundary of a control volume. Finally, the potential vorticity q_i that is materially conserved within each layer becomes

$$q_i = \frac{1}{h_i} \left\{ \Omega_{z0} - \varepsilon \nabla \cdot (\overline{z}_i \mathbf{\Omega}) + \mathrm{Ro} \left(\frac{\partial v_i}{\partial x} - \frac{\partial u_i}{\partial y} \right) \right\}. \tag{2.77}$$

The vertical component Ω_z of the rotation vector is replaced by the component perpendicular to the layer's midsurface $z = \overline{z}_i(x, y, t)$. We expect this change to be significant in the dynamics of cross-equatorial ocean currents, since the change in sign of Ω_z at the equator severely constrains the ability of fluid parcels to cross the equator (*e.g.* Stommel and Arons, 1960b; Nof and Olson, 1993). In our non-traditional equations, this constraint may be at least partly alleviated by the interaction of non-traditional Coriolis effects with suitable topography. We investigate the role of the complete Coriolis force in cross-equatorial currents in Chapters 4–6.

Chapter 3

Hyperbolicity and linear plane waves in the non-traditional multi-layer shallow water equations

This chapter is based upon Stewart and Dellar (2011b).

3.1 Introduction

In this chapter we investigate the hyperbolicity of, and linear plane waves in, the multi-layer shallow water equations with complete Coriolis force. While the single-layer shallow water equations are always hyperbolic under the traditional approximation, or in the absence of rotation, the multi-layer shallow water equations may lose hyperbolicity when there is a sufficiently large difference between the horizontal velocities in two adjacent layers (Long, 1956; Houghton and Isaacson, 1970; Liska and Wendroff, 1997). The equations then become elliptic, and thus *ill-posed* for solving initial value problems (Renardy and Rogers, 2004). Small perturbations to the initial data with characteristic wavenumber k will typically grow at a rate proportional to k. This ill-posedness of the layer-averaged equations is a reflection of the three-dimensional configuration sketched in Figure 3.1 being subject to a Kelvin–Helmholtz instability when the tangential velocity is discontinuous at any of the internal boundaries $z = \eta_i(x, y, t)$. Disturbances with sufficiently short wavelengths will grow, even when the layers are stably stratified, *i.e.* $\rho_i < \rho_{i+1}$ for $i = 1, \ldots, N-1$. The growth rate becomes proportional to the wavenumber in the short-wave limit. However, this rapid growth of short waves is suppressed when the vertical acceleration is neglected, as it is under the hydrostatic approximation employed in traditional shallow water theory (Long, 1956; Kelder and Teitelbaum, 1991).

The non-rotating multi-layer shallow water equations are hyperbolic provided the velocity dif-

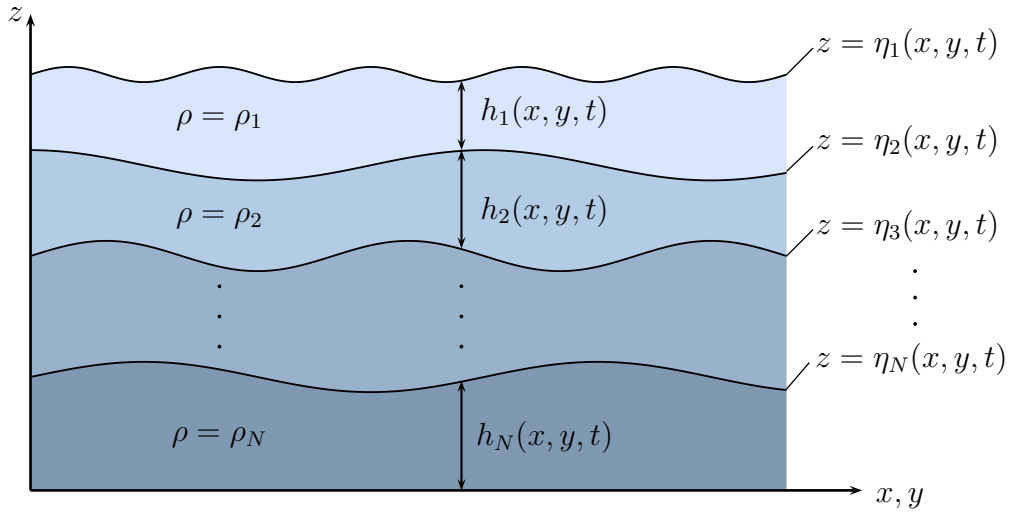

Figure 3.1: A schematic of the multi-layer shallow water model considered in this chapter. We restrict our attention to the case of flat bottom topography, $\eta_{N+1}(x, y) \equiv 0$.

ference between adjacent layers is less than a critical threshold that depends upon the stratification, measured by the density difference between the layers. Long (1956) showed that the two-layer equations with a rigid lid are hyperbolic when the velocity difference is less than a threshold $(g'H)^{1/2}$ set by the reduced gravity g' and the total depth H of the two layers. Houghton and Isaacson (1970) showed that the two-layer equations with a free surface are hyperbolic when the velocity difference is less than twice the internal wave speed (see §3.3.2). These results are summarised in Liska and Wendroff (1997), who also showed that multi-layer extensions of the Green and Naghdi (1976) equations are unconditionally ill-posed even for arbitrarily small velocity differences between adjacent layers. Miles and Salmon (1985) showed that the Green–Naghdi equations may be derived under the same assumption of columnar motion used in shallow water theory by including vertical accelerations associated with horizontally converging and diverging motions.

Vertical acceleration is necessary for the development of Kelvin–Helmholtz instability between layers, and it is this mechanism that underlies the ill-posedness of the Green-Naghdi equations. Our multi-layer shallow water equations retain the vertical component of the Coriolis force, but neglect vertical acceleration, so we should not expect them to exhibit the same ill-posedness. Nevertheless, an analysis of hyperbolicity serves as an important test of the validity of our equations, particularly their suitability for solving initial value problems numerically. In §3.3 we show that the non-traditional stably-stratified two-layer shallow water equations are hyperbolic for all geophysically reasonable fluid velocities. The equations still become ill-posed when the velocity difference between the layers becomes large, but typically non-traditional effects modify this condition by no more than 5%. The equations also become ill-posed for very large eastward velocities in either of

the layers, which corresponds to the vertical component of the Coriolis force exceeding gravity, an extreme example of the Eötvös effect (*e.g.* Persson, 2005). Including additional layers does not lead to any substantial deviation from these results.

In §3.4 and §3.5 we analyse linear plane waves in the non-traditional shallow water equations. The behaviour of such waves under the traditional approximation is well-documented (*e.g.* Zeitlin, 2007), as they provide a simple description of the behaviour of large-scale internal waves in the ocean. Long waves with frequencies ω near the inertial frequency f account for a substantial proportion of the wave activity in the ocean (Munk and Phillips, 1968; Fu, 1981), and typically exceed the $(\omega^2 - f^2)^{-1/2}$ factor included in the widely-used Garrett and Munk (1972, 1979) models for the energy spectrum. Hughes (1964), Saint-Guily (1970) and LeBlond and Mysak (1978) have given dispersion relations for internal waves in a continuously stratified fluid with the complete Coriolis force. These dispersion relations are anisotropic, because the horizontal component of the rotation vector defines a preferred horizontal direction. Moreover, waves may exist with frequencies below the inertial frequency $f = 2\Omega \sin\phi$, where ϕ is the latitude and Ω is the magnitude of the Earth's rotation vector. Such waves do not exist under the traditional approximation.

Thuburn, Wood, and Staniforth (2002a,b) studied the effects of relaxing the traditional approximation on linear waves in a continuously stratified fluid on a sphere, and on the non-traditional analogue of the standard f-plane. They identified a scaling for long waves on an f-plane that is analogous to the one we find in §3.4.3 below. Kasahara (2003) began an extended, primarily numerical, study of linear waves in continuously stratified fluids on non-traditional analogues of f-planes and β-planes (Kasahara and Gary, 2010). Kasahara (2007) studied non-traditional effects for linear initial value problems, in contrast to other work based on normal mode analyses. These studies identified a family of waves involving non-traditional effects that are characterised by large vertical wavenumbers, wavenumbers that tend to infinity in the limit of vanishing non-traditional effects, and localised at horizontal boundaries.

Gerkema and Shrira (2005b,a) drew attention to the properties of a branch of short sub-inertial waves in continuously stratified fluids that do not exist under the traditional approximation. We derive our shallow water equations using a small aspect ratio, or long wave, approximation, so we cannot capture these short sub-inertial waves. However, our equations do support a branch of long sub-inertial waves with a dramatically altered structure. The fast surface wave mode connects to the slowest internal wave mode in the limit of long wavelengths, and the connection occurs via long sub-inertial waves. The longest, most energetic waves in the ocean are thus most affected by the complete Coriolis force.

3.2 The multi-layer shallow water equations with complete Coriolis force

In Chapter 2 we derived equations to describe the behaviour of multiple superposed shallow layers of incompressible fluids with constant densities in a frame rotating about an arbitrary axis, and retained arbitrary orientation of the bottom topography $\eta_{N+1}(x,y) = h_b(x,y)$. In this chapter we investigate hyperbolicity and linear waves in these equations when the bottom topography is flat, $h_b \equiv 0$. A schematic of this multi-layer shallow water model is presented in Figure 3.1. In Chapter 2 we also preserved a general nondimensionalisation of the governing equations by leaving the Rossby and Burger numbers, Ro and Bu, unspecified. In this chapter it is convenient to choose a specific nondimensionalisation, using the gravity wave speed as our horizontal velocity scale, and the external Rossby radius of deformation as our horizontal lengthscale,

$$c = \sqrt{gH}, \qquad R_d = \frac{c}{2\Omega}. \tag{3.1}$$

Note that we define R_d using the absolute planetary rotation Ω, rather than its local vertical component Ω_z. The layers in Figure 3.1 are labelled by $i = 1, \ldots, N$, with dimensionless thicknesses $h_i(x,y,t)$, pressures $p_i(x,y,z,t)$, horizontal velocities $\boldsymbol{u}_i = (u_i(x,y,z,t), v_i(x,y,z,t))$, vertical velocities $w_i(x,y,z,t)$, and densities ρ_i. These are related to their dimensional counterparts via

$$\boldsymbol{x} = \frac{\tilde{\boldsymbol{x}}}{R_d}, \quad z = \frac{\tilde{z}}{H}, \quad t = 2\Omega\tilde{t}, \quad \boldsymbol{u}_i = \frac{\tilde{\boldsymbol{u}}_i}{c}, \quad w_i = \frac{\tilde{w}_i}{2\Omega H}, \quad p_i = \frac{\tilde{p}_i}{\rho_i c^2}, \tag{3.2}$$

where the tilde $\tilde{}$ denotes a dimensional variable. This nondimensionalisation corresponds to choosing Ro = Bu = 1 in the notation of Chapter 2. The dimensionless governing equations in the i^{th} layer are

$$\frac{\partial \boldsymbol{u}_i}{\partial t} + (\boldsymbol{u}_i \cdot \nabla)\,\boldsymbol{u}_i + w_i \frac{\partial \boldsymbol{u}_i}{\partial z} + \Omega_z \hat{\boldsymbol{z}} \times \boldsymbol{u}_i + \varepsilon \boldsymbol{\Omega} \times \hat{\boldsymbol{z}} w_i + \nabla p_i = 0, \tag{3.3a}$$

$$\varepsilon^2 \left(\frac{\partial w_i}{\partial t} + \boldsymbol{u}_i \cdot \nabla w_i + w_i \frac{\partial w_i}{\partial z} \right) + \varepsilon(\Omega_x v_i - \Omega_y u_i) + \frac{\partial p_i}{\partial z} + 1 = 0, \tag{3.3b}$$

$$\nabla \cdot \boldsymbol{u}_i + \frac{\partial w_i}{\partial z} = 0. \tag{3.3c}$$

The ratio of vertical to horizontal lengthscales

$$\varepsilon = \frac{H}{R_d} = 2\Omega\sqrt{\frac{H}{g}}, \tag{3.4}$$

measures the importance of the non-traditional component of the Coriolis force, whilst ε^2 measures the importance of vertical accelerations. For typical parameters, $g = 9.8\,\mathrm{m\,s^{-1}}$, $\Omega = 7.3 \times 10^{-5}\,\mathrm{rad\,s^{-1}}$ and $H = 500\,\mathrm{m}$, this ratio is small, $\varepsilon \approx 1.0 \times 10^{-3}$. However, as our analysis of linear

plane waves shows, the importance of non-traditional effects in internal motions is more accurately represented by replacing g in (3.4) by a reduced gravity $g' = g\Delta\rho/\rho$, where ρ is a typical density and $\Delta\rho$ is a typical density difference between adjacent layers. The internal aspect ratio may be as large as $\varepsilon_{\text{internal}} \approx 0.1$, since $\Delta\rho/\rho$ may be as small as 10^{-4} in parts of the ocean.

Equations (3.3a)–(3.3c) are formulated in a pseudo-Cartesian coordinate system with the z-axis pointing radially outwards, anti-parallel to the local gravitational acceleration. Such coordinates are commonly used to represent the behaviour in some region of the Earth's surface (*e.g.* Vallis, 2006; White, 2002; Salmon, 1998; Pedlosky, 1987; Gill, 1982). They are *pseudo*-Cartesian because the horizontal x and y coordinate lines lie within a surface of constant geopotential, even though the resulting curvature terms in the metric are neglected. This is the correct interpretation of the β-plane approximation to spherical geometry (Phillips, 1973).

We have written the dimensionless horizontal and vertical components of the Earth's rotation vector as $\boldsymbol{\Omega} = (\Omega_x, \Omega_y)$ and Ω_z respectively. We allow an arbitrary orientation of the x- and y-axes, because it is often convenient to rotate axes so that waves propagate parallel to the x-axis. Letting θ be the angle between an eastward-pointing vector and the direction of the positive x-axis, we write

$$\Omega_x = \cos\phi \sin\theta, \quad \Omega_y = \cos\phi\cos\theta, \quad \Omega_z = \sin\phi, \tag{3.5}$$

where ϕ is the latitude. The conventional axes in geophysical fluid dynamics correspond to taking $\theta = 0$. In principle, ϕ should vary with $\boldsymbol{x}$, but in the present work we take ϕ to be constant, thus restricting our attention to waves whose wavelengths are short compared with the Earth's radius. This approximation was named the non-traditional f-plane by Gerkema and Shrira (2005b).

In Chapter 2 we derived the multi-layer shallow water equations from (3.3a)–(3.3c) by expanding the governing equations asymptotically in ε and averaging over the depth in each layer, and also by averaging the action in Hamilton's variational principle of mechanics. This leads to the shallow water mass conservation equation

$$\frac{\partial h_i}{\partial t} + \nabla \cdot (h_i \overline{\boldsymbol{u}}_i) = 0, \tag{3.6}$$

and momentum conservation equation

$$\begin{aligned} &\frac{\partial \overline{\boldsymbol{u}}_i}{\partial t} + (\overline{\boldsymbol{u}}_i \cdot \nabla)\overline{\boldsymbol{u}}_i + \left(\Omega_z - \tfrac{1}{2}\varepsilon \boldsymbol{\Omega} \cdot \nabla\left(\eta_i + \eta_{i+1}\right)\right) \hat{\boldsymbol{z}} \times \overline{\boldsymbol{u}}_i + \tfrac{1}{2}\varepsilon\, \boldsymbol{\Omega} \times \hat{\boldsymbol{z}}\, \frac{\partial}{\partial t}(\eta_i + \eta_{i+1}) \\ &+ \nabla \left\{ \eta_i + \tfrac{1}{2}\varepsilon h_i(\overline{v}_i\Omega_x - \overline{u}_i\Omega_y) + \frac{1}{\rho_i}\sum_{j=1}^{i-1} \rho_j h_j \left(1 + \varepsilon\left(\overline{v}_j\Omega_x - \overline{u}_j\Omega_y\right)\right) \right\} = 0. \end{aligned} \tag{3.7}$$

Here $\overline{\boldsymbol{u}}_i$ is the depth-averaged horizontal velocity in the i^{th} layer. We will henceforth drop the overbar notation in $\overline{\boldsymbol{u}}_i$. The Coriolis acceleration due to the vertical velocity w_i in the (3.3a) corresponds approximately to the non-traditional term proportional to $\partial_t(\eta_i + \eta_{i+1})$ in (3.7). The non-traditional

contribution to the pressure in (3.3b), named the quasi-hydrostatic pressure by White and Bromley (1995), leads to the appearance of non-traditional terms in the pressure gradient. The final non-traditional term corrects the traditional planetary vorticity Ω_z. The complete planetary vorticity in the i^{th} layer, $\Omega_z - \frac{1}{2}\varepsilon\boldsymbol{\Omega}\cdot\nabla\left(\eta_i + \eta_{i+1}\right)$, is the component of the Earth's rotation vector normal to the layer's mid-surface. This expression may also be interpreted as the layer-average of an Ertel potential vorticity formulated using Lagrangian labels in the vertical (Dellar and Salmon, 2005).

3.3 Hyperbolicity of the two-layer shallow water equations

In the three-dimensional Euler equations a vortex sheet, an interface across which the tangential velocity is discontinuous, is subject to a Kelvin–Helmholtz instability whose growth rate is proportional to the wavenumber k of the disturbance. Stable stratification suppresses the Kelvin–Helmholtz instability at large lengthscale, but sufficiently short lengthscales always remain unstable (Lamb 1932, §232; Chandrasekhar 1961, §101). However, neglect of the vertical acceleration, the hydrostatic approximation, tames the Kelvin–Helmholtz instability to the extent that it may be completely suppressed by sufficiently strong stratification (Long, 1956; Kelder and Teitelbaum, 1991). The shallow water equations are founded on the assumption of approximately columnar motion, and so cannot describe the onset of Kelvin–Helmholtz instability. The non-rotating two-layer shallow water equations become ill-posed if the the conditions for growth of the Kelvin-Helmholtz instability are satisfied in the underlying Euler equations, (Houghton and Isaacson, 1970; Liska and Wendroff, 1997). This ill-posedness occurs through a loss of hyperbolicity, in the sense described in detail below. Instead, the system of partial differential equations becomes elliptic, so small disturbances to initial data may be subject to arbitrarily large growth rates.

The non-rotating multi-layer shallow water equations, as derived using the hydrostatic approximation, typically remain hyperbolic as long as the velocity difference between adjacent layers remains sufficiently small compared with the speed of internal waves (*e.g.* Long, 1956; Lawrence, 1990; Liska et al., 1995; Liska and Wendroff, 1997). This serves as a measure of the strength of the stable stratification. Including rotation under the traditional approximation, *i.e.* about a vertical axis, has no effect on the hyperbolicity of shallow water models, as described below. Including the complete Coriolis force makes the single-layer shallow water equations ill-posed when the Eastward velocity is very large (Dellar and Salmon, 2005). Under these conditions the vertical component of the Coriolis acceleration exceeds the downward acceleration due to gravity, the so-called Eötvös effect (*e.g.* Persson, 2005). We expect that the multi-layer equations should exhibit some combination of these features. In the following we describe a loss of hyperbolicity as ill-posedness, since elliptic

systems are certainly ill-posed for initial value problems (Renardy and Rogers, 2004). However, we do not have a definite proof of well-posedness in the region of hyperbolicity because the relevant theory (*e.g.* Benzoni-Gavage and Serre, 2007) has only been developed for hyperbolic systems that are either linear, or symmetrizable in the sense of Friedrichs (1954). We know that our systems are not symmetrizable, because the eigenvalues calculated below are not always real.

3.3.1 Requirements for hyperbolicity

We limit our discussion to the two-layer shallow water equations with no topography. Including additional layers makes the analysis below vastly more complicated. We have verified that the three-layer case is qualitatively identical to the two-layer case described below, and we expect the same to be true for four or more layers. Taking $i = 1, 2$ and $\eta_3 = 0$ in (3.6) and (3.7) yields

$$\frac{\partial \boldsymbol{u}_1}{\partial t} + (\boldsymbol{u}_1 \cdot \nabla)\boldsymbol{u}_1 + \left[\Omega_z - \varepsilon \boldsymbol{\Omega} \cdot \nabla \left(h_2 + \tfrac{1}{2}h_1\right)\right] \hat{\boldsymbol{z}} \times \boldsymbol{u}_1 + \nabla \left[h_2 + h_1 + \tfrac{1}{2}\varepsilon\, h_1(v_1\Omega_x - u_1\Omega_y)\right] - \varepsilon\, \boldsymbol{\Omega} \times \hat{\boldsymbol{z}}\, \nabla \cdot \left(\tfrac{1}{2}h_1\boldsymbol{u}_1 + h_2\boldsymbol{u}_2\right) = 0, \tag{3.8a}$$

$$\frac{\partial h_1}{\partial t} + \nabla \cdot (h_1 \boldsymbol{u}_1) = 0, \tag{3.8b}$$

$$\frac{\partial \boldsymbol{u}_2}{\partial t} + (\boldsymbol{u}_2 \cdot \nabla)\boldsymbol{u}_2 + \left[\Omega_z - \tfrac{1}{2}\varepsilon \boldsymbol{\Omega} \cdot \nabla h_2\right] \hat{\boldsymbol{z}} \times \boldsymbol{u}_2 - \varepsilon\, \boldsymbol{\Omega} \times \hat{\boldsymbol{z}}\, \nabla \cdot \left(\tfrac{1}{2}h_2\boldsymbol{u}_2\right) + \nabla \left[h_2 + \rho_r h_1 + \tfrac{1}{2}\varepsilon\, h_2(v_2\Omega_x - u_2\Omega_y) + \rho_r \varepsilon\, h_1\,(v_1\Omega_x - u_1\Omega_y)\right] = 0, \tag{3.8c}$$

$$\frac{\partial h_2}{\partial t} + \nabla \cdot (h_2 \boldsymbol{u}_2) = 0, \tag{3.8d}$$

where $\rho_r = \rho_1/\rho_2$ is the density ratio. In constructing (3.8a) and (3.8c), we have used the mass conservation equations (3.8b) and (3.8d) to remove the time derivatives of h_1 and h_2 from (3.7).

Following Whitham (1974), we write (3.8a–*d*) as a quasilinear system of first-order partial differential equations

$$\frac{\partial \boldsymbol{v}}{\partial t} + \mathbf{C}_x \cdot \frac{\partial \boldsymbol{v}}{\partial x} + \mathbf{C}_y \cdot \frac{\partial \boldsymbol{v}}{\partial y} + \boldsymbol{b} = 0, \tag{3.9}$$

where $\boldsymbol{v} = (u_1, v_1, h_1, u_2, v_2, h_2)$ is the vector of dependent variables. The coefficient matrices are

$$\mathbf{C}_x = \begin{bmatrix} u_1 - \varepsilon\, h_1 \Omega_y & \frac{1}{2}\,\varepsilon\, h_1 \Omega_x & 1 + \varepsilon\,(v_1\,\Omega_x - u_1\,\Omega_y) \\ \frac{1}{2}\,\varepsilon\, h_1 \Omega_x & u_1 & 0 \\ h_1 & 0 & u_1 \\ -\varepsilon \rho_r\, h_1 \Omega_y & \varepsilon \rho_r\, h_1 \Omega_x & \rho_r\,[1 + \varepsilon\,(v_1 \Omega_x - u_1 \Omega_y)] \\ 0 & 0 & 0 \\ 0 & 0 & 0 \end{bmatrix}$$

$$\begin{bmatrix} -\varepsilon\, h_2\, \Omega_x & 0 & 1 + \varepsilon\,(v_1\,\Omega_x - u_2\,\Omega_y) \\ \varepsilon\, h_2\, \Omega_x & 0 & \varepsilon\,(u_2 - u_1)\,\Omega_x \\ 0 & 0 & 0 \\ u_2 - \varepsilon\, h_2\, \Omega_y & \frac{1}{2}\,\varepsilon\, h_2\, \Omega_x & 1 + \varepsilon\,(v_2\,\Omega_x - u_2\,\Omega_y) \\ \frac{1}{2}\,\varepsilon\, h_2\, \Omega_x & u_2 & 0 \\ h_2 & 0 & u_2 \end{bmatrix}, \tag{3.10}$$

and

$$\mathbf{C}_y = \begin{bmatrix} v_1 & -\frac{1}{2}\,\varepsilon\, h_1 \Omega_y & 0 \\ -\frac{1}{2}\,\varepsilon\, h_1 \Omega_y & v_1 + \varepsilon\, h_1 \Omega_x & 1 + \varepsilon\,(v_1\,\Omega_x - u_1\,\Omega_y) \\ 0 & h_1 & v_1 \\ 0 & 0 & 0 \\ -\varepsilon\,\rho_r\, h_1 \Omega_y & \varepsilon\,\rho_r\, h_1 \Omega_x & \rho_r\,[1 + \varepsilon\,(v_1\,\Omega_x - u_1\,\Omega_y)] \\ 0 & 0 & 0 \end{bmatrix}$$

$$\begin{bmatrix} 0 & -\varepsilon\, h_2\, \Omega_y & \varepsilon\,(v_1 - v_2)\,\Omega_y \\ 0 & \varepsilon\, h_2\, \Omega_x & 1 + \varepsilon\,(v_2\,\Omega_x - u_1\,\Omega_y) \\ 0 & 0 & 0 \\ v_2 & -\frac{1}{2}\,\varepsilon\, h_2\, \Omega_y & 0 \\ -\frac{1}{2}\,\varepsilon\, h_2\, \Omega_y & v_2 + \varepsilon\, h_2\, \Omega_x & 1 + \varepsilon\,(v_2\,\Omega_x - u_2\,\Omega_y) \\ 0 & h_2 & v_2 \end{bmatrix}, \tag{3.11}$$

and $\boldsymbol{b}$ is a vector algebraic terms proportional to Ω_z,

$$\boldsymbol{b} = \begin{bmatrix} -\Omega_z v_1 \\ \Omega_z u_1 \\ 0 \\ -\Omega_z v_1 \\ \Omega_z u_1 \\ 0 \end{bmatrix}. \tag{3.12}$$

Equation (3.9) is a system of six dependent variables and three independent variables. This system is formally hyperbolic (Whitham, 1974, §5.9) if there are linear combinations of its six equations that transform the separate partial derivatives in t, x, y into directional derivatives of the components v_m, with directions that are confined to a two-dimensional characteristic surface $S(t, x, y) = 0$. Singularities in the solution are confined to propagating along these surfaces, which are the analogues of the characteristic curves for hyperbolic systems in one spatial dimension. The hyperbolicity property is thus independent of the algebraic terms in the vector $\boldsymbol{b}$.

Taking the inner product of (3.9) with a constant vector $\boldsymbol{\ell}$ yields

$$\sum_{m=1}^{6} \left\{ \ell_m \frac{\partial v_m}{\partial t} + \left[\sum_{n=1}^{6} \ell_n (C_x)_{n,m} \right] \frac{\partial v_m}{\partial x} + \left[\sum_{n=1}^{6} \ell_n (C_y)_{n,m} \right] \frac{\partial v_m}{\partial y} \right\} + \sum_{m=1}^{6} \ell_m b_m = 0. \tag{3.13}$$

The terms in braces $\{\cdots\}$ correspond to a directional derivative of v_m along the direction given by the coefficients of $(\partial_t v_m, \partial_x v_m, \partial_y v_m)$. The system (3.9) is hyperbolic if the directions of the directional derivatives of $v_1, \ldots, v_6$ are all parallel to the surface $S(t, x, y) = 0$, *i.e.* they are all perpendicular to the normal to this surface,

$$(\boldsymbol{\ell}, \boldsymbol{\ell} \cdot \mathbf{C}_x, \boldsymbol{\ell} \cdot \mathbf{C}_y) \cdot \nabla_t S = \boldsymbol{\ell} \cdot (\mathbf{I}, \mathbf{C}_x, \mathbf{C}_y) \cdot \nabla_t S = 0, \tag{3.14}$$

where $\mathbf{I}$ is the 6×6 identity matrix, and $\nabla_t = (\partial_t, \partial_x, \partial_y)$. This linear system of equations for $\boldsymbol{\ell}$ only has a non-zero solution when the determinant of the matrix $(\mathbf{I}, \mathbf{C}_x, \mathbf{C}_y) \cdot \nabla_t S$ is zero,

$$\left| \mathbf{I} \frac{\partial S}{\partial t} + \mathbf{C}_x \frac{\partial S}{\partial x} + \mathbf{C}_y \frac{\partial S}{\partial y} \right| = 0. \tag{3.15}$$

This condition is independent of $\boldsymbol{\ell}$. Equation (3.15) defines the shapes of the characteristic surfaces S close to a point (t_0, x_0, y_0) by relating the derivatives $\partial_t S$, $\partial_x S$, and $\partial_y S$ at that point.

Writing the normal at a point (t_0, x_0, y_0) as $(\partial_t S, \partial_x S, \partial_y S) = (-\omega, k_x, k_y)$ transforms (3.15) into

$$|k_x \mathbf{C}_x + k_y \mathbf{C}_y - \omega \mathbf{I}| = 0. \tag{3.16}$$

This relation between k_x, k_y, and ω defines the possible orientations of the surface $S = 0$ at (t_0, x_0, y_0), and hence the local shapes of the characteristic surfaces. Provided at least one of k_x and k_y are nonzero, we may write $k_x = k\cos\Theta$, $k_y = k\sin\Theta$. Equation (3.16) then reduces to

$$|\cos\Theta\,\mathbf{C}_x + \sin\Theta\,\mathbf{C}_y - \lambda\mathbf{I}| = 0, \tag{3.17}$$

with $\lambda = \omega/k$ being the speed at which disturbances propagate in the direction Θ. The exceptional case with $k_x = k_y = 0$ has the characteristic surface tangent to the xy plane, and hence disturbances propagating with infinite speed. Equation (3.17) determines λ to be one of the eigenvalues $\lambda_1, \ldots, \lambda_6$ of the matrix $\cos\Theta\,\mathbf{C}_x + \sin\Theta\,\mathbf{C}_y$, and (3.14) shows that $\boldsymbol{\ell}_1, \ldots, \boldsymbol{\ell}_6$ are the corresponding left eigenvectors. These eigenvalues determine the speeds at which disturbances propagate, or equivalently the gradients of the corresponding characteristic surfaces S_j with respect to the t-axis. The system (3.9) is not hyperbolic if, for any value of Θ, one or more of the eigenvalues λ_j becomes complex. The corresponding characteristic surface S_j is then at least partly complex.

In summary, for given values of the dependent variables $\boldsymbol{v}$ in $\mathbf{C}_x$ and $\mathbf{C}_y$, the system (3.9) is hyperbolic if, for all real Θ, the matrices $\cos\Theta\,\mathbf{C}_x + \sin\Theta\,\mathbf{C}_y$ possess only real eigenvalues, and complete sets of eigenvectors. This is taken as the fundamental condition for hyperbolicity in more recent work such as Godlewski and Raviart (1996) and Benzoni-Gavage and Serre (2007), instead of Whitham's (1974) condition based on characteristic surfaces. Establishing the hyperbolicity of a system in two spatial dimensions is thus equivalent to establishing the hyperbolicity of the reduced one-dimensional system for disturbances propagating at an arbitrary angle Θ with respect to the xy axes. As our system (3.8a–d) is expressed in a vector-invariant form, we may absorb the angle Θ by a suitable rotation of the axes before expressing (3.8a–d) in components. Establishing the hyperbolicity of the system (3.8a–d) thus reduces to verifying that the eigenvalues of $\mathbf{C}_x$ are real for all angles θ as defined in (3.5). Once again, this condition is independent of the algebraic terms in the vector $\boldsymbol{b}$.

In the remainder of this section we focus on determining whether the eigenvalues λ of the matrix $\mathbf{C}_x$ are real. The characteristic equation yields a sixth-order polynomial in λ with two trivial roots

that are always real, $\lambda = u_1$ and $\lambda = u_2$. The remaining four roots are given by the roots of

$$\begin{aligned}
&\lambda^4 + \Big[\varepsilon\,\Omega_y(h_1+h_2) - 2(u_1+u_2)\Big]\,\lambda^3 \\
&\quad + \Big[\ \big(h_1h_2(\sigma|\mathbf{\Omega}|^2 - \tfrac{1}{4}\Omega_x^2) - \Omega_x^2(h_1^2+h_2^2)\big)\,\varepsilon^2 \\
&\qquad - \left(2\,\Omega_y(u_2h_1+u_1h_2) + \Omega_x(h_1v_1+h_2v_2)\right)\varepsilon \\
&\qquad\quad + u_1^2 + u_2^2 + 4\,u_2u_1 - h_2 - h_1\ \Big]\,\lambda^2 \\
&\quad + \Big[\ 2(u_1h_2 + u_2h_2 - u_1u_2(u_1+u_2)) - \tfrac{1}{4}\,h_1h_2\Omega_y\Omega_x^2(h_1+h_2)\varepsilon^3 \\
&\qquad + \big(\Omega_x^2\left(\tfrac{1}{2}u_1h_2^2 + \tfrac{1}{2}u_2h_1^2 + 2u_1h_1h_2(1-\sigma)\right) + \Omega_x\Omega_y h_1h_2\left((1-2\sigma)v_1 - v_2\right)\big)\,\varepsilon^2 \\
&\qquad\quad + \big(2\Omega_x\left(u_1h_2v_2 + u_2h_1v_1\right) + \Omega_y\left(u_1^2h_2 + u_2^2h_1 - 2\sigma h_1h_2\right)\big)\,\varepsilon\ \Big]\,\lambda \\
&\quad + \Big[\ \tfrac{1}{4}\Omega_x^3h_1h_2\left(h_2v_1 + h_1v_2\right)\varepsilon^3 + \left(u_1^2u_2^2 - h_1u_2^2 - h_2u_1^2 + \sigma h_1h_2\right) \\
&\qquad + \tfrac{1}{4}\Omega_x^2\left(h_1h_2\left(h_1 + h_2 + 4v_1v_2 - 4(1-\sigma)\left(u_1^2+v_1^2\right)\right) - h_1^2u_2^2 - h_2^2u_1^2\right)\varepsilon^2 \\
&\qquad\quad + \Omega_x\left(h_1h_1\left(v_2 + (2\sigma-1)v_1\right) - h_1v_1u_2^2 - h_2v_2u_1^2\right)\varepsilon + \tfrac{1}{16}h_1^2h_2^2\Omega_x^4\varepsilon^4\ \Big] = 0.
\end{aligned} \tag{3.18}$$

3.3.2 Discriminant of the quartic

There are formulae for the roots of a quartic polynomial (*e.g.* Abramowitz and Stegun, 1964), but they offer little insight into a quartic as complicated as (3.18). Instead, following Lawrence (1990), some insight into the nature of the roots may be gained by considering the discriminant of the quartic (*e.g.* Irving, 2004). The discriminant D of a quartic with roots $\lambda_1, \lambda_2, \lambda_3, \lambda_4$ is defined to be

$$D = (\lambda_1-\lambda_2)^2\,(\lambda_1-\lambda_3)^2\,(\lambda_1-\lambda_4)^2\,(\lambda_2-\lambda_3)^2\,(\lambda_2-\lambda_4)^2\,(\lambda_3-\lambda_4)^2, \tag{3.19}$$

but the discriminant may be computed directly from the coefficients without first finding the roots. The coefficients in the quartic (3.18) are all real, so the roots are either real, or they occur in complex conjugate pairs. The quartic has two real roots and two complex conjugate roots when the discriminant $D < 0$, and when $D > 0$ the quartic has either four real roots or two pairs of complex conjugate roots.

The quartic becomes tractable in the special case of equal equilibrium depths ($h_1 = h_2 = 1$), and under the traditional approximation (equivalent to setting $\varepsilon = 0$). Under these assumptions, the quartic (3.18) has roots (Houghton and Isaacson, 1970; Liska and Wendroff, 1997)

$$\lambda = \frac{1}{2}\,(u_1+u_2) \pm_\alpha \sqrt{1 + \frac{1}{4}\,(u_1-u_2)^2 \pm_\beta \sqrt{(u_1-u_2)^2 + 1 - \sigma}}, \tag{3.20}$$

where $\pm_\alpha$ and $\pm_\beta$ may take signs independently, and $\sigma = (\rho_2 - \rho_1)/\rho_2$ is the relative density difference between the two layers. The eigenvalues λ are complex when the difference between the velocities

parallel to the x-axis lies in the range

$$\left(1-\sqrt{1-\sigma}\right)^{1/2} < \tfrac{1}{2}|u_1-u_2| < \left(1+\sqrt{1-\sigma}\right)^{1/2}. \tag{3.21}$$

The lower and upper limits are the internal and surface wave speeds respectively, so the eigenvalues are always real when $\frac{1}{2}|u_1-u_2|$ is smaller than the internal wave speed. The eigenvalues are also real when $\frac{1}{2}|u_1-u_2|$ is larger than the surface wave speed, because disturbances at the interface between the two layers are advected away from each other before they can grow. By the analysis in §3.3.1, if the velocity difference between the layers in any direction θ lies within the range (3.21), two-layer shallow water equations are ill-posed.

We may obtain the same condition (3.21) from the discriminant,

$$D = 16\left((u_1-u_2)^4 - 8\,(u_1-u_2)^2 + 16\,\sigma\right)\left((u_1-u_2)^2+1-\sigma\right)^2. \tag{3.22}$$

All four roots are real when $D>0$, but when $D<0$ there are two complex roots and the system is ill-posed. In general we do not expect the nature of the quartic (3.18) to differ dramatically when $\varepsilon \neq 0$, as for realistic parameters $\varepsilon \ll 1$. There is an explicit criterion for $D>0$ to correspond to four real roots (Garver, 1933; Ku, 1965; Wang and Qi, 2005). Unless stated otherwise, this condition is satisfied when $D>0$ in all the cases considered below.

3.3.3 Loss of hyperbolicity due to shear

The hyperbolicity condition (3.21) for the traditional two-layer shallow water equations suggests that the velocity difference between the two layers will largely determine the hyperbolicity in the non-traditional case. Our velocity scale is the surface gravity wave speed ($\approx 100\,\mathrm{m\,s^{-1}}$), so typical geophysical fluid velocities are $10^{-4} \lesssim |\boldsymbol{u}_{1,2}| \lesssim 10^{-2}$. The region close to $\boldsymbol{u}_1 = 0$ and $\boldsymbol{u}_2 = 0$ is thus most relevant. In this section we consider velocities $\boldsymbol{u}_1$ and $\boldsymbol{u}_2$ that are $\mathcal{O}(1)$ or smaller, and whose difference is very small, $U = |\boldsymbol{u}_2 - \boldsymbol{u}_1| \ll 1$. Condition (3.21) suggests that the maximum allowable velocity difference that permits hyperbolicity should satisfy $U \sim \sigma^{1/2}$ as $\sigma \to 0$. In physical terms, this is because only a small restoring force from buoyancy is available to counteract the Kelvin–Helmholtz instability when σ is small.

In the non-traditional case the eigenvalues λ depends strongly on both the magnitude and direction of the velocity difference, with respect to the orientation θ of the x and y axes. It is therefore convenient to write the velocity difference as $\boldsymbol{u}_2 - \boldsymbol{u}_1 = (U\cos\psi, U\sin\psi)$, where $U \geq 0$ and $0 \leq \psi < 2\pi$. We will also restrict our attention to the case of equal layer depths ($h_1 = h_2 = 1$) for simplicity. Our results do not differ substantially when $h_1 \neq h_2$, but the algebra becomes much more difficult to interpret.

For a given orientation θ, we seek to calculate the curve $D = 0$ in velocity space, as this determines the range of velocity differences close to $U = 0$ for which the eigenvalues are real. We can make some analytical progress in this direction by assuming $\sigma \ll 1$, $\varepsilon \ll 1$, and $U \ll 1$, because (3.21) suggests that the most relevant part of the velocity space is close to $U = 0$. Neglecting large powers of ε, σ and U, in the discriminant yields

$$\begin{aligned} D = {} & (1-\sigma)^2 \left(2\sigma - 12\sigma\varepsilon u_\mathrm{e} + \varepsilon^2 \sin^2\theta \cos^2\phi\right) \\ & + 2\varepsilon\cos\phi(1-\sigma)^2(\sin\psi\sin\theta - 3\sigma\cos\psi\cos\theta)(1 - 5\,\varepsilon\cos\phi\, u_\mathrm{e})\, U \\ & + \tfrac{1}{4}(1-\sigma)\cos^2\psi \left\{(1-5\sigma)(20\,\varepsilon\cos\phi\, u_\mathrm{e} - 4)\right. \\ & \quad \left. - \varepsilon^2\cos^2\phi\,(2 + \sin^2\theta + 40\,u_\mathrm{e}^2 + 10\tan\psi\sin 2\theta)\right\} U^2 \\ & + \mathrm{O}(U^3, \varepsilon^3, \sigma^3, \varepsilon^2\sigma), \end{aligned} \tag{3.23}$$

where $u_\mathrm{e} = u_1\cos\theta - v_1\sin\theta$ is the eastward velocity in the upper layer. Note that the approximation (3.23) does not represent a consistent asymptotic approximation of D. Typically $U \sim \sigma^{1/2}$ on the boundary where $D = 0$, so it would be more consistent to neglect terms that are $\mathcal{O}(\sigma^2)$ if we are neglecting terms that are $\mathcal{O}(U^3)$. However, the most important feature of (3.23) is the neglect of high-order powers of U, and we retain some higher powers of σ because they simplify the resulting expression. We may simplify (3.23) further to obtain

$$|U\cos\psi - \varepsilon\cos\phi\sin\theta\tan\psi| < \sqrt{2\sigma} + \mathcal{O}(\varepsilon^2, \sigma^{3/2}, \sigma^{1/2}\varepsilon). \tag{3.24}$$

This is a somewhat basic, but more intuitive approximation to the curve $D = 0$. In the traditional case ($\varepsilon = 0$), we approximately recover (3.21), where the sign of D is determined solely by the component of the velocity difference parallel to the x-axis, $U\cos\psi$. The term proportional to ε introduces the leading-order influence of the complete Coriolis force, though the $\tan\psi$ term causes the approximation to diverge as ψ approaches $\pi/2$ and $3\pi/2$. With $\varepsilon \neq 0$, the sign of D is dependent on the velocity differences parallel to both the x and y axes, and also varies with θ, the orientation of the axes. Both approximations (3.23) and (3.24) break down for very large eastward velocity u_e, so we will consider the case of large velocities separately in §3.3.4.

In Figure 3.2(a) we plot the curve $D = 0$ in velocity space with $\theta = \pi/4$, $\phi = \pi/12$, and $u_\mathrm{e} = 0$. We have used $\sigma = \varepsilon = 0.01$, because neither parameter will typically exceed this value in the ocean. The asymptotic solution given by (3.23) agrees well with a numerical calculation of the locus $D = 0$, in which we used a bisection search to find the U at which D vanished for each ψ. Both solutions show a substantial departure from curve $D = 0$ under the traditional approximation, which depends only on the velocity difference in the direction of the x-axis. The simpler approximation (3.24)

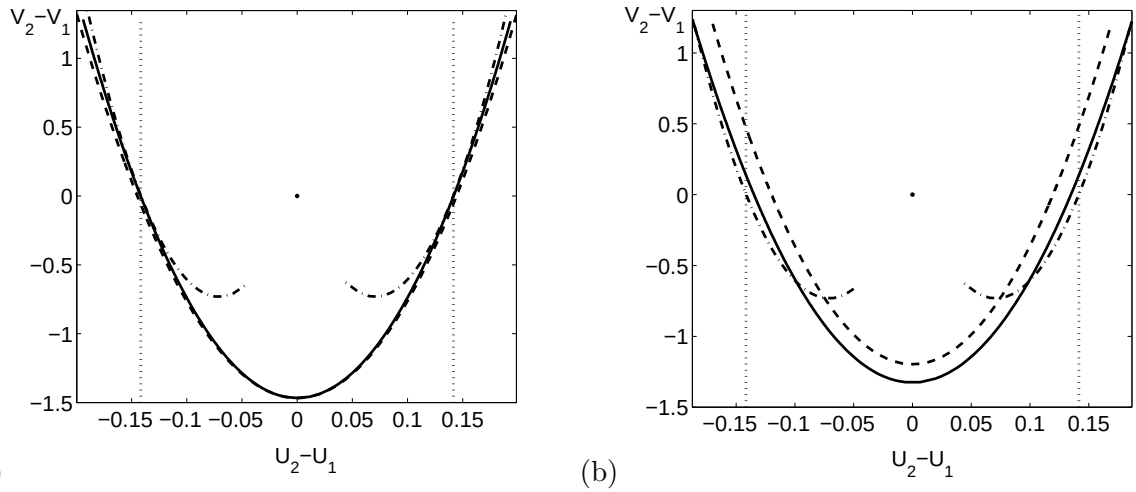

Figure 3.2: Plots of the curve $D = 0$ in the space of velocity differences parallel $(u_2 - u_1)$ and perpendicular $(v_2 - v_1)$ to the x-axis, with $\theta = \pi/4$, $\phi = \pi/12$, and $\sigma = \varepsilon = 0.01$. Panel (a) has $u_e = 0$, and panel (b) has $u_e = 10$. The curve has been calculated numerically (solid line), asymptotically using (3.23) (dashed line), (3.24) (dashed-dotted line), and under the traditional approximation (dotted vertical lines). In each case the two-layer shallow water equations are ill-posed outside the curve $D = 0$, and may be hyperbolic inside the curve, close to (0,0).

works well for values of ψ that are sufficiently far from $\pi/2$ and $3\pi/2$. It diverges rapidly at these points due to the $\tan\psi$ in the $\mathcal{O}(\varepsilon)$ term. Figure 3.2(b) shows the case of large absolute velocities in the layers, with $u_e = 10$. The asymptotic solution of (3.23) has started to deviate noticeably from the numerical solution, although the comparison is still quite good. The simpler condition (3.24) does not capture changes due to the different value of u_e.

As discussed in §3.3.1, for fixed velocities the two-layer shallow water equations are ill-posed if the eigenvalues λ are complex for any direction θ. The most useful measure of their hyperbolicity is the maximum velocity difference $U_{\max}$ in any direction ψ such that the eigenvalues are real for all θ. In Figure 3.3 we plot $U_{\max}$ against the relative density difference σ, calculated numerically, using the approximation (3.23), and in the traditional case (3.21). Despite the dramatic change in the shape of the curve $D = 0$, shown in Figure 3.2, there is very little change in $U_{\max}$ between the traditional and non-traditional cases.

By far the largest influence on the hyperbolicity is the density contrast σ, which sets the speed of internal waves. From (3.21) the internal wave speed is $U_{\text{int}} = \left(1 - \sqrt{1-\sigma}\right)^{1/2} \sim (\sigma/2)^{1/2}$ as $\sigma \to 0$. Figure 3.4 shows the ratio of $U_{\max}$ for the two-layer equations with complete Coriolis force to the corresponding value U_{trad} under the traditional approximation. From these plots we conclude that in geophysically reasonable parameter regimes the condition for hyperbolicity reduces by no more

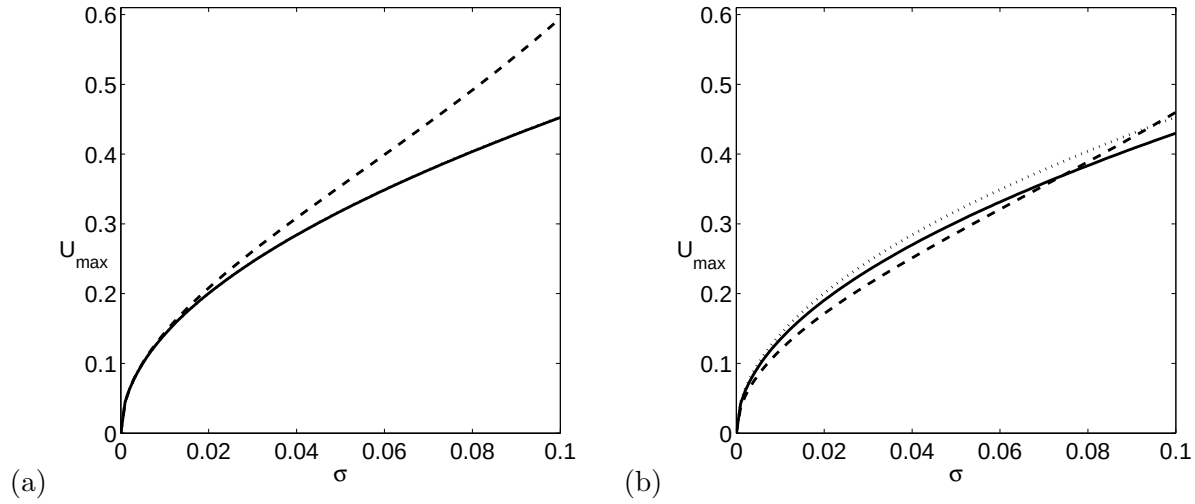

Figure 3.3: Plot of the maximum velocity difference $U_{\max}$ for which the two-layer equations are hyperbolic, as a function of the density difference σ, with $\phi = \pi/12$, and $\varepsilon = 0.01$. Panel (a) shows $u_{\mathrm{e}} = 0$, and panel (b) shows $u_{\mathrm{e}} = 10$. The plots have been calculated numerically (solid line), asymptotically using (3.23) (dashed line), and for the traditional case (dotted line). The dotted line is obscured by the solid line in panel (a).

than 5% through the inclusion of non-traditional effects in the equations.

3.3.4 Loss of hyperbolicity due to the Eötvös effect

The results presented in the preceding section are only valid when the eastward velocity of the layers is not too large. When the eastward velocity in either layer is sufficiently large, the upward acceleration due to the non-traditional component of the Coriolis force (3.3b) may counteract the downward acceleration due to gravity. This is known as the Eötvös effect (*e.g.* Persson, 2005). Though one might not expect such large velocities to arise in the context of geophysical fluid dynamics, we include a brief discussion here to complete our analysis.

For simplicity, we restrict our attention to a large eastward velocity in the lower layer, setting $\boldsymbol{u}_1 = 0$, $u_{\mathrm{n}} = u_2 \sin\theta + v_2 \cos\theta = 0$, and taking $u_{\mathrm{e}} = u_2 \cos\theta - v_2 \sin\theta \to \infty$. The lower layer northward and eastward velocities are u_{n} and u_{e} respectively. With these assumptions we obtain an expression for the discriminant D of the quartic (3.18) as a polynomial in u_{e},

$$\begin{aligned} D = &- 4h_1h_2\varepsilon\cos\phi\cos^8\theta\left(4+\varepsilon^2h_1\cos^2\phi\right)u_{\mathrm{e}}^9 \\ &+ h_1h_2\cos^6\theta\left(4+\varepsilon^2h_1\cos^2\phi\right)\left[4\cos^2\theta\right. \\ &\left.+\varepsilon^2\cos^2\phi\left(-4h_1\cos^2\theta(3+\sigma)+h_2\left(1-17\sin^2\theta\right)\right)\right]u_{\mathrm{e}}^8+\cdots. \end{aligned} \tag{3.25}$$

The coefficient of u_{e}^9 is strictly negative, so for all $\varepsilon > 0$ the discriminant is negative for sufficiently

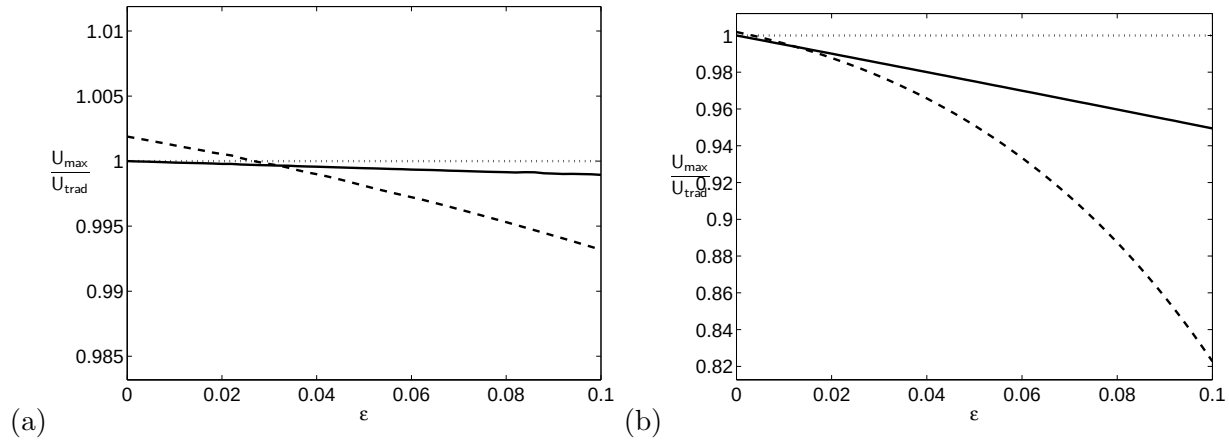

Figure 3.4: Plot of the maximum velocity difference $U_{\max}$ for which the two-layer equations are hyperbolic as a function of ε, divided by the traditional ($\varepsilon = 0$) value U_{trad}, for $\phi = \pi/12$ and $\sigma = 0.001$. Panel (a) shows $u_{\text{e}} = 0$, whilst panel (b) shows $u_{\text{e}} = 1$. The plots have been calculated numerically (solid line), asymptotically using (3.23) (dashed line), and for the traditional case (dotted line). The asymptotic solution does not satisfy $U_{\max}/U_{\text{trad}} \to 1$ as $\varepsilon \to 0$ because it is a truncated expansion in both ε and σ.

large and positive u_{e}. Only in the singular limit $\varepsilon \to 0$ is the discriminant positive for arbitrarily large u_{e}. For $\cos\theta \neq 0$, we neglect u_{e}^7 and smaller powers in (3.25), we find that $D < 0$ when

$$u_{\text{e}} \gtrsim \frac{1}{\varepsilon \cos\phi} + \mathcal{O}(\varepsilon). \tag{3.26}$$

Dropping terms of $\mathrm{O}(\varepsilon)$, this condition may be rearranged using (3.5) as

$$1 + \varepsilon(\Omega_x v_2 - \Omega_y u_2) \gtrsim 0, \tag{3.27}$$

which is exactly the condition for the sum of the gravitational and Coriolis accelerations in (3.3b) to remain negative. This condition is independent of θ, and so we conclude that (3.26) is sufficient for the system to be ill-posed. This matches the same condition found by Dellar and Salmon (2005) for the hyperbolicity of the single-layer shallow water equations with complete Coriolis force. We may derive an analogous result for large eastward velocities in the upper layer. If we allow the eastward velocities in both layers to tend to infinity together, we actually find that $D > 0$ because all four eigenvalues are complex. However, the condition for hyperbolicity (3.26) holds independently for the eastward velocities in each layer.

We may also verify that large northward/southward velocities do not make the system ill-posed. In the case that $\boldsymbol{u}_1 = u_{\text{e}} = 0$ and $u_{\text{n}} \to \infty$, the discriminant is

$$D = h_1 h_2 \sin^8\theta \left(4 + \varepsilon^2 h_1 \cos^2\phi\right)\left(4 + \varepsilon^2 \cos^2\phi \left(4h_1(1-\sigma) + h_2\right)\right) u_{\text{n}}^8 + \cdots. \tag{3.28}$$

Thus $D > 0$ for sufficiently large u_{n}. In the case $\sin\theta = 0$, all terms containing u_{n} disappear from

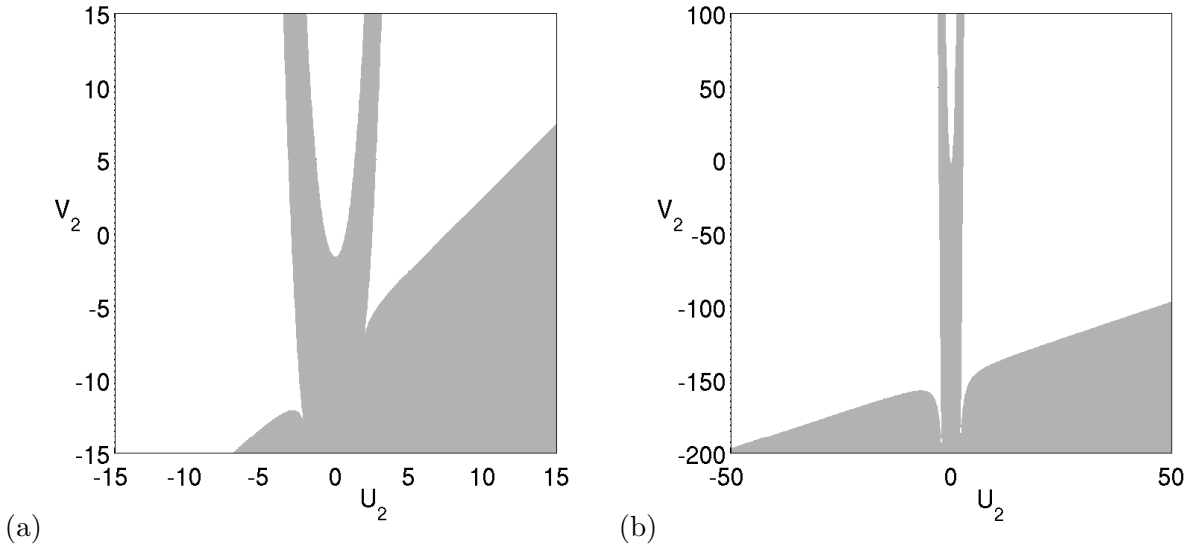

Figure 3.5: Plots of the regions where some eigenvalues of the Jacobian matrix $\mathbf{C}_x$ are complex (shaded) over a range of lower-layer velocities $\boldsymbol{u}_2$. The upper layer velocity is zero, $\phi = \pi/12$, $\theta = \pi/4$, and $h_1 = h_2 = 1$. Panel (a): $\sigma = \varepsilon = 0.2$. Panel (b): $\sigma = \varepsilon = 0.01$.

(3.18), so the eigenvalues are real for all u_n. The same result holds for large northward/southward velocities in the upper layer.

We illustrate our results from this and the previous section in Figure 3.5. We have computed the region of lower-layer velocities $\boldsymbol{u}_2$ for which some eigenvalues of the Jacobian matrix $\mathbf{C}_x$ are complex. In this calculation the upper layer is stationary, and we have used specimen parameters $\phi = \pi/12$, $\theta = \pi/4$, $h_1 = h_2 = 1$. Figure 3.5(a) uses exaggerated values of σ and ε to illustrate the qualitative features of the region close to $\boldsymbol{u}_2 = 0$. The eigenvalues become complex when $|u_2|$ becomes too large, but then become real again for even larger $|u_2|$, as they do under the traditional approximation. However, with the complete Coriolis force they also become complex when v_2 becomes too large and negative, or when the eastward velocity is very large. The same qualitative features are present in Figure 3.5(b) with more realistic values of σ and ε. The latter case shows a very clear separation between the two asymptotic regimes examined above, *i.e.* between the regime of very small velocity difference between the layers, and the regime of very large absolute velocities within the layers.

In summary, the analysis of the hyperbolicity of our multi-layer shallow water equations is complicated by the many extra non-traditional terms involving ε, and by the loss of isotropy due to the preferred direction defined by the horizontal component of the rotation vector. However, geophysically reasonable fluid velocities are all much smaller than the surface gravity wave speed, and our non-traditional shallow water equations are hyperbolic in this regime. Figure 3.3 shows that

the threshold velocity difference $U_{\max}$, below which the system is hyperbolic, differs little between the traditional and non-traditional cases. These results do not differ substantially in systems of more than two layers, so we conclude that the multi-layer shallow water equations are hyperbolic in approximately the same regime as the traditional equations.

3.4 Linear plane waves in the two-layer shallow water equations

In §3.3 we showed that the hyperbolicity of the multi-layer shallow water equations is not substantially affected by the inclusion of the complete Coriolis force. We now investigate the properties of linear plane waves around an equilibrium state of rest. The behaviour of linear plane waves in the traditional two-layer shallow water equations is well-established in geophysical fluid dynamics (*e.g.* Gill, 1982, §6.2), as they offer an intuitive description of the interaction of rotation and stratification in large-scale wave phenomena. When rotating uniformly about a vertical axis, the equations are invariant to rotations of the horizontal axes, and so linear waves are isotropic. The only interdependence between layers is through the pressure gradient, as may be seen in (3.8a) and (3.8c) by setting $\varepsilon = 0$. This simple vertical structure allows the linearised equations to be exactly decomposed into barotropic and baroclinic modes (*e.g.* Zeitlin, 2007), corresponding to surface waves and internal waves respectively.

When the complete Coriolis force is included, (3.8a) and (3.8c) are no longer invariant under rotations about the vertical axis, so linear waves should be anisotropic. Dellar and Salmon (2005) showed that this is the case for linear waves in the non-traditional single-layer shallow water equations. In the non-traditional two-layer equations we also expect to see a disruption of the vertical structure, because each layer is at a different distance from the oblique axis of rotation. In this section we show that the waves modes make a transition from barotropic to baroclinic modes at long wavelengths, so the modes can no longer be decomposed. In the range of wavelengths over which this transition takes place, the structure of the waves changes dramatically, and they are no longer recognisable as either surface waves or internal waves.

3.4.1 Dispersion relation

We consider an equilibrium state in which the dimensional heights of both layers are constant, $\tilde{h}_1 = H_1$ and $\tilde{h}_2 = H_2$, and the fluid velocities are zero, $\boldsymbol{u}_1 = \boldsymbol{u}_2 = 0$. We choose $H = H_1$ as the height scale for our nondimensionalisation in (3.2), so the dimensionless equilibrium heights are $h_1 = 1$ and $h_2 = R$, where $R = H_2/H_1$ is the ratio of layer thicknesses. It is straightforward to show that this steady state is a solution of the two-layer equations (3.8a–*d*). We perturb the equilibrium

state by setting $\boldsymbol{u}_1 = \boldsymbol{u}_1'$, $h_1 = 1 + h_1'$, $\boldsymbol{u}_2 = \boldsymbol{u}_2'$, and $h_2 = R + h_2'$, where $|\boldsymbol{u}_1'|, |h_1'|, |\boldsymbol{u}_2'|, |h_2'| \ll 1$. Substituting into (3.8a–d) and neglecting products of small terms, we obtain

$$\frac{\partial \boldsymbol{u}_1'}{\partial t} + \Omega_z \hat{\boldsymbol{z}} \times \boldsymbol{u}_1' - \varepsilon\, \boldsymbol{\Omega} \times \hat{\boldsymbol{z}}\, \nabla \cdot \left(\tfrac{1}{2}\boldsymbol{u}_1' + R\boldsymbol{u}_2'\right) + \nabla \left[\left(h_1' + h_2'\right) + \tfrac{1}{2}\varepsilon \left(v_1'\Omega_x - u_1'\Omega_y\right)\right] = 0, \tag{3.29a}$$

$$\frac{\partial h_1'}{\partial t} + \nabla \cdot \boldsymbol{u}_1' = 0, \tag{3.29b}$$

$$\frac{\partial \boldsymbol{u}_2'}{\partial t} + \Omega_z \hat{\boldsymbol{z}} \times \boldsymbol{u}_2' - \tfrac{1}{2}\varepsilon R\, \boldsymbol{\Omega} \times \hat{\boldsymbol{z}}\, \nabla \cdot \boldsymbol{u}_2' + \nabla \left(h_2' + \rho_r h_1'\right) + \nabla \left[\tfrac{1}{2}\varepsilon R \left(v_2'\Omega_x - u_2'\Omega_y\right) + \rho_r \varepsilon \left(v_1'\Omega_x - u_1'\Omega_y\right)\right] = 0, \tag{3.29c}$$

$$\frac{\partial h_2'}{\partial t} + R\nabla \cdot \boldsymbol{u}_2' = 0. \tag{3.29d}$$

We seek plane wave solutions of the form $\boldsymbol{u}_1', h_1', \boldsymbol{u}_2', h_2' \sim \exp[\mathrm{i}(kx + ly - \omega t)]$. The wave vector is $\boldsymbol{k} = (k, l)$, and defines a direction of propagation in the horizontal plane. For convenience we choose θ, the orientation of the x and y axes, such that the x-axis points in the direction of the wave vector. Our perturbations are therefore proportional to $\exp[\mathrm{i}(kx - \omega t)]$, and θ defines the direction of wave propagation. Note that θ appears in (3.29a–d) only through the horizontal component of the rotation vector $\boldsymbol{\Omega}$, so we expect the waves to be anisotropic only when the complete Coriolis force is included. Substituting $\boldsymbol{u}_1', h_1', \boldsymbol{u}_2', h_2' \sim \exp[\mathrm{i}(kx - \omega t)]$ into (3.29a–d) yields a matrix of coefficients whose determinant must be zero to guarantee non-trivial solutions for the perturbation velocities and layer thicknesses,

$$\begin{aligned}
&\omega^4 + \varepsilon\, \Omega_y k(1+R)\, \omega^3 \\
&+ \left\{ -2\Omega_z^2 - k^2(1+R) + \varepsilon^2 \Omega_y^2 \sigma R k^2 - \tfrac{1}{4}\left(1 + R^2 + 4R(1-\sigma)\right)\varepsilon^2 \Omega_x^2 k^2 \right\} \omega^2 \\
&+ \left\{ -\varepsilon\, \Omega_y \Omega_z^2 (1+R)k - 2\,\sigma\varepsilon\, \Omega_y R k^3 - \tfrac{1}{4}\varepsilon^3 \Omega_y \Omega_x^2 R(R+1)k^3 \right\} \omega \\
&+ \left\{ \Omega_z^4 + k^4 \sigma R + \Omega_z^2\, k^2 R + \tfrac{1}{16} k^4 \varepsilon^4 \Omega_x^4 R^2 \right. \\
&\qquad \left. + \tfrac{1}{4} k^2 \varepsilon^2 \Omega_x^2 \left(k^2 R(1+R) + \Omega_z^2 \left(1 + R^2\right)\right) \right\} = 0.
\end{aligned} \tag{3.30}$$

Here $\sigma = 1 - \rho_r = (\rho_2 - \rho_1)/\rho_2$ is the dimensionless density difference. There are also two geostrophic modes with $\omega = 0$, but they are not substantially altered by the non-traditional component of the Coriolis force.

Figure 3.6 shows some numerically-generated plots of the dispersion relation (3.30), computed using relatively large values of σ and ε so that all of the dispersion curves are visible on the same plot. We show in §3.4.5 below that the waves with higher frequency, and consequently larger phase velocities, are surface waves in which the free and internal surfaces move in phase. The lower-frequency

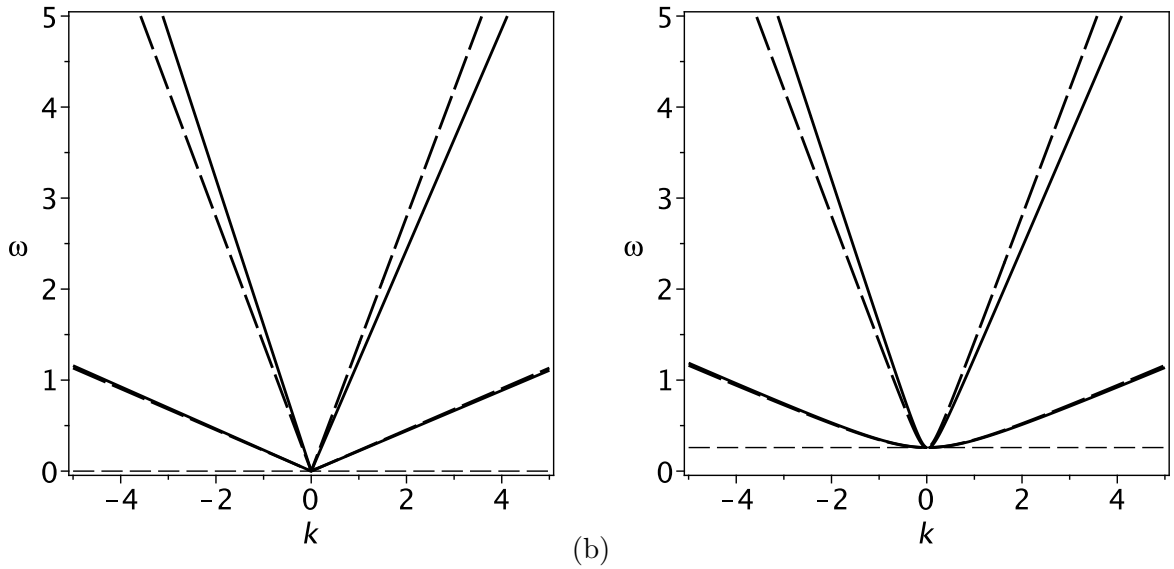

Figure 3.6: Dispersion curves for traditional (thick dashed lines) and non-traditional (solid lines) east/west-propagating waves at (a) the equator, and (b) at 15 °N (right), with parameters $\varepsilon = 0.2$, $\sigma = 0.1$, and $R = 1$. The horizontal thin dashed line marks the inertial frequency.

waves are internal waves, in which the free surface is approximately flat and the internal surface oscillates. When the complete Coriolis force is included, the waves acquire an east/west asymmetry due to the θ-dependence of Ω_x and Ω_y. However, there is no substantial difference between the traditional and non-traditional frequencies for $\mathcal{O}(1)$ wavelengths, *i.e.* dimensional wavelengths comparable to the deformation radius R_d. We show below that more dramatic changes occur for very short and very long waves.

3.4.2 Asymptotic solutions

As discussed in §3.3.2, there are formulae for the exact roots of (3.30), but such an approach is impractical for a quartic whose coefficients are already long algebraic expressions. Computed solutions, like those shown in Figure 3.6, are of limited use in describing the general behaviour of the waves, so instead we employ an asymptotic expansion in the small aspect ratio ε,

$$\omega = \omega_\varepsilon^{(0)} + \varepsilon\,\omega_\varepsilon^{(1)} + \varepsilon^2\omega_\varepsilon^{(2)} + \cdots. \tag{3.31}$$

Substituting into (3.30) and equating powers of ε gives the first three terms in this expansion,

$$\omega_\varepsilon^{(0)} = \pm_\alpha \sqrt{\sin^2\phi + \tfrac{1}{2}k^2\left(1 + R \pm_\beta \sqrt{(1+R)^2 - 4\sigma R}\right)}, \tag{3.32a}$$

$$\omega_\varepsilon^{(1)} = -\tfrac{1}{4}k\cos\phi\cos\theta\left(1 + R \pm_\beta \sqrt{(1+R)^2 - 4\sigma R}\right), \tag{3.32b}$$

$$\begin{aligned}\omega_\varepsilon^{(2)} = \frac{1}{16\omega_\varepsilon^{(0)}\sqrt{1+2R+R^2-4\sigma R}}\Big[&\pm_\beta 2R(1-\sigma)\sin^2(2\phi)\sin^2\theta \\ &\pm_\beta\ k^2\cos^2\phi\Big\{(R+1)\left((R+1)^2 - 2R\sigma\right) \\ &+\ \left(R^2+1+2(1-\sigma)R(1+\sin^2\theta)\right)\sqrt{(1+R)^2-4\sigma R}\Big\}\Big].\end{aligned} \tag{3.32c}$$

The $\pm_\alpha$ and $\pm_\beta$ may take signs independently of one another, so the leading-order term $\omega_\varepsilon^{(0)}$ has four solutions as expected. These solutions are the wave frequencies under the traditional approximation. The higher-order terms $\omega_\varepsilon^{(1)}$ and $\omega_\varepsilon^{(2)}$ represent corrections due to non-traditional effects. These corrections depend on θ, so the non-traditional waves are indeed anisotropic. The linear dependence of $\omega_\varepsilon^{(1)}$ on k introduces the east/west asymmetry, decreasing the frequencies of eastward-propagating waves and increasing the frequencies of westward-propagating waves. However, $\omega_\varepsilon^{(1)} \to 0$ as $\theta \to \pm\pi/2$, and $\omega_\varepsilon^{(0)}$ and $\omega_\varepsilon^{(2)}$ are even functions of k, so we expect this asymmetry to vanish in northward- and southward-propagating waves. This is consistent with the governing equations (3.8a–*d*). The non-traditional components of the Coriolis force act zonally and vertically, but not meridionally.

Setting $k = 0$ in the full dispersion polynomial (3.30) gives $\omega = \pm_\alpha \sin\phi$ regardless of the value of ε, so the frequency of very long waves must approach the inertial frequency as $k \to 0$. Setting $k = 0$ in our asymptotic expansion (3.32a–*c*) yields $\omega_\varepsilon^{(0)} = \pm_\alpha \sin\phi$, so the leading order term is exact and higher-order terms introduce errors. The next term in the expansion is

$$\omega_\varepsilon^{(3)} \sim \pm_\beta \frac{R\sin^2\phi\cos^3\phi\cos\theta\sin^2\theta(1-\sigma)}{k\sqrt{(1+R)^2-4\sigma R}} = \mathrm{O}\left(\frac{1}{k}\right) \quad \text{as} \quad k \to 0, \tag{3.33}$$

so the expansion becomes disordered in the limit as $k \to 0$, and cannot describe the behaviour of long waves.

A natural alternative approach is to fix ε and pose an expansion of ω in powers of k instead,

$$\omega = \omega_k^{(0)} + k\omega_k^{(1)} + k^2\omega_k^{(2)} + \cdots. \tag{3.34}$$

This is guaranteed to remain ordered in the limit $k \to 0$, but is only valid for $k \ll 1$. Substituting

(3.34) into the dispersion polynomial (3.30) and equating powers of k yields

$$\omega_k^{(0)} = \pm_\gamma \sin\phi, \tag{3.35a}$$

$$\omega_k^{(1)} = \tfrac{1}{4}\varepsilon\,\cos\phi\left[-(1+R)\cos\theta \pm_\delta \sqrt{(1-R)^2\cos^2\theta + 4R(1-\sigma)}\right], \tag{3.35b}$$

$$\omega_k^{(2)} = \pm_\gamma \frac{1}{16\sin\phi}\left\{4(1+R) + \varepsilon^2\cos^2\phi\left((1+R)^2 - 2\sigma R\right)\right.$$
$$\left. \mp_\delta \frac{\cos\theta\left((1+R)^2 - 4\sigma R\right)\left(4 + \varepsilon^2(1+R)\cos^2\phi\right)}{\sqrt{\cos^2\theta(1-R)^2 + 4R(1-\sigma)}}\right\}. \tag{3.35c}$$

Here again we use subscripts $\pm_\gamma$ and $\pm_\delta$ to denote that these operators may take signs independently of one another. Notice that $\omega_k^{(1)}$ is $\mathcal{O}(\varepsilon)$, just as previously $\omega_\varepsilon^{(1)}$ was $\mathcal{O}(k)$, so the two approximations $\omega_k^{(0)} + k\omega_k^{(1)}$ and $\omega_\varepsilon^{(0)} + \varepsilon\omega_\varepsilon^{(1)}$ coincide when k, ε and θ are all close to 0. However, the higher-order terms $\omega_k^{(n)}$ for $n \geq 3$ diverge as $\varepsilon \to 0$. We return to this in the next subsection.

The expansion (3.35a–c) shows that $\partial\omega/\partial k \neq 0$ at $k = 0$ when non-traditional effects are included ($\epsilon \neq 0$). This means that some wave frequencies close to $k = 0$ must lie below the inertial frequency. Gerkema and Shrira (2005a) obtained an analogous result for linear waves in a continuously-stratified fluid, and showed that the behaviour of very long waves ($k \to 0$) is independent of the stratification. Very long waves in the two-layer shallow water equations do depend on σ, the relative density difference between the layers, but they are only strongly affected when propagating almost eastward/westward. Restricting our attention to positive frequencies, the dispersion relation in the limit $k \to 0$ is

$$\omega = \sin\phi + \frac{\varepsilon\, k}{4}\cos\phi\left[-(1+R)\cos\theta \pm_\delta \sqrt{(1-R)^2\cos^2\theta + 4R(1-\sigma)}\right] + \mathcal{O}(k^2). \tag{3.36}$$

Equation (3.36) is most easily interpreted by restricting $\theta \in [-\pi/2, \pi/2]$ so that $\cos\theta \geq 0$. Then $k > 0$ corresponds to eastward-propagating waves, and $k < 0$ corresponds to westward-propagating waves. The root corresponding to the negative branch of $\pm_\delta$ is always larger than the inertial frequency for $k < 0$, and always smaller for $k > 0$, so there is always one eastward-propagating sub-inertial wave mode. The root corresponding to the positive branch of (3.36) is smaller than the inertial frequency for $k > 0$ when $|\theta|$ is below the critical angle

$$\theta_\mathrm{c} = \sin^{-1}\sqrt{\sigma},. \tag{3.37}$$

The second sub-inertial mode also propagates eastward if $|\theta| < \theta_\mathrm{c}$, while if $|\theta| > \theta_\mathrm{c}$ the second sub-inertial mode propagates westward. When $|\theta| = \theta_\mathrm{c}$ there is only a single sub-inertial mode. As σ is typically very small ($\lesssim 10^{-3}$) in the ocean, we only expect to find two sub-inertial waves propagating in the same direction when $|\theta| \lesssim 2\,^\circ$.

Figure 3.7 shows the long-wave dispersion relation for waves propagating in various directions. We have again used exaggerated values of σ and ε to make both the surface and internal wave branches visible on the same plot. Figure 3.7(a) shows the case of east/west-propagating waves, where the asymptotic solutions are indistinguishable from the numerical results. As predicted, the non-traditional terms lower the frequencies of eastward-propagating waves, and increase the frequencies in westward-propagating waves. Sub-inertial frequencies are present for both surface and internal waves, although the latter are difficult to see on these axes.

In fact, east/west-propagating waves ($\theta = 0$) are special cases, and the dispersion relation for northeast/southwest propagating waves ($\theta = \pi/4$) shown in Figure 3.7(b) is more typical. Here sub-inertial waves propagate in both directions because $\theta > \theta_c$. More importantly, one branch of the dispersion relation appears to correspond to a surface wave mode for $k < 0$, but to an internal wave mode for $k > 0$. Similarly, the other branch corresponds to an internal wave mode for $k < 0$, and to a surface wave mode for $k > 0$. This transition will be explored in §3.4.5.

Figure 3.7(d) shows waves propagating at the critical angle θ_c, and confirms that there is only one sub-inertial wave. The shape of the non-traditional dispersion relation gives some insight into the transition from separate internal and surface wave branches when $\theta = 0$, to branches that change from surface to internal waves and vice versa when $\theta \neq 0$. For north/south-propagating waves, shown in Figure 3.7(c), the dispersion curves are symmetric about $k = 0$, as predicted by our expansion for small ε, and the sub-inertial region encompasses the largest range of wave numbers. This suggests that north/south-propagating long internal waves may be most influenced by non-traditional effects.

3.4.3 A distinguished limit as $\varepsilon, k \to 0$

Our small-k expansion was motivated by the breakdown of our small-ε expansion in the limit $k \to 0$. However, we encounter an equivalent breakdown of our small k expansion when ε is small. The leading-order term $\omega_k^{(0)}$ is accurate for any ε at $k = 0$, but the higher order terms in k introduce an error. Similarly to (3.33) above, we find that

$$\omega_k^{(3)} \sim \pm_\delta \frac{R \sin^2\theta (1-\sigma)\left((1+R)^2 - 4\sigma R\right)}{2\,\varepsilon \cos\phi \sin^2\phi \left\{(1-R)^2\cos^2\theta + 4R(1-\sigma)\right\}^{3/2}} = \mathcal{O}\left(\frac{1}{\varepsilon}\right) \quad \text{as} \quad \varepsilon \to 0, \tag{3.38}$$

so the expansion in k becomes disordered when $\varepsilon = \mathcal{O}(k)$. This mutual disordering suggests a combined asymptotic limit as both $k, \varepsilon \to 0$. We seek a scaling

$$k = \varepsilon^a K, \tag{3.39}$$

with some exponent a, such that we obtain the global behaviour of the solution from letting $\varepsilon \to 0$ while K remains $\mathcal{O}(1)$. We determine a by requiring that both our existing asymptotic expansions

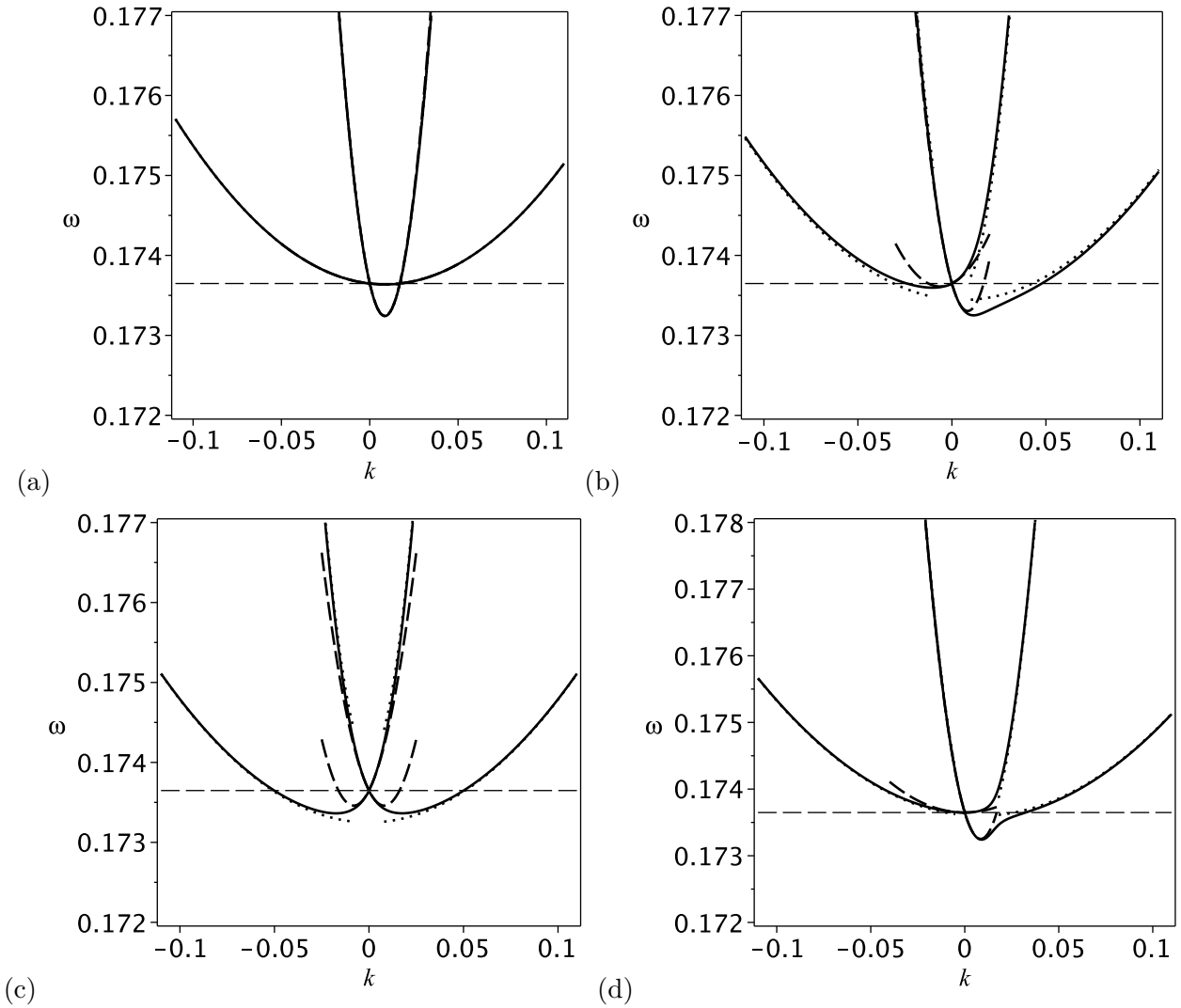

Figure 3.7: Long-wave dispersion curves for waves propagating (a) east/west, (b) northeast/southwest, (c) north/south, and (d) at the critical angle. All plots are at 10 °N with $\sigma = \varepsilon = 0.1$ and $R = 1$. Numerical solutions are shown solid, small ε asymptotics using thick dashed lines, and small k asymptotics using dotted lines. The horizontal thin dashed line marks the inertial frequency.

remain bounded as $\varepsilon, k \to 0$. That is, we require that $\varepsilon^i \omega_\varepsilon^{(i)} \to 0$ and $k^i \omega_k^{(i)} \to 0$ as $\varepsilon, k \to 0$ for all i. For latitude $\phi \neq 0$ and $i \geq 1$, it may be shown that $\omega_\varepsilon^{(i)} \sim k^{2-i}$ as $k \to 0$, and similarly that $\omega_k^{(i)} \sim \varepsilon^{2-i}$ as $\varepsilon \to 0$. Using the scaling (3.39), we therefore require that

$$\left.\begin{array}{lllll} \varepsilon^i \omega_\varepsilon^{(i)} & \sim & \varepsilon^i k^{a(2-i)} & = & \varepsilon^{i+a(2-i)} K^{2-i} \\ k^i \omega_k^{(i)} & \sim & k^i \varepsilon^{2-i} & = & \varepsilon^{ai+(2-i)} K^i \end{array}\right\} \to 0 \quad \text{as} \quad \varepsilon \to 0, \quad i \geq 1. \tag{3.40}$$

We therefore require $i + a(2-i) > 0$ and $ai + (2-i) > 0$ for all $i \geq 1$. This immediately yields $a > 0$ from the cases $i = 1$ and $i = 2$, and for $i \geq 3$ rearranges into the constraints

$$1 - \frac{2}{i} < a < \left(1 - \frac{2}{i}\right)^{-1} \quad \text{for} \quad i \geq 3. \tag{3.41}$$

whose only solution is $a = 1$. Hence $k = \varepsilon K$ is the appropriate scaling to study the distinguished limit as $\varepsilon, k \to 0$.

A more physical motivation for the scaling $k = \varepsilon K$ may be obtained directly from the linearised equations (3.29). For plane waves proportional to $\exp[\mathrm{i}(kx - \omega t)]$ the two continuity equations (3.29b) and (3.29d) become

$$\omega h_1' = k u_1', \quad \omega h_2' = R k u_2'. \tag{3.42}$$

The frequency ω remains $\mathcal{O}(1)$ as $k \to 0$, at any latitude $\phi \neq 0$, so we must have $h_1', h_2' \to 0$ as $k \to 0$. At $k = 0$, the linearised shallow water momentum equations (3.29a) and (3.29c) reduce to

$$\omega \boldsymbol{u}_1' + \mathrm{i}\Omega_z \hat{\boldsymbol{z}} \times \boldsymbol{u}_1', \quad \omega \boldsymbol{u}_2' + \mathrm{i}\Omega_z \hat{\boldsymbol{z}} \times \boldsymbol{u}_2', \tag{3.43}$$

which describes an inertial oscillation in each layer with frequency equal to the vertical component of the dimensionless planetary vorticity Ω_z. Thus, the velocity perturbations u_1' and u_2' remain $\mathcal{O}(1)$ as $k \to 0$. From (3.42), we deduce that the height perturbations h_1' and h_2' are proportional to k in the limit as $k \to 0$. In other words, for long waves the perturbations to the free and internal surfaces become vanishingly small relative to the velocity perturbations. We now evaluate the relative magnitudes of terms in the x-component (3.29a) of the momentum equation,

$$\omega u_1' - \mathrm{i}\Omega_{z0} v_1' + \varepsilon \Omega_y k \left(\tfrac{1}{2} u_1' + R u_2'\right) - k \left(h_1' + h_2' + \tfrac{1}{2}\varepsilon \left(v_1' \Omega_x - u_1' \Omega_y\right)\right) = 0. \tag{3.44}$$

The pressure gradient $k(h_1' + h_2')$ is $\mathcal{O}(k^2)$, while the non-traditional terms are $\mathcal{O}(\varepsilon k)$, as $k \to 0$. The non-traditional terms become comparable in magnitude to the hydrostatic pressure gradient for sufficiently long waves with $k = \mathcal{O}(\varepsilon)$.

Setting $k = \varepsilon K$, the dispersion relation (3.30) contains only even powers of ε. This motivates an asymptotic expansion of the form

$$\omega = \omega^{(0)} + \varepsilon^2 \omega^{(1)} + \varepsilon^4 \omega^{(2)} + \cdots. \tag{3.45}$$

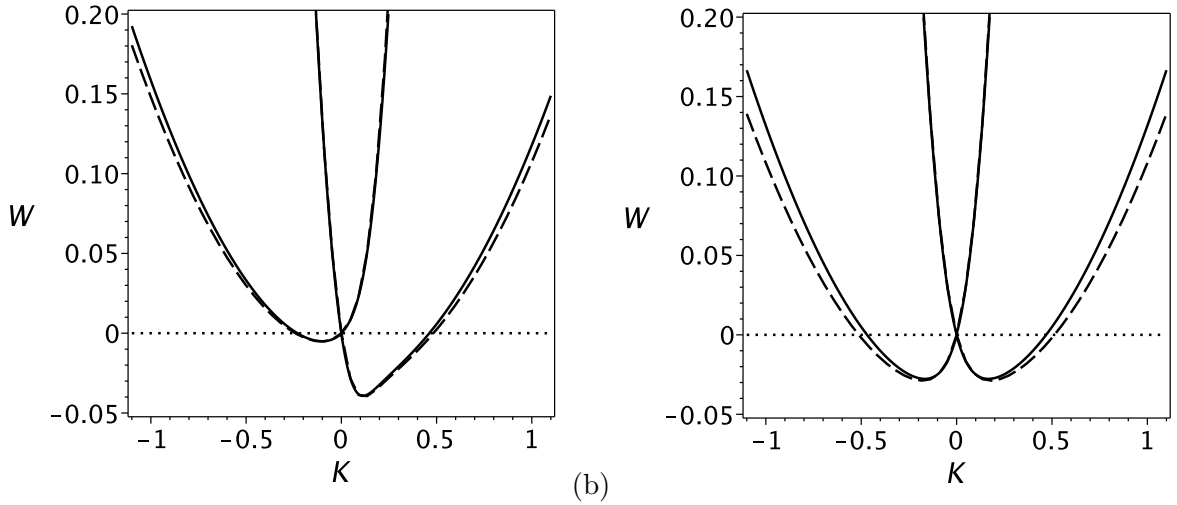

Figure 3.8: Dispersion relations for waves propagating (a) northeast/southwest, and (b) north/south, at 10 °N with $\varepsilon = 0.2$. Here $K = k/\varepsilon$ is the rescaled wavenumber, and $W = (\omega - \sin\phi)/\varepsilon^2$ is the rescaled deviation of the frequency from the inertial frequency. Numerical solutions are shown solid, and the asymptotic solutions in the distinguished limit are shown dashed.

Collecting terms in powers of ε^2, the $\mathcal{O}(1)$ solution is

$$\omega^{(0)} = \pm \sin\phi. \tag{3.46}$$

At $\mathcal{O}(\varepsilon^2)$, we obtain a quadratic polynomial that determines $\omega^{(1)}$,

$$\begin{aligned} &\sin^2\phi\,\omega^{(1)2} + \tfrac{1}{2}K\sin\phi\,(\cos\theta\cos\phi\sin\phi \mp K)\,\omega^{(1)} \\ &\quad + \tfrac{1}{4}K^2R\left(K\sigma\,(K \mp 2\cos\phi\sin\phi\cos\theta) - \cos^2\phi\sin^2\phi\left(\sin^2\theta - \sigma\right)\right) = 0. \end{aligned} \tag{3.47}$$

These roots describe four wave modes, depending on which sign of the $\mp$ operator is taken. Figure 3.8 shows the wave frequencies when $k = \mathcal{O}(\varepsilon)$. Following the above scalings, we plot numerical solutions in the form $W = (\omega - \sin\phi)/\varepsilon^2$ against $K = k/\varepsilon$, which gives a universal picture of the dispersion relation as $\varepsilon \to 0$ with $k = \mathcal{O}(\varepsilon)$. The leading-order approximation to W is $\omega^{(1)}$. We use a very large value $\varepsilon = 0.2$ to make the distinction between the asymptotic and numerical solutions visible in Figure 3.8.

3.4.4 Properties of sub-inertial waves

The combination of (3.46) and (3.47) accurately captures the behaviour of long waves, and allows us to derive some analytical results for long sub-inertial waves. We first obtain an estimate for the wavelength at which non-traditional effects become important by determining the width of the sub-inertial region, *i.e.* the nonzero wavenumbers at which the frequency is again equal to the inertial

frequency. Setting $\omega^{(1)} = 0$ and solving for K yields

$$k_{\text{inertial}} = \tfrac{1}{2}\varepsilon \sin(2\phi) \left(\cos\theta \pm \sin\theta \sqrt{1/\sigma - 1} \right), \tag{3.48}$$

which confirms that the width of the sub-inertial range of wavenumbers is $\mathcal{O}(\varepsilon)$ as $\varepsilon \to 0$. For $|\theta| \leq \pi/2$ we may rearrange (3.48) to show that both solutions for k_{inertial} are only positive when $|\theta| < \theta_{\text{c}}$, as defined in (3.37). We thus recover our earlier result from §3.4.2 for the direction of propagation of sub-inertial waves.

A straightforward conversion back to dimensional variables gives a dimensional wavenumber $\tilde{k} \sim H/R_d^2$ that is much larger than any oceanographic lengthscale. However, the width is also $\mathcal{O}(\sigma^{-1/2})$ when the density ratio σ is small. Sub-inertial waves become much shorter in weakly-stratified layers, and in §3.5 we will show that this scaling changes to $k_{\text{inertial}} \sim \varepsilon/\sigma$ for three or more layers.

The approximate solution (3.48) is not valid in the limit $\sigma \to 0$ for fixed ε. We may obtain an exact expression for k_{inertial} by setting $\omega = \sin\phi$ in the dispersion relation (3.30) and solving for k. In this case k_{inertial} depends on the layer depth ratio R, whereas the approximate expression (3.48) does not, so we set $R = 1$ for simplicity. The exact expression is

$$k_{\text{inertial}} = \frac{\varepsilon\, \Omega_z \left(\sigma\Omega_y + \frac{1}{4}\varepsilon^2 \Omega_y \Omega_x^2 \pm \Omega_x \sqrt{(1-\sigma)\left(\sigma + \frac{1}{2}\varepsilon^2\Omega_x^2 + \frac{1}{16}\varepsilon^4\Omega_x^2(\Omega_y^2 + \Omega_x^2)\right)} \right)}{\sigma + \frac{1}{2}\varepsilon^2\Omega_x^2 + \frac{1}{16}\varepsilon^4\Omega_x^4} \tag{3.49}$$

where Ω_x, Ω_y and Ω_z are the dimensionless components of the rotation vector, defined in (3.5). There are $\mathcal{O}(\varepsilon^2)$ terms in the denominator of (3.49), so (3.48) is only valid for σ finite, or in a further distinguished limit in which $\sigma = \mathcal{O}(\varepsilon)$ as $\varepsilon \to 0$.

Equation (3.48) implies that the sub-inertial region will be widest when $\theta = \pm\pi/2$, corresponding to north/south-propagating waves. Hughes (1964) showed that poleward-propagating waves in a continuously stratified fluid could not travel beyond a critical latitude ϕ_{c}, which was expressed by Gerkema et al. (2008) as

$$\phi_{\text{c}} = \pm \sin^{-1} \left[\frac{\tilde{\omega}^2}{4\Omega^2} - \frac{\tilde{\omega}^2}{N^2} \left(\frac{\tilde{\omega}^2}{4\Omega^2} - 1 \right) \right]^{1/2}, \tag{3.50}$$

where $\tilde{\omega}$ is the dimensional wave frequency, and N is the buoyancy or Brunt–Väisälä frequency. To obtain a similar result for our two-layer system we use (3.47) to find the minimum frequency ω_{min}. This arises when $k = k_{\text{min}}$, given by

$$k_{\text{min}} = \pm\tfrac{1}{2}\varepsilon \sin(2\phi) \left(\frac{(1-\sigma)\sqrt{R}}{(1+R+2\sqrt{\sigma R})\sqrt{\sigma}} \right)^{1/2} + \mathcal{O}\left(\varepsilon^3\right). \tag{3.51}$$

Using (3.46) and (3.47), we rewrite the minimum frequency as

$$\omega_{\text{min}} = |\sin\phi| \left(1 - \tfrac{1}{2}\varepsilon^2 \cos^2\phi \frac{(1-\sigma)R}{1+R+2\sqrt{\sigma R}} + \mathcal{O}\left(\varepsilon^4\right) \right). \tag{3.52}$$

Poleward-propagating waves of a given frequency ω only exist at latitudes for which $\omega_{\min} < \omega$. The so-called turning latitude ϕ_c, at which incident waves must be reflected, is given by $\omega = \omega_{\min}$, so (3.52) gives

$$\sin\phi_c = \pm\omega\left(1 + \tfrac{1}{2}\varepsilon^2(1-\omega^2)\frac{(1-\sigma)R}{1+R+2\sqrt{\sigma R}}\right) + \mathcal{O}\left(\varepsilon^4\right). \tag{3.53}$$

There is an analogy between this result and the turning latitude for the waves in a continuously stratified Boussinesq fluid, as studied by Gerkema and Shrira (2005b,a). For strong stratification with $N \gg 2\Omega$ the minimum frequency is (Gerkema et al., 2008)

$$\omega_{\min} = |\sin\phi|\left(1 - \tfrac{1}{2}\kappa^2\cos^2\phi + \mathcal{O}\left(\kappa^4\right)\right), \tag{3.54}$$

where $\kappa = 2\Omega/N \ll 1$. This may be rearranged to give an expression for the turning latitude,

$$\sin\phi_c = \pm\omega\left(1 + \tfrac{1}{2}\kappa^2\left(1-\omega^2\right)\right) + \mathcal{O}\left(\kappa^4\right). \tag{3.55}$$

The similarity between the forms of (3.55) and (3.53) suggests that the role of κ in the continuously-stratified case is similar to that of ε in our layered model. As $\varepsilon = H/R_d = 2\Omega\sqrt{H/g}$ and $\kappa = 2\Omega/N = 2\Omega/\sqrt{-g/\rho_0\,\mathrm{d}\rho/\mathrm{d}z}$, where ρ_0 is a reference density and $\rho(z)$ is the stratification, our layer height H is analogous to the density scale height $-\rho_0/(\mathrm{d}\rho/\mathrm{d}z)$. The approximation (3.55) also follows from the more general expression (3.50) for the turning latitude by writing the dimensional frequency as $\tilde{\omega} = 2\Omega\omega$ and expanding the right hand side of (3.50) in powers of κ. The quantity κ differs by a factor of $\sin\phi$ from the frequency ratio f/N that appears in the three-dimensional quasigeostrophic equations (*e.g.* Pedlosky, 1987; White, 2002). This factor is due to our use of Ω rather than $\Omega_z = \Omega\sin\phi$ in our definition of the deformation radius R_d. With this identification of ϵ in a layered model with κ in a continuously stratified fluid, our scaling for long near-inertial waves corresponds with the scaling for very shallow internal waves in Thuburn et al. (2002b).

Whilst the minimum frequency $\omega_{\min}$ and the corresponding turning latitude ϕ_c have an interesting analogy with continuously-stratified waves, the expansion (3.45) in the distinguished limit shows that the deviation of $\omega_{\min}$ from the traditional case is only $\mathcal{O}(\varepsilon^2)$. A more dynamically relevant property is that the group velocity $c_g = \mathrm{d}\omega/\mathrm{d}k$ vanishes at $\omega = \omega_{\min}$, so a packet of waves with wavenumbers around $k_{\min}$ would be stationary. Equation (3.51) shows that $k_{\min} \sim \varepsilon/\sigma^{1/4}$, so these waves are even longer than the estimate (3.48) suggests, but our findings in §3.5 suggest that they may be somewhat shorter in the case of multiple layers. A further consequence of the shift in $k_{\min}$ is that the inertial oscillations at $k = 0$ have non-zero group velocity when the non-traditional effects are accounted for, but this is less relevant to realistic oceanic motions. Gerkema and Shrira (2005a) found similar results for long waves in the continuously stratified case. The group velocity was again non-zero at $k = 0$, but there was no zero of the group velocity close to $k = 0$. Instead, the frequency decreased monotonically towards a minimum $\omega_{\min}$ as $k \to \infty$.

3.4.5 Structure of sub-inertial waves

In §3.4.4 we showed that relaxing the traditional approximation leads to interesting and unexpected changes in the wave frequencies. We now show that the structure of the waves also changes dramatically in the sub-inertial region created by the complete Coriolis force . We illustrate this by considering the relationship between the perturbations h_1' and h_2' to the layer thicknesses. For perturbations of the form $\exp[\mathrm{i}(kx-\omega t)]$, the linearised equations (3.29a–d) may be rearranged to give

$$r_h = \frac{h_1'}{h_2'} = \frac{4k^2 + 4\varepsilon k\,(\mathrm{i}\,\Omega_x\Omega_z - \omega\Omega_y) + 2\varepsilon^2 k^2\Omega_x^2}{4\omega^2 - 4\Omega_z^2 - 4k^2 + 4\omega\varepsilon k\Omega_y - \varepsilon^2 k^2\Omega_x^2}. \tag{3.56}$$

The imaginary term in the numerator of r_h causes the layer heights to oscillate out of phase. This does not occur under the traditional approximation ($\varepsilon = 0$). We first consider the behaviour of r_h when k is not close to 0. Using our asymptotic expansion (3.31) for ω in powers of ε, we expand (3.56) as

$$r_h = \frac{2}{R - 1 \pm_\beta \sqrt{(1+R)^2 - 4\sigma R}}\left(1 + \mathrm{i}\,\varepsilon\,\frac{\sin\theta\sin(2\phi)}{2k} + \mathcal{O}\left(\varepsilon^2\right)\right) \quad \text{as} \quad \varepsilon \to 0, \tag{3.57}$$

where $\pm_\beta$ takes the same sign as in (3.32a). The leading-order term is equal to that obtained under the traditional approximation, and is independent of the wave number. The positive root is approximately equal to $1/R = H_1/H_2$, and corresponds to h_1' and h_2' oscillating together. This gives rise to surface waves. The negative root is approximately equal to -1, so $h_1' + h_2' \approx 0$. This root corresponds to internal waves. Including non-traditional terms leads to an $\mathcal{O}(\varepsilon)$ complex correction to the eigenmode, which causes the surfaces to oscillate slightly out of phase. This effect will be least pronounced for very short waves ($k \to \infty$), and most pronounced in long waves ($k \to 0$), although we cannot accurately consider the latter limit using an expansion in ε alone, as shown in §3.4.3.

We obtain a similar expansion of r_h in powers of k by substituting (3.34) into (3.56). However, only the leading-order term is simple enough to interpret directly,

$$r_h = \frac{2(\pm_\gamma \mathrm{i}\,\sin\theta - \cos\theta)}{(1-R)\cos\theta \pm_\delta \sqrt{(1-R)^2\cos^2\theta + 4R(1-\sigma)}} + \mathcal{O}(k) \quad \text{as} \quad k \to 0, \tag{3.58}$$

where $\pm_\gamma$ and $\pm_\delta$ take the same signs as in (3.35a) and (3.35b). There is an $\mathcal{O}(1)$ complex contribution to r_h at $k = 0$, even as $\varepsilon \to 0$, which identifies the traditional approximation as a singular limit. In other words, for ε arbitrarily close to zero, there is an $\mathcal{O}(1)$ change in the wave structure for sufficiently small k.

To obtain a reliable picture of the behaviour of r_h close to $k = 0$, we use the distinguished limit expansion from §3.4.3. We may use this to obtain an expansion of $r_h(K)$ in powers of ε, but we omit this result because it is difficult to interpret. Instead we present plots of the real and

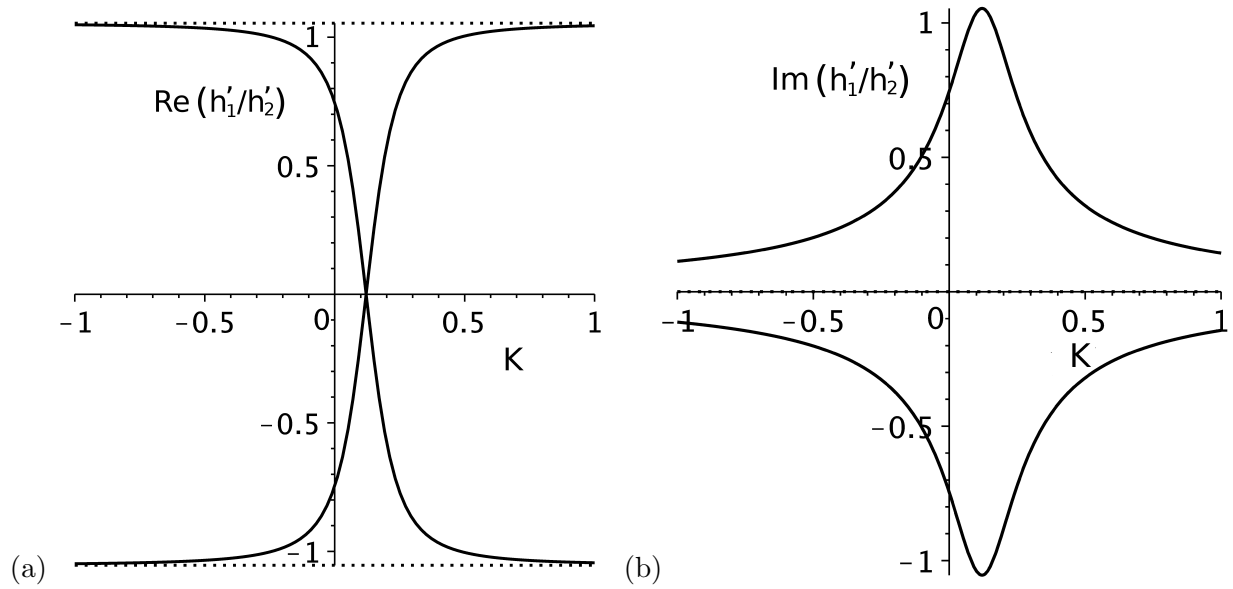

Figure 3.9: The (a) real and (b) imaginary parts of the perturbation height ratio $r_h = h_1'/h_2'$ for traditional (dotted lines) and non-traditional (solid lines) long waves propagating northeast/southwest at 10 ° North with $\sigma = \varepsilon = 0.1$ and $R = 1$.

imaginary parts of r_h as functions of $K = k/\varepsilon$ in Figure 3.9. We have used the same parameter values that were used to plot the dispersion curves for northeast/southwest-propagating waves in Figure 3.8, and we show only the wave modes with positive frequencies. The real part of r_h makes a transition from surface to internal waves, or vice versa, in the range of sub-inertial wavenumbers. The complex part of r_h also becomes most prominent in the sub-inertial region, peaking when the real part reaches zero. The waves in the sub-inertial region are thus neither surface nor internal waves, so their structure has been dramatically altered by the inclusion of non-traditional terms. This alteration of the structure disappears at the equator ($\phi = 0$) and in zonally-propagating waves ($\theta = 0$), and is most prominent in north/south-propagating waves at mid-latitudes.

In Figure 3.10 we illustrate the alteration of the wave structure by the non-traditional component of the Coriolis force. We plot schematic profiles of the upper surface $z = \eta_1$ of a wave whose internal surface $z = \eta_2$ has a cosine profile, for $R = 1$ and $\sigma \ll 1$. Under the traditional approximation, the upper surface profiles distinctly correspond to a surface wave mode and an internal wave mode. In the non-traditional case, corresponding to the wavenumber at which $r_h = 0$ in Figure 3.9, the upper surface oscillates out of phase with the internal surface in both modes of propagation. This may constrain the amplitude of long internal waves, because perturbations to the internal surface require even larger perturbations to the upper surface when the complete Coriolis force is included. Under the traditional approximation the upper surface may remain approximately flat while the internal

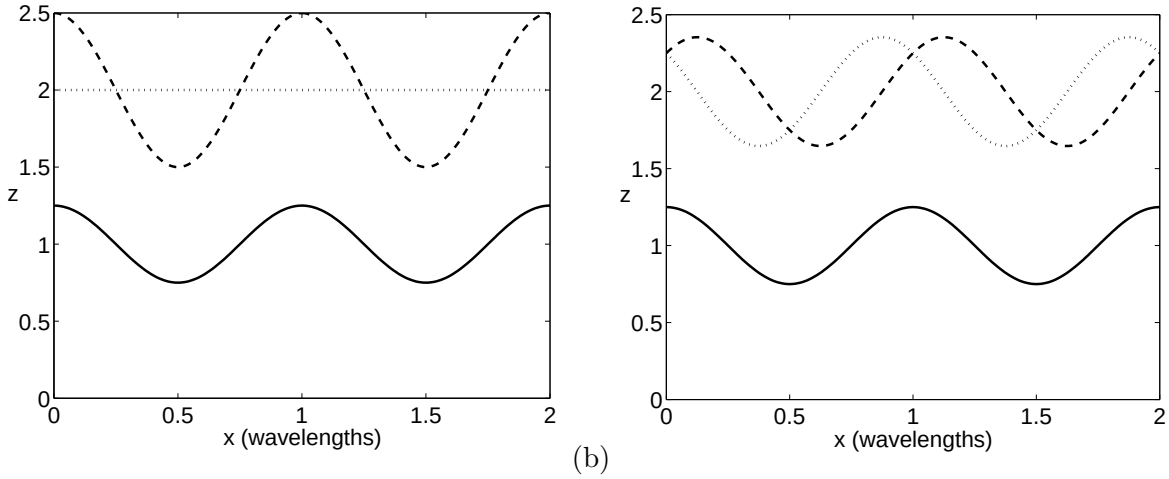

Figure 3.10: A schematic plot of the surface heights in linear plane waves close to the inertial frequency. Panel (a) shows the height of upper surface $z = \eta_1$ for both the surface (dashed line) and internal (dotted line) wave modes, for a fixed internal surface profile $z = \eta_2$ (solid line). Panel (b) shows the same modes with non-traditional effects included, for the wavenumber in Figure 3.9 at which $r_h = 0$.

surface fluctuates. The principal restoring force acting on the internal surface is the reduced gravity, so perturbations to the internal surface require less energy than perturbations to the upper surface, which is subject to the full force of gravity. Thus, for the same wave energy, we expect long internal waves to have a smaller amplitude when the complete Coriolis force is included.

3.4.6 Structure of short waves

Non-traditional plane waves also exhibit some interesting structural changes at short wavelengths, where the ratio of the layer depth to the wavelength is smaller. However, these changes tend not to be as dramatic as those associated with sub-inertial waves. Manipulating (3.29a–d) with all variables proportional to $\exp[\mathrm{i}(kx - \omega t)]$, gives an expression for the ratio of the lower layer velocities,

$$r_v = \frac{v_2'}{u_2'} = \frac{-\mathrm{i}\Omega_z + \frac{1}{2}\varepsilon k R \Omega_x}{\omega}. \tag{3.59}$$

Under the traditional approximation ($\varepsilon = 0$), r_v is purely imaginary. For long waves $\omega \to \pm\Omega_z$ and $r_v \to \mp\mathrm{i}$, so the longitudinal and horizontal transverse velocities are of equal magnitude, but oscillate $\pi/2$ radians out of phase. In other words, long waves are circularly polarised. For short waves $|\omega| \to \infty$ and $r_v \to 0$, so the transverse velocity vanishes and the waves are unaffected by rotation. These short waves thus resemble sound waves, using the analogy between shallow water theory and adiabatic gas dynamics with adiabatic exponent $\gamma = 2$, though they still have vertical velocities if one interprets shallow water theory as being an approximation to motions under the full three-dimensional fluid equations.

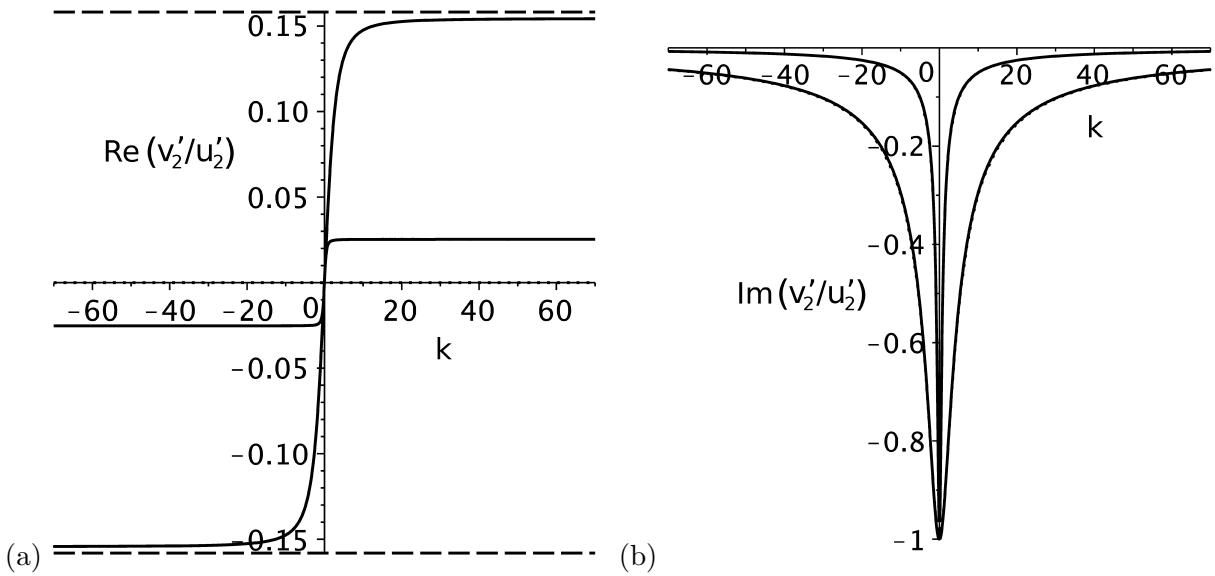

Figure 3.11: The (a) real and (b) imaginary parts of the ratio $r_v = v_2'/u_2'$ of the lower-layer perturbation velocities for traditional (dotted lines) and non-traditional (solid lines) long waves propagating northeast/southwest at 10 ° North with $\sigma = \varepsilon = 0.1$ and $R = 1$. The dashed line represents the asymptotic solution for infinitesimally short internal waves.

Including non-traditional effects leads to an additional real term proportional to k in the numerator of (3.59). In the short wave limit ω is also proportional to k,

$$\omega \sim \pm_\alpha k \sqrt{\tfrac{1}{2}\left(1 + R \ \pm_\beta \sqrt{(1+R)^2 - 4\sigma R}\right)} + \mathcal{O}(\varepsilon) \quad \text{as} \quad |k| \to \infty, \tag{3.60}$$

so we expect r_v to tend to a real constant as $|k| \to \infty$. For surface waves, corresponding to the '$+_\beta$' root, we exploit the density difference σ as a second small parameter to write

$$r_v \to \pm\tfrac{1}{2}\varepsilon \cos\phi \sin\theta \, \frac{R}{\sqrt{1+R}} + \mathcal{O}\left(\sigma\varepsilon, \varepsilon^2\right) \quad \text{as} \quad |k| \to \infty, \tag{3.61}$$

while for internal waves, corresponding to the '$-_\beta$' root, we find

$$r_v \to \pm\tfrac{1}{2}\varepsilon \cos\phi \sin\theta \, \frac{R^{3/2}\sqrt{1+R}}{\sqrt{\sigma}} + \mathcal{O}\left(\sigma^{1/2}\varepsilon, \sigma^{-1/2}\varepsilon^2\right) \quad \text{as} \quad |k| \to \infty. \tag{3.62}$$

Non-traditional effects cause the transverse velocity to oscillate in phase with the longitudinal velocity, even in the short wave limit. The $\sqrt{\sigma}$ in the denominator of (3.62) makes the transverse velocity much more prominent in internal waves. The effective deformation radius of internal waves is smaller by a factor of $\sqrt{\sigma}$, since the restoring force due to buoyancy is weaker for internal waves. The effective aspect ratio between the vertical lengthscale and the relevant deformation radius is thus $\varepsilon/\sqrt{\sigma}$.

Equation (3.59) is analogous to the expression in Gerkema et al. (2008) for the ratio of the horizontal velocity perturbations in a continuously stratified fluid. In our notation, this expression

becomes

$$\frac{|v'|}{|u'|} = \left|\frac{(\Omega_x \mu_\pm - \Omega_z)}{\omega}\right|, \quad \mu_\pm = \frac{\kappa^2 \Omega_x \Omega_z \pm \kappa\sqrt{\omega^2 - \Omega_z^2 + \kappa^2\omega^2(\Omega_x^2 - \omega^2 - \Omega_z^2)}}{1 + \kappa^2(\Omega_x^2 - \omega^2)}. \tag{3.63}$$

Under the traditional approximation ($\Omega_x \equiv 0$) or close to the inertial frequency ($|\omega| \to |\Omega_z|$) we find that $v'/u' \to \pm\mathrm{i}$. Waves in a continuously stratified fluid thus become circularly polarised close to the inertial frequency, as in (3.59) for our two-layer system. If non-traditional effects are included, $\Omega_x = 0$ is only satisfied for east/west-propagating waves. For other directions of propagation, the term proportional to μ_+ in (3.63) causes the waves to become elliptically polarised close to the inertial frequency. van Haren and Millot (2004) discuss observations of such elliptically polarised near-inertial waves in weakly-stratified regions of the Mediterranean Sea. A similar situation arises in the two-layer shallow water equations. The non-traditional part of (3.59) vanishes for infinitely long waves with $k = 0$ and $\omega = \Omega_z$, so these waves are circularly polarised. From (3.48), we know that there are one or two positive wave numbers k_{inertial} at which $\omega = \Omega_z$, and these waves become elliptically polarised.

Figure 3.11 shows plots of the real and imaginary parts of r_v for waves with positive frequency. The corresponding plot for negative frequencies may be obtained by reflecting the left-hand plot about the vertical axis and the right-hand plot about the horizontal axis. The imaginary part of r_v is identical in the traditional and non-traditional cases, and represents the part of the transverse velocity that oscillates $\pi/2$ out of phase with the longitudinal velocity. This part is large for long waves, but negligible for short waves, as described above. The plot also shows that the real part of the eigenmode only matches the traditional case ($r_v = 0$) at $k = 0$, while (3.62) gives the asymptotic behaviour of the real part of r_v as $|k| \to \infty$. The ratio v_1'/u_1' of the upper-layer velocities exhibits very similar behaviour to the behaviour we have shown for the ratio of lower-layer velocities $r_v = v_2'/u_2'$.

Vertical velocities cause zonal (east-west) accelerations in the three-dimensional Euler equations with the complete Coriolis force. Vertical motions appear in shallow water theory through changes in the layer depths, *i.e.* through $\partial_t h_1 = -\nabla \cdot (h_1 \boldsymbol{u}_1)$ and $\partial_t h_2 = -\nabla \cdot (h_2 \boldsymbol{u}_2)$, which is the origin of the divergence terms in (3.8a) and (3.8c). Oscillations of the layer heights therefore force oscillations of the transverse velocity for all but directly east/west-propagating waves. In the deep ocean, where the stratification is particularly small, the ratio of transverse to longitudinal velocities may be as large as 0.15 for internal waves.

3.5 Linear plane waves in the multi-layer shallow water equations

In this section we extend our analysis of linear plane waves from §3.4 to include three or more layers. Under the traditional approximation, increasing the number of layers leads to a predictable increase

in the number of of internal wave modes, so multi-layer plane waves do not differ substantially from two-layer plane waves. However, as we have seen in §3.4, including the complete Coriolis force connects the internal and surface modes at very long wavelengths, and it is not clear how these connections will change when more layers are added. We show here that two-layer plane waves are a special case whose frequency matches the inertial frequency when $k = k_{\text{inertial}} \sim \varepsilon/\sqrt{\sigma}$. For multiple layers with equal relative density differences σ, this critical wavenumber is much larger, $k_{\text{inertial}} \sim \varepsilon/\sigma$, so much shorter waves are influenced by the non-traditional component of the Coriolis force.

3.5.1 Dispersion relation

Each layer of fluid is governed by a set of shallow water equations, defined by (3.6) and (3.7). Following the approach detailed in §3.4.1, linearising the N-layer shallow water equations yields a set of $3N$ equations for the $3N$ dependent variables u_i', v_i', h_i'. Seeking solutions proportional to $\exp[\mathrm{i}(kx - \omega t)]$ and rearranging the equations, we obtain a polynomial of order $2N$ in ω, similar to (3.30),

$$\omega^{2N} + c_{2N-1}\omega^{2N-1} + \cdots + c_1\omega + c_0 = 0. \tag{3.64}$$

As in (3.30), we have factored out the N geostrophic modes with $\omega = 0$. Each coefficient c_n for $n = 1, \ldots, 2N-1$ is a function of k that depends on the layer thicknesses $R_i = H_i/H$, for $i = 1, \ldots, N$, the relative density differences $\sigma_i = (\rho_{i+1} - \rho_i)/\rho_{i+1}$, for $i = 1, \ldots, N-1$, the non-traditional parameter ε, the latitude ϕ and the direction of propagation θ. For $N > 2$ it is most efficient to proceed with the analysis using a symbolic manipulation package.

The solutions of equation (3.64) describe N wave modes of positive frequency ($\omega > 0$) and N wave modes of negative frequency ($\omega < 0$). We restrict our attention to the positive modes, because for every negative mode $\omega^{(-)}(k)$ there exists a positive mode $\omega^{(+)}(k)$ that satisfies $-\omega^{(+)}(k) = \omega^{(-)}(-k)$, and vice versa. Under the traditional approximation ($\varepsilon = 0$) the dispersion polynomial (3.64) contains no odd powers, $c_{2n-1} = 0$ for $n = 1, \ldots, N$, and so it may be solved exactly for a larger number of layers. The dispersion relation in this case strongly resembles the traditional dispersion relation shown in Figure 3.6, having one fast barotropic mode and $N-1$ slower baroclinic modes. The minimum frequency for all modes is the inertial frequency $\omega_{\text{inertial}} = \sin\phi$.

Following our earlier analysis of the two-layer system we expect relaxing the traditional approximation (taking $\varepsilon \neq 0$) to produce little change in the dispersion relation at large wavenumbers. However, we expect non-traditional effects to be prominent close to $k = 0$. We may obtain the most complete picture of the behaviour close to $k = 0$ using the distinguished limit expansion described in §3.4.3. For any number of layers N, we set $k = \varepsilon K$ and substitute the expansion

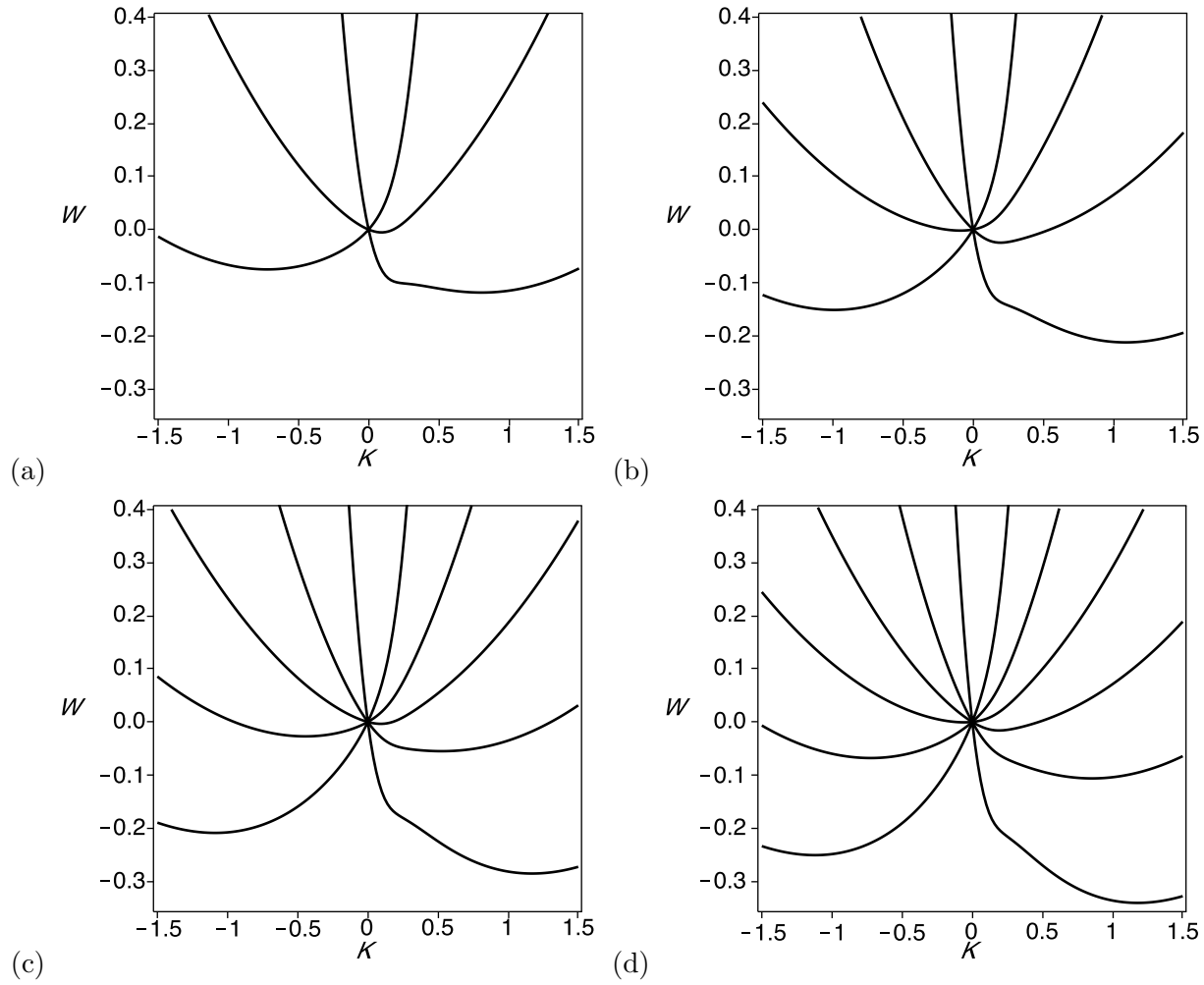

Figure 3.12: Dispersion relations for (a) three, (b) four, (c) five, and (d) six layers of fluid governed by the shallow water equations. The plots have been generated numerically using the distinguished limit $\varepsilon, k \to 0$, so $K = k/\varepsilon$ is the scaled dimensionless wavenumber and $W = (\omega - \sin\phi)/\varepsilon^2$ is the scaled deviation of the frequency from the inertial frequency. In each case $\phi = \pi/12$, $\theta = \pi/4$, and $\sigma_i = 0.1$ and $R_i = 1$ for $i = 1, \ldots, N$. We plot only the modes corresponding to positive frequencies, $\omega > 0$.

$\omega = \omega^{(0)} + \varepsilon^2\omega^{(1)} + \cdots$ into the dispersion polynomial (3.64). The leading-order solution for wave modes with positive frequencies is $\omega^{(0)} = \sin\phi$, as in (3.46). This satisfies the $\mathcal{O}(\varepsilon^{2n})$ dispersion polynomial for $n = 0, \ldots, N-1$. At $\mathcal{O}(\varepsilon^{2N})$ we obtain a polynomial of order N for the first correction $\omega^{(1)}$,

$$\omega^{(1)N} + \hat{c}_{N-1}\omega^{(1)N-1} + \cdots + \hat{c}_1\omega^{(1)} + \hat{c}_0 = 0. \tag{3.65}$$

The coefficients $\hat{c}_n$ are functions of K, σ_i, R_i, ϕ and θ, as in (3.64), but with no dependence on the non-traditional parameter ε.

In Figure 3.12 we show the dispersion relation for typical parameters and increasing numbers of fluid layers. The deviation of the frequency from the inertial frequency in the slowest baroclinic mode becomes more pronounced for larger N. In the limit of infinitely many layers, we might expect to recover the continuously-stratified results of Gerkema and Shrira (2005a), in which the frequency tends to a minimum as $k \to \infty$. We discuss this further in §3.5.2. For any number of layers, the slowest baroclinic mode connects to the fast barotropic mode through the inertial frequency at $k = 0$. This may be shown by keeping ε fixed and considering the limit $k \to 0$, as in §3.4.2. Substituting $\omega = \sin\phi + k\omega_k^{(1)} + \cdots$ into the dispersion polynomial (3.64) and collecting terms of $\mathcal{O}(k^N)$, we obtain distinct non-zero solutions for the linear corrections $\omega_k^{(1)}$ to the inertial frequency. Each wave mode passes through the inertial frequency with a different group velocity, *i.e.* a different gradient in the $k - \omega$ plane. If the modes are only to cross at $k = 0$, the slowest mode must connect to the fastest, the second slowest to the second fastest, and so on. We have calculated the dispersion relations and verified these trends up to $N = 7$, as shown in Figure 3.12, but for larger numbers of layers the algebra becomes prohibitively complicated.

3.5.2 Inertial wavenumber

As shown in §3.4.4, including the complete Coriolis force dramatically alters the structure of waves in the range of subinertial wavenumbers. The wave modes exhibit $\mathcal{O}(1)$ changes in the ratios of the layer depths at long wavelengths, and lose a clear distinction between surface waves and internal waves. A useful estimate of the wavelength at which the wave modes become strongly affected by the non-traditional component of the Coriolis force is k_{inertial}, the wavenumbers at which the wave frequency is equal to the inertial frequency. In two layers we showed that $k_{\text{inertial}} \sim \varepsilon/\sqrt{\sigma}$ as $\varepsilon \to 0$ for fixed σ.

The complexity of the dispersion polynomial for N-layer plane waves (3.64) makes it difficult in general to obtain any analytical results about properties of subinertial waves. However, it is relatively straightforward to determine k_{inertial} approximately using the distinguished limit with

$k = \mathcal{O}(\varepsilon)$ as $\varepsilon \to 0$. Substituting $\omega^{(1)} = 0$ into (3.65) yields a polynomial in K,

$$\hat{c}_0(K) = \left(\prod_{i=1}^{N} R_i\right) K^N \left[\left(\prod_{i=1}^{N-1} \sigma_i\right) K^N + C_{N-1}K^{N-1} + \cdots + C_1 K + C_0\right] = 0. \tag{3.66}$$

The dimensionless layer depths R_i are all exact divisors of $\hat{c}_0(K)$, so the coefficients C_n depend only on ϕ, θ, and the density differences $\sigma_1, \ldots, \sigma_{N-1}$. The roots of (3.66) are the scaled inertial wavenumbers $K_{\text{inertial}} = k_{\text{inertial}}/\varepsilon$. Each wave mode passes through the inertial frequency twice, once at $k = 0$, which corresponds to one of the N roots $K = 0$ in (3.66), and again at a nonzero wavenumber that defines the inertial wavenumber for the mode.

Putting $N = 3$ into (3.66) gives the unscaled inertial wave numbers for the three-layer shallow water equations,

$$k_{\text{inertial}} = \tfrac{1}{2}\varepsilon \sin(2\phi)\cos\theta,\ \tfrac{1}{2}\varepsilon \sin(2\phi)\left(\cos\theta \pm \sin\theta \sqrt{\frac{1-\sigma_1\sigma_2}{\sigma_1\sigma_2}}\right). \tag{3.67}$$

The maximum inertial wavenumber scales as $k_{\text{inertial}} \sim \varepsilon/\sqrt{\sigma_1\sigma_2}$, or as $k_{\text{inertial}} \sim \varepsilon/\sigma$ if $\sigma_1 = \sigma_2 = \sigma$. The range of sub-inertial wavenumbers is thus considerably larger in three layers than it is in two, for which $k_{\text{inertial}} \sim \varepsilon/\sqrt{\sigma}$. We find the same scaling for k_{inertial} when more than three layers are included. For example, in five layers the largest roots for k_{inertial} are

$$k_{\text{inertial}} = \tfrac{1}{2}\varepsilon \sin(2\phi)\left(\cos\theta \pm_\alpha \frac{\sin\theta}{\sigma}\sqrt{\tfrac{1}{2}(1-\sigma)\left(3+\sigma \pm_\beta \sqrt{5-2\sigma+\sigma^2}\right)}\right), \tag{3.68}$$

where $\pm_\alpha$ and $\pm_\beta$ may take signs separately, and we have chosen $\sigma_1 = \sigma_2 = \sigma_3 = \sigma_4 = \sigma$ for simplicity. For $N > 5$ it is still possible to show that $k_{\text{inertial}} \sim \varepsilon/\sigma$, but the algebra involved in finding more detailed expressions becomes prohibitively complicated.

The exact formula for k_{inertial} may be obtained for small N, and in certain special cases, by setting $\omega = \sin\phi$ in the dispersion polynomial (3.64) and solving for k. The exact general formula for $N = 2$ is given in equation (3.49). Our expressions (3.67) and (3.68) for k_{inertial} are derived using the distinguished limit $k = \mathcal{O}(\varepsilon)$ as $\varepsilon \to 0$, and by expanding ω in powers of ε^2. They are only accurate approximations to the exact formulae for k_{inertial} when $\varepsilon^2 \ll \sigma$. We illustrate this in Figure 3.13(a), where we plot the maximum inertial wavenumber k_{inertial} against the density difference σ for $N = 4$. We fix $\varepsilon = 10^{-3}$, $R_1 = R_2 = R_3 = R_4 = 1$, and $\sigma_1 = \sigma_2 = \sigma_3 = \sigma$, so the system describes four layers with equilibrium depths of approximately 500 m, and with equal relative density differences. We use $\theta = \pi/2$ and $\phi = \pi/4$, corresponding to north/south-propagating waves at mid-latitude, because this allows us to obtain an exact expression for k_{inertial}, and because (3.67) and (3.68) suggest that these parameters should maximise k_{inertial}. The solution calculated using the distinguished limit begins to diverge substantially from the exact solution when $\sigma \approx \varepsilon^2 = 10^{-6}$.

In Figure 3.13(b) we illustrate the change in the maximum inertial wavenumber k_{inertial} as the number of layers increases. We have calculated the points marked by white circles by fixing $\theta = \pi/2$,

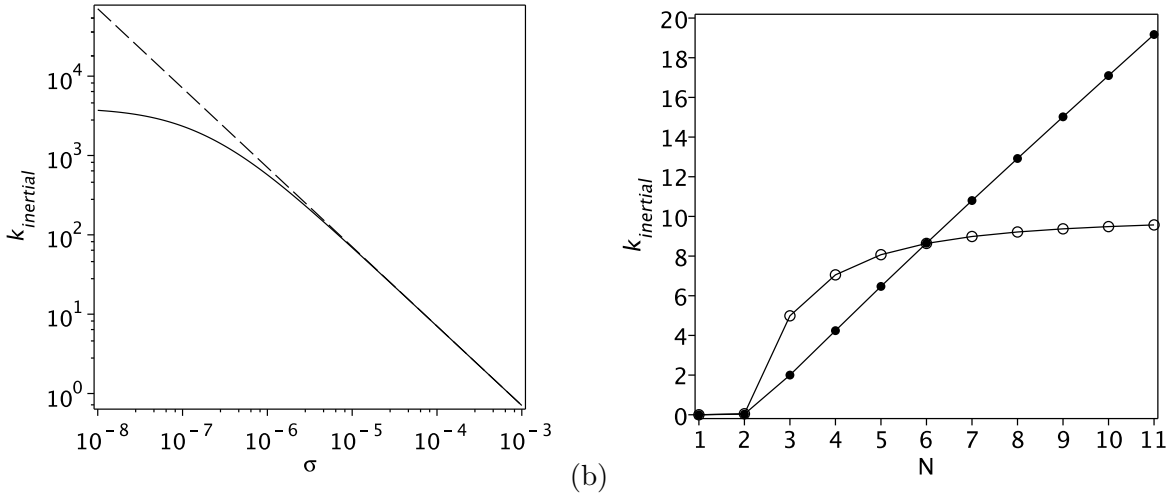

Figure 3.13: Plots of the maximum inertial wavenumber k_{inertial} against (a) the density difference between layers, σ, and (b) the number of layers, N. In each case the waves propagate north/south ($\theta = \pi/2$) at mid-latitude ($\phi = \pi/4$), and the relative density differences are all equal, $\sigma_i = \sigma$, $R_i = R$. In (a), $N = 4$, $R = 1$, $\varepsilon = 10^{-3}$, and we vary σ. In (b), the white circles correspond to $R = 1$, $\sigma = 10^{-4}$, $\varepsilon = 10^{-3}$, and we vary N alone. The black circles correspond to a layer of fixed depth, $\varepsilon = 2 \times 10^{-3}$, $R = 1/N$, and fixed total density difference, $\sigma = 10^{-3}/(N-1)$.

$\phi = \pi/4$, $\varepsilon = 10^{-3}$, $R_i = 1$ for $i = 1, \ldots, N$, and $\sigma_i = 10^{-4}$ for $i = 1, \ldots, N-1$, so that we isolate changes in k_{inertial} due to changes in N alone. Incrementing N by 1 corresponds to stacking an additional 500 m thick layer of fluid on top of the existing layers, whose density is 0.01% less than the density of the layer immediately below. The maximum inertial wavenumber increases with N, but it grows so slowly for larger N that it may approach a limiting value as $N \to \infty$. This limit is somewhat artificial, as eleven layers corresponds to a total depth of 5500 m, which is close to the maximum depth of any ocean on Earth.

The points marked by black circles in Figure 3.13(b) correspond to a more physically relevant case, in which we choose a fixed total equilibrium depth of $H = 2000$ m as our vertical lengthscale. This defines $\varepsilon \approx 2 \times 10^{-3}$ from (3.4), and also defines the horizontal lengthscale as $R_d \approx 960$ km. For a given number of layers N, we divide the total layer depth equally between the layers, so $R_i = 1/N$ for $i = 1, \ldots, N$. We also keep the total absolute density difference between the 1st and N^{th} layers approximately constant by setting $\sigma_i^{(N)} = \sigma_1^{(2)}/(N-1)$ for $i = 1, \ldots, N-1$, where $\sigma_i^{(N)}$ is the relative density difference between layers i and $i+1$. We choose $\sigma_1^{(2)} = 10^{-3}$, so the density varies by 0.1% between the top and bottom layers. The maximum inertial wavenumber k_{inertial} varies linearly with N between $N = 2$ and $N = 11$. This is consistent with our approximate expressions (3.67) and (3.68) for k_{inertial}, which indicate that $k_{\text{inertial}} \sim \varepsilon/\sigma$ for $\varepsilon^2 \ll \sigma$. This gives $k_{\text{inertial}} \sim \varepsilon N$

when rewritten in terms of N. We expect this linear relationship to continue until $\sigma \approx \varepsilon^2$, *i.e.* until $N \approx 250$ in this example, at which point the inertial wavenumber should be $k_{\text{inertial}} \approx 500$. The corresponding dimensional wavelength $\tilde{\lambda}_{\text{inertial}} \approx 12\,\text{km}$ is then comparable to the total depth of the layer.

Our analysis of the limit $N \to \infty$ is restricted by the difficulty of performing the necessary algebraic manipulations in reasonable time for $N > 11$, even with the aid of symbolic computation. However, our computations for $N \leq 11$ and the solutions of (3.66), obtained via the distinguished limit $k = \mathcal{O}(\varepsilon)$ as $\varepsilon \to 0$, suggest that as $N \to \infty$ we recover the result for the continuously-stratified case found by Gerkema and Shrira (2005a), in which there exists a sub-inertial mode at all wavenumbers. Figure 3.13(b) also highlights the special case of two layers $N = 2$. The inertial wavenumber for $N = 2$ is much smaller than for $N \geq 3$ because $k_{\text{inertial}} \sim \varepsilon/\sqrt{\sigma} \ll \varepsilon/\sigma$, as shown in §3.4.4. One would expect the two-layer shallow water equations to exhibit the same scaling for k_{inertial} as the multi-layer equations. The two-layer equations also permit an internal wave mode whose natural horizontal lengthscale is the internal deformation radius. This scaling suggests another distinguished limit linking k, σ, and ε, because our existing asymptotic expressions for k_{inertial} become disordered unless $\epsilon \ll \sqrt{\sigma}$.

3.6 Discussion

The traditional multi-layer shallow water equations have been used widely as a conceptual model for many oceanographic phenomena. By capturing interactions between barotropic and baroclinic modes, they offer a better model for the behaviour of a continuously stratified fluid than the single-layer shallow water equations (*e.g.* LeBlond and Mysak, 1978). Following the single-layer work of Dellar and Salmon (2005), in Chapter 2 we extended the multi-layer shallow water equations to include the complete Coriolis force, while retaining all the expected conservation properties for energy, momentum, and potential vorticity. In this chapter we have demonstrated that the additional "non-traditional" terms in the equations minimally affect their domain of hyperbolicity, the region of parameter space in which our equations are well-posed for initial value problems, but dramatically change the properties of long linear plane waves.

Following the characterisation of hyperbolicity for first-order systems of PDEs in Whitham (1974), we have shown that the two-layer shallow water equations are hyperbolic provided the velocities in both layers are smaller than the internal wave speed, which is around $1\,\text{m}\,\text{s}^{-1}$ for a stratification of $\sigma = 10^{-4}$ in the ocean. The domain of hyperbolicity thus encompasses all realistic fluid velocities. More precisely, the maximum velocity difference $U_{\max}$ at which the equations cease

being hyperbolic differs little from its value under the traditional approximation. However, the analysis is complicated by the anisotropy that arises from the preferred direction defined by the horizontal component (Ω_x, Ω_y) of the rotation vector. There is no preferred horizontal direction under the traditional approximation, because $\mathbf{\Omega}$ has only a vertical component. Our equations may also become non-hyperbolic for very large eastward velocities, because the non-traditional vertical component of the Coriolis acceleration may exceed the acceleration due to gravity. Again, this does not occur for geophysically realistic fluid velocities.

Extending our analysis to three or more layers requires us to determine the nature of roots of polynomials of degree six or higher. Some further calculation in this direction suggests that the domain of hyperbolicity of the equations in three or more layers is not qualitatively different to the domain for two layers. We conclude that the non-traditional multi-layer shallow water equations are hyperbolic in regions of parameter space that differ little from the regions where their traditional counterparts are hyperbolic, and that these regions encompass all geophysically reasonable parameter regimes.

Our study of the dispersion relation for linear plane waves in the two-layer equations, and of the eigenvectors relating the perturbations h_1', h_2' etc, indicates a number of differences from the behaviour under the traditional approximation. Again, the horizontal component of the rotation vector defines a preferred direction, so the dispersion relation becomes horizontally anisotropic. This anisotropy is manifested in the east/west asymmetry of the dispersion relation plotted in Figure 3.6.

The two-layer equations support two wave modes, which may typically be identified either as surface (barotropic) waves, in which the layer thickness perturbations h_1' and h_2' oscillate in phase, or as internal (baroclinic) waves in which the layer thickness perturbations oscillate π radians out of phase and the upper surface is nearly flat. Under the traditional approximation, this separation into surface and internal waves persists at all wavelengths, and the dimensional frequencies $\tilde{\omega}$ of the wave modes are bounded below by the inertial frequency $2\Omega|\sin\phi|$. Including the complete Coriolis force permits a range of long waves with frequencies below the inertial frequency. These were named "sub-inertial" waves by Gerkema and Shrira (2005b,a). Sub-inertial waves exhibit $\mathcal{O}(1)$ modifications in their structure due to the non-traditional component of the Coriolis force, as shown in Figure 3.10, so they no longer qualify as either surface or internal waves. Moreover, eastward-propagating surface waves connect with westward-propagating internal waves via the long sub-inertial waves, and *vice versa*. These changes arise because the non-traditional component of the Coriolis force becomes comparable to the gravitational pressure gradient at sufficiently long wavelengths (see below).

The long sub-inertial waves in our two-layer equations share many qualitative properties with the short sub-inertial waves in continuously stratified fluids identified by Gerkema and Shrira (2005b,a).

For example, both types of waves connect branches of waves that are unconnected under the traditional approximation. Both types of sub-inertial waves also exhibit universal behaviours at near-inertial frequencies, and their existence reflects the singular nature of the traditional approximation as a perturbation in ε. In this respect, the existence of long waves is more surprising than the existence of short waves. Short waves introduce a short horizontal lengthscale that is closer in magnitude to the vertical lengthscale. One might thus expect the traditional approximation, being based on a small aspect ratio, to become invalid for sufficiently short waves. Conversely, one would initially expect the traditional approximation to hold especially well for long waves.

Our analysis in §3.4.3 shows that this counter-intuitive effect on long waves may be explained in terms of a distinguished asymptotic limit. This limit is characterised by waves whose dimensionless wavelength, relative to the Rossby deformation radius R_d, is comparable to the aspect ratio $\varepsilon = H/R_d$. Comparing the magnitudes of terms in the horizontal momentum equations, this distinguished limit arises because the pressure gradient is $\mathcal{O}(k^2)$ for disturbances with dimensionless wavenumber k, while the non-traditional terms are $\mathcal{O}(\varepsilon k)$. For sufficiently long waves the formally small non-traditional effects thus appear at leading order in the momentum equation. There is an $\mathcal{O}(1)$ change in the structure of these waves for arbitrarily small ε, the conventional measure of the strength of non-traditional effects, so the linear wave solution under the traditional approximation is singularly perturbed. Our scaling corresponds to that for shallow near-inertial waves in Thuburn et al. (2002b) if we identify $\varepsilon = H/R_d$ with the natural aspect ratio $\kappa = 2\Omega/N$ for a continuously stratified fluid, which appears in three-dimensional quasi-geostrophic theory.

In the multi-layer shallow water equations with $N > 2$, the fast barotropic wave mode always connects to the slowest baroclinic mode through the sub-inertial wavenumbers. This mode always attains the lowest sub-inertial frequency, and encompasses the largest range of sub-inertial wavenumbers. For a fluid with fixed total equilibrium depth and fixed total density variation, the maximum inertial wavenumber k_{inertial} varies linearly with N as long as the relative density difference σ between layers satisfies $\sigma \gg \varepsilon^2$. It is plausible that $k_{\text{inertial}} \to \infty$ as $N \to \infty$, which would be consistent with the results of Gerkema and Shrira (2005a) for waves in a continuously-stratified fluid. However, demonstrating this is difficult due to the complicated algebra associated with the multi-layered linear wave problem for many layers.

The inertial wave number k_{inertial} provides a useful estimate of the wavelength at which linear plane waves are strongly affected by the inclusion of the complete Coriolis force. In §3.5.2 we show that for $N > 2$, the inertial wavenumber is proportional to ε, and inversely proportional to σ, for

all but east/west-propagating waves,

$$k_{\text{inertial}} \sim \frac{\varepsilon}{\sigma} \quad \text{or} \quad \tilde{\lambda}_{\text{inertial}} \sim \frac{\sigma g}{\Omega^2}, \tag{3.69}$$

where $\tilde{\lambda}_{\text{inertial}}$ is the dimensional inertial wavelength. For Earth-like parameters and weak stratification ($\sigma = 10^{-4}$), this inertial wavelength is about 180 km, which is typical for large-scale ocean waves. For waves longer than this, oscillations of the internal surfaces associated with the slowest baroclinic mode must be accompanied by substantial oscillations of the free surface, as illustrated in Figure 3.10. As oscillations of the free surface require much more energy than oscillations of an internal surface for a given amplitude, internal wave propagation may be constrained by the non-traditional component of the Coriolis force. The longest waves, which carry the most energy, are most strongly affected by this change in structure, which makes this a relevant consideration for internal waves in the real ocean.

This analysis of long waves does not exclude the possibility of strong non-traditional effects arising elsewhere in a geophysical context. The non-traditional terms in (3.8a) are all nonlinear, and we have not accounted for any nonlinear effects here. We have also completely neglected the influence of bottom topography. As fluid moves up or down a slope, its vertical velocity is coupled with its horizontal velocity via the non-traditional component of the Coriolis force. An immediate consequence of varying bottom topography h_b is to change the effective Coriolis parameter that appears in the shallow water potential vorticity from f to $f_{\text{eff},2} = f - \nabla \cdot ((h_b + \frac{1}{2}h_2)\mathbf{\Omega})$ in the lower layer, and similarly in the upper layer. In this formula $\mathbf{\Omega}$ is the dimensional horizontal component of the rotation vector, and $f = 2\Omega \sin\phi$. Topography that varies strongly with latitude over large distances could substantially influence the large-scale dynamics through the non-traditional component of the Coriolis force. Looking to wider applications, we expect non-traditional effects to be even more pronounced on Jupiter, which has a much larger radius and rate of rotation, but stronger gravity. Using parameters from Dowling and Ingersoll (1989), the above estimate (3.69) suggests that non-traditional effects should become pronounced at $\tilde{\lambda}_{\text{inertial}} \approx 80$ km, so virtually all wavelengths large enough to contribute to planetary-scale atmospheric motions should be strongly affected by the non-traditional component of the Coriolis force.

Chapter 4

Cross-equatorial flow of abyssal ocean currents and the complete Coriolis force

This chapter is based upon Stewart and Dellar (2011c).

4.1 Introduction

We now turn our attention to the role of the complete Coriolis force in ocean currents, and in particular to abyssal ocean currents that cross the equator. As discussed in Chapter 1, the almost-horizontal orientation of the rotation vector, weak density stratification, and variable bathymetry combine to maximise the effect of the non-traditional component of the Coriolis force. Yet, to the best of our knowledge, there have been no previous studies of the complete Coriolis force in the context of abyssal ocean currents.

We base our study on the Antarctic Bottom Water (AABW) due to its unusual behaviour close to the equator. The AABW originates from ice melting in the Weddell Sea on the coast of Antarctica, and flows north through the Atlantic as a deep western boundary current, until it reaches the equator. Much of the current then turns east, but a substantial portion continues northwest through the Ceara Abyssal Plain, where it has been observed as far as 11°N (Friedrichs and Hall, 1993). A series of observations in the 1990s (Hall et al., 1994, 1997; Rhein et al., 1998), conclude that, of approximately 5 Sv (1 Sv $= 10^6\,\mathrm{m}^3\,\mathrm{s}^{-1}$) approaching the equator, around 2 Sv crosses into the northern hemisphere. In Figure 4.1 we plot the large-scale features of the bathymetry in the relevant area close to the equator. We highlight the almost-westward channel that the AABW passes through to reach the northern hemisphere. The structure and orientation of this channel is

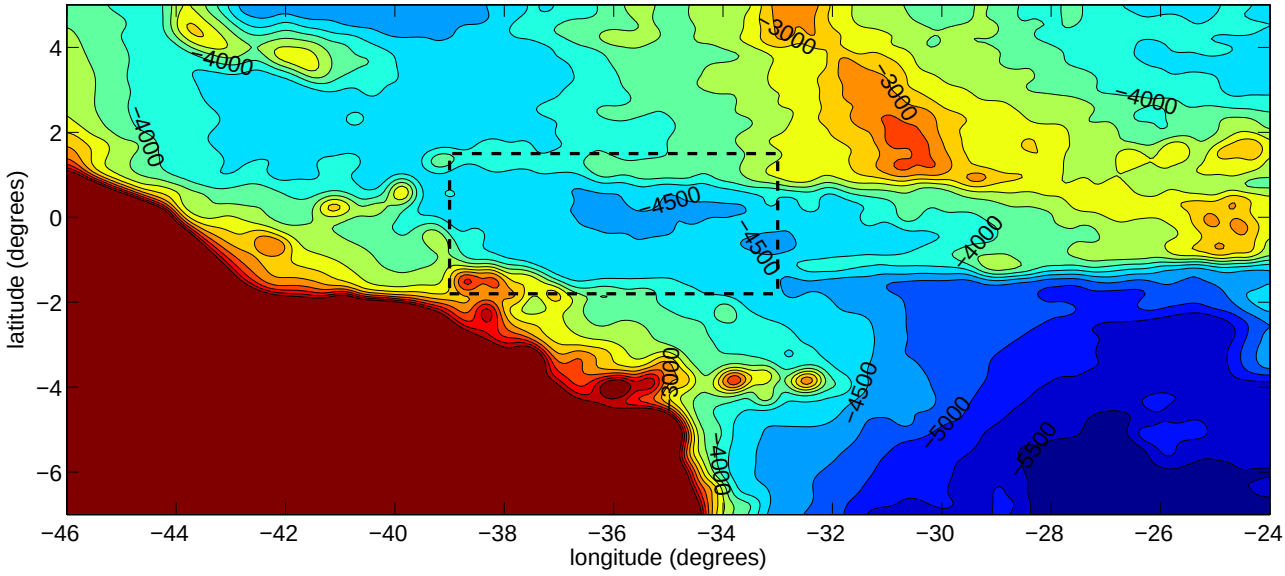

Figure 4.1: Contours of the bathymetry in the region where the AABW crosses the equator, shaded at intervals of 250 m. The data have been taken from Amante and Eakins (2009), and smoothed via ten applications of a nine-gridpoint average (c.f Choboter and Swaters, 2004) to remove small-scale features. A longitudinally averaged profile view of the area within the dashed rectangle is shown in Figure 4.2(a).

important for cross-equatorial transport of the AABW, particularly in the context of the complete Coriolis force.

Cross-equatorial flow is inhibited by the change in the sign of f, the locally vertical component of the Earth's rotation vector, across the equator. To conserve potential vorticity, the flow must acquire relative vorticity, and this limits the extent to which it can penetrate into the northern hemisphere (Killworth, 1991). Edwards and Pedlosky (1998) investigated this process using a shallow water model, and concluded that modification of the potential vorticity via dissipation is required to permit the flow observed in currents like the AABW. A major result of this chapter is that the potential vorticity constraint may be alleviated by the action of the non-traditional component of the Coriolis force in an equatorial zonal channel. We discuss this further in §4.3.

In this chapter we investigate abyssal cross-equatorial flow using one-dimensional solutions of the non-traditional multi-layer shallow water equations derived in Chapter 2. This is a somewhat idealised approach to a problem that has been the subject of sophisticated analytical approaches (*e.g.* Nof, 1990; Nof and Olson, 1993) and numerical investigations (*e.g.* Nof and Borisov, 1998; Choboter and Swaters, 2000). However, previous authors have only accounted for the almost-westward orientation of the equatorial channel, shown in Figure 4.1, in simulations that use the complete equatorial bathymetry, for example Stephens and Marshall (2000) and Choboter and

Swaters (2004). Additionally, all of these studies employ the traditional approximation, neglecting the non-traditional component of the Coriolis force. Our approach isolates the equatorial channel bathymetry and the action of the non-traditional component of the Coriolis force, allowing us to draw fundamental conclusions about their role in the abyssal dynamics.

Our work may be compared with that of Schopp and Colin de Verdière (1997), who studied flow at low Rossby number in a rotating spherical annulus. They showed that fluid could cross the equatorial plane in Taylor columns aligned with the rotation axis (which is locally horizontal at the equator), but could not pass beyond the cylindrical plane aligned with the planet's rotation axis and tangent to the equator. Additionally, Raymond (2000) studied large-scale atmospheric cross-equatorial flows using a linear two-dimensional solution of the continuously-stratified fluid equations, and found a class of oscillations that depend entirely on the non-traditional component of the Coriolis force. Our shallow water equations, discussed further in §4.2, provide a more intuitive and less restrictive model of an abyssal current, whilst retaining the complete Coriolis force.

The structure of this chapter is as follows. In §4.2 we briefly review the non-traditional multi-layer shallow water equations in the context of abyssal flow on an equatorial β-plane. In §4.3, we discuss the modification of the potential vorticity by the complete Coriolis force, and describe the influence that this should have on the AABW. In §4.4 and §4.5, we consider steady and unsteady solutions for the flow of an abyssal current in a zonally uniform channel. This illustrates how the action of the non-traditional component of the Coriolis force in a zonal channel may facilitate the equatorial crossing of the AABW. In §4.6, we revisit the one-dimensional cross-equatorial geostrophic adjustment problem of Killworth (1991), and show that the action of the complete Coriolis force on the current's angular momentum allows more fluid to adjust further across the equator. Finally, in §4.7 we discuss our results and their implications.

4.2 Shallow water equations on a non-traditional β-plane

Shallow water theory underlies all of the analysis in this chapter. The standard shallow water equations offer a useful conceptual model of an abyssal current, as used previously for analytical (Nof and Olson, 1993) and numerical (Choboter and Swaters, 2004) studies of the AABW. In this chapter we use the extended shallow water equations that include the complete Coriolis force, derived by Dellar and Salmon (2005) and extended to arbitrarily many layers in Chapter 2. In this section we discuss the validity and properties of the non-traditional shallow water equations on an equatorial β-plane.

Our starting point is the three-dimensional Euler equations for an incompressible fluid on a

non-traditional equatorial β-plane (Grimshaw, 1975; Dellar, 2011),

$$\frac{\mathrm{D}u}{\mathrm{D}t} - 2\Omega_z v + 2\Omega_y w + \frac{1}{\rho}\frac{\partial p}{\partial x} = 0, \tag{4.1a}$$

$$\frac{\mathrm{D}v}{\mathrm{D}t} + 2\Omega_z u + \frac{1}{\rho}\frac{\partial p}{\partial y} = 0, \tag{4.1b}$$

$$\frac{\mathrm{D}w}{\mathrm{D}t} - 2\Omega_y u + \frac{1}{\rho}\frac{\partial p}{\partial z} + g = 0, \tag{4.1c}$$

$$\frac{\partial u}{\partial x} + \frac{\partial v}{\partial y} + \frac{\partial w}{\partial z} = 0. \tag{4.1d}$$

These equations are formulated in a set of pseudo-Cartesian curvilinear coordinates with x directed eastward, y northward, and z vertically upwards. The x and y coordinates define curved surfaces of constant geopotential, so the combination of the gravitational and centrifugal accelerations appears only through the g term in the vertical momentum equation. The geometrical difficulties that arise in the derivation of the mid-latitude β-plane approximation (*e.g.* Veronis, 1963, 1981; Phillips, 1973; Dellar, 2011) are greatly reduced for the equatorial β-plane approximation.

The components of the three-dimensional velocity are u, v, and w, p is the fluid pressure, ρ is the constant density, and $D/Dt = \partial_t + u\partial_x + v\partial_y + w\partial_z$ is the material time derivative. The Coriolis parameters are $\Omega_y = \Omega$ (constant) and $\Omega_z = \beta y$ with $\beta = 2\Omega/R_E$, where Ω is the Earth's rotation frequency and R_E the Earth's radius. The latitude coordinate may be taken to be $y = R_E \sin\phi$, where ϕ is latitude. Equations (4.1) are the equatorial form of the non-traditional β-plane equations derived by Grimshaw (1975) using Mercator coordinates.

For our purposes it is sufficient to use the quasihydrostatic form of these equations that omits the Dw/Dt term in (4.1c). The quasihydrostatic approximation was introduced by White and Bromley (1995) as a less severe form of the widely used hydrostatic approximation that omits both the Dw/Dt and the $-2\Omega_y u$ terms from the vertical momentum equation. The quasihydrostatic form of (4.1a)–(4.1d) may be derived from the Euler equations for flow on a rotating sphere under the following assumptions:

(i) the ratio of vertical to horizontal length scales is small (the *shallow water* approximation), $\alpha = \mathcal{H}/\mathcal{L} \ll 1$;

(ii) the ratio of the horizontal length scale to the Earth radius is small, $\varepsilon = \mathcal{L}/R_E \ll 1$.

Dellar (2011) derived (4.1a)–(4.1d) by approximating the Lagrangian for the three-dimensional Euler equations in spherical geometry using assumptions (i) and (ii) in the distinguished limit

$$\alpha \sim \varepsilon \ll 1. \tag{4.2}$$

The familiar conservation laws for energy, angular momentum, and potential vorticity in spherical geometry may be derived from symmetries of a Lagrangian via Noether's theorem that relates

symmetries to conservation laws. Conservation of energy arises from a translation symmetry in time, and conservation of zonal angular momentum arises from a rotational symmetry about the Earth's axis. Material conservation of potential vorticity arises from a more subtle particle relabelling symmetry (Ripa, 1981; Salmon, 1982a). Dellar's (2011) derivation of the quasihydrostatic three-dimensional equations on an equatorial β-plane preserves all these symmetries in the approximated Lagrangian, so the resulting equations inherit exact conservation laws for energy, angular momentum, and potential vorticity. Grimshaw (1975) previously gave a direct proof of potential vorticity conservation on the non-traditional β-plane by manipulating (4.1a)–(4.1d).

Multi-layer shallow water theory describes the behaviour of a number of superposed layers of fluid of thickness $h_i(x, y, t)$, for $i = 1, \ldots, N$, overlying an arbitrary bottom topography $z = h_b(x, y)$. Throughout this chapter we refer to the actual measured height of the ocean bed as 'bathymetry', and to the model ocean bed as 'topography'. This is represented schematically in Figure 1.2. In Chapter 2 we derived the multi-layer shallow water equations from (4.1a)–(4.1d) by making the further assumption of columnar motion in the three-dimensional Lagrangian, following Miles and Salmon's (1985) derivation of the Green and Naghdi (1976) equations, and Dellar and Salmon's (2005) derivation of the single layer shallow water equations with the complete Coriolis force. Being derived from a Lagrangian, the resulting shallow water equations inherit conservation laws for energy, angular momentum, and potential vorticity from the three-dimensional equations (4.1a)–(4.1d). For example, the potential vorticity conservation law for a single layer is given by equation (4.6) in §4.3.

We denote the depth-averaged horizontal fluid velocity as $\boldsymbol{u}_i(x, y, t) = (u_i(x, y, t), v_i(x, y, t))$ in each layer, for $i = 1, \ldots, N$, and the density of each layer by ρ_i. The position of the upper surface of each layer is $z = \eta_i(x, y, t)$, where $z = \eta_1(x, y, t)$ corresponds to the free surface of the fluid, and $z = \eta_{N+1}(x, y) = h_b(x, y)$ corresponds to the bottom topography. Following Chapter 2 and Dellar (2011), the multi-layer shallow water equations on the non-traditional equatorial β-plane may be written as

$$\frac{\mathrm{D}_i \boldsymbol{u}_i}{\mathrm{D}t} + \left(\beta\, y - \Omega \frac{\partial}{\partial y}\left(\eta_i + \eta_{i+1}\right)\right) \hat{\boldsymbol{z}} \times \boldsymbol{u}_i + \Omega \frac{\partial}{\partial t}\left(\eta_i + \eta_{i+1}\right) \hat{\boldsymbol{x}} + \nabla \left(g\, \eta_i - \Omega h_i u_i + \frac{1}{\rho_i} \sum_{j=1}^{i-1} \rho_j h_j \left(g - 2\,\Omega u_j\right) \right) = 0, \tag{4.3}$$

$$\frac{\partial h_i}{\partial t} + \nabla \cdot \left(h_i \boldsymbol{u}_i\right) = 0. \tag{4.4}$$

The advective derivative is written $\mathrm{D}_i/\mathrm{D}t \equiv \partial/\partial t + \boldsymbol{u}_i \cdot \nabla$, where $\nabla \equiv (\partial/\partial x, \partial/\partial y)$. We write $\hat{\boldsymbol{x}}$ and $\hat{\boldsymbol{z}}$ for the unit vectors in the x and z directions respectively. The non-traditional contributions to the pressure gradient arise due to the change from hydrostatic to quasihydrostatic balance (White and Bromley, 1995) through the retention of the $-2\Omega_y u$ term in the vertical momentum equation

(4.1c). The other terms modify the fluid's angular momentum to reflect the fact that changes in the layer depth correspond to changes in the fluid's perpendicular distance from the axis of rotation, analogous to the $2\Omega_y w_i$ term in (4.1a).

The existence of exact conservation laws for angular momentum and potential vorticity might appear at odds with the statements found in White and Bromley (1995) and Marshall et al. (1997) that including the complete Coriolis force while making the shallow atmosphere approximation together preclude conservation laws for angular momentum and potential vorticity. However, it is important to distinguish between the *shallow water* approximation, given by condition (i) above, and the *shallow atmosphere* approximation, associated with the complete neglect of terms involving the ratio of the vertical lengthscale to the planetary radius. For example, the shallow atmosphere approximation is commonly taken to imply the replacement of true spherical radius r by the constant Earth's radius R_E in the Euler equations formulated in spherical polar coordinates.

We use the name "shallow water" to reflect the status of (4.3) and (4.4) as depth-averaged equations derived under the approximation (i) of small aspect ratio α. However, the shallow water momentum equation retains various terms proportional to Ωh_i and $\Omega\eta_i$ that are formally $\mathcal{O}(\alpha)$ smaller than the other terms, just as the Green and Naghdi (1976) equations retains small terms of $\mathcal{O}(\alpha^2)$ arising from the Dw/Dt term in the three-dimensional Euler equations. The retained terms are formally proportional to $\mathcal{H}/R_E$, so our equations are "deep atmosphere" shallow water equations. One justification for retaining these formally small terms is that the leading-order term in the expansion of the relevant part of the Lagrangian is a "null Lagrangian" that does not contribute to the equations of motion (Dellar, 2011). In other words, the leading-order term in the expansion of the vector potential for $\mathbf{\Omega}$ is a constant, whose curl vanishes.

Equations (4.3) and (4.4) describe the motion of fluid columns aligned with the locally vertical axis. Following the Taylor–Proudman theorem, one might expect the columns to be aligned with the axis of rotation, which is perpendicular to the locally vertical axis at the equator. However, motion predominantly in vertical columns is still compatible with the three-dimensional Euler equations under the small aspect ration assumption $\alpha = \mathcal{H}/\mathcal{L} \ll 1$, even when the rotation axis is locally horizontal. Additionally, the real AABW flow is strongly inertial (Nof and Olson, 1993; Nof and Borisov, 1998) slightly stratified, and subject to the action of bottom friction. All these effects will tend to inhibit the fluid from moving in Taylor columns. We thus expect our shallow water model to provide a useful qualitative description of the behaviour of the AABW.

4.3 The role of potential vorticity

The ability of fluid to cross the equator is strongly constrained by conservation of potential vorticity (*e.g.* Killworth, 1991). We shall now examine the mechanisms by which this constraint is imposed, and the influence of the complete Coriolis force upon it.

Let us consider a single layer of fluid governed by the non-traditional shallow water equations, with horizontal velocity $\boldsymbol{u}(x,y,t) = (u(x,y,t), v(x,y,t))$ and thickness $h(x,y,t)$, overlying topography $z = h_b(x,y)$. The angular momentum conservation law for the layer is (c.f. Ripa, 1982, 1997)

$$\frac{\mathrm{D}\tilde{u}}{\mathrm{D}t} = -\frac{1}{h}\frac{\partial}{\partial x}\left[\tfrac{1}{2}h^2\left(g - 2\Omega u\right)\right] - \left(g - 2\Omega u\right)\frac{\partial h_b}{\partial x}, \quad \tilde{u} = u - \tfrac{1}{2}\beta y^2 + 2\Omega\overline{z}, \tag{4.5}$$

where $\tilde{u}$ is the (zonal) angular momentum and $\overline{z} = h_b + h/2$ is the half-layer height, or equivalently the average vertical position of the fluid in a column. Equation (4.5) thus equates changes in angular momentum with the torque exerted by zonal pressure gradients. The term proportional to Ω in $\tilde{u}$ as defined in (4.5) is a non-traditional Coriolis term that accounts for the change in a fluid column's average distance from the rotation axis due to changes in h and h_b.

The quantity $\tilde{u}$ is also the canonical momentum in the Lagrangian formulation, and appears in the potential vorticity conservation law,

$$\frac{\mathrm{D}q}{\mathrm{D}t} = 0, \quad q = \frac{1}{h}\left(\beta y - 2\Omega\frac{\partial\overline{z}}{\partial y} + \zeta\right) = \frac{\hat{\boldsymbol{z}}\cdot(\nabla\times\tilde{\boldsymbol{u}})}{h}, \tag{4.6}$$

where $\zeta = \partial_x v - \partial_y u$ is the relative vorticity and $\tilde{\boldsymbol{u}} = (\tilde{u}, v)$. The last term in (4.6) is the general expression for the conserved potential vorticity in terms of the canonical momenta $\tilde{u}$ and $\tilde{v} = v$, as given by the particle relabelling symmetry (Salmon, 1988). Equation (4.6) may also be interpreted as the depth average of a three-dimensional Ertel potential vorticity (see Dellar and Salmon, 2005).

Now consider fluid columns moving northwards across the equator under the traditional approximation, equivalent to setting $\Omega = 0$ in (4.6). The βy term in (4.6) changes sign as the columns cross the equator, the line $y = 0$, which requires a corresponding change in h and/or ζ to conserve q. Hua et al. (1997) have shown that the fluid will be subject to an inertial instability if the three-dimensional Ertel potential vorticity Q_E does not have the same sign as y. This suggests that equator-crossing fluid should have $Q_E \approx 0$, which Hua et al. (1997) showed is consistent with PEQUOD data for the deep ocean (Firing, 1987). The change in the planetary vorticity βy in each fluid column must thus typically be balanced by a change in the relative vorticity ζ. Killworth (1991) has shown that this necessary generation of relative vorticity severely constrains the penetration of inviscid fluid across the equator into the northern hemisphere.

Including the complete Coriolis force offers an alternative means of balancing the change in the planetary vorticity βy as fluid crosses the equator. In fact, the βy term is balanced completely by

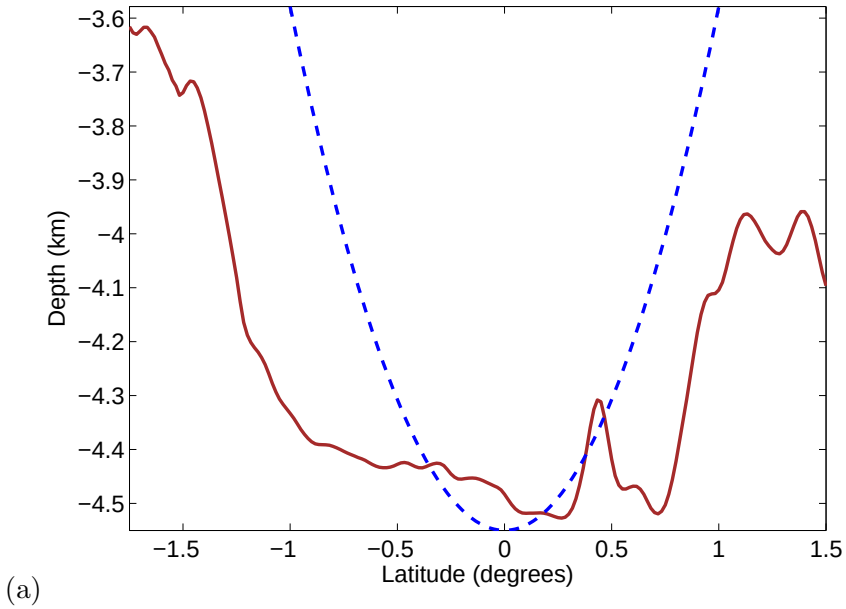

(a)

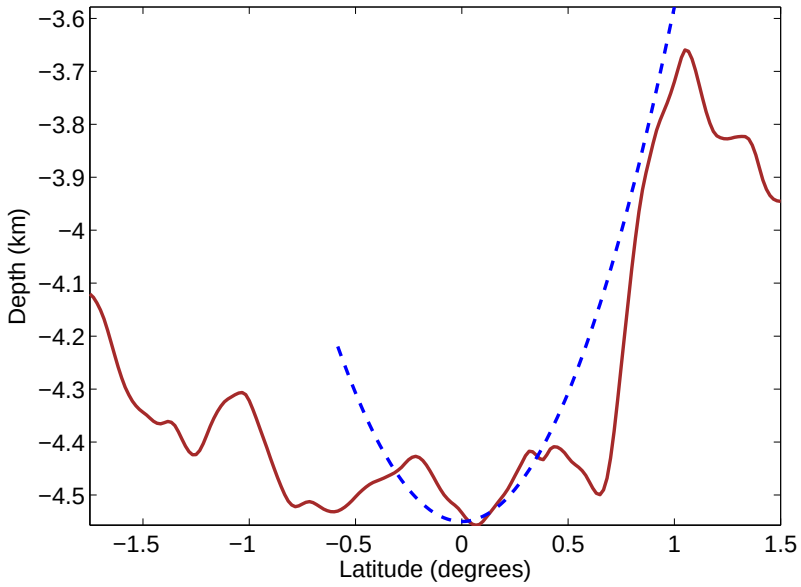

(b)

Figure 4.2: A comparison of the measured bathymetry (data from Amante and Eakins, 2009) in the western equatorial Atlantic with the ideal topography described by (4.7). The bathymetry has been zonally averaged between (a) 39°W and 34°W, as marked in Figure 4.1, and (b) 36°W and 33°W.

the topography alone if

$$h_b = h_0 + \frac{\beta}{4\Omega} y^2 = h_0 + \frac{1}{2R_E} y^2, \tag{4.7}$$

where h_0 is a constant reference height. This describes a zonal channel that is symmetric about the equator, a configuration which is particularly relevant for the AABW. In Figure 4.2 we compare the zonally-averaged bathymetry in the western equatorial Atlantic ocean with the ideal topography described by (4.7). We find a good qualitative agreement between the shapes of the channels

between 39°W and 34°W, and remarkably good agreement on the northern side of the channel between 36°W and 33°W. As a result, we expect that including the complete Coriolis force should play a particularly important role in the equatorial crossing of the AABW. The AABW traverses a zonal channel, so the non-traditional component of the Coriolis force should at least partly balance the change in sign of the traditional component. The fluid should then be able to cross the equator without needing to generate as much relative vorticity.

This process may be understood more intuitively in spherical geometry, though we will retain the equatorial β-plane approximation, $\Omega_y \approx \Omega$ and $\Omega_z \approx \beta y$. The first two terms in the numerator of the potential vorticity (4.6) may be written as

$$\beta y - 2\Omega \frac{\partial \overline{z}}{\partial y} = 2\boldsymbol{\Omega} \cdot \nabla_3 \left(z - \overline{z} \right) = \zeta_p, \tag{4.8}$$

where $\nabla_3 = (\partial_x, \partial_y, \partial_z)$ is the three-dimensional gradient vector. The right-hand side of (4.8), which we will refer to as the complete planetary vorticity ζ_p, is the component of the three-dimensional rotation vector $\boldsymbol{\Omega}$ that lies normal to the half-layer height of the fluid at any point (see Dellar and Salmon, 2005). This may also be interpreted as the depth-average of the component normal to surfaces of constant Lagrangian label $c = (z - h_b)/(h - h_b)$. In a layer of constant depth, $h \equiv H$ say, the planetary vorticity is 0 wherever $\boldsymbol{\Omega}$ is parallel to the local topography. Thus, the ideal topography described by (4.7) corresponds to the equatorial part of the spherical earth being levelled in such a way that the fluid layer lies parallel to the rotation axis, as illustrated in Figure 4.3. The condition $\zeta_p \equiv 0$ is equivalent to the condition that the planetary contribution to the angular momentum (4.5) is everywhere constant, $\tilde{u}_p = 2\Omega\overline{z} - \frac{1}{2}\beta y^2 \equiv$ constant. This provides a more intuitive interpretation of Figure 4.3, where the fluid remains at an approximately constant distance from the rotation axis, and so does not require a large change in its relative angular momentum u as it crosses the equator.

The importance of the non-traditional component of the Coriolis force is typically estimated using dimensionless numbers such as the ratio of vertical to horizontal lengthscales, or the ratio of the inertial frequency f to the Brunt–Väisälä frequency N (*e.g.* Gerkema et al., 2008). The ratio f/N determines the ratio of vertical to horizontal lengthscales in the three-dimensional quasigeostrophic regime (*e.g.* Pedlosky, 1987; White, 2002). Another relevant dimensionless number is based on the velocity scale $2\Omega\mathcal{H}$, which is the change in zonal velocity experienced by a fluid parcel that changes its height by the vertical lengthscale $\mathcal{H}$ while conserving angular momentum (White and Bromley, 1995).

To see how this velocity scale enters our analysis, the magnitude of the non-traditional Coriolis term $-2\Omega\,\partial\overline{z}/\partial y$ relative to the traditional Coriolis term βy may be estimated as

$$\delta = \frac{2\Omega\mathcal{H}}{\beta\mathcal{L}^2} = \frac{\mathcal{H}R_E}{\mathcal{L}^2}, \tag{4.9}$$

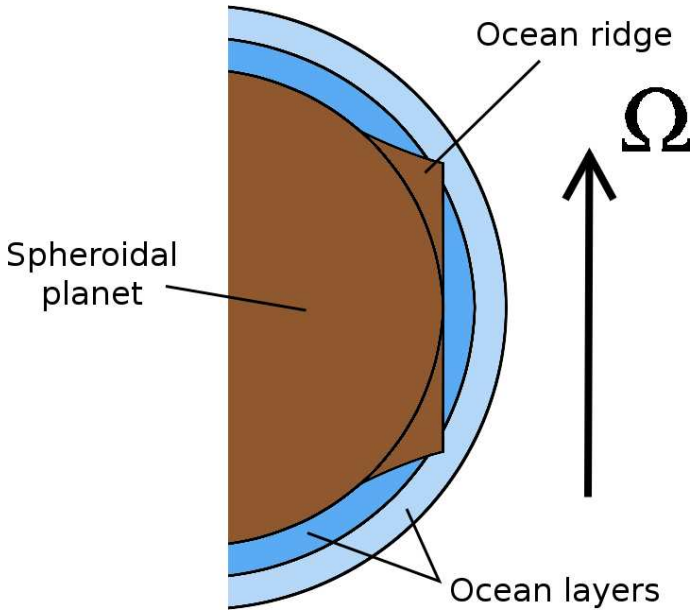

Figure 4.3: A greatly exaggerated illustration of the conditions under which the fluid would experience no change in planetary vorticity, or equivalently no change in planetary angular momentum, in the region close to the equator. Large submarine ridges form a channel-like equatorial topography, such that fluid moving close to the equator remains at a constant distance from the rotation axis.

where $\mathcal{L}$ and $\mathcal{H}$ are vertical and horizontal lengthscales respectively. If we naively define $\mathcal{L} = 300\,\mathrm{km}$ and $\mathcal{H} = 500\,\mathrm{m}$, based on Figure 4.2, we obtain $\delta \approx 0.04$. For a more systematic approach we take the horizontal lengthscale $\mathcal{L}$ to be the equatorial deformation radius

$$\mathcal{L} = R_d = \frac{(g'\mathcal{H})^{1/4}}{\beta^{1/2}} \quad \text{so} \quad \delta = 2\Omega\sqrt{\frac{\mathcal{H}}{g'}}, \tag{4.10}$$

where g' is a reduced gravity (see next section). The second equation may also be interpreted as defining

$$\delta = 2\Omega\mathcal{H}/\sqrt{\mathcal{H}g'} \tag{4.11}$$

to be the ratio of the non-traditional velocity scale $2\Omega\mathcal{H}$ to the internal wave speed $\sqrt{\mathcal{H}g'}$. Even for weak stratification ($g' \approx 10^{-3}$) we obtain $\delta \approx 0.1$. However, the analysis of this and later sections shows that these scaling arguments underestimate the influence of the non-traditional component of the Coriolis force.

Equation (4.9) also suggests a characteristic horizontal lengthscale $\mathcal{L} = \sqrt{\mathcal{H}R_E}$ on which non-traditional effects become significant near the equator. This lengthscale was first obtained by Stern (1963) and Bretherton (1964) in their studies of low frequency Poincaré (or gyroscopic) waves that are trapped near the equator, and later by Colin de Verdière and Schopp (1994) in their theory of nonlinear motions near the equator.

4.4 Steady flow in a zonally-uniform channel

As a first step towards understanding more thoroughly how the complete Coriolis force influences the flow of the AABW, we approximate the bathymetry between 39°W, 34°W, 1.5°S and 1.5°N as a zonally-uniform channel (see Figure 4.1). We consider the steady flow of a shallow fluid layer over this topography to illustrate how the complete Coriolis force might influence a current crossing the equator.

4.4.1 Solution for a single layer

We seek a steady, zonally-symmetric solution of the single-layer shallow water equations equations, representing an abyssal current flowing beneath a deep, quiescent upper layer. The components of (4.3) and (4.4) reduce to

$$v\frac{\partial \tilde{u}}{\partial y} = 0, \tag{4.12a}$$

$$-u\frac{\partial \tilde{u}}{\partial y} + \frac{\partial}{\partial y}\left(\tfrac{1}{2}u^2 + \tfrac{1}{2}v^2 + g'(h_b + h) - \Omega h u\right) = 0, \tag{4.12b}$$

$$\frac{\partial}{\partial y}(hv) = 0, \tag{4.12c}$$

where $g' = g\Delta\rho/\rho$ is the reduced gravity, ρ is the density of the active layer, and $\rho - \Delta\rho$ is the density of the deep layer above. Equation (4.12a) is the depth-averaged equivalent of equation (35) of Colin de Verdière and Schopp (1994), which states that the velocity in the meridional–vertical plane must be parallel to lines of constant absolute angular momentum in zonally symmetric flow. The depth-averaged form (4.12a) states that for non-zero meridional velocity, $v \neq 0$, the angular momentum must be constant

$$\tilde{u} = u - \tfrac{1}{2}\beta y^2 + 2\Omega(h_b + \tfrac{1}{2}h) = A, \tag{4.13}$$

where A is constant. Thus the half-layer height of the fluid, $\overline{z} = h_b + \frac{1}{2}h$, traces a line of constant absolute angular momentum. Even in cases where $v \equiv 0$, we will use (4.13) to close the system (4.12a)–(4.12c). Substituting (4.13) into (4.12b) yields an exact derivative with respect to y, which may be integrated to obtain a Bernoulli-like equation,

$$\tfrac{1}{2}u^2 + \tfrac{1}{2}v^2 + g'(h_b + h) - \Omega h u = B, \tag{4.14}$$

where B is the (arbitrary) Bernoulli constant. The $-\Omega h u$ term in (4.14) is an additional contribution to the pressure created by the complete Coriolis force, and the subsequent change from hydrostatic to quasihydrostatic balance in the vertical momentum equation. Finally, the mass conservation

equation (4.12c) may be integrated to obtain

$$hv = T, \tag{4.15}$$

where T is the constant meridional transport. Equations (4.13)–(4.15) express conservation of angular momentum, Bernoulli energy, and mass respectively. They form an algebraic system of equations that may be combined into a quartic polynomial in u. This must be solved at all points along the y-axis, subject to

$$u(y_0) = U, \quad v(y_0) = V, \quad h(y_0) = H, \tag{4.16}$$

at some location $y = y_0$. In all cases examined here, only one of the four solutions to the quartic is real at all points in y and satisfies the boundary conditions (4.16).

We will consider the specific case of a parabolic bottom topography that is half as steep as the ideal topography (4.7), such that it has the approximate measurements of the channel depicted in Figure 4.2,

$$h_b(y) = \frac{y^2}{4R_E}. \tag{4.17}$$

In Figure 4.4 we present a typical solution for fluid crossing the equator over parabolic topography. This may be thought of as a simplistic representation of the AABW entering and exiting the equatorial channel. A comparatively shallow, 200 metres deep, layer of fluid enters flowing directly northwards at $15\,\mathrm{cm\,s^{-1}}$. Gravity keeps the upper surface close to horizontal, so the layer thickens and slows as it approaches the centre of the channel, and then becomes symmetrically swifter and shallower on the opposite site of the equator.

For small density differences ($\Delta\rho/\rho \lesssim 10^{-4}$), the upper surface dips with the topography. We have chosen $g' = 5 \times 10^{-4}\,\mathrm{m^2\,s^{-1}}$ in Figure 4.4 to illustrate this. Figure 4.5(a) reveals that this is because a large westward velocity is required at the equator to conserve angular momentum (4.13), and this must be balanced by a gravitational pressure gradient in (4.14). This westward velocity is much weaker when the complete Coriolis force is included, because in a zonal channel the fluid is subject to less variation in its distance from the rotation axis, as explained in §4.3. As a result, fluid particles flowing across the channel cover a much smaller westward distance as they do so. In the case plotted in Figure 4.5, the particle path compares better with the dimensions of the real AABW channel in Figure 4.1 when the complete Coriolis force is included. However, this fit is entirely dependent on the choice of inflow velocity V.

This solution illustrates the mechanism described in §4.3. When the complete Coriolis is included, the fluid is subject to a smaller change in planetary angular momentum, and so it acquires a smaller relative angular momentum at the equator itself. Equivalently, the fluid acquires a smaller

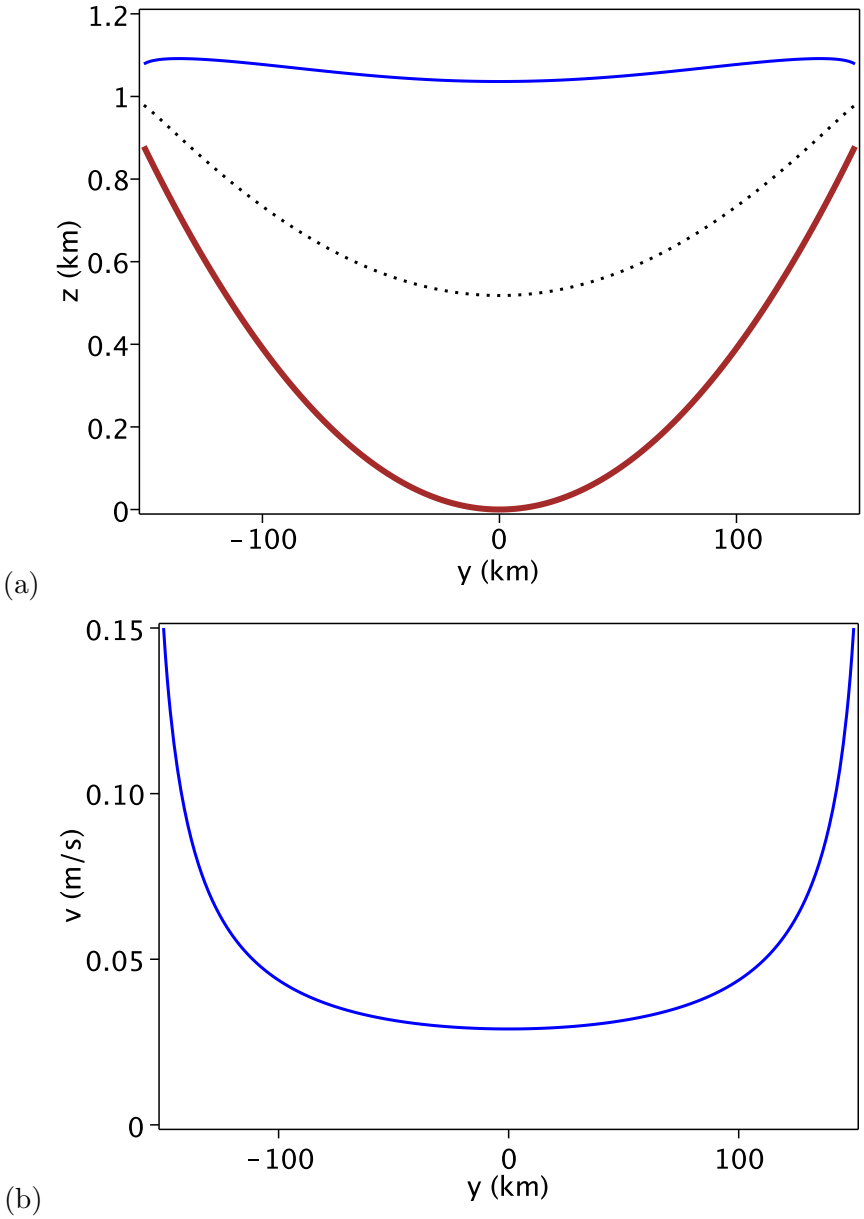

Figure 4.4: Plots of the solution described by (4.13)–(4.15), for the case $y_0 = -150\,\mathrm{km}$, $U = 0\,\mathrm{m\,s^{-1}}$, $V = 0.15\,\mathrm{m\,s^{-1}}$, $H = 200\,\mathrm{m}$, and $g' = 5 \times 10^{-4}\,\mathrm{m^2\,s^{-1}}$. In (a) we show the bottom topography (thick line), the height of the layer above it (thin line), and the half-layer depth (dotted line). In (b) we show the meridional velocity. Both plots include the complete Coriolis force, as there is no perceptible change in these variables when the traditional approximation is made.

relative vorticity as it crosses the equator. The velocities in Figure 4.4 and Figure 4.5 are around an order of magnitude larger than those measured in the AABW (c.f. Hall et al., 1997), so the zonal velocity is arguably more realistic when the complete Coriolis force is included. We have chosen a meridional inflow of $V = 0.15\,\mathrm{m\,s^{-1}}$ so that the velocities are of consistent magnitude, and so that the particle paths in Figure 4.5 are comparable with the dimensions of the AABW's real

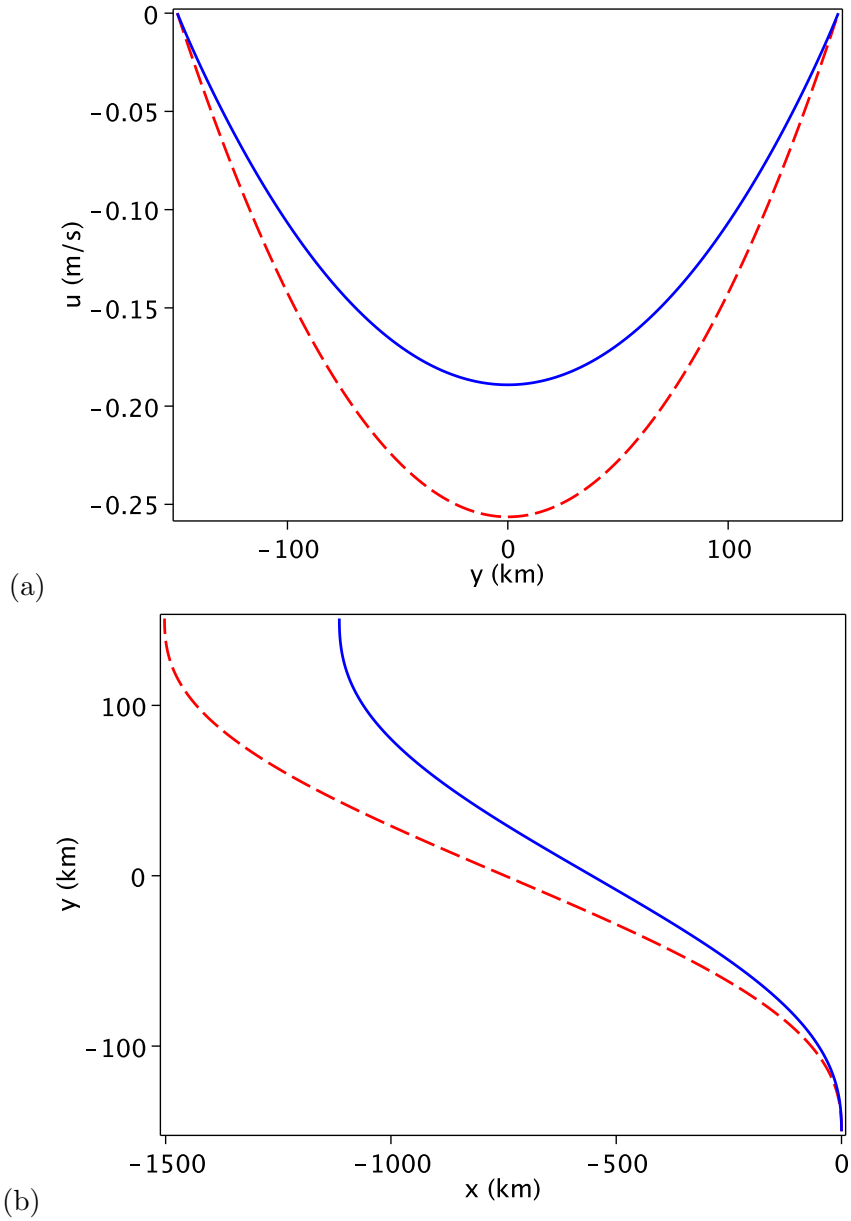

Figure 4.5: Further plots of the solution presented in Figure 4.4. In (a) we show variation of the zonal velocity across the channel, whilst in (b) we show the path of a fluid particle entering at the southern side of the channel. In both cases we plot solutions with (solid lines) and without (dashed lines) the non-traditional component of the Coriolis force.

bathymetry. Such large velocities may be attributed to the absence of bottom friction and viscosity in this idealised model. The largest vertical velocities attained in the solution are on the order of $10^{-3}\,\mathrm{m\,s^{-1}}$, so the flow does remain approximately horizontal, as required by shallow water theory.

4.4.2 Vanishing layer depth

A special case of the above solution arises when the layer outcrops from the edge of the channel. This could be a more realistic representation of the flow of the AABW, which tends to lean against the sides of the channel as it traverses the equatorial bathymetry (Hall et al., 1997). In this case, $h = 0$ at $y = y_0$, so there is no meridional transport, $T = 0$, and thus $v \equiv 0$ everywhere. We see from (4.12a)–(4.12c) that a stationary solution, $u = v = 0$, $h + h_b =$ constant, is possible. However, we will seek solutions for a zonally-flowing current with zero potential vorticity, satisfying (4.13). We assume that the AABW adheres to this state to avoid being subject to an inertial instability (Hua et al., 1997).

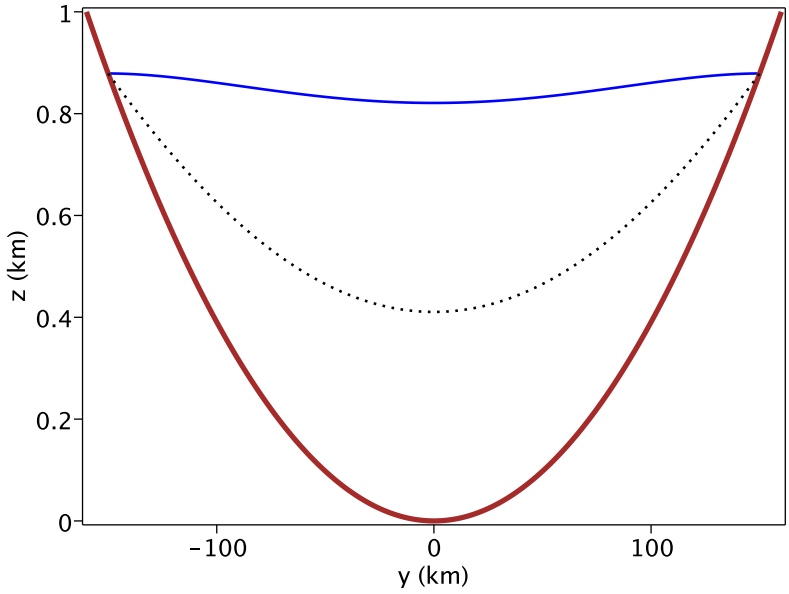

Figure 4.6: An outcropping solution of (4.13)–(4.15), with $y_0 = -150\,\mathrm{km}$, $U = 0\,\mathrm{m\,s^{-1}}$, $V = 0\,\mathrm{m\,s^{-1}}$, $H = 0\,\mathrm{m}$ and $g' = 5 \times 10^{-4}\,\mathrm{m^2\,s^{-1}}$. We plot the bottom topography (thick line), the height of the layer above it (thin line), and the half-layer depth (dotted line).

When $v = 0$, equations (4.13) and (4.14) may be combined to form a quadratic polynomial in h. Figure 4.6 shows a plot of the layer thickness for similar parameters as those used in Figure 4.4, but modified so that the depth vanishes at the edge of the channel. The zonal velocity profile is very similar to that shown in Figure 4.5(a).

In this case the fluid is not crossing the equator, but rather flowing westward along the equator. We might expect to observe behavior like this in the AABW over short stretches of the equatorial bathymetry. This solution presents a different interpretation of the role of the complete Coriolis force. Including the non-traditional terms leads to smaller westward velocities, and therefore a smaller transport along the channel. Therefore, if the AABW were to exhibit steady, zonally-

symmetric flow at some point in the equatorial bathymetry, the complete Coriolis force would actually constrain the amount of fluid transported through the channel.

4.4.3 Interaction with the upper ocean

We may extend the solution presented in §4.4.1 to include multiple layers of fluid. This allows us to study the interaction of the AABW with overlying layers like the Lower North Atlantic Deep Water (LNADW), which flows southward across the equator above the AABW. Applying the conditions of steady ($\partial/\partial t \equiv 0$), zonally symmetric ($\partial/\partial x \equiv 0$) flow to (4.3) and (4.4), the multi-layer shallow water equations may be written as

$$\frac{\partial}{\partial y}\left(u_i - \tfrac{1}{2}\beta y^2 + 2\Omega\left(\eta_{i+1} + \tfrac{1}{2}h_i\right)\right) = 0, \tag{4.18a}$$

$$\frac{\partial}{\partial y}\left(\tfrac{1}{2}\left|\boldsymbol{u}_i\right|^2 + g\eta_i - \Omega h_i u_i + \frac{1}{\rho_i}\sum_{j=1}^{i-1}\rho_j h_j(g - 2\Omega u_j)\right) = 0, \tag{4.18b}$$

$$\frac{\partial}{\partial y}\left(h_i v_i\right) = 0, \tag{4.18c}$$

for $i = 1, \ldots, N$. As in the single-layer case, we have written (4.18a)–(4.18c) such that they take the form of exact derivatives with respect to y. Integrating yields a system of $3N$ algebraic equations for u_i, v_i, and h_i,

$$u_i - \tfrac{1}{2}\beta y^2 + 2\Omega\left(\eta_{i+1} + \tfrac{1}{2}h_i\right) = A_i, \tag{4.19a}$$

$$\tfrac{1}{2}u_i^2 + \tfrac{1}{2}v_i^2 + g\eta_i - \Omega h_i u_i + \frac{1}{\rho_i}\sum_{j=1}^{i-1}\rho_j h_j(g - 2\Omega u_j) = B_i, \tag{4.19b}$$

$$h_i v_i = T_i. \tag{4.19c}$$

Here A_i, B_i and T_i are determined by imposing

$$u_i(y_0) = U_i, \quad v_i(y_0) = V_i, \quad h_i(y_0) = H_i, \tag{4.20}$$

at some location $y = y_0$.

In principle, equations (4.19a)–(4.19c) may be solved directly to obtain a solution for all y. We see from (4.19a) that the i^{th} layer will only be substantially influenced by the non-traditional component of the Coriolis force, if there are large variations of the half-layer depth $\overline{z}_i = \eta_{i+1} + \frac{1}{2}h_i$ with y. The surface at $z = \eta_{i+1}$ of the layer below acts as effective topography for the i^{th} layer. It plays an analogous role in the multi-layer case to the role played by h_b for a single layer. Typically we will only see large deformations in the surface of a given layer η_i when the surface below, η_{i+1}, also has large deformations, and when the density difference between that layer and the layer above

is very small, $\sigma_i = (\rho_i - \rho_{i-1})/\rho_i \ll 1$. We quantify what "very small" means in terms of a Froude number in the next subsection. Thus, if the actual bottom topography $h_b = \eta_{N+1}$ forms a channel about the equator, then we only expect fluid in the i^{th} layer to be steered by the channel, and therefore experience strong non-traditional effects, if there are very small density variations between all of the layers below.

In Figure 4.7 we plot a solution to (4.19a)–(4.19c) with the same parameters as in Figure 4.4, but with an overlying southward-flowing layer. This solution is an idealised representation of the AABW flowing north across the equatorial channel, with the southward-flowing LNADW above. The AABW layer is very similar to the single layer shown in Figure 4.4 and Figure 4.5(a). The upper LNADW layer may influence the AABW only through its contribution to the pressure gradient in (4.18b). The large westward velocity at the equator, seen in Figure 4.5(a), accelerates the fluid downward via the non-traditional term in the vertical momentum equation (4.1c). This must be balanced by the gravitational pressure gradient, leading to slight dip in the surfaces of the layers at the equator in Figure 4.7. However, this effect is not pronounced unless the density differences at the layer surfaces are very small. In this case the AABW surface is almost flat, so the LNADW is not steered by the channel.

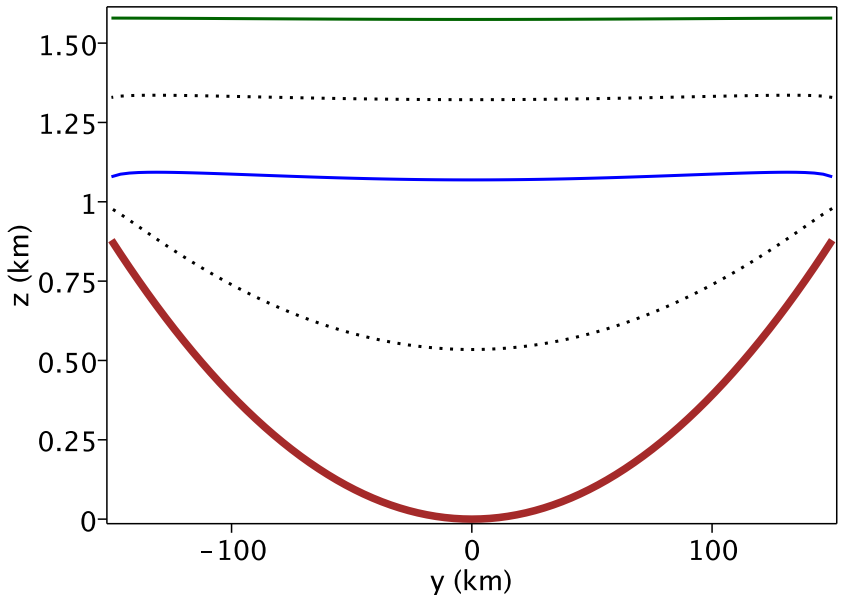

Figure 4.7: The steady solution for a northward-flowing AABW layer beneath a southward-flowing LNADW layer. Here $y_0 = -150\,\text{km}$, $U_1 = U_2 = 0\,\text{m}\,\text{s}^{-1}$, $V_1 = -0.1\,\text{m}\,\text{s}^{-1}$, $V_2 = 0.5\,\text{m}\,\text{s}^{-1}$, $H_1 = 500\,\text{m}$ and $H_2 = 200\,\text{m}$. The density differences are $\sigma_1 = 10^{-3}$ and $\sigma_2 = 5 \times 10^{-5}$, so the solution is similar to that presented in Figure 4.4. We plot the layer surfaces (thin solid lines), the bottom topography (thick solid line) and the half-layer depths (dotted lines).

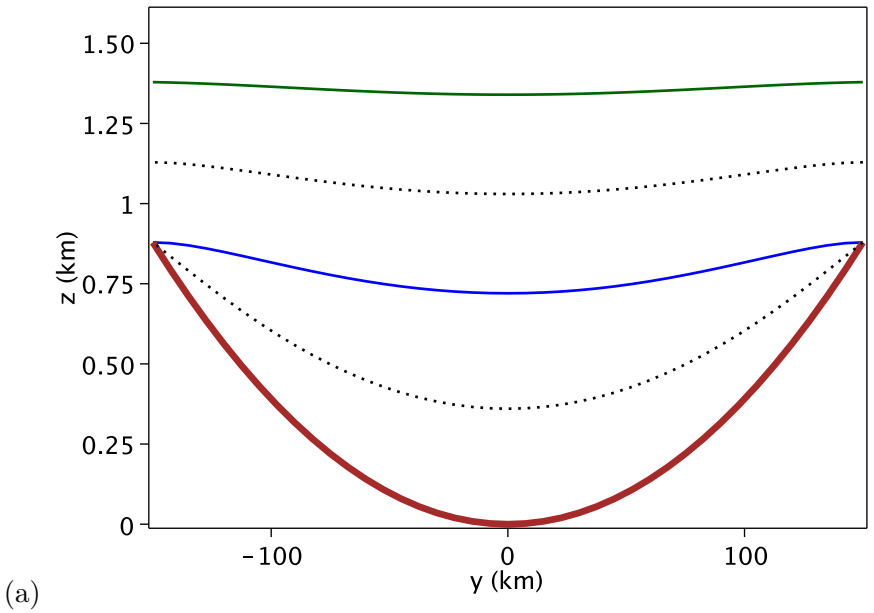

(a)

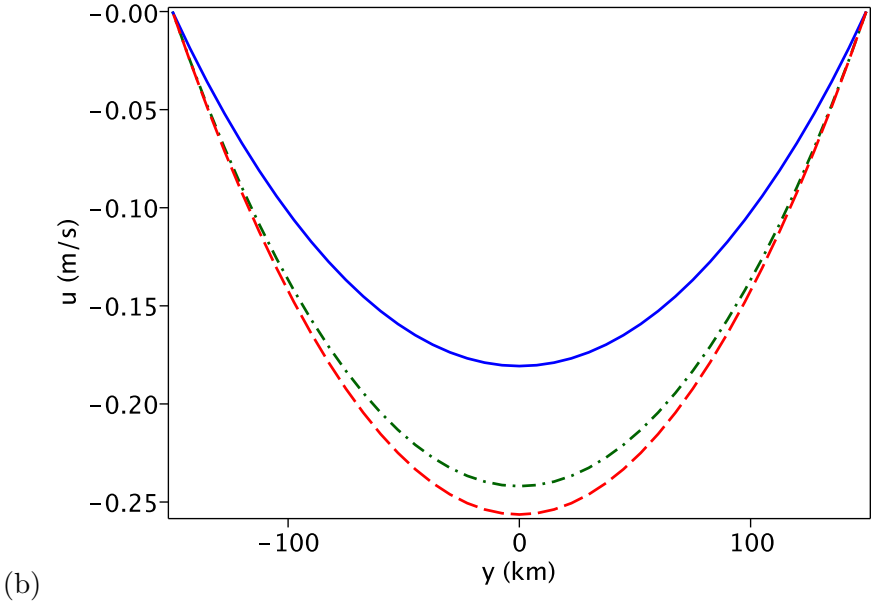

(b)

Figure 4.8: The steady solution for an upper LNADW layer flowing south over an outcropping AABW layer. In panel (a) the plotted curves have the same meaning as in Figure 4.7, and the parameters are the same except $V_2 = 0\,\mathrm{m\,s^{-1}}$, $H_2 = 0\,\mathrm{m}$, and $\sigma_2 = 5 \times 10^{-6}$. In panel (b) we plot the zonal velocity profiles in the lower (solid line) and upper (dash-dotted line) layers, and the zonal velocity under the traditional approximation (dashed line), which is identical in both layers.

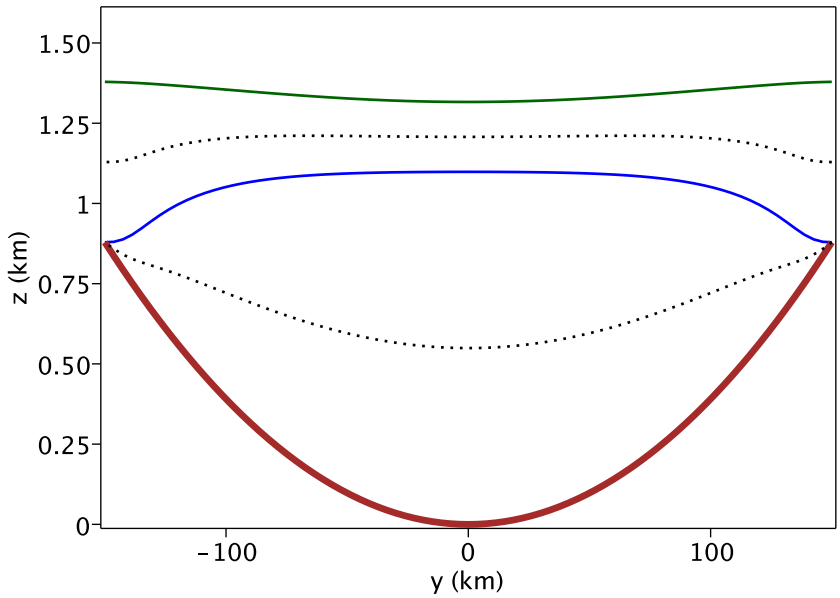

Figure 4.9: A steady two-layer solution with a very small density difference between the layers, $\sigma_2 = 1\times10^{-6}$, and all other parameters matching Figure 4.8(a). Under the traditional approximation, the same parameters yield a solution that strongly resembles Figure 4.8(a).

In Figure 4.8 we plot a solution in which the LNADW is steered by the topography, because the density difference between the two active layers is small, $\sigma_2 = (\rho_2 - \rho_1)/\rho_2 = 2.5 \times 10^{-6}$. In this case the AABW surface intersects the channel edges. This can be thought of as a representation of the mid-channel state of the AABW, with the LNADW flowing over the top. The surface of the AABW layer dips towards the equator, providing a gravitational pressure gradient to balance the strong westward flow and the non-traditional vertical acceleration in (4.18b). The LNADW flows over the channel-shaped AABW-surface, and therefore acquires a smaller westward velocity as it crosses the equator.

For even smaller σ_2, gravitational effects become so weak in the lower layer that the solution jumps to a different physical regime, in which the AABW surface protrudes upward towards the middle of the channel. This configuration is illustrated in Figure 4.9, where $\sigma_2 = 1 \times 10^{-6}$. The gravitational pressure gradient due to bending of the internal interface is too small to balance the strong westward flow of the AABW. Instead the LNADW surface must deform to provide this pressure gradient. This is due to the non-traditional contribution to the pressure gradient in (4.18b), and does not occur under the traditional approximation, where the solution resembles Figure 4.8(a) even as $\sigma_2 \to 0$.

We conclude that the upper ocean has a minimal effect of the AABW layer. Whilst it is possible in theory for the shape of the underlying topography to be transmitted to the upper layers, for

typical parameters there is almost no deformation of the surface of the AABW layer, and therefore the upper layers are not substantially influenced by the complete Coriolis force. In the real AABW we might expect the upper ocean to be steered by the channel if the isopycnals approximately followed the bathymetry, but observations (*e.g.* Hall et al., 1997) suggest that this is typically not the case.

4.4.4 The small Froude number limit

As discussed in the previous section, the surfaces of the layers will not exhibit large deformations unless the density differences between them are very small. More precisely, the surfaces will be approximately flat as long as the Froude numbers are small,

$$\mathrm{Fr}_i = \frac{\mathcal{U}^2}{\sigma_i g \mathcal{H}} \ll 1, \qquad \sigma_i = \frac{\rho_i - \rho_{i-1}}{\rho_i}, \tag{4.21}$$

where $\mathcal{U}$ and $\mathcal{H}$ are typical velocity and height scales respectively, and $\sigma_i g$ is the relevant reduced gravity. We show this formally by scaling

$$\boldsymbol{u}_i = \mathcal{U}\,\hat{\boldsymbol{u}}_i, \qquad h = \mathcal{H}\,\hat{h}_i, \tag{4.22}$$

and rewriting (4.19b) as

$$\hat{\eta}_i + \frac{1}{\rho_i}\sum_{j=1}^{i-1}\rho_j \hat{h}_j + \mathrm{Fr}\left(\tfrac{1}{2}\hat{u}_i^2 + \tfrac{1}{2}\hat{v}_i^2\right) - \delta\,\mathrm{Fr}\left(\tfrac{1}{2}\hat{h}_i\hat{u}_i + \frac{1}{\rho_i}\sum_{j=1}^{i-1}\rho_j\hat{h}_j\hat{u}_j\right) = B_i. \tag{4.23}$$

A factor of $1/(g\mathcal{H})$ has been absorbed into the constants B_i, and we introduce a measure of the strength of non-traditional effects through

$$\delta = \frac{2\Omega\mathcal{H}}{\mathcal{U}}, \tag{4.24}$$

the ratio of the non-traditional velocity scale $2\Omega\mathcal{H}$ to the fluid velocity scale $\mathcal{U}$. Assuming $\delta = \mathcal{O}(1)$ and $\mathrm{Fr} \ll 1$, the leading-order form of (4.23) in Fr may be rearranged into

$$\hat{\eta}_i = \tilde{B}_i, \quad \text{for} \quad i = 1, \ldots, N, \tag{4.25}$$

where the $\tilde{B}_i$ are linear combinations of the B_i.

Returning to dimensional variables and applying the boundary conditions (4.20), the layer heights are all constants,

$$h_i(y) = H_i, \quad \text{for} \quad i = 1, \ldots, N-1, \tag{4.26}$$

except for the bottom layer, whose height must vary to keep its upper surface flat,

$$h_N(y) = H_N + h_b(y) - h_b(y_0). \tag{4.27}$$

This assumes that the lowest layer does not outcrop from the topography. The meridional velocity follows immediately from (4.19c) for conservation of mass, *i.e.* $v_i = V_i$ for $i < N$, and

$$v_N(y) = \frac{V_N H_N}{H_N + h_b(y) - h_b(y_0)}. \tag{4.28}$$

Finally, the zonal velocity is unaffected by the non-traditional component of the Coriolis force in all but the lowest layer,

$$u_i(y) = U_i + \tfrac{1}{2}\beta\left(y^2 - y_0^2\right), \qquad \text{for } i = 1, \ldots, N, \tag{4.29}$$

$$u_N(y) = U_N + \tfrac{1}{2}\beta\left(y^2 - y_0^2\right) - \Omega(h_b(y) - h_b(y_0)) \tag{4.30}$$

This explicit leading-order solution confirms that, in the case of strongly-stratified layers, the layer surfaces are approximately flat, and only the lowest layer is influenced by the complete Coriolis force, unless the layer surfaces outcrop from the topography.

4.5 Unsteady flow in a steep-sided channel

The steady-state solutions discussed in §4.4 provide useful insight into the role of the complete Coriolis force. However, this raises the question as to whether a cross-equatorial flow would ever evolve into such states. Additionally, we have not discussed how an equatorial channel affects flow from a point far south of the equator to a point far north, which requires a modification of the fluid's potential vorticity. We therefore now consider time-dependent solutions of the one-dimensional shallow water equations, using a steep-sided channel whose dimensions better reflect those of the actual equatorial bathymetry.

4.5.1 Time-dependent shallow water model of the AABW

We represent the AABW as a single fluid layer that is governed by the non-traditional shallow water equations with a reduced gravity,

$$\frac{\partial u}{\partial t} + \Omega\frac{\partial h}{\partial t} + v\left(\frac{\partial u}{\partial y} - \beta y + 2\Omega\frac{\partial}{\partial y}\left(h_b + \tfrac{1}{2}h\right)\right) = 0, \tag{4.31a}$$

$$\frac{\partial v}{\partial t} + v\frac{\partial v}{\partial y} + \left(\beta y - 2\Omega\frac{\partial}{\partial y}\left(h_b + \tfrac{1}{2}h\right)\right)u + \frac{\partial}{\partial y}\left(g'(h_b + h) - \Omega h u\right) = 0, \tag{4.31b}$$

$$\frac{\partial h}{\partial t} + \frac{\partial}{\partial y}(hv) = 0. \tag{4.31c}$$

We obtain the time-dependent solution to (4.31a)–(4.31c) via numerical integration. Equation (4.31a) contains time derivatives of both u and h, so we rewrite it as a material conservation law for the angular momentum $\tilde{u}$ on an equatorial β-plane (Ripa, 1982, 1997),

$$\frac{\partial \tilde{u}}{\partial t} + v\frac{\partial \tilde{u}}{\partial y} = 0, \quad \tilde{u} = u - \tfrac{1}{2}\beta y^2 + 2\Omega\left(h_b + \tfrac{1}{2}h\right). \tag{4.32}$$

This is the zonally symmetric form of (4.5). From (4.6), the zonally symmetric potential vorticity is

$$q = \frac{\hat{\boldsymbol{z}} \cdot (\nabla \times \tilde{\boldsymbol{u}})}{h} = -\frac{1}{h}\frac{\partial \tilde{u}}{\partial y}. \tag{4.33}$$

Thus in the one-dimensional case, uniformly zero potential vorticity ($q \equiv 0$) is equivalent to constant angular momentum, $\tilde{u} =$ constant. Equation (4.31b) may also be rewritten as

$$\frac{\partial v}{\partial t} + \frac{\partial \Phi}{\partial y} = u\frac{\partial \tilde{u}}{\partial y}, \quad \Phi = \tfrac{1}{2}u^2 + \tfrac{1}{2}v^2 + g'(h_b + h) - \Omega h u, \tag{4.34}$$

in terms of $\tilde{u}$ and a modified pressure Φ. The forms of (4.32) and (4.34) are more convenient for numerical integration.

4.5.2 Numerical approach

We prescribe an inflow at the upstream (southern) boundary, $y = y_u$, with a fixed depth $h = H$ and velocity $(u, v) = (U, V)$. In the rest of the domain we prescribe a thin, stationary fluid layer to avoid the computational difficulties associated with the layer outcropping from the dry bed. To avoid an initial discontinuity, the upstream conditions conditions are connected smoothly to the interior of the domain via a short exponential tail, as shown in Figure 4.10(a). Following Salmon (2002), we prevent the layer depth from approaching zero by using a modified pressure,

$$\tilde{\Phi} = \tfrac{1}{2}u^2 + \tfrac{1}{2}v^2 - \Omega h u + g'\left[h_b + h - h\left(\frac{h_0}{h}\right)^4\right] \tag{4.35}$$

The additional term in $\tilde{\Phi}$ becomes large when $h \ll h_0$, preventing the layer thickness from decreasing further, but is negligible in the bulk of the fluid where $h \gg h_0$. The layer thickness is initially set to $h = h_0/2$ away from the southern boundary.

The front of the fluid tends to steepen towards a discontinuity when it encounters such a thin layer, so we include an artificial viscosity in (4.32) and (4.34) to maintain numerical stability,

$$\frac{\partial \tilde{u}}{\partial t} = -v\frac{\partial \tilde{u}}{\partial y} - ru + \frac{\nu_n}{h}\frac{\partial}{\partial y}\left(h\frac{\partial v}{\partial y}\right), \tag{4.36}$$

$$\frac{\partial v}{\partial t} = u\frac{\partial \tilde{u}}{\partial y} - \frac{\partial \tilde{\Phi}}{\partial y} - rv + \frac{\nu_n}{h}\frac{\partial}{\partial y}\left(h\frac{\partial v}{\partial y}\right). \tag{4.37}$$

The form of the viscosity has been chosen to conserve momentum (see Shchepetkin and O'Brien, 1996), whilst the term proportional to $r(y,t)$ represents the leading-order effect of bottom friction. Equations (4.36) and (4.37) serve as the basis of our numerical solution, along with the mass continuity equation (4.31c), which we rearrange into

$$\frac{\partial h}{\partial t} = -\frac{\partial}{\partial y}\left(hv\right). \tag{4.38}$$

This model is not intended to accurately represent the effects of dissipation on an equatorial current. The numerical viscosity serves only to damp spurious oscillations arising due to the coarseness of the discretisation, and the bottom friction term offers an idealised representation of the modification of potential vorticity by dissipative processes. Pedlosky (1987) showed that a bottom Ekman layer may be represented in the shallow water equations as a linear Rayleigh friction with coefficient $r \sim (fA_z)^{1/2}/\,h$, where A_z is the vertical eddy viscosity. The Coriolis parameter f varies as $f \approx \beta y$ on the equatorial β-plane, so we define r as

$$r(y,t) = \kappa_f \left(\frac{H}{h}\right)\left|\frac{y}{y_u}\right|^{\frac{1}{2}}. \tag{4.39}$$

The time scale for frictional dissipation at $y = y_u$ is $\tau_f \sim 1/\kappa_f$. This formula for r was derived using the traditional approximation, and the Ekman layer can be substantially altered by the inclusion of the complete Coriolis force (Leibovich and Lele, 1985). Equation (4.39) becomes especially dubious close to the equator, where $f \to 0$,because the leading-order balance between Coriolis and viscous forces in the Ekman layer breaks down. In the limit of vanishingly small Rossby number, the fluid should form Taylor columns aligned with the axis of rotation, and therefore parallel to the Earth's surface at the equator. Our shallow water equations retain the assumption of columnar motion close to the equator, on the basis that this is consistent with the shallow-layer approximation, and because the stratification of the real ocean makes this a more appropriate model of a cross-equatorial current. A parametrisation of bottom friction applicable to this situation has not been formally derived, so we use (4.39) as a simple mechanism for potential vorticity modification. Removing the explicit dependence of r on y does not lead to any qualitative changes in our results.

We represent the bathymetry close to the equator using an idealised steep-sided channel that is qualitatively similar to the averaged bathymetry shown in Figure 4.2, but which flattens off away from the equator. Specifically, we use a channel of the form

$$h_b(y) = h_b^{(0)}\left[1 - \exp\left(\left|\frac{y}{y_w}\right|^n\right)\right], \tag{4.40}$$

which defines a channel of height $h_b^{(0)}$ and half-width y_w. For the solutions presented below, we use $h_b^{(0)} = 700\,\mathrm{m}$, $y_w = 125\,\mathrm{km}$ and $n = 4$. We approximate the solution in the region $[y_u, y_d]$, where y_d

is the downstream (northern) boundary, using discrete values $\{\tilde{u}_m(t), v_m(t), h_m(t)\}$ at the regularly spaced points y_m for $m = 1, \ldots, M$. We approximate the y-derivatives on the right hand sides of (4.36)–(4.38) using second-order centred finite differences, and integrate forward in time using the fourth-order Runge-Kutta scheme. This requires recalculation of the zonal velocity u from the angular momentum $\tilde{u}$ at each time step. We halt the integration when the solution reaches a steady state, as defined by the pointwise variations of all variables $\{\tilde{u}_m, v_m, h_m\}$ being less than 0.1% over a period of 100 days.

The inclusion of a second-order term in (4.37) complicates this problem, as it necessitates additional boundary conditions for $\tilde{u}$, v and h. In fact, even without this term, the prescription of boundary conditions for $\tilde{u}$, v and h at the upstream edge of the domain is somewhat difficult. The two-dimensional non-rotating shallow water equations have characteristics with speeds v and $v \pm \sqrt{g'h}$ (*e.g.* Whitham, 1974), so for small velocities $|v| < \sqrt{g'h}$ there are characteristics propagating in both directions. Information is then able to propagate towards both the northern and southern boundaries, but the solution cannot describe the behaviour of the fluid beyond these boundaries. A completely rigorous numerical solution would require a boundary condition for the northward-propagating characteristic at the southern boundary, and one for the southward-propagating characteristic at the northern boundary.

We circumvent these difficulties by employing sponge layers (*e.g.* Israeli and Orszag, 1981) at the edges of the computational domain. These sponge layers absorb outward-propagating waves whilst minimally affecting the interior. At $y = y_u$ we fix $u = U$, $v = V$, $h = H$, and at $y = y_d$ we artificially fix $u = v = 0$, $h = h_0$, as the actual behaviour of the current beyond the northern boundary is unknown. At the southern boundary the first S gridpoints $y_1, \ldots, y_S$ form the sponge layer. After each time step the values of u_m, v_m and h_m in the sponge layer are multiplied by a sponge coefficient s_m to relax them towards the boundary values, U, V and H. We choose s_m such that the cumulative relaxation factor after one sponge time scale T_s varies linearly from 0 to 1 across the layer,

$$s_m = \left(\frac{m-1}{S-1}\right)^{\Delta t/T_s}, \tag{4.41}$$

where Δt is the length of a time step. An analogous process takes place at the northern boundary, with u_m and v_m relaxed towards 0, and h_m relaxed towards h_0. A drawback of using sponge layers is that the solution will not exactly correspond to the prescribed upstream boundary conditions, which are not rigidly enforced by the sponge layers.

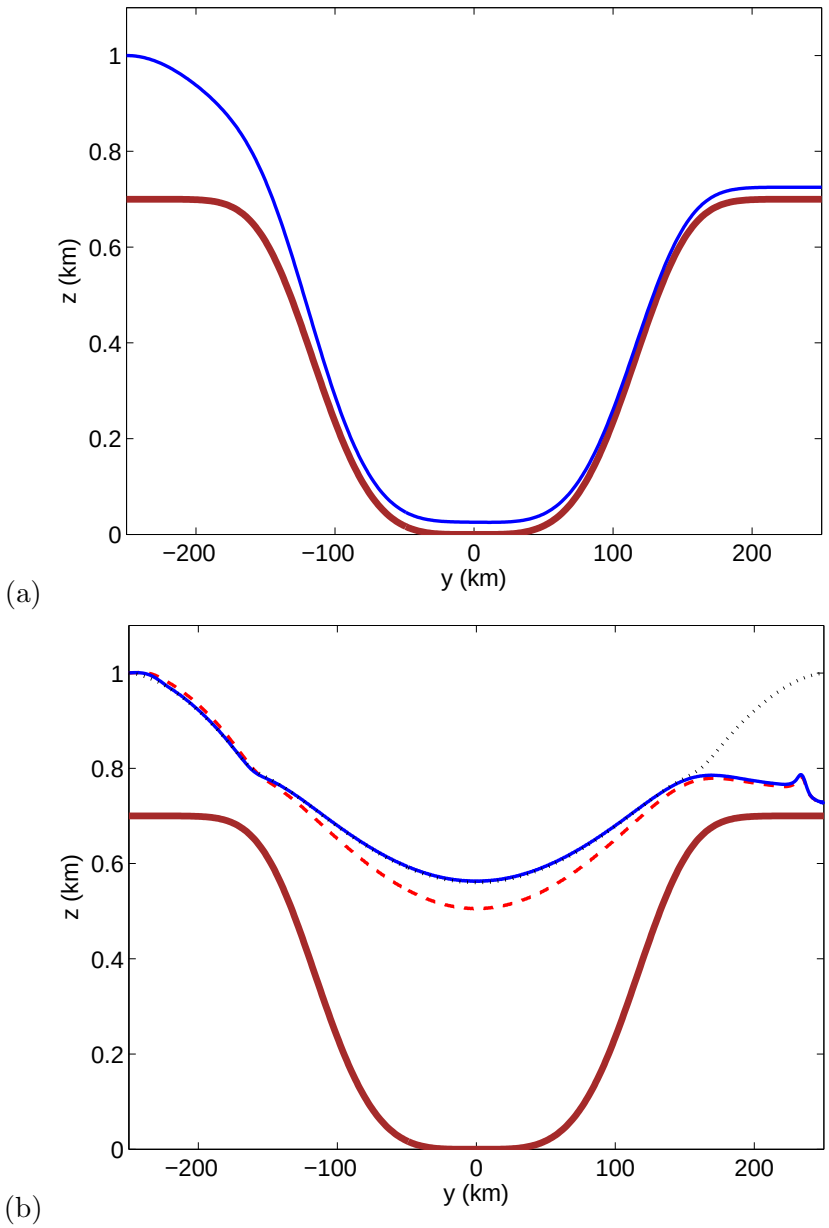

Figure 4.10: Snapshots of the computed solution to (4.31a)–(4.31c) at (a) $t = 0$ and (b) $t = 4000$ days, in the absence of friction ($\kappa_f = 0$). The thick solid line marks the height of the bottom topography, and the dotted line shows the steady solution calculated via the method of §4.4.1, including the complete Coriolis force. The height of the fluid surface is plotted under the traditional approximation (dashed line) and including the complete Coriolis force (thin solid line).

4.5.3 Results

In all of the solutions discussed here, the upstream conditions are $u = U = 0$, $v = V = 10\,\mathrm{cm\,s^{-1}}$, and $h = H = 300\,\mathrm{m}$, and the reduced gravity is $g' = 5 \times 10^{-4}\,\mathrm{m\,s^{-2}}$. We discretise the solutions using $M = 501$ points from the upstream position $y_u = -250\,\mathrm{km}$ to the downstream position

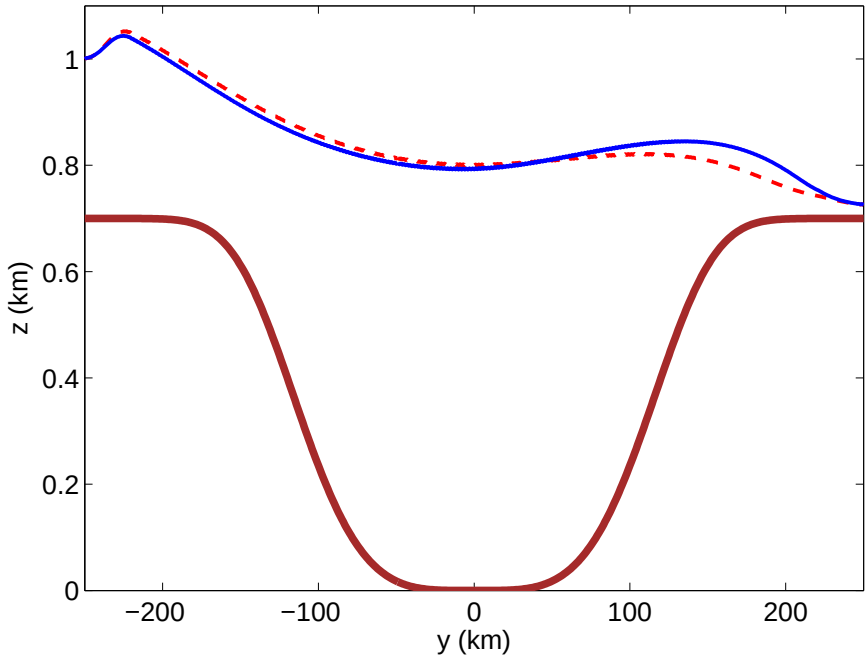

Figure 4.11: Computed steady-state solution to (4.31a)–(4.31c) with moderately strong bottom friction, $\kappa_f = 3 \times 10^{-2}\,\text{days}^{-1}$. The height of the fluid surface is plotted under the traditional approximation (dashed line) and including the complete Coriolis force (thin solid line), and the thick solid line marks the height of the bottom topography.

$y_d = +250\,\text{km}$, giving a grid spacing of $\Delta y = 1\,\text{km}$. Sponge layers of width $S = 30$ gridpoints occupy the regions $220\,\text{km} \leq |y| \leq 250\,\text{km}$ at both edges of the domain. We use $h_0 = 50\,\text{m}$, so the initial layer thickness away from the southern boundary is 25 m, and the numerical viscosity coefficient is $\nu_n = 200\,\text{m}^2\,\text{s}^{-1}$.

In Figure 4.10 we plot the computed solution to (4.36)–(4.38) without bottom friction ($\kappa_f = 0$). The current fills the equatorial channel, and eventually tends towards the steady state shown in Figure 4.10(b), where it closely resembles the analytical solution obtained via the method of §4.4.1. The only pronounced discrepancy lies close to the northern boundary, where the northern sponge layer damps the computed solution away from the analytical solution. Making the traditional approximation, *i.e.* neglecting all terms multiplied by Ω in (4.36)–(4.37), leads to the fluid layer being somewhat shallower in the equatorial channel, but the solution is otherwise almost identical. Figure 4.11 shows the corresponding steady solution for strong frictional dissipation ($\kappa_f = 3 \times 10^{-2}\,\text{days}^{-1}$). Now the fluid surface no longer dips at the equator, but instead tends to slope downwards to the north, so that the gravitational pressure gradient partly balances the bottom friction term in (4.37). Including the complete Coriolis force makes almost no difference to this case.

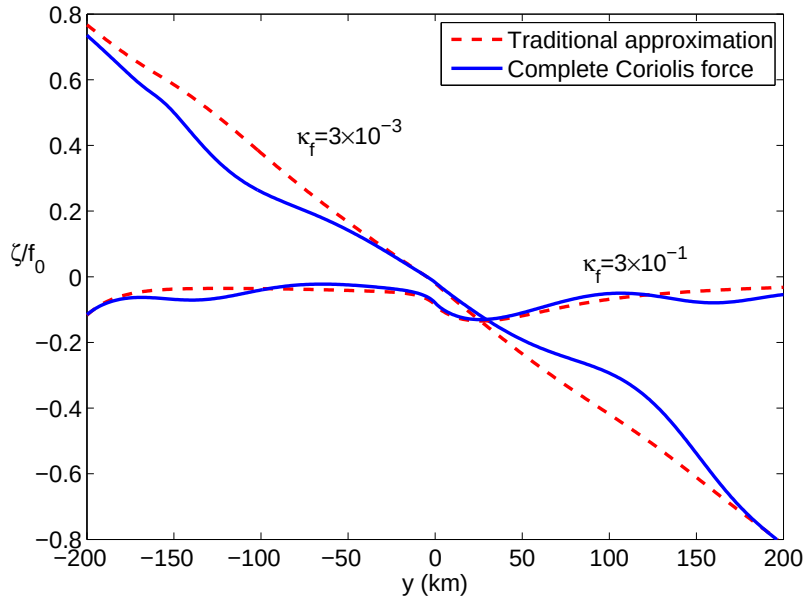

Figure 4.12: Plots of the steady-state relative vorticity profile across the channel, illustrating the contrast between the cases of strong friction ($\kappa_f = 3 \times 10^{-1}\,\text{days}^{-1}$) and weak friction ($\kappa_f = 3 \times 10^{-3}\,\text{days}^{-1}$). The relative vorticity ζ is scaled by the magnitude of the upstream planetary vorticity, $|f_0| = 2\Omega \sin(|y_u|/R_E)$.

For fluid to travel from far south of the equator to far north of the equator, its potential vorticity must be modified by the action of dissipation, as otherwise it must acquire a prohibitively large relative vorticity (Edwards and Pedlosky, 1998). Including friction in (4.36) allows the fluid to change its angular momentum $\tilde{u}$, and therefore its potential vorticity, as it crosses the equator. In Figure 4.12 we plot the steady-state relative vorticity profiles for several values of the friction parameter κ_f. When $\kappa_f \lesssim 10^{-3}\,\text{days}^{-1}$, $\tilde{u}$ is approximately constant, and so there is a large change in relative vorticity across the channel. As predicted in §4.4, the effect of including the complete Coriolis force is most pronounced where the topographic gradients are largest. We see from the solution for $\kappa_f = 3 \times 10^{-3}\,\text{days}^{-1}$ that fluid moving from the southern slope to the northern slope of the channel (from $y \approx -100\,\text{km}$ to $y \approx +100\,\text{km}$) requires a much smaller change in relative vorticity when the complete Coriolis force is accounted for, around 30% to 40% less in this case. However, fluid moving beyond the edges of the channel, from far south of the equator to far north, experiences the same change in relative vorticity regardless of whether the complete Coriolis force is included.

A larger κ_f allows friction to modify the fluid's potential vorticity more readily, so the fluid no longer requires such a large change in its relative vorticity. In Figure 4.13(a) we plot the change $\Delta\zeta$ in the relative vorticity as fluid moves from $y = -200\,\text{km}$ to $y = +200\,\text{km}$, over a range of values of κ_f. The solution changes rapidly from a state of zero potential vorticity at $\kappa_f \lesssim 10^{-2}\,\text{days}^{-1}$,

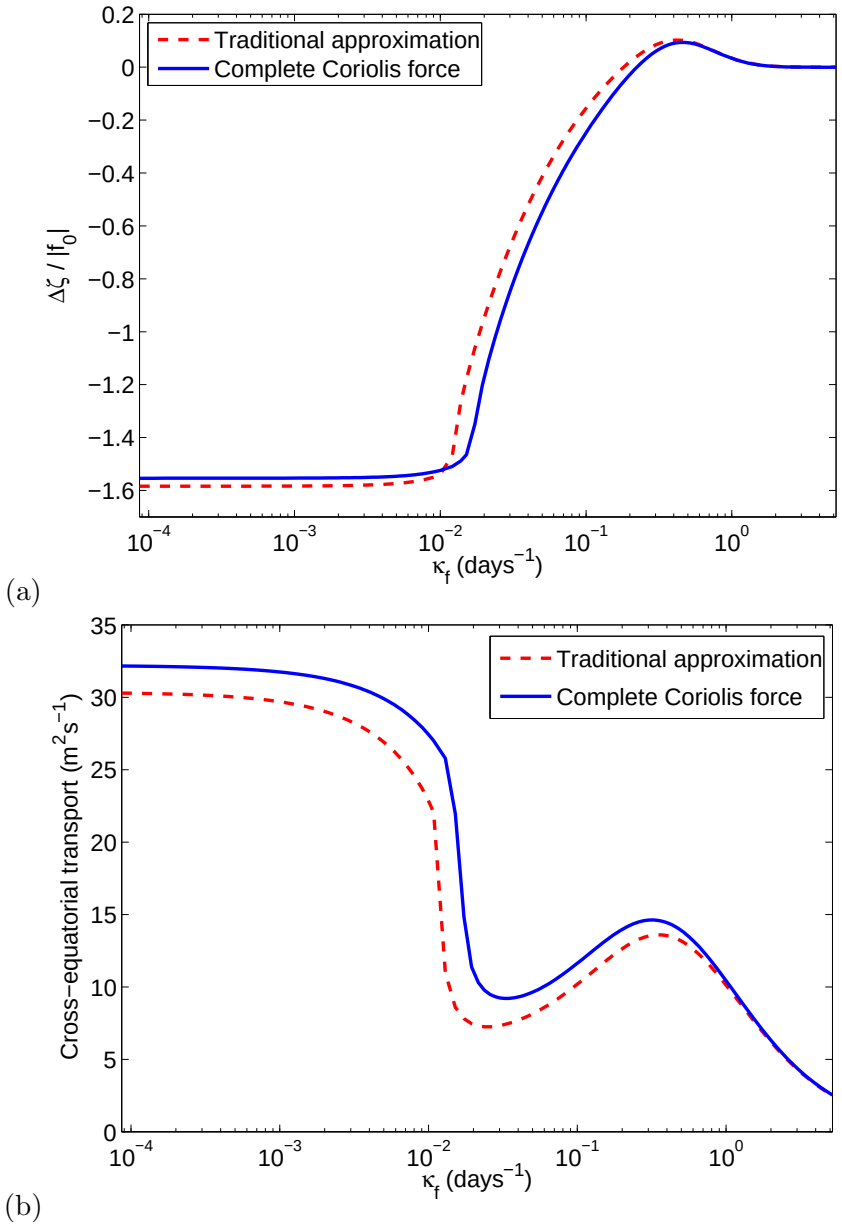

Figure 4.13: (a) the computed change in relative vorticity, and (b) the steady-state cross-equatorial transport, with the complete Coriolis force (solid lines) and under the traditional approximation (dashed lines). The change in relative vorticity is calculated as $\Delta\zeta = \zeta(y = +200\,\mathrm{km}) - \zeta(y = -200\,\mathrm{km})$, and is scaled by the magnitude of the upstream planetary vorticity, $|f_0| = 2\Omega\sin(|y_u|/R_E)$.

to a friction-dominated state with $\Delta\zeta \approx 0$ at $\kappa_f \gtrsim 5 \times 10^{-1}\,\mathrm{days}^{-1}$. The influence of the complete Coriolis force is less pronounced at larger values of κ_f, even over large topographic gradients, and $\Delta\zeta$ is almost identical with or without the complete Coriolis force.

In Figure 4.13(b) we plot the cross-equatorial transport over the same range of κ_f. At $\kappa_f \approx 10^{-2}\,\mathrm{days}^{-1}$ there is a very rapid drop in the transport. This corresponds to a rapid change in the shape of the fluid surface, characterised by a change from that shown in Figure 4.10(b) to that shown

in Figure 4.11. The transport increases again to a local maximum at $\kappa_f \approx 3 \times 10^{-1}\,\text{days}^{-1}$, and finally approaches zero when $\kappa_f \gtrsim 5 \times 10^{-1}\,\text{days}^{-1}$. This behaviour is due to a separation between the scales over which frictional effects are important in (4.36) and (4.37). In (4.37), friction becomes comparable to advection when

$$\kappa_f \left(\frac{H}{h}\right) \left|\frac{y}{y_u}\right|^{\frac{1}{2}} v \sim v\frac{\partial v}{\partial y}, \quad \text{or} \quad \kappa_f \sim \frac{V^2}{VL} \approx 1.7 \times 10^{-2}\,\text{days}^{-1}, \tag{4.42}$$

where $L = y_d - y_u$ is the length of the domain. This agrees approximately with the rapid change in the cross-equatorial transport and the shape of the fluid surface. In (4.36), friction becomes comparable to the upstream angular momentum when

$$\kappa_f \left(\frac{H}{h}\right) \left|\frac{y}{y_u}\right|^{\frac{1}{2}} u \sim u\frac{\partial \tilde{u}}{\partial y}, \quad \text{or} \quad \kappa_f \sim \beta|y_u| \approx 5 \times 10^{-1}\,\text{days}^{-1}. \tag{4.43}$$

This is consistent with Figure 4.13(a), as $\Delta\zeta \approx 0$ when $\kappa_f \gtrsim 5 \times 10^{-1}\,\text{days}^{-1}$.

As stated earlier, the sponge layers at the boundaries of the computational domain allow for some variation in the effective boundary conditions in the solution. Our solutions tend to approach a state in which $\Delta\zeta$ is almost identical with or without non-traditional effects, but the cross-equatorial transport becomes larger when non-traditional effects are included. This result is consistent over all values of κ_f, though for $\kappa_f \gtrsim 5 \times 10^{-1}\,\text{days}^{-1}$ the difference between the transports becomes vanishingly small. We conclude that for a given modification of the relative or potential vorticity, a stronger cross-equatorial flow is possible when the complete Coriolis force is included.

4.6 Cross-equatorial geostrophic adjustment

In the preceding sections we focused on the role that the combination of the complete Coriolis force and channel-like equatorial topography plays in cross-equatorial transport of the AABW. In this section we consider a body of fluid that lies initially at rest in the southern hemisphere, and subsequently adjusts towards a state of geostrophic balance by radiating energy in the form of inertia-gravity waves. This problem was first studied by Killworth (1991), who showed that a fluid's ability to adjust across the equator is severely constrained by the change in sign of f. Geostrophic adjustment is likely to be responsible for a proportion of the cross-equatorial flow of the AABW. We find that including the complete Coriolis force increases both the cross-equatorial transport and the distance the fluid reaches in the northern hemisphere. For simplicity, we will illustrate this with a flat topography ($h_b \equiv 0$).

4.6.1 The one-dimensional geostrophic adjustment problem

We restrict our attention to a one-dimensional adjustment problem, so the fluid is governed by (4.31a)–(4.31c). In the absence of topography ($h_b = 0$) it is convenient to non-dimensionalise these equations by setting

$$\boldsymbol{u} = \mathcal{U}\,\hat{\boldsymbol{u}}, \quad h = \mathcal{H}\,\hat{h}, \quad y = R_d\,\hat{y}, \quad t = \frac{R_d}{\mathcal{U}}\,\hat{t}, \tag{4.44}$$

where $\mathcal{H}$ is a vertical lengthscale, $\mathcal{U} = \sqrt{g'\mathcal{H}}$ is the characteristic wave speed base on the reduced gravity, and $R_d = \sqrt{\mathcal{U}/2\beta}$ is the equatorial radius of deformation, modified slightly from (4.10) to match the convention used by Killworth (1991). We henceforth drop the hat $\hat{}$ notation for dimensionless variables. Under this non-dimensionalisation, (4.31a)–(4.31c) reduce to

$$\frac{\partial u}{\partial t} + \delta\frac{\partial h}{\partial t} + v\left(\frac{\partial u}{\partial y} - \tfrac{1}{2}y + \delta\frac{\partial h}{\partial y}\right) = 0, \tag{4.45a}$$

$$\frac{\partial v}{\partial t} + v\frac{\partial v}{\partial y} + \left(\tfrac{1}{2}y - \delta\frac{\partial h}{\partial y}\right)u + \frac{\partial}{\partial y}\left(h - \delta h u\right) = 0, \tag{4.45b}$$

$$\frac{\partial h}{\partial t} + \frac{\partial}{\partial y}\left(hv\right) = 0, \tag{4.45c}$$

where $\delta = \Omega\sqrt{\mathcal{H}/g'}$ is modified from its earlier definition in (4.10) to match the conventions used by Killworth (1991).

Figure 4.14 shows a typical initial state for the one-dimensional geostrophic adjustment problem. The bulk of the fluid lies in the southern hemisphere, with a layer of finite depth h_0 projecting north across the equator, and the velocity is initially zero everywhere. We use an initial height profile of the form

$$h(y,0) = h_0 + \frac{1-h_0}{2}\left[1 + \tanh\left(\frac{Y-y}{W}\right)\right], \tag{4.46}$$

such that $h \to 1$ as $y \to -\infty$ and $h \to h_0$ as $y \to \infty$. The adjusted state is strongly dependent on the initial position Y of the front that marks the northern boundary of the fluid, whilst W measures the distance over which the height drops from 1 to h_0, and is fixed at $W = 0.1$ in our solutions. Killworth (1991) obtained a quasi-analytical solution to the case where $h_0 = 0$ under the traditional approximation, but the inclusion of non-traditional terms renders this intractable. We therefore compute the adjusted state by solving an initial value problem for the system (4.45). We use a finite value $h_0 > 0$ to avoid computational issues associated with the fluid surface intersecting the bottom topography.

4.6.2 Numerical approach

We obtain our numerical solutions using the centred scheme of Kurganov and Tadmor (2000). This scheme is total variation diminishing for scalar conservation laws, so we multiply (4.45a) and (4.45b)

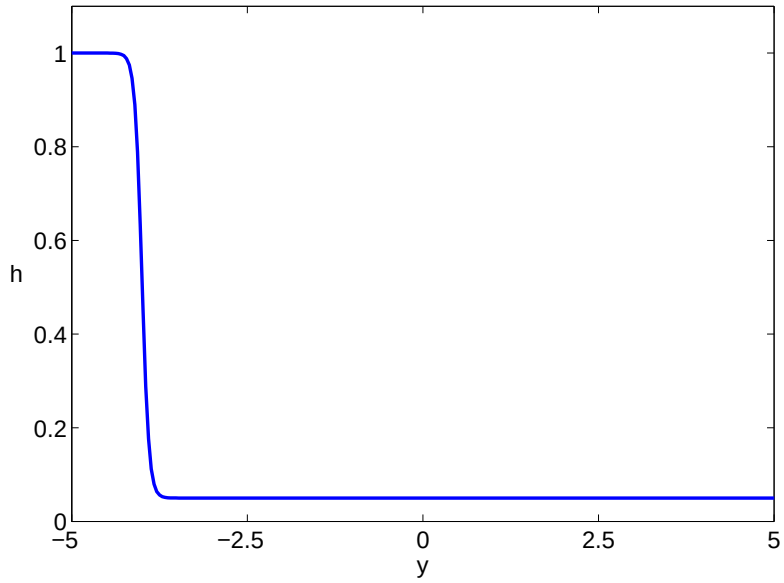

Figure 4.14: A typical initial state for the cross-equatorial geostrophic adjustment problem. In this example $h_0 = 0.05$ and $Y = -1.9$.

by h and use (4.45c) to rewrite them as conservation laws for the momenta,

$$\frac{\partial}{\partial t}\left(hu + \delta h^2\right) + \frac{\partial}{\partial y}\left(huv + \delta h^2 v\right) = \tfrac{1}{2} yhv, \tag{4.47a}$$

$$\frac{\partial}{\partial t}\left(hv\right) + \frac{\partial}{\partial y}\left(hv^2 + \tfrac{1}{2}h^2 - \delta h^2 u\right) = -\tfrac{1}{2} yhu. \tag{4.47b}$$

Equation (4.45c) is already in conservation form. The traditional components of the Coriolis force appear as nonlinear source terms on the right hand sides of (4.47a) and (4.47b). The y-dependence of f means that y-momentum is not conserved, as fluid moving in the y-direction is subject to a latitudinally varying acceleration by the Coriolis force. The x-momentum is conserved because f is independent of x, so (4.47a) may rewritten as an exact conservation law, but this makes little difference to the computed solution. The Kurganov and Tadmor (2000) scheme is a semi-discrete one, formulated as a system of ordinary differential equations (ODEs) for the evolution of cell-averaged quantities. The spatial discretisation is used to construct discrete fluxes across cell boundaries. The algebraic terms may be easily included alongside the numerical fluxes in the ODE system. No operator splitting is necessary, as would be the case for a Godunov method.

We discretise the domain $y \in [-20, 20]$ using an evenly-spaced grid of N points. The spatial discretisation of Kurganov and Tadmor (2000) uses a 5-point stencil, so we introduce two additional 'ghost' points beyond each boundary of the domain to impose zero-gradient boundary conditions. We integrate forward in time using the second order total variation diminishing Runge–Kutta scheme of Shu and Osher (1989). The integration is numerically stable as long as the ratio of the grid spacing

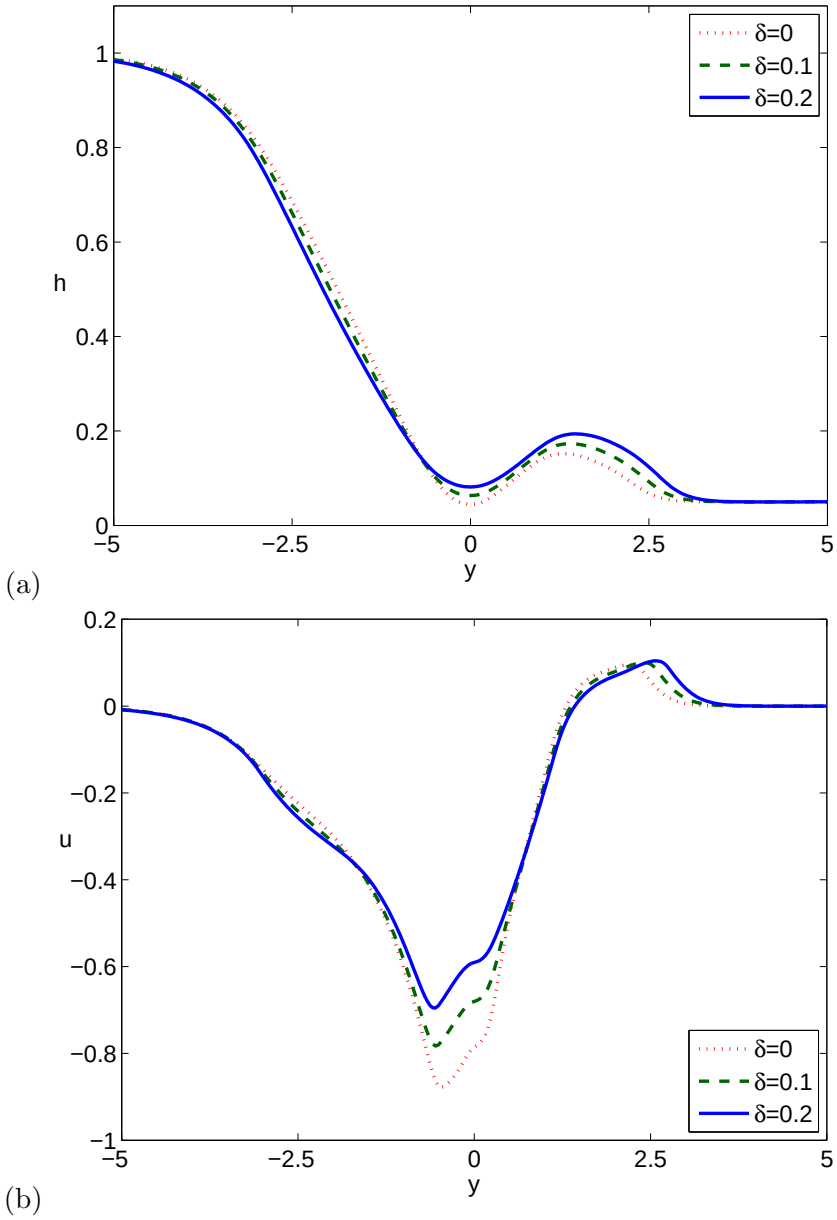

Figure 4.15: Adjusted (a) height and (b) zonal velocity for the initial height profile shown in Figure 4.14, for various values of the non-traditional parameter δ. The time-dependent solution has been calculated on a grid of 1025 points, and then averaged over the interval from $t = 800$ and $t = 1000$ to remove equatorially trapped waves.

Δy to the time step Δt exceeds the maximum local wave speed $\lambda_{\max}$ at every grid point. This is calculated from the fluxes in (4.47a)–(4.47b) and (4.45c). At each time step we make Δt as large as possible whilst satisfying $\Delta t \leq 0.9\Delta y/\lambda_{\max}$ at all grid points.

4.6.3 Results

Figure 4.15 shows the adjusted height and zonal velocity reached from the initial condition shown in Figure 4.14, corresponding to (4.46) with $Y = -1.9$. The adjusted meridional velocity is zero everywhere. Equatorially trapped waves prevent the solution from ever reaching a true steady state, so we plot the averages of the instantaneous profiles over the interval from $t = 800$ and $t = 1000$. For a given initial condition, the adjusted state depends only on the non-traditional parameter δ. Using $\Omega = 10^{-4}\,\mathrm{rad\,s^{-1}}$ and $\mathcal{H} = 1000\,\mathrm{m}$, $\delta = 0.1$ corresponds to $g' = 10^{-3}\,\mathrm{m\,s^{-2}}$, and $\delta = 0.2$ corresponds to $g' = 2.5 \times 10^{-4}\,\mathrm{m\,s^{-2}}$. These values give length scales for the flow of $R_d = 148\,\mathrm{km}$ and $R_d = 105\,\mathrm{km}$, respectively. This adjusted state is typical when the initial front position Y is sufficiently close to the equator to permit cross-equatorial flow. The fluid depth has a local minimum very close to the equator, leading to a strong westward jet at the equator and a weaker eastward jet north of the equator. Including the complete Coriolis force leads to a larger volume of fluid crossing the equator, and penetrating further into the northern hemisphere. This corresponds to a weaker westward equatorial jet and a slightly stronger eastward jet north of the equator.

The adjusted state varies strongly with Y, the position of the front in the initial conditions. Figure 4.16 shows the computed cross-equatorial transport T, and final position y_f, of fluid that lies initially at the front $y = Y$. We define y_f by

$$\int_{y_f}^{\infty} h_a(y)\,\mathrm{d}y = \int_{Y}^{\infty} h\,(y, t = 0)\,\mathrm{d}y, \tag{4.48}$$

where $h_a(y)$ denotes the adjusted height field, and we define the cross-equatorial transport by

$$T = \int_{0}^{y_f} h_a(y)\,\mathrm{d}y = \int_{0}^{\infty} h_a(y)\,\mathrm{d}y - \int_{Y}^{\infty} h\,(y, t = 0)\,\mathrm{d}y. \tag{4.49}$$

This cross-equatorial transport will be negative if the final position of the front lies south of the equator. This transport T then gives the additional volume of fluid required in the northern hemisphere to allow fluid from $y = Y$ to reach the equator.

Figure 4.16 shows that including the complete Coriolis force leads to a larger cross-equatorial transport, T, and a deeper penetration y_f into the northern hemisphere for all starting positions Y. This is most pronounced in the range $-2.5 < Y < -1.5$, where including the complete Coriolis force allows fluid to penetrate up to 2 deformation radii further than it does under the traditional approximation. This is most easily understood in terms of the fluid's angular momentum. Rewriting (4.45a) as a material derivative, as we did with (4.32), we obtain

$$\frac{\mathrm{D}\tilde{u}}{\mathrm{D}t} = 0, \quad \tilde{u} = u - \tfrac{1}{4}y^2 + \delta h, \tag{4.50}$$

where $\mathrm{D}/\mathrm{D}t \equiv \partial/\partial t + v\partial/\partial y$, and $\tilde{u}$ is the dimensionless angular momentum. Thus $\tilde{u}$ is conserved following the fluid. Under the traditional approximation ($\delta = 0$), the planetary angular momentum

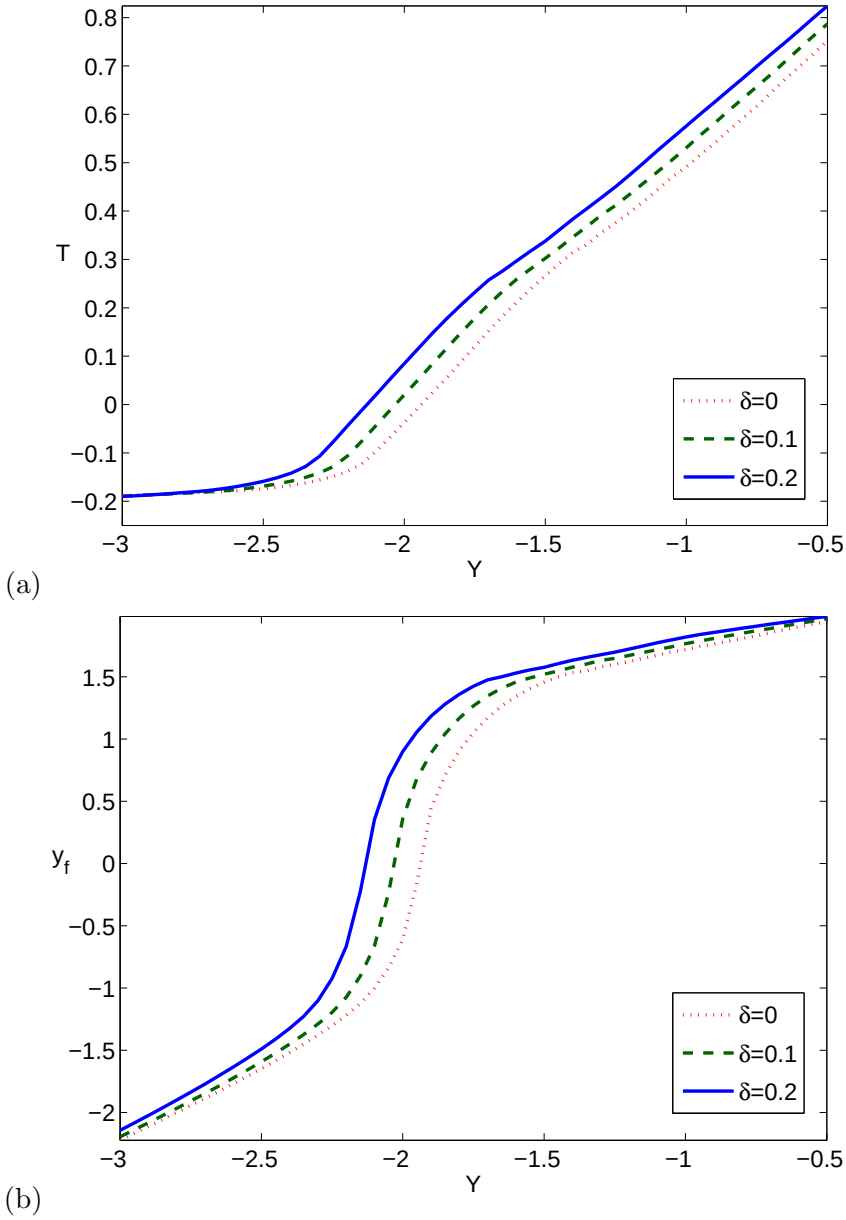

Figure 4.16: (a) Cross-equatorial transport, T, and (b) final position of the initial front, y_f, plotted against the initial position of the front, Y. We have constructed the plots using the long-time averages of the numerical solution for a range of values of Y. In all cases we have take $h_0 = 0.05$ and used $N = 1025$ points.

$\tilde{u}_p = -\frac{1}{4}y^2$ increases towards the equator. To cross the equator, fluid starting at rest must generate a large negative zonal velocity u, which may be thought of as a relative angular momentum, to balance the increase in $\tilde{u}_p$. Including the complete Coriolis force ($\delta \neq 0$) accounts for the fact that changing a fluid column's depth changes the average distance of the fluid parcels within it from the axis of rotation, and therefore changes their average planetary angular momentum $\tilde{u}_p = -\frac{1}{4}y^2 + \delta h$. A layer of fluid crossing the equator will thus experience a smaller change in $\tilde{u}_p$ if its thickness

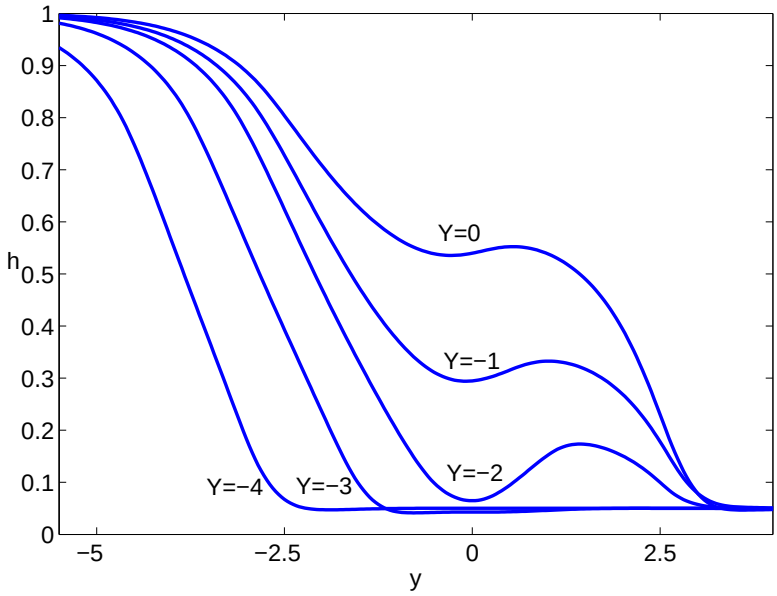

Figure 4.17: Adjusted height profiles for $\delta = 0.2$, $h = 0.05$, $N = 1025$, and, from left to right, $Y = -4$, $Y = -3$, $Y = -2$, $Y = -1$ and $Y = 0$. Non-traditional effects are most prominent in the $Y = -2$ case, when the depth has a pronounced minimum at the equator.

decreases towards the equator. In Figure 4.17 we plot the adjusted depth profiles for several values of Y. In general, the surface of the layer tends to dip towards the equator, reducing the fluid's planetary angular momentum and thereby facilitating cross-equatorial flow. In particular, the dip is most pronounced, whilst still centred on the equator, around $Y \approx -2$. This explains the prominence of non-traditional effects in the range $-2.5 < Y < -1.5$.

The adjusted state also strongly depends on the initial depth h_0 to the north of the front. Killworth (1991) showed that if $h_0 \lesssim 0.04$ then an analytical steady-state solution may not exist for $-1.9 \lesssim Y \lesssim -1.5$. Computing the time-dependent solution with similar parameters leads to adjusted states in which the depth approaches zero at the equator. In Figure 4.18 we plot the adjusted height profile for $h_0 = 0.01$ and $Y = -2.0$, computed with a high resolution (8193 gridpoints). Close to $y = 0$, the depth h tends rapidly to zero with increasing resolution. In the example shown in Figure 4.18, all three curves have minima below 10^{-53}, and the $\delta = 0$ curve falls below 10^{-118}. The adaptive time-stepping of our numerical scheme allows us to compute the solution at such small layer thicknesses without h intersecting the ocean bed. The appearance of these extremely small values of h suggest that we should seek a solution in the form of two disconnected regions separated by an interval of vanishing depth.

Note that $Y = -2.0$ lies slightly outside the range determined by Killworth (1991) to possess no steady-state solutions, because our initial condition (4.46) contains a sharp slope rather than a true

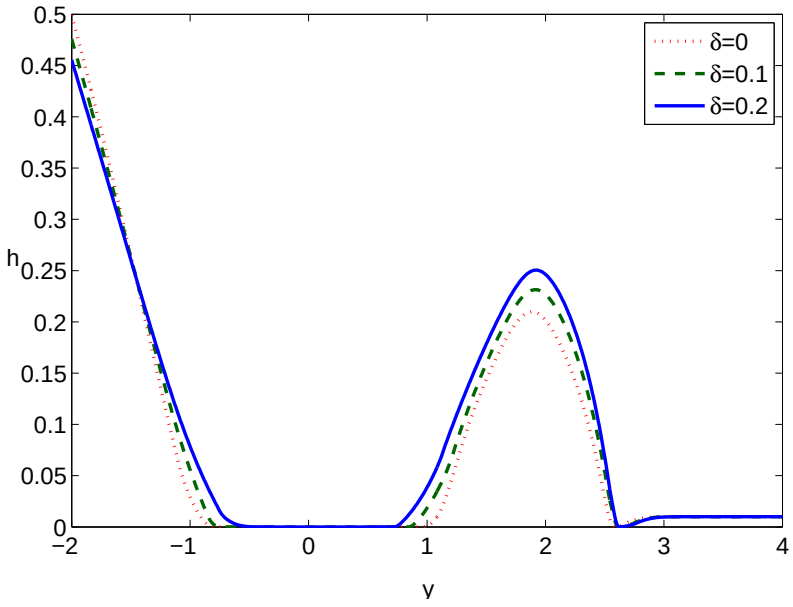

Figure 4.18: Adjusted height profile for $Y = -2.0$ and $h_0 = 0.01$, for different values of the non-traditional parameter, δ. This solution has been computed at a high resolution using 8193 gridpoints. Close to $y = 0$, h becomes vanishingly small with increasing resolution, indicating that the fluid has split into separate water masses on either side of the equator.

discontinuity. This solution suggests that in the exact adjusted state, the fluid should separate into two separate masses on either side of the equator. This cannot be described using the formulation of Killworth (1991), because the analytical solution depends on a continuous map $y \to y_0$ from the position of a given fluid element in the adjusted state, y, to the position of that fluid element in the initial state, y_0. This map becomes discontinuous if the fluid splits into two separate water masses in the adjusted state, so the analytical solution cannot be calculated.

Figure 4.19 shows the final position y_f of the front for values of the initial northern depth in the range $0.01 \leq h_0 \leq 1$. This shows that fluid can penetrate further into the northern hemisphere when the complete Coriolis force is included, regardless of the values of h_0 or Y. The increase in the penetration distance y_f is most pronounced for small h_0, where the adjusted height dips further towards the equator. The corresponding reduction in the planetary angular momentum facilitates cross-equatorial flow when the complete Coriolis force is included, as described above. However, this difference vanishes as $h_0 \to 0$, where all of the curves in Figure 4.19 appear to converge just above $y_f = 2$. This agrees with Killworth's (1991) finding that fluid can only penetrate around two deformation radii north of the equator via the process of geostrophic adjustment alone.

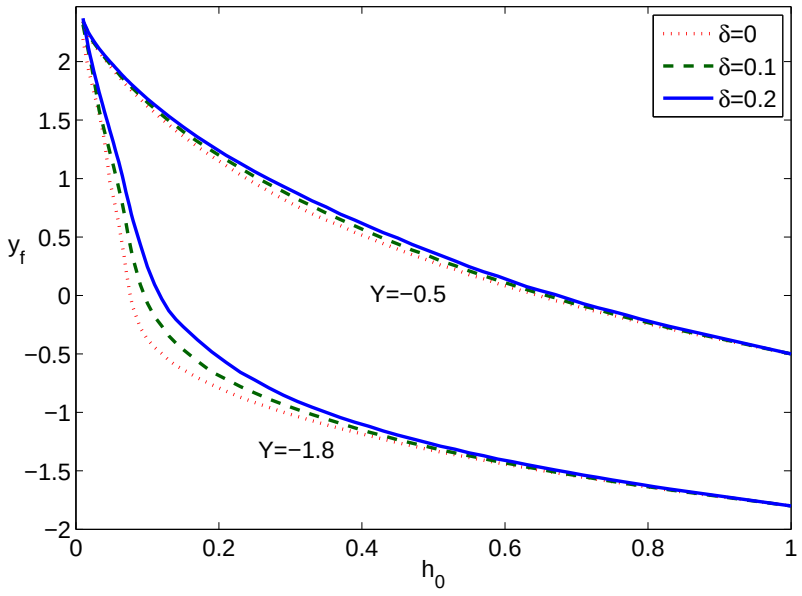

Figure 4.19: Position of the front after adjustment, y_f, plotted for a range of downstream depths h_0, and for two different starting positions, $Y = -2.0$ and $Y = -0.5$. All solutions have been calculated using $N = 1025$ gridpoints.

4.7 Discussion

In this chapter we have considered the role of the "non-traditional" component of the Coriolis force in cross-equatorial transport of ocean currents, with particular emphasis on the AABW. Our approach does not attempt to describe completely the physics of interhemispheric exchange, but rather focuses on highly idealised scenarios to isolate key features. Specifically, we have focused on the interaction of non-traditional Coriolis effects with channel-like equatorial topography, and shown that this combination should facilitate the crossing of the AABW. This may explain why so much of the AABW penetrates into the northern hemisphere, whilst many other equatorial currents are blocked by the equator.

The most important contribution of the non-traditional component of the Coriolis force lies in the potential vorticity, which is well established across the oceanographic and atmospheric sciences as a critical dynamical variable (*e.g.* Muller, 1995). Material conservation of potential vorticity exerts a much stronger constraint on the evolution of the flow than global conservation of energy or momentum, which may be transported over large distances by waves with almost no net displacement of fluid. For example, Killworth (1991) showed that potential vorticity conservation prevents fluid from penetrating further than around two deformation radii across the equator via geostrophic adjustment alone. It is due to this non-traditional contribution to the potential vorticity that the

effect of the non-traditional component of the Coriolis force far exceeds the scaling estimates given in §4.3. In the presence of a zonal equatorial channel, the non-traditional term may balance the change in $f \approx \beta y$ as fluid crosses the equator. This means that the fluid need not acquire as much relative vorticity in crossing to the northern hemisphere.

The analytical solutions of §4.4 provide two descriptions of the influence of the complete Coriolis force on the AABW. The solutions that describe a current crossing a zonal equatorial channel, such as those in §4.4.1, illustrate the mechanism described above. Less relative vorticity is generated as the fluid crosses the equator because the non-traditional terms partially balance the change in f. However, the actual cross-equatorial transport is identical in both the traditional and non-traditional cases. The alternative solution of §4.4.2, in which the layer outcrops from the edges of the channel, may be thought of as a snapshot of the AABW as it traverses the equatorial channel. In this case the flow is purely zonal, and the including non-traditional effects leads to smaller westward velocities. Thus, in this case the complete Coriolis force reduces the transport of the current.

In §4.5 we considered the time-dependent flow of a current northward across the equator, through a channel resembling the bathymetry of Figure 4.2(a). In the absence of friction, the computed steady state shown in Figure 4.10(b) closely resembles the analytical solution obtained in §4.4. This scenario is not entirely realistic, as the flow of the AABW is not zonally symmetric. However, the solution illustrates that the channel need not be the perfect parabola defined in (4.7) to facilitate an equatorial crossing. In fact, as Figure 4.12 shows, having steep slopes at the edges of the channel and an almost-flat section in the middle will greatly reduce the relative vorticity required to cross the equator.

Whilst these solutions shed light on the interaction of the non-traditional component of the Coriolis force with sharply-varying topography, fluid that exits the equatorial channel must acquire the same large relative vorticity that it would under the traditional approximation. We have therefore included a simple representation of bottom friction in our numerical solutions, which allows the fluid to modify its potential vorticity as it crosses the equator. Stronger frictional dissipation leads to a smaller change in the relative vorticity as the fluid crosses the equator, and this change is almost identical when when the complete Coriolis force is included. However, for an approximately identical change in the relative vorticity, the cross-equatorial transport is always larger when the complete Coriolis force is included.

Finally, we revisited the one-dimensional cross-equatorial geostrophic adjustment problem of Killworth (1991). Including the complete Coriolis force hinders the analytical approach to this problem, so we used the high-resolution total variation diminishing scheme of Kurganov and Tadmor (2000) to obtain accurate solutions to the inviscid shallow water equations. It would be of little

value to apply this scheme to the cross-equatorial flow problem of §4.5, as the explicit friction and sponge layer damping negate any advantage conferred by a total variation diminishing scheme.

The non-traditional component of the Coriolis force allows more fluid to adjust further across the equator, regardless of the initial position of the front, as shown in Figure 4.16, or of the initial northern depth, as shown in Figure 4.19. Each fluid parcel must conserve angular momentum (4.50) as it crosses the equator, which requires a large westward velocity to balance the increase in planetary angular momentum. Including the complete Coriolis force accounts for the fact that changes in the fluid depth correspond to changes in the average distance of the fluid in a column from the axis of rotation, and therefore contribute to the angular momentum. The depth of the adjusted fluid layer tends to dip towards the equator, reducing the westward velocity required to cross the equator. The fluid's planetary angular momentum would be reduced further in the presence of a channel straddling the equator, so we expect that the AABW's bathymetry would lead to an even larger cross-equatorial transport by geostrophic adjustment if the complete Coriolis force was included.

This study has neglected zonal variations, which are likely to be very important in the actual evolution of the AABW. The one-dimensional solutions presented here may be unstable to zonal perturbations, and indeed there is no reason to expect that a two-dimensional solution should ever reach a steady state. Indeed, Hall et al. (1997) found that the AABW exhibits substantial time-variability. The generation of relative vorticity as the current crosses the equator may lead to the formation of eddies capable of pumping fluid back into the southern hemisphere, though this may be offset by modification of the potential vorticity by dissipation. We extend our analysis of cross-equatorial flow through a channel to two-dimensional steady and unsteady solutions in Chapters 5 and 6 respectively.

Although we can not claim to describe accurately the behaviour of the AABW using the idealised conditions presented in this chapter, we still obtain a useful insight into the role of the complete Coriolis force. It is interesting to see that the non-traditional component of the Coriolis force substantially influences the solutions, where in previous studies it has invariably been neglected. This work confirms that including the complete Coriolis force is vital for an accurate representation of abyssal current flows close to the equator.

Chapter 5

Flow through an idealised equatorial channel under the complete Coriolis force

This chapter is based upon Stewart and Dellar (2011a).

5.1 Introduction

In this chapter we investigate how an obliquely-orientated equatorial channel might enhance or inhibit cross-equatorial flow of an abyssal current, with particular emphasis on the role of the non-traditional component of the Coriolis force. We focus on the Antarctic Bottom Water (AABW), an abyssal current that originates in the Weddell Sea near Antarctica, where meltwater flows down the Antarctic continental rise and northward into the Atlantic ocean. As the AABW flows northward toward the equator, it mixes with the overlying Lower North Atlantic Deep Water (LNADW), so its northward transport decreases with latitude. McCartney and Curry (1993) reported a northward transport of 7.0 Sv at 30°S (1 Sv = $10^6\,\mathrm{m^3 s^{-1}}$), dropping to 5.5 Sv at 11°S. They give a geostrophic estimate of 4.3 Sv for the cross-equatorial transport, but later measurements by Hall et al. (1994), Hall et al. (1997), and Rhein et al. (1998) place this figure closer to 2 Sv. In Figure 5.1 we plot the depth of the large-scale bathymetry around the Ceara abyssal plain, where the AABW crosses the equator. We highlight the west-northwesterly channel formed between the continental rise to the southwest and the Mid-Atlantic Ridge to the northeast. In Figure 5.2 we plot the averaged profile of this channel shown, illustrating its characteristically steep sides and relatively flat middle. The AABW approaches the equator as a deep western boundary current, but a large portion of it follows the bathymetric contours eastward, exiting the region shown in Figure 5.1 at the eastern

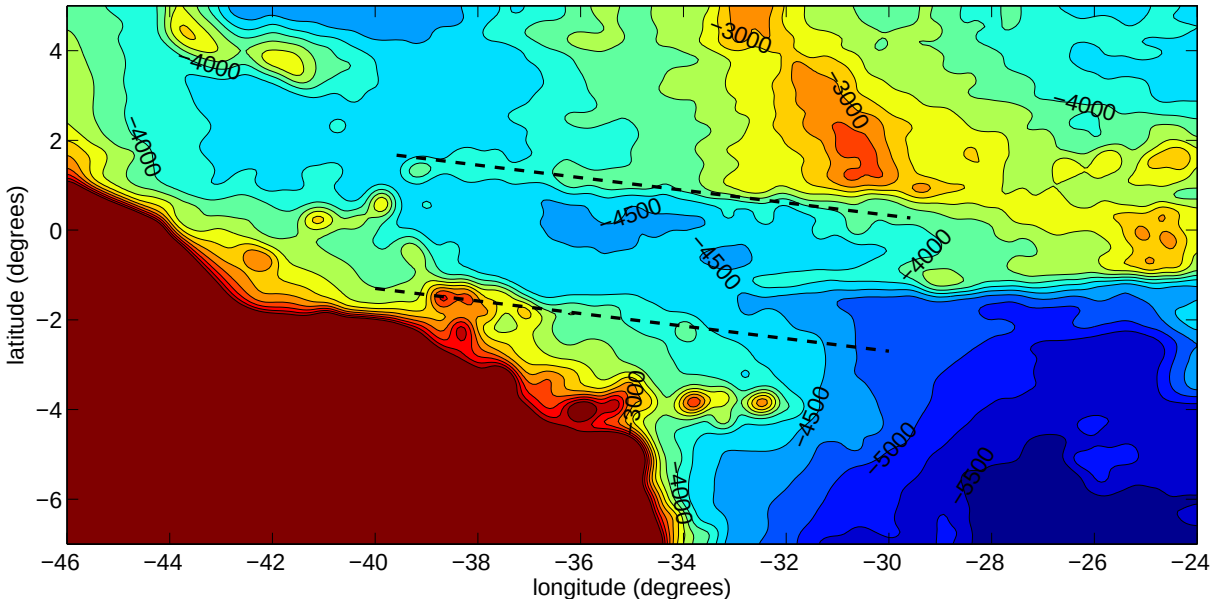

Figure 5.1: Contours of the bathymetry in the region where the AABW crosses the equator. The data has been taken from Amante and Eakins (2009), interpolated onto a grid of 331 by 181 points, and smoothed via ten applications of a nine-gridpoint average (c.f Choboter and Swaters, 2004) to remove small-scale features and highlight the large-scale structure. The dotted lines highlight the northwesterly cross-equatorial channel, whose average profile is shown in Figure 5.2.

edge between 1°S and 2°S. This explains the substantial drop in transport between 11°S and 0°.

This chapter may be compared with the work of Nof (1990), who investigated cross-equatorial flow using analytical solutions to the shallow water equations. He showed that a northward-flowing western boundary current is blocked by the equator and must turn eastward. Nof and Olson (1993) used a similar method to study cross-equatorial flow through northward abyssal channel. They showed that the presence of an opposing wall permits the current to cross the equator, where it makes a transition to a northward-flowing eastern boundary current. Nof and Borisov (1998) compared numerical time-integrations of the shallow water equations with the results of a "solid-balls" model, which tracks the positions of a large number of free particles, in an idealised northward cross-equatorial channel. Their solutions consistently cross the channel close to the equator, and show that anywhere between 0% and 100% of the incoming flow may exit into the northern hemisphere, depending on parameters such as the channel steepness and lateral dissipation. Choboter and Swaters (2000) conducted a similar study, comparing the frictional-geostrophic equations and full shallow water equations. The pronounced differences between the flows predicted by these models suggests that cross-equatorial abyssal flow is a strongly inertial process. None of these authors consider the influence of the non-traditional component of the Coriolis force, which we expect to

feature prominently in the dynamics of abyssal currents, as discussed in Chapter 1. Additionally, these authors consider only a northward channel. Stephens and Marshall (2000) and Choboter and Swaters (2004) have studied the almost-westward channel highlighted in Figure 5.1, but only as part of large-scale numerical simulations using realistic bathymetry. A key result of this chapter is that the behaviour of a cross-equatorial abyssal current depends strongly on the orientation of the channel.

The non-traditional shallow water equations derived in Chapter 2 serve as the basis for all of the analysis in this chapter. In Chapter 4 we used these equations to study cross-equatorial flow of a zonally symmetric abyssal current. We discussed the contribution of the non-traditional component of the Coriolis force to the shallow water potential vorticity, and showed that in a zonal equatorial channel this contribution may partially balance the change in sign of the traditional Coriolis parameter, f, as fluid crosses the equator. Equivalently, fluid crossing the equator through a zonal channel requires a smaller change in its zonal angular momentum, as including the complete Coriolis force accounts for changes in the angular momentum with the depth of the fluid. Analytical and numerical solutions for zonally symmetric flow confirm this analysis, and show that a larger cross-equatorial transport is possible when the complete Coriolis force is included. Including dissipation, which allows modification of the potential vorticity, further reduces the relative vorticity that the fluid must acquire to cross the equator. We also considered a one-dimensional cross-equatorial geostrophic adjustment problem in the absence of topography, and showed that more fluid can always adjust further across the equator when the complete Coriolis force is included.

In Chapter 4 we restricted our attention to zonally-symmetric solutions, yet the dynamical consequences of the fluid acquiring a large relative vorticity as it crosses the equator may only be realised when zonal variations are permitted. In this chapter we investigate the cross-equatorial flow of an abyssal current using asymptotic solutions of the shallow water equations in an idealised channel, orientated at an oblique angle to the equator. The structure of this chapter is as follows. In §5.2 we briefly review the $1\frac{1}{2}$-layer shallow water equations with a complete representation of the Coriolis force. In §5.3 we present steady asymptotic solutions for steady flow of a long, narrow current through a flat-bottomed channel with vertical walls, directed at an arbitrary angle to the equator. These solutions provide a useful description of cross-equatorial flow through an abyssal channel, but their validity is dubious in the case of an almost-westward channel like the one shown in Figure 5.1. In §5.4 we modify our asymptotic scaling for the case of an almost-zonal channel. This modified scaling permits an arbitrary channel profile, improving on the idealised square channel of §5.3. Finally, in §5.5 we discuss our results and their implications for the AABW.

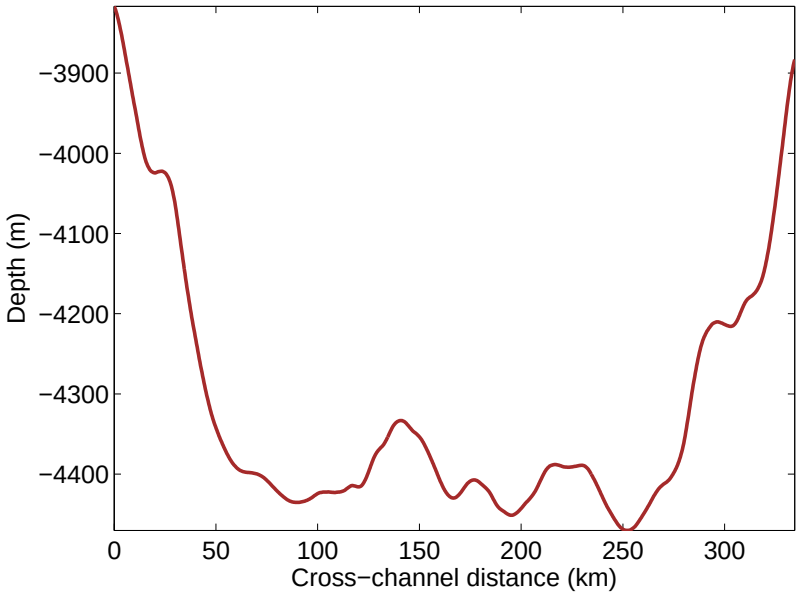

Figure 5.2: Profile of the west-northwesterly bathymetric channel highlighted in Figure 5.1, averaged from northwest to southeast. The average has been taken over the full bathymetric data of Amante and Eakins (2009), rather than over the smoothed bathymetry plotted in Figure 5.1.

5.2 Shallow water equations on a "non-traditional" β-plane

We model the cross-equatorial flow of abyssal currents using the shallow water equations, which describe the behaviour of a homogeneous layer of fluid whose depth is small compared to its breadth. The assumption of columnar motion that underlies the shallow water equations permits a two-dimensional treatment of three-dimensional dynamics, so they may serve as a useful conceptual description of complicated oceanographic phenomena. This has motivated the use of shallow water equations in several previous analytical (Nof, 1990; Nof and Olson, 1993) and numerical (Nof and Borisov, 1998; Stephens and Marshall, 2000; Choboter and Swaters, 2000, 2004) investigations of cross-equatorial currents.

In Figure 5.3 we present a schematic of the "$1\frac{1}{2}$-layer" shallow water equations, which we use to model the flow of an abyssal current. An active lower layer with depth-averaged horizontal velocity $\boldsymbol{u}(x, y, t)$, thickness $h(x, y, t)$ and constant density ρ, flows beneath a quiescent upper layer with a much smaller depth-averaged horizontal velocity $\boldsymbol{u}_0 \ll \boldsymbol{u}$, much greater thickness $h_0 \gg h$, and slightly smaller density $\rho - \Delta\rho$. The upper layer is assumed to react passively to motions of the internal surface $z = \eta(x, y, t)$, such that the lower layer is governed approximately by the one-layer shallow water equations with the gravitational acceleration g replaced by the reduced gravity $g'\Delta\rho/\rho$. The active layer flows directly over a prescribed bottom topography $z = h_b(x, y)$. Throughout this

chapter we refer to the actual measured height of the ocean bed as 'bathymetry', and to the model ocean bed as 'topography'.

The coordinates x and y are defined relative to equatorial β-plane coordinates X, Y, Z, in which X is directed eastwards, Y northwards, and Z upwards. The "non-traditional" equatorial β-plane (Grimshaw, 1975) is characterised by $\Omega_X = 0$, $\Omega_Y = \Omega$ (constant), and $\Omega_Z = \frac{1}{2}\beta Y$ with parameter $\beta = 2\Omega/R_E$. Dellar (2011) has derived the non-traditional equatorial β-plane equations by making approximations in Hamilton's variational principle that describes ideal fluid motions in spherical geometry. This derivation from Hamilton's principle ensures that the approximate equations inherit the expected conservation laws for energy, angular momentum, and potential vorticity.

We will use the $1\frac{1}{2}$-layer shallow water equations on the non-traditional equatorial β-plane to describe the flow of an abyssal current through an obliquely-oriented channel, so it is useful to allow for arbitrary orientations of the horizontal axes. We define θ as the positive angle from North to the y-axis, so $\theta = 0$ corresponds to conventional GFD axes. Throughout this chapter we choose $\theta \in [-\pi/2, \pi/2]$, so the x-axis points across the channel and the y-axis points along the channel.

At the core of shallow water theory is the assumption that the fluid layer moves in columns aligned with the locally vertical axis (e.g Pedlosky, 1987), justified by the assumption that the vertical lengthscale is small compared to the corresponding horizontal length scale. The pressure is then predominantly hydrostatic, and the horizontal pressure gradient predominantly independent of depth. We say "predominantly" because we relax both these assumptions to derive the non-traditional shallow water equations given below. The Taylor–Proudman theorem states that at low Rossby number, an inviscid fluid should form columns aligned with the axis of rotation. This axis coincides with the locally vertical axis under the traditional approximation. If the complete Coriolis force is accounted for, the axis of rotation only coincides with the locally vertical axis at the poles, so away from the poles there is a discrepancy between the alignments of the columns as described by shallow water theory and by the Taylor-Proudman theorem. However, shallow water theory only requires that the layer depth be much smaller than the horizontal lengthscale, which is typically smaller than the planetary radius, so there is geometrically little difference between the two alignments over most of the Earth's surface. The exception is close to the equator, where the axis of rotation is almost perpendicular to the locally vertical axis. We will assume that the fluid moves in columns aligned with the locally vertical axis, even at the equator, as this is consistent with the assumption of a small aspect ratio, and because this description compares more favourably with measurements of the AABW (*e.g.* Hall et al., 1997). Additionally, previous studies of abyssal equator crossing currents (*e.g.* Nof and Borisov, 1998; Choboter and Swaters, 2004) suggest that inertia is an essential element in this process, so one would not expect the fluid to move in Taylor

columns.

Dellar and Salmon (2005) derived a set of shallow water equations that include a complete representation of the Coriolis force, and in Chapter 2 we extended this derivation to the case of arbitrarily many fluid layers. These non-traditional equations may be obtained by averaging the three-dimensional Euler equations over each layer, or by averaging the action in Hamilton's variational principle formulation of mechanics. Both derivations rely on the assumptions of a small aspect ratio, and of columnar motion aligned with the locally vertical axis, as detailed above. The $1\frac{1}{2}$-layer shallow water equations on the non-traditional equatorial β-plane may be written as

$$\frac{\partial \boldsymbol{u}}{\partial t} + (\boldsymbol{u}\cdot\nabla)\boldsymbol{u} + \left(\beta Y - 2\boldsymbol{\Omega}_H\cdot\nabla\left(h_b + \tfrac{1}{2}h\right)\right)\hat{\boldsymbol{z}}\times\boldsymbol{u} + \boldsymbol{\Omega}_H\times\hat{\boldsymbol{z}}\frac{\partial h}{\partial t} + \nabla\left(g'(h_b+h) + h(\Omega_x v - \Omega_y u)\right) = 0, \tag{5.1}$$

$$\frac{\partial h}{\partial t} + \nabla\cdot(h\boldsymbol{u}) = 0. \tag{5.2}$$

Here $\nabla \equiv (\partial/\partial x, \partial/\partial y)$ is the two-dimensional gradient operator, $\boldsymbol{\Omega}_H = (\Omega_x, \Omega_y)$ is the horizontal rotation vector, g' is the reduced gravity, and $\hat{\boldsymbol{z}}$ is the unit vector in the z-direction. Under arbitrary orientation of the horizontal axes, the vertical component of the rotation vector on an equatorial β-plane is $\Omega_z = \frac{1}{2}\beta Y$, where $Y = y\cos\theta + x\sin\theta$ is the meridional distance from the equator. Making the traditional approximation corresponds to discarding all terms proportional to Ω_x or Ω_y. The non-traditional component of the Coriolis force connects vertical and zonal velocities in the full three-dimensional equations. The $\boldsymbol{\Omega}_H\times\hat{\boldsymbol{z}}\,\partial_t h$ term corresponds to the non-traditional zonal acceleration due to vertical velocity, and the non-traditional contribution to the pressure gradient corresponds to non-traditional vertical acceleration due to zonal velocity. The inclusion of this additional term in the vertical momentum equation defines what White and Bromley (1995) call quasi-hydrostatic balance, the non-traditional extension of the hydrostatic balance between the pressure gradient and buoyancy.

The $-2\boldsymbol{\Omega}_H\cdot\nabla\left(h_b + \frac{1}{2}h\right)$ term in (5.1), which appears as a correction to the traditional planetary vorticity βY, is arguably the most important. It corresponds directly to a modification of the materially conserved potential vorticity by the non-traditional component of the Coriolis force,

$$\frac{\mathrm{D}q}{\mathrm{D}t} = 0, \quad q = \frac{1}{h}\left(\beta Y - 2\boldsymbol{\Omega}_H\cdot\nabla\left(h_b + \tfrac{1}{2}h\right) + \frac{\partial v}{\partial x} - \frac{\partial u}{\partial y}\right). \tag{5.3}$$

Here the traditional planetary vorticity is replaced by the complete planetary vorticity,

$$\beta Y - 2\boldsymbol{\Omega}_H\cdot\nabla(h_b + \tfrac{1}{2}h) \approx 2\boldsymbol{\Omega}\cdot\nabla\left(z - \overline{z}\right), \tag{5.4}$$

where $\overline{z}(x,y,t) = h_b + \frac{1}{2}h$ is the mid-surface of the layer, or the layer-average of z. The complete planetary vorticity is thus the component of $2\boldsymbol{\Omega}$ normal to the mid-surface. This is more easily

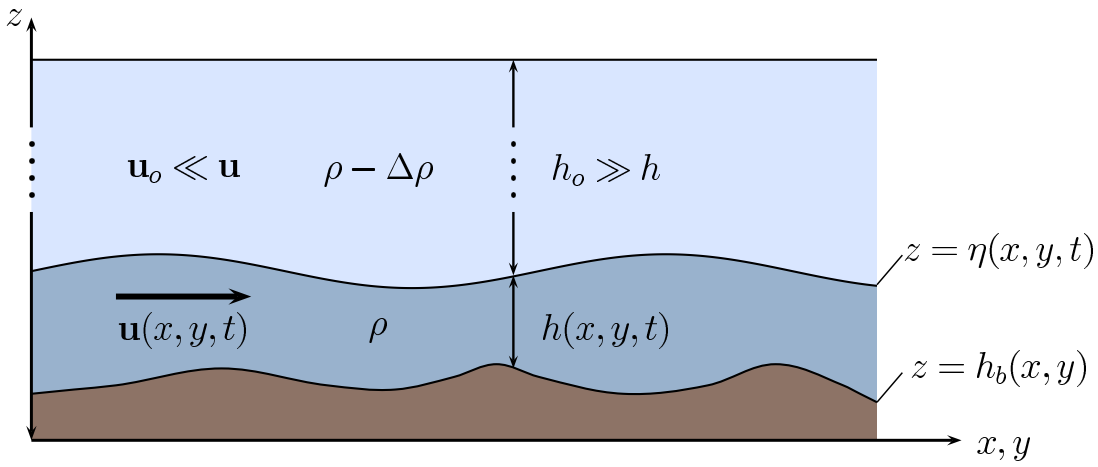

Figure 5.3: A schematic of the $1\frac{1}{2}$-layer shallow water model, in which an active fluid layer flows beneath a deep, quiescent upper layer.

understood in terms of angular momentum, which is related to the potential vorticity via $q = (\nabla \times \tilde{\boldsymbol{u}})/h$, with

$$\tilde{u} = u + 2\Omega R\cos\theta, \quad \tilde{v} = v - 2\Omega R\sin\theta, \tag{5.5}$$

where R is the perpendicular distance of the fluid from the axis of rotation on the non-traditional equatorial β-plane. Using $\beta = 2\Omega/R_E$, this may be written as

$$R = \overline{z} + R_E\left(1 - \tfrac{1}{2}\left(\frac{Y}{R_E}\right)^2\right) \approx (R_E + \overline{z}\,)\cos\phi. \tag{5.6}$$

where $\phi = Y/R_E$ is the latitude. The rightmost expression in (5.6) is the more intuitive geometric perpendicular distance from the axis of rotation. and the left hand side of (5.6) approximates this to $\mathcal{O}(\phi^4, \phi^2\,\overline{z}/R_E) \equiv \mathcal{O}(\phi^4, \phi^3\,\overline{z}/Y)$, where $\overline{z} \ll Y \ll R_E$ for typical values of $\overline{z}$ and Y. Thus the approximation is consistent in the distinguished limit $\overline{z}/Y \sim Y/R_E$, as shown formally by Dellar (2011). Making the traditional approximation corresponds to neglecting the dependence of R on $\overline{z}$, thereby neglecting contributions to the angular momentum due to changes in the average depth of the fluid, and hence changes in the average distance from the rotation axis of fluid parcels within a column.

As discussed in §5.1, inviscid fluid crossing the equator must conserve the potential vorticity given in equation (5.3). Typically the relative vorticity $\zeta = \partial_x v - \partial_y u$ is smaller in magnitude than the vertical component of the planetary vorticity βY, so as βY changes sign over the equator, the fluid can only conserve potential vorticity by acquiring an unusually large relative vorticity ζ. This prevents fluid penetrating far into the opposite hemisphere (Killworth, 1991) unless dissipative processes are present to modify the potential vorticity (Edwards and Pedlosky, 1998). The non-

traditional contribution to the potential vorticity may partially balance the βY term, and so may facilitate cross-equatorial flow. A cross-equatorial current would require almost no change in ζ if,

$$2\boldsymbol{\Omega} \cdot \nabla (z - \overline{z}) = 0 \iff \overline{z} = \overline{z}_0 + \frac{Y^2}{2R_E}, \tag{5.7}$$

i.e. if the mid-surface of the layer were everywhere parallel to the rotation vector. This is equivalent to requiring that R be everywhere constant in (5.6).

In Chapter 4 we showed that the shape of the equatorial channel shown in Figure 5.1 is remarkably similar to the meridional parabola described by the right hand side of (5.7), and concluded that the non-traditional component of the Coriolis force should facilitate the flow of the AABW across this channel. We showed that including the complete Coriolis force increases the transport of a one-dimensional current crossing a steep-sided zonally-symmetric equatorial channel, even when potential vorticity modification is introduced via bottom friction. However, this analysis omits zonal variations in both the model topography and the dynamics, which is crucial for a complete description of any oceanographic phenomenon. In this chapter we redress this shortcoming by considering two-dimensional shallow water solutions for an abyssal current traversing an obliquely-oriented cross-equatorial channel.

5.3 Flow through an equatorial channel with vertical walls

In this section we obtain asymptotic solutions for steady flow of a current, represented by the $1\frac{1}{2}$-layer shallow water equations, through a channel that crosses the equator. We approximate the bathymetry shown in Figure 5.2 as a channel with parallel vertical walls and a flat bottom, directed at an angle θ to the equator. A schematic of this channel is shown in Figure 5.4. The method of solution is similar to that of Nof and Olson (1993) for a meridional channel, but it is complicated by the inclusion of the complete Coriolis force and the arbitrary orientation of the channel. We show that the current tends to cross the channel as it crosses the equator, and that the along-channel transport is larger when the complete Coriolis force is accounted for.

5.3.1 Governing equations

As illustrated in Figure 5.4, we align the y-axis along the channel and the x-axis across the channel, such that the equator is described by the line $y\cos\theta + x\sin\theta = 0$. Without loss of generality we position the walls of the channel at $x = \pm W$, and let the current enter from the south at $y = -y_u$, the prescribed upstream position. Here it is bounded to the west by the wall of the channel at $x = -W$, and has an eastern front described by $x = R(y)$. We need only prescribe the upstream

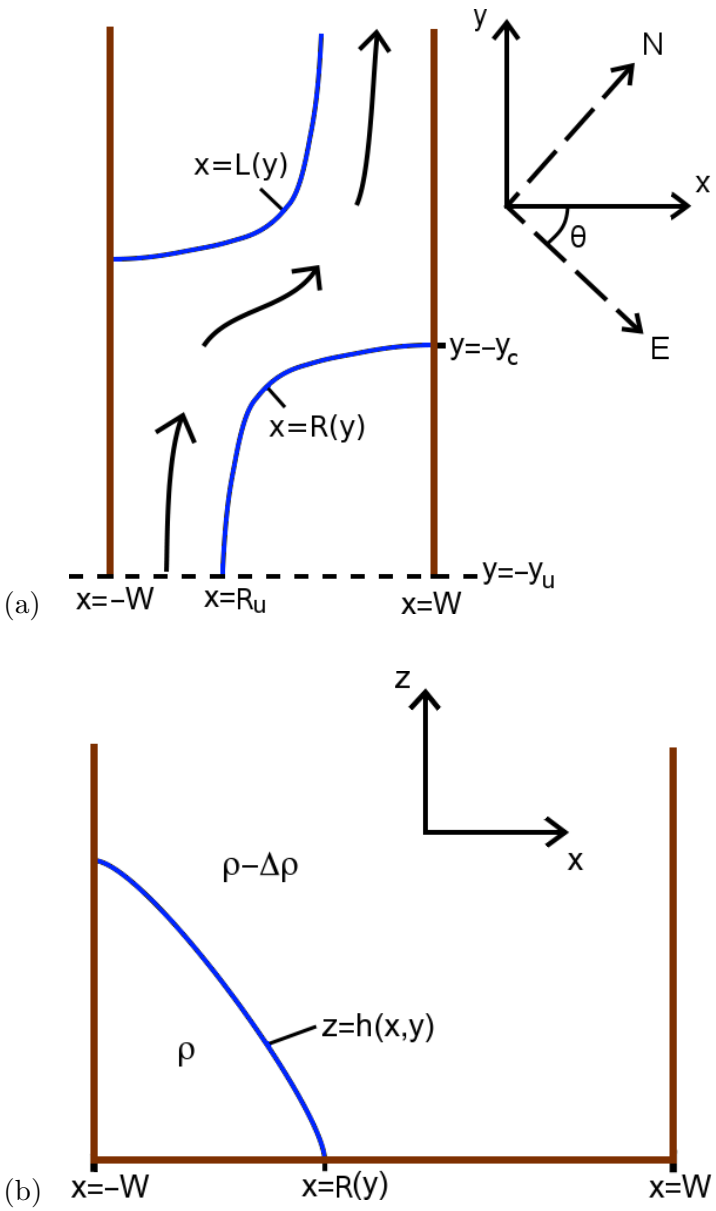

Figure 5.4: Schematic of the asymptotic channel-crossing solution presented in §5.3, viewed (a) from above, and (b) along the channel. In a typical solution the current enters at the southern edge leaning up against the western wall, crosses the channel as it crosses the equator, and exits at the northern edge leaning against the eastern wall.

width of the current, $R(-y_u) = R_u$, and the upstream depth at the wall, $h(-W, -y_u) = H_u$, to define the solution completely, as we will show in §5.3.3. In the northern hemisphere we make the ansatz that the current has a western front at $x = L(y)$, and is bounded to the east by the wall at $x = W$. This is motivated by the form of the solution in $y < 0$, which crosses the channel as $y \to 0$.

We seek a steady solution of the $1\frac{1}{2}$-layer shallow water equations, (5.1) and (5.2), with flat

bottom topography, $h_b \equiv 0$. This allows us to rewrite the governing equations in the form

$$hq\,\hat{\boldsymbol{z}} \times \boldsymbol{u} + \nabla\Phi = 0, \tag{5.8a}$$

$$\nabla \cdot (h\boldsymbol{u}) = 0, \tag{5.8b}$$

where q is the potential vorticity,

$$q = \frac{1}{h}\left(\beta(y\cos\theta + x\sin\theta) - \boldsymbol{\Omega}\cdot\nabla h + \frac{\partial v}{\partial x} - \frac{\partial u}{\partial y}\right), \tag{5.9}$$

and Φ is defined as

$$\Phi = \tfrac{1}{2}u^2 + \tfrac{1}{2}v^2 + g'h + h(\Omega_x v - \Omega_y u). \tag{5.10}$$

We seek a solution of the form shown in Figure 5.4, requiring that there be no flow normal to the boundary $x = -W$, and that the fluid depth vanishes at the front $x = R(y)$,

$$h = 0 \ \text{ at } \ x = R(y), \qquad u = 0 \ \text{ at } \ x = -W. \tag{5.11}$$

At the upstream edge, $y = -y_u$, we prescribe the position of the front and the depth of the fluid at the wall,

$$R = R_u \ \text{ at } \ y = -y_u, \qquad h = H_u \ \text{ at } \ x = -W,\ y = -y_u. \tag{5.12}$$

As we will show in §5.3.3, the boundary conditions (5.11) and the upstream conditions (5.12) completely define the asymptotic solution.

The governing equations (5.8a)–(5.8b) and boundary conditions (5.11)–(5.12) are difficult to solve in their present form. However, we can make analytical progress by assuming that the potential vorticity is zero throughout the fluid. Hua et al. (1997) showed that fluid is subject to inertial instability if its potential vorticity and vertical planetary vorticity have opposite signs, $QY < 0$, where Q is the three-dimensional potential vorticity with complete Coriolis force and Y is the meridional coordinate. Thus the potential vorticity tends to homogenise to zero within around 3° of the equator. The measurements of Firing (1987) corroborate this finding when the complete Coriolis force is accounted for. It is therefore quite plausible that an abyssal cross-equatorial current should approach a state of zero potential vorticity close to the equator. Setting $q = 0$ immediately yields

$$\beta(y\cos\theta + x\sin\theta) - \Omega\left(\frac{\partial h}{\partial x}\sin\theta + \frac{\partial h}{\partial y}\cos\theta\right) + \frac{\partial v}{\partial x} - \frac{\partial u}{\partial y} = 0, \tag{5.13}$$

and substituting $q = 0$ into (5.8a) leads to a Bernoulli-type equation

$$\nabla\left(\tfrac{1}{2}u^2 + \tfrac{1}{2}v^2 + g'h + \Omega h\,(v\sin\theta - u\cos\theta)\right) = 0. \tag{5.14}$$

Finally we rewrite the mass conservation equation (5.8b) as

$$\frac{\partial}{\partial x}(hu) + \frac{\partial}{\partial y}(hv) = 0, \tag{5.15}$$

such that (5.13)–(5.15) forms our set of exact two-dimensional governing equations.

5.3.2 Asymptotic expansion

We solve (5.13)–(5.15) via an asymptotic expansion in a small parameter ε, to be defined. We first define the fundamental velocity and length scales of the problem as the internal gravity wave speed and internal radius of deformation, respectively,

$$c = \sqrt{g' H_u}, \quad R_d = \sqrt{\frac{c}{\beta}}. \tag{5.16}$$

Using the equatorial planetary radius, $R_E \approx 6400\,\mathrm{km}$, and Earth's rate of rotation $\Omega \approx 7.3 \times 10^{-5}\,\mathrm{rad\,s^{-1}}$, we obtain $\beta \approx 2.3 \times 10^{-11}\,\mathrm{rad\,m^{-1}\,s^{-1}}$. Then using typical values of $g' = 10^{-3}\,\mathrm{m\,s^{-2}}$ and $H_u = 500\,\mathrm{m}$, we obtain $c \approx 0.71\,\mathrm{m\,s^{-1}}$ and $R_d \approx 180\,\mathrm{km}$. We assume that the appropriate dynamical lengthscale in the y-direction is the upstream distance y_u, and that this is much larger than R_d. We define the small parameter ε as

$$\varepsilon = \left(\frac{R_d}{y_u}\right)^2 \ll 1. \tag{5.17}$$

The channel indicated by the dashed lines in Figure 5.1 has an approximate total length of 1130 km, and lies more south of the equator than north, so here $y_u \approx 980\,\mathrm{km}$ and $\varepsilon \approx 0.03$. However, the plotted channel may not be the optimal representation of the bathymetric channel, so perhaps a less conservative estimate for y_u is the half-length of the channel, $y_u \approx 560\,\mathrm{km}$, which yields $\varepsilon \approx 0.1$. In the analysis below we neglect $\mathcal{O}(\varepsilon)$ contributions to equations (5.13) and (5.14), even though these contributions may only be an order of magnitude smaller than the leading-order contributions in the AABW. However, we will show in §5.3.8 that the solution does not change dramatically when we include $\mathcal{O}(\varepsilon)$ terms.

Scaling the y-coordinate by $y_u = \varepsilon^{-1/2} R_d$ assumes slow variations of the solution in the y-direction. We simultaneously assume rapid variations in the x-direction, scaling the x-coordinate by $\varepsilon^{1/2} R_d = R_d^2/y_u$. We scale the along-channel velocity by the internal gravity wave speed c, so we must scale the across-channel velocity by εc to ensure that the mass conservation equation (5.15) is of balanced order in ε. Finally, we scale h by the upstream depth at the wall, H_u. Our complete non-dimensionalisation may be written as

$$x = \varepsilon^{1/2} R_d\,\hat{x}, \quad y = \varepsilon^{-1/2} R_d\,\hat{y}, \quad u = \varepsilon c \hat{u}, \quad v = c\hat{v}, \quad h = H_u\,\hat{h}, \tag{5.18}$$

where the hat $\hat{}$ denotes an $\mathcal{O}(1)$ dimensionless variable. These scales describes a flow that varies slowly along the channel and rapidly across the channel, and which has very small cross-channel velocities.

Substituting (5.18) into the zero-potential vorticity equation (5.13) yields

$$\hat{y}\cos\theta + \varepsilon\,\hat{x}\sin\theta - \delta\frac{\partial \hat{h}}{\partial \hat{x}}\sin\theta - \varepsilon\,\delta\frac{\partial \hat{h}}{\partial \hat{y}}\cos\theta + \frac{\partial \hat{v}}{\partial \hat{x}} - \varepsilon^2\frac{\partial \hat{u}}{\partial \hat{y}} = 0, \tag{5.19}$$

and the Bernoulli equation (5.14) becomes

$$\hat{\nabla}\left(\tfrac{1}{2}\varepsilon^2\hat{u}^2+\tfrac{1}{2}\hat{v}^2+\hat{h}+\delta\,\hat{h}\,\hat{v}\sin\theta-\varepsilon\,\delta\,\hat{h}\,\hat{u}\cos\theta\right)=0, \tag{5.20}$$

where

$$\delta=\Omega\sqrt{\frac{H_u}{g'}} \tag{5.21}$$

measures the strength of non-traditional effects. The parameter δ is the ratio of the non-traditional velocity scale ΩH, the change in zonal velocity experienced by a fluid parcel that rises a distance H while conserving angular momentum (White and Bromley, 1995), to the internal wave speed c. For the approximate values of Ω, H_u and g' listed above, $\delta\approx 0.05$ is actually comparable to ε, but we will see that this measure underestimates its effect on the solutions in §5.3.9. We may formally pose an asymptotic expansion of (5.19) and (5.20) in ε, of the form $\hat{h}=\hat{h}^{(0)}+\varepsilon\hat{h}^{(1)}+\cdots$ etc. However, in this section we will consider only the leading order solution, which is equivalent to simply neglecting all terms of $\mathcal{O}(\varepsilon)$ in (5.19) and (5.20).

We will henceforth drop the hat $\hat{}$ notation for dimensionless quantities, and instead use a star * to denote dimensional quantities. At leading order in ε, the governing equations (5.19), (5.20), and (5.15) reduce to

$$y\cos\theta-\delta\frac{\partial h}{\partial x}\sin\theta+\frac{\partial v}{\partial x}=0, \tag{5.22a}$$

$$\nabla\left(\tfrac{1}{2}v^2+h+\delta\,h\,v\sin\theta\right)=0, \tag{5.22b}$$

$$\frac{\partial}{\partial x}(hu)+\frac{\partial}{\partial y}(hv)=0, \tag{5.22c}$$

subject to the following dimensionless boundary conditions,

$$u=0 \quad \text{at} \quad x=-W, \tag{5.23a}$$

$$h=0 \quad \text{at} \quad x=R(y), \tag{5.23b}$$

$$h=1 \quad \text{at} \quad x=-W,\ y=-1, \tag{5.23c}$$

$$R=R_u \quad \text{at} \quad y=-1, \tag{5.23d}$$

where $W=W^\star/\varepsilon R_d$ and $R=R^\star/\varepsilon R_d$ are the dimensionless positions of the wall and the front respectively.

5.3.3 Solution in the southern hemisphere

The across-channel velocity u appears in the governing equations only in (5.22c). We may therefore eliminate u by integrating (5.22c) from $x=-W$ to $x=R(y)$ and simplifying using (5.23a) and

(5.23b), which yields

$$\int_{-W}^{R(y)} hv \, \mathrm{d}x = T, \tag{5.24}$$

where T is the constant dimensionless along-channel transport. We will solve (5.22a) and (5.22b) for h and v, subject to (5.24). In principle, u may then be calculated, once h and v have been determined, by integrating (5.22c) with respect to x,

$$u(x,y) = -\frac{1}{h(x,y)} \frac{\partial}{\partial y} \int_{-W}^{x} h\left(x',y\right)\, v\left(x',y\right)\, \mathrm{d}x'. \tag{5.25}$$

Equation (5.22a) is an exact derivative with respect to x, and (5.22b) is an exact gradient, so we integrate to obtain

$$xy\cos\theta - \delta\, h \sin\theta + v = A(y), \tag{5.26a}$$

$$\tfrac{1}{2}v^2 + h + \delta\, h\, v \sin\theta = B, \tag{5.26b}$$

where A is an arbitrary function of y, and B is the Bernoulli constant. Equations (5.26a) and (5.26b) form an algebraic system that completely determine h and v in terms of B and $A(y)$. We first find B by substituting the upstream conditions (5.23c) and (5.23d) into the algebraic equations (5.26a) and (5.26b). This yields four algebraic equations for four unknowns, $v(-W,-1)$, $v(R_u,-1)$, $A(-1)$ and B, which may be solved to obtain

$$B = \tfrac{1}{2}\left[\frac{1 + \frac{1}{2}x_u^2\cos^2\theta + \frac{3}{2}\delta^2\sin^2\theta - \delta x_u \sin(2\theta)}{x_u\cos\theta - 2\delta\sin\theta}\right]^2, \tag{5.27}$$

where $x_u = R_u + W$ is the upstream width of the current. With B known, $A(y)$ may be determined by substituting the boundary condition (5.23b) that holds at the front $x = R(y)$ into (5.26a) and (5.26b), and eliminating $v|_{x=R}$,

$$A(y) = Ry\cos\theta + \sqrt{2B}. \tag{5.28}$$

The positive root for v has been chosen to ensure northward flow.

We may now determine v and h as functions of x, y and $R(y)$ by substituting (5.27) and (5.28) into (5.26a) and (5.26b), and then solving algebraically. Under the traditional approximation this is straightforward and leads to

$$v_{\mathrm{trad}} = \sqrt{2B} - (x-R)y\cos\theta, \tag{5.29a}$$

$$h_{\mathrm{trad}} = \sqrt{2B}\,(x-R)y\cos\theta - \tfrac{1}{2}(x-R)^2y^2\cos^2\theta. \tag{5.29b}$$

We omit the corresponding expressions when the complete Coriolis force is included, as they are considerably more complicated and difficult to interpret directly. To complete the solution in $y < 0$,

we require the shape of the eastern front $x = R(y)$. We first calculate the constant transport T by integrating (5.24) at $y = -1$,

$$T = \int_{-W}^{R_u} h(x,-1)\, v(x,-1)\, \mathrm{d}x, \tag{5.30}$$

where $h(x,-1)$ and $v(x,-1)$ are determined exactly by substituting $R = R_u$ and $y = -1$ into (5.26a) and (5.26b). In principle we may then find $R(y)$ for arbitrary y by substituting the known expressions for $v(x,y,R(y))$, $h(x,y,R(y))$, and T into (5.24), and integrating with respect to x. However, it is typically more practical simply to use (5.24) to compute R for any required value of y. A typical solution is presented in Figure 5.5.

5.3.4 Solution in the northern hemisphere

As the current approaches the equator, its width, if unrestricted by the opposing wall at $x = W$, would approach infinity. This is because the depth h approaches 0 as $y \to 0$. In the traditional solution (5.29b) it is straightforward to show that $h_{\mathrm{trad}} \to 0$ as $y \to 0$ unless $R(y) \to \infty$ as $y \to 0$. More generally, taking the limit $y \to 0$ in (5.26a), (5.26b), and (5.28), and eliminating v and A yields

$$h\left(1 + 2\sqrt{2B}\,\delta\sin\theta + \tfrac{3}{2}\delta^2 h\sin^2\theta\right) \to 0 \quad \text{as} \quad y \to 0, \tag{5.31}$$

assuming $y\,R(y) \to 0$ as $y \to 0$. Thus either $h \to 0$ or

$$h \to -\frac{1 + 2\sqrt{2B}\,\delta\sin\theta}{\frac{3}{2}\delta\sin^2\theta} \tag{5.32}$$

as $y \to 0$. We require $h > 0$ for a physical solution, so the limit (5.32) is only valid for $\theta < 0$, and only then if $\sqrt{2B} > 1/2\delta$. Substituting (5.23b) into (5.26b) yields $v|_{x=R} = \sqrt{2B}$, so condition (5.32) is a valid limit for h as $y \to 0$ only if

$$v|_{x=R} > \frac{1}{2\delta}. \tag{5.33}$$

Typically $\delta \ll 1$, so this condition states that the along-channel velocity at the front must be much larger than the gravity wave speed. We therefore discount solutions corresponding to the limit (5.32) as unphysical.

Thus the only physical limit in (5.31) as $y \to 0$ is $h \to 0$. In order to conserve mass, the northward transport T must remain constant as $y \to 0$ in (5.24). The velocity at the front is $v|_{x=R} = \sqrt{2B}$, which excludes the possibility of $v \to \infty$ as $y \to 0$, so instead the width of the current must approach infinity, $R(y) \to \infty$ as $y \to 0$. From this behaviour Nof (1990) concluded that, in the absence of an opposing channel wall, a northward-flowing western boundary current should be blocked by the equator and turn eastward. In our problem the flow is confined by an opposing wall at $x = W$, and so the front must make contact with the wall at some point $y = -y_c < 0$, where $R(-y_c) = W$. This

is illustrated in Figure 5.4, and is also visible in the specimen solution presented in Figure 5.5. At $y = -y_c$ the solution varies rapidly with y, so the assumptions underlying our asymptotic solution are no longer valid. Following Nof and Olson (1993), we consider the solution only in the range $-1 \le y < -y_c$, and connect the flow in the southern hemisphere $y < 0$ to the northern hemisphere $y > 0$ by requiring that the transport T and the Bernoulli energy B are conserved across $y = 0$. Despite the breakdown of the asymptotic expansion close to $y = 0$, conservation of transport T and Bernoulli energy B must be preserved because they are a direct result of the exact mass conservation equation (5.8b) and the assumption of zero potential vorticity in (5.8a).

We now show that the solution in the northern hemisphere ($y > 0$) may be chosen to be symmetric to the solution in the southern hemisphere ($y < 0$) under a rotation of π radians about the origin. We denote quantities associated with the northern hemisphere using a prime $'$, so the dependent variables are $v'(x', y')$, $h'(x', y')$, and the current has a western front where

$$h' = 0 \quad \text{at} \quad x' = L(y'). \tag{5.34}$$

The leading-order governing equations, (5.26a) and (5.26b), may be rewritten for the northern hemisphere as

$$(x' - L(y'))\, y' \cos\theta - \delta\, h' \sin\theta + v' = \sqrt{2B'}, \tag{5.35a}$$

$$\tfrac{1}{2} v'^2 + h' + \delta\, h'\, v' \sin\theta = B', \tag{5.35b}$$

where we have used (5.34) to determine the function $A'(y') = \sqrt{2B'} + L(y')\, y' \cos\theta$, analogous to $A(y)$ in (5.26a). Let $v(x, y)$, $h(x, y)$, $R(y)$, $y < 0$ describe the solution in the southern hemisphere, satisfying (5.26a), (5.26b), (5.23b)–(5.23d) and (5.24). Now let $x = -x'$ and $y = -y' < 0$ and suppose that the northern solution is related to the southern solution via $v'(x', y') = v(x, y)$, $h'(x', y') = h(x, y)$ and $L(y') = -R(y)$. Substituting these definitions into (5.35a) and (5.35b) yields

$$(x - R(y))\, y \cos\theta - \delta\, h(x, y) \sin\theta + v(x, y) = \sqrt{2B'}, \tag{5.36a}$$

$$\tfrac{1}{2} v^2(x, y) + h(x, y) + \delta\, h(x, y)\, v(x, y) \sin\theta = B'. \tag{5.36b}$$

Comparison of (5.35a) and (5.35b) with (5.26a) and (5.26b) shows that these equations are satisfied only if $B' = B$. The northern flow must also conserve total along-channel transport T', where

$$T' = \int_{L(y')}^{W} h'v' \,\mathrm{d}x' = -\int_{-L(y')}^{-W} h'v' \,\mathrm{d}(-x') = \int_{-W}^{R(y)} hv \,\mathrm{d}x = T. \tag{5.37}$$

Thus the symmetric solution guarantees conservation of B and T across $y = 0$. The symmetry of the problem allows us to analyse all possible solutions by considering only the flow in $y < 0$.

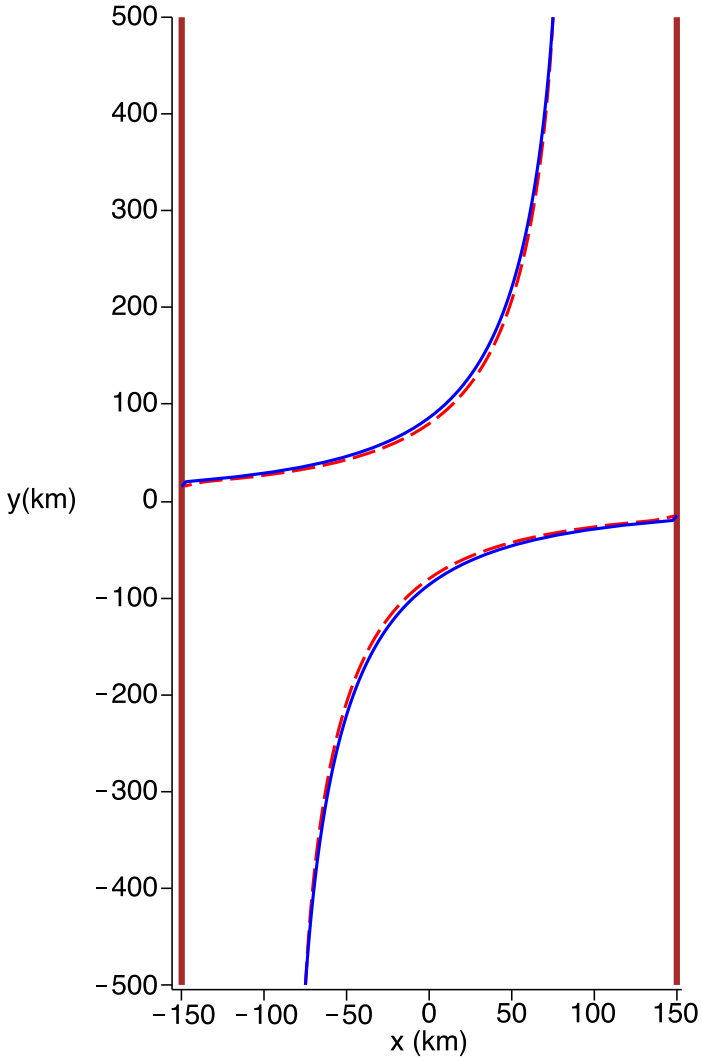

Figure 5.5: Plot of a typical solution for cross-equatorial flow in a square channel. We show the fronts at the eastern ($x = R(y)$) and western ($x = L(y)$) edges of the current, under the traditional approximation (dashed line) and with the complete Coriolis force (solid line). The thick solid lines show the edges of the channel. We have chosen the dimensions ($y_u = 500\,\mathrm{km}$, $W^\star = 150\,\mathrm{km}$, $H_u = 500\,\mathrm{m}$) to match approximately the channel shown in Figure 5.1, though the orientation is less extreme, $\theta = \pi/4$. We have used earth-like values of $\Omega = 7.3 \times 10^{-5}\,\mathrm{rad\,s^{-1}}$ and $R = 6400\,\mathrm{km}$, with a reduced gravity of $g' = 10^{-3}\,\mathrm{m\,s^{-2}}$, corresponding to $\Delta\rho/\rho = 10^{-4}$.

5.3.5 Condition for unidirectional flow

The solution described in §5.3.3 is only physically plausible if the flow of the current is unidirectional, *i.e.* if $v > 0$ everywhere. This is typically the most restrictive constraint on the solution. We will first discuss the no-backflow condition under the traditional approximation ($\delta = 0$), and then generalise to the more complicated non-traditional case ($\delta \neq 0$).

The along-channel velocity is positive everywhere if

$$v_{\text{trad}}(x,y) = \sqrt{2B} + (R(y) - x)\, y \cos\theta > 0, \tag{5.38}$$

for all $-1 \leq y < -y_c$ and $-W \leq x \leq R(y)$. For a fixed value of y, the minimum of v_{trad} lies at $x = -W$, so in fact (5.38) may be simplified to

$$v_{\text{trad}}(-W,y) = \sqrt{2B} + (R(y) + W)\, y \cos\theta > 0, \tag{5.39}$$

for all $-1 \leq y < -y_c$. It may be shown, using (5.29a), (5.29b) and (5.24), that

$$v_{\text{trad}}(-W,y) \to -\sqrt{2B} \quad \text{as} \quad y \to 0. \tag{5.40}$$

so if y_c is sufficiently close to 0, there will be backflow at the western edge of the channel at $y = -y_c$. However, y_c only approaches 0 in the limit of very large channel width ($W \to \infty$), which violates the asymptotic assumption of a long narrow channel. Additionally, the assumption of a solution that varies slowly with y is no longer valid close to $y = y_c$, so we may attribute any backflow that arises here to the breakdown of the asymptotic ordering. Typically the minimum of $v_{\text{trad}}(-W,y)$ lies at $y = -1$, in which case the no-backflow condition (5.39) becomes

$$v_{\text{trad}}(-W,-1) = \sqrt{2B} - x_u \cos\theta > 0 \quad \text{or} \quad x_u < \frac{\sqrt{2}}{\cos\theta}. \tag{5.41}$$

Thus there is no backflow as long as the upstream width x_u is not too large. This requirement is most restrictive at $\theta = 0$, corresponding to a northward channel, and least restrictive as $\theta \to \pm\pi/2$, corresponding to an almost-eastward or almost-westward channel. Even if the minimum of v_{trad} does not lie at $(-W,-1)$, condition (5.41) must still be satisfied to avoid backflow at the upstream edge.

In the non-traditional case ($\delta \neq 0$), we may obtain an equation for v as a function of x, y and $R(y)$ by eliminating A and h between (5.26a), (5.26b) and (5.28). It may be shown that $v(x,y) > 0$ if

$$\sqrt{2B} + (R(y) - x) y \cos\theta + B\delta \sin\theta > 0. \tag{5.42}$$

The left hand side of (5.42) is not an expression for v in general, but does reduce to v_{trad} if $\delta = 0$. Again, for fixed y the minimum of (5.42) lies at $x = -W$, so there is no backflow in the solution if

$$\sqrt{2B} + (R(y) + W) y \cos\theta + B\delta \sin\theta > 0, \tag{5.43}$$

for all $-1 \leq y < -y_c$. The term proportional to δ in (5.43) complicates the analysis of the backflow condition. Even at $y = -1$, where $R = R_u$, (5.43) and (5.27) together yield a quartic polynomial in x_u that must be solved to obtain a condition analogous to (5.41). This means that for each solution considered in this section, we must check that (5.43) is satisfied via direct computation.

5.3.6 Dependence on x_u, θ, and δ

Under our asymptotic scaling (5.18), the governing equations and boundary conditions depend on only four dimensionless parameters: δ, θ, R_u and W. In fact, the solution does not depend on R_u and W independently, but rather on the upstream width of the current, $x_u = R_u + W$. In the following we fix δ and θ, and consider only the dependence of the solution on x_u.

To see this, consider the boundary condition (5.23b) at the eastern front front of the current. Substituting this into (5.26a) and (5.26b) yields

$$v|_{x=R(y)} = \sqrt{2B} = \frac{1 + \frac{1}{2}x_u^2 \cos^2\theta + \frac{3}{2}\delta^2 \sin^2\theta - \delta x_u \sin(2\theta)}{x_u \cos\theta - 2\delta \sin\theta}, \tag{5.44}$$

for all $-1 \leq y < -y_c$. Thus, both $v|_{x=R}$ and $h|_{x=R}$ depend only on δ, θ and x_u. We now rewrite equations (5.26a) and (5.26b), which determine v and h as functions of x, y and $R(y)$, in the form

$$(x - R)y\cos\theta - \delta\, h \sin\theta + v = \sqrt{2B}, \tag{5.45a}$$

$$\tfrac{1}{2}v^2 + h + \delta\, h\, v \sin\theta = B, \tag{5.45b}$$

where we have used (5.28) to eliminate $A(y)$. This rewriting shows that v and h depend on x only through the distance $(x - R)$ from the front. We may therefore write the solution as a function of $x - R$ and y, so $v = v(x - R, y)$ and $h = h(x - R, y)$. We may calculate the along-channel transport T by solving (5.45a) and (5.45b) for h and v at $y = -1$. Changing the integration variable in (5.30) from x to $\xi = x - R_u$ yields

$$T = \int_{-W}^{R_u} h(x, -1)\, v(x, -1)\, \mathrm{d}x = \int_{-x_u}^{0} h(\xi, -1)\, v(\xi, -1)\, \mathrm{d}\xi. \tag{5.46}$$

From (5.27) we know that $B = B(x_u, \theta, \delta)$, so (5.45a) and (5.45b) show that v and h also depend only on x_u, θ and δ, in addition to $x - R(y)$ and y. Integrating hv from $\xi = -x_u$ to $\xi = 0$ in (5.46) can only introduce an additional dependence on x_u, so the transport must also be depend only on x_u, $T = T(x_u, \theta, \delta)$. This may be shown directly by carrying out the integration in (5.46) to obtain an algebraic expression for T. Under the traditional approximation ($\delta = 0$), the transport does not depend on x_u at all,

$$T_{\text{trad}} = \frac{1}{2\cos\theta}. \tag{5.47}$$

When the complete Coriolis force is included ($\delta \neq 0$), T depends strongly on x_u, as shown in Figure 5.6. In this case the algebraic expression for T is much too large to interpret directly.

It remains to be shown that the shape of the front, $x = R(y)$, depends only on x_u, and remains unchanged for variations of W or R_u as long as x_u is held constant. We consider a solution $v(x, y)$, $h(x, y)$, corresponding to a western wall at $x = -W$ and an eastern front at $x = R(y)$. We then

shift the western wall to $x = -W + \Delta W$, keeping x_u, δ and θ fixed, and denote the corresponding solution as $v'(x, y)$, $h'(x, y)$, with an eastern front at $x = R(y) + \Delta R(y)$. For convenience we define $V = hv$ and $V' = h'v'$, the mass fluxes in the y-direction. From (5.45a) and (5.45b) we know that $V'(x, y) = V(x - \Delta R, y)$, because V is a function of $x - R$, and V' is an identical function of $x - (R + \Delta R)$. As x_u is identical in each solution, the transport T must also be identical, so from (5.24),

$$\begin{aligned}\int_{-W}^{R} V(x,y)\,\mathrm{d}x = T &= \int_{-W+\Delta W}^{R+\Delta R} V'(x,y)\,\mathrm{d}x \\ &= \int_{-W+\Delta W}^{R+\Delta R} V(x-\Delta R,y)\,\mathrm{d}x = \int_{-W+\Delta W-\Delta R}^{R} V(x,y)\,\mathrm{d}x \\ &= \int_{-W}^{R} V(x,y)\,\mathrm{d}x + \int_{-W+\Delta W-\Delta R}^{-W} V(x,y)\,\mathrm{d}x. \end{aligned} \tag{5.48}$$

In a solution with no backflow, $V(x, y) > 0$ everywhere, and so the leftmost and rightmost expressions in (5.48) are equal only if $\Delta R(y) = \Delta W$ for all y. Therefore, changing the channel width from W to $W + \Delta W$ does not produce any *relative* change in the solution if the upstream width x_u is fixed. The entire solution is simply shifted by a distance ΔW in the x-direction. In our asymptotic expansion we have neglected the x-variation of the vertical component of the rotation vector, and our equatorial β-plane approximation neglects all variation of the horizontal components, so we should expect the solution to be invariant under translations in the x-direction. Note, however, that the position $y = -y_c$, at which the front meets the eastern wall $x = W$, does vary with W.

5.3.7 Effect of including the complete Coriolis force

As outlined in §5.1, we wish to determine how the non-traditional component of the Coriolis force might enhance or hinder cross-equatorial flow of an abyssal current. We are therefore principally interested in the cross-equatorial transport $T = T(x_u, \theta, \delta)$. In Figures 5.6(a) and 5.6(b) we illustrate the dependence of T on x_u and θ respectively, for typical parameter values. Including the complete Coriolis force leads to a larger cross-equatorial transport in a northwestward channel, and a smaller transport in a northeastward channel. The difference is more pronounced when the current is narrower upstream. In Figure 5.6(a) we extend the plot only as far as $x_u = 2$, as condition (5.41) states that for $\theta = \pi/4$, a larger width will lead to backflow in the current.

The most striking feature of these plots is that there are points at which T approaches infinity. These asymptotes correspond to zeros in the denominator of the Bernoulli constant B, *i.e.*where

$$x_u \cos\theta - 2\delta \sin\theta = 0 \tag{5.49}$$

in (5.27). Solutions of (5.49) correspond to a breakdown of cross-channel geostrophic balance.

Equations (5.22a) and (5.22b) together imply a geostrophic equation for the along-channel velocity v,

$$\left(y\cos\theta - \delta\sin\theta\frac{\partial h}{\partial x}\right)v = \frac{\partial}{\partial x}(h + \delta h v\sin\theta). \tag{5.50}$$

Setting $\delta = 0$ in (5.50) immediately yields the familiar, traditional geostrophic relationship between v and $\partial h/\partial x$, though the x-dependent part of the Coriolis parameter has been neglected as it appears at $\mathcal{O}(\varepsilon)$ in (5.19). The non-traditional $\mathcal{O}(\delta)$ terms in (5.50) are proportional to v and $\partial v/\partial x$, so we obtain an explicit expression for v by substituting (5.22a) back into (5.50) to eliminate $\partial v/\partial x$,

$$v = \frac{\left(1 + \delta^2 h\sin^2\theta\right)\dfrac{\partial h}{\partial x} - \delta y h\cos\theta\sin\theta}{y\cos\theta - 2\delta\sin\theta\dfrac{\partial h}{\partial x}}. \tag{5.51}$$

The denominator of (5.51) reduces exactly to (5.49) on applying the upstream condition $y = -1$ and replacing $\partial h/\partial x$ by its average,

$$\overline{\frac{\partial h}{\partial x}} = \frac{1}{x_u}\int_{-W}^{R_u}\frac{\partial h}{\partial x}\,\mathrm{d}x = \frac{1}{x_u}\left(h|_{x=R_u} - h|_{x=-W}\right) = -\frac{1}{x_u}. \tag{5.52}$$

If the mean gradient $\overline{\partial h/\partial x}$ of h approaches $-(1/2\delta)\cot\theta$, then the gradient of h at some point $x \in [-W, R_u]$ must also approach $-(1/2\delta)\cot\theta$, by the mean value theorem, so the along-channel velocity tends to infinity by (5.51). In the traditional case ($\delta = 0$), geostrophic balance breaks down only as $y\cos\theta \to 0$, or $\theta \to \pm\pi/2$.

Including the complete Coriolis force thus leads to a larger transport in a northwestward channel, because a stronger flow is required to preserve the cross-channel geostrophic balance (5.51). Similarly, a weaker flow is required to maintain cross-channel geostrophic balance in a northeastward channel. These effects are more pronounced when the channel is closer to eastward or westward (θ closer to $\pm\pi/2$), as then the zonal component of the along-channel velocity is larger, and the non-traditional Coriolis terms connect zonal and vertical motions in the full three-dimensional equations. However, if the orientation of the channel is very close to westward ($\theta \to \pi/2$), or if the current is very narrow in a northwestward channel ($\theta > 0$, $x_u \to 0$), then the solution breaks down. Beyond the asymptotes marked in Figure 5.6, where $x_u\cot\theta < 2\delta$, the solution no longer satisfies the boundary condition (5.23c) at the western wall. We will return to the case the case of an almost-westward or almost-eastward channel in §5.4, using a modified asymptotic scaling.

5.3.8 Extended solution with $\delta = \mathcal{O}(\varepsilon)$

For the physical parameters discussed in §5.3.2, which are relevant to the AABW, we obtain $\varepsilon \approx \delta \approx 0.1$. In this case, we expect terms that are $\mathcal{O}(\varepsilon)$ to be as important as terms that are $\mathcal{O}(\delta)$.

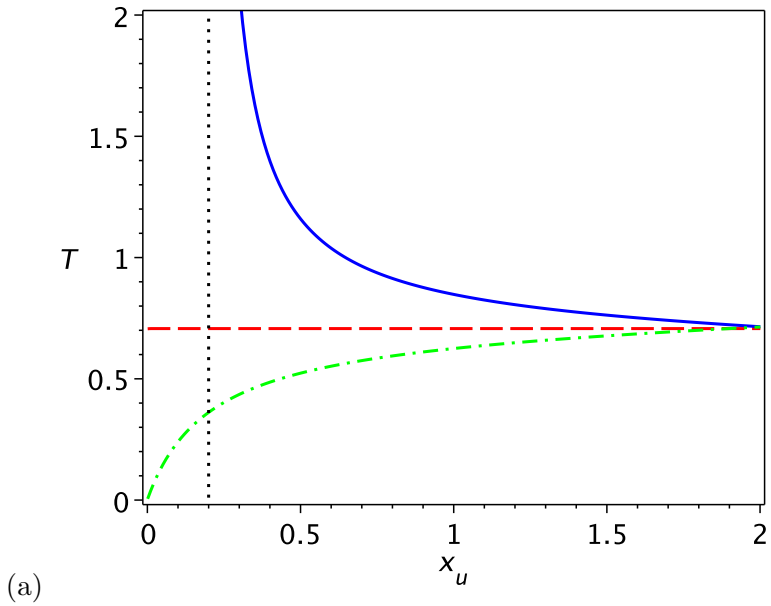

(a)

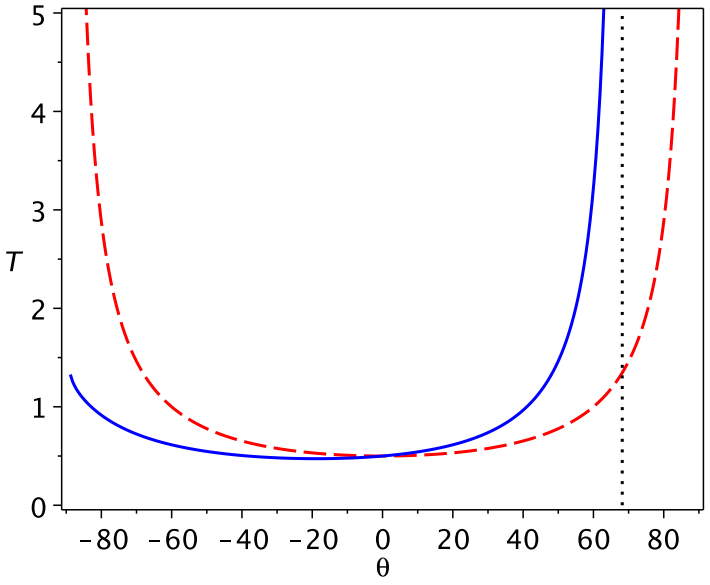

(b)

Figure 5.6: Plots illustrating the change in the along-channel transport T when the complete Coriolis force is included. In (a) we plot T against x_u for $\delta = 0$ (dashed line), and for $\delta = 0.1$ with $\theta = 45°$ (solid line) and $\theta = -45°$ (dash-dotted line). In (b) we plot T against θ (measured in degrees) for $x_u = 0.5$ with $\delta = 0$ (dashed line) and $\delta = 0.1$ (solid line). The dotted lines mark the asymptotes when $\delta = 0.1$.

We will now consider the distinguished asymptotic limit in which $\delta = \mathcal{O}(\varepsilon)$. This is consistent for a layer of vanishing depth $H_u \to 0$ with other parameters fixed, because $\delta, \varepsilon \sim H_u^{1/2}$.

We may proceed formally by posing an asymptotic expansion of (5.19) and (5.20) in ε, *e.g.* $\hat{h} = \hat{h}^{(0)} + \varepsilon\hat{h}^{(1)} + \cdots$. However, in the combined limit $\delta = \mathcal{O}(\varepsilon)$, the leading-order solution to (5.19) and (5.20) is simply the traditional solution ($\varepsilon = \delta = 0$) described in §5.3.3–5.3.6. In this case the

asymptotes shown in Figure 5.6, a crucial feature of the solution, are fixed at $\theta = \pm\pi/2$, and are not modified by higher-order corrections to the leading-order solution. It may be possible to correct this non-uniform convergence of the asymptotic expansion via the method of strained coordinates (*e.g.* Lighthill, 1949; Hinch, 1991).

A more practical, if less rigorous, alternative is simply to truncate our asymptotic expansion of (5.19) and (5.20), retaining terms up to $\mathcal{O}(\varepsilon)$. This yields

$$y\cos\theta + \varepsilon x\sin\theta - \delta\frac{\partial h}{\partial x}\sin\theta + \frac{\partial v}{\partial x} = 0, \tag{5.53a}$$

$$\nabla\left(\tfrac{1}{2}v^2 + h + \delta\, h\, v\sin\theta\right) = 0. \tag{5.53b}$$

Note that (5.53a) and (5.54a) differ from (5.22a) and (5.22b) only in the addition of the $\varepsilon x\sin\theta$ term in (5.53a) that accounts for the x-dependence of the Coriolis parameter f. Integrating (5.53a) and (5.54a) yields a set of algebraic equations analogous to (5.26a) and (5.26b),

$$(x-R)y\cos\theta + \tfrac{1}{2}\varepsilon(x^2-R^2)\sin\theta - \delta h\sin\theta + v = \sqrt{2B}, \tag{5.54a}$$

$$\tfrac{1}{2}v^2 + h + \delta\, h\, v\sin\theta = B, \tag{5.54b}$$

where again B is the Bernoulli constant, and we have determined the function of integration in (5.54a) using the boundary condition (5.23b) at the edge of the current. The method of solution is identical to that described in §5.3.3, but the additional term in (5.54a) leads to several qualitative changes in the results, described below. This solution retains the antisymmetry property, *i.e.* $v(x,y) = v(-x,-y)$, $h(x,y) = h(-x,-y)$, $L(y) = -R(-y)$ for $y > 0$, which may be shown via a procedure similar to that described in §5.3.4. As in §5.3.5, we must ensure that the flow is unidirectional for the solution to be valid, but a simple condition analogous to (5.41) may not be found even in the traditional case ($\delta = 0$). We have therefore checked this via direct computation for each solution presented here.

In §5.3.3, our neglect of the $\varepsilon x\sin\theta$ term in (5.53a) means that the dynamic equator in the leading-order problem always lies at $y = 0$. In the traditional case ($\delta = 0$) cross-channel geostrophic balance (5.50) requires that $\partial h/\partial x \to 0$ as the current approaches the equator (as $y \to 0$). The current's height must become vanishingly small and its width infinitely large as it approaches the equator, $h \to 0$, $R \to \infty$ as $y \to 0$, to conserve along-channel transport and satisfy the condition of zero thickness at the eastern front, (5.23b). This broadening of the current is eventually blocked by the opposing channel wall at $x = +W$. The same broadening also occurs in the non-traditional case, as shown in §5.3.4, but the mechanism is less intuitive.

The $\varepsilon x\sin\theta$ term in (5.53a) accounts for the fact that the equator actually lies along the line $y = -\varepsilon x\tan\theta$. We determine where the current is blocked by setting $h = 0$ in (5.54a) and (5.54b),

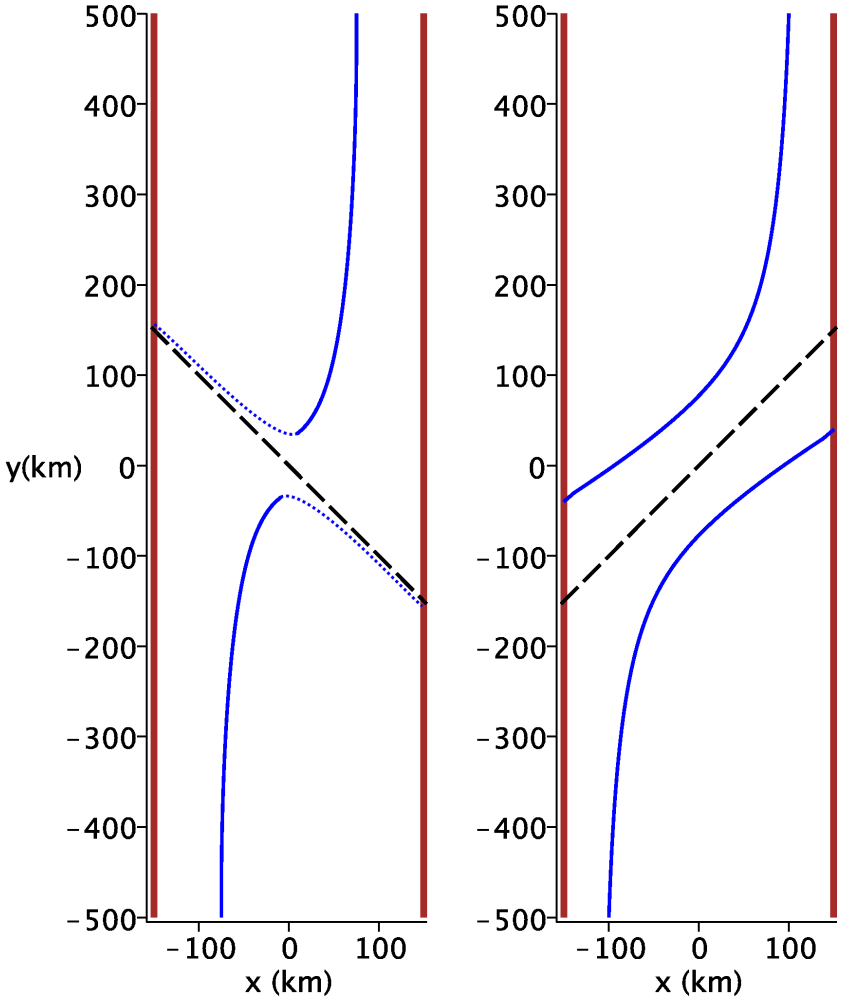

Figure 5.7: Typical plots of the eastern and western fronts (solid lines) of the current when the x-dependence of the Coriolis parameter f is retained. The left figure corresponds to a northwestward channel, $\theta = \pi/4$, and the right figure to a northeastward channel, $\theta = -\pi/4$. In each case the dashed line marks the equator. Both solutions break down close to $y = 0$, and we have artificially continued the solution up to the equator in the $\theta = \pi/4$ case (dotted lines), for the purpose of illustration

which yields $v = \sqrt{2B}$ and

$$(x - R)\left(y\cos\theta + \tfrac{1}{2}\varepsilon(x + R)\sin\theta\right) = 0. \tag{5.55}$$

The height of the current must thus approach zero as $x \to R(y)$, which corresponds to the edge of the current, and as $y \to -\frac{1}{2}\varepsilon(x + R(y))\tan\theta$, which is almost identical to the line marking the equator. This suggests that the equator should still act as a barrier to cross-equatorial flow, in the absence of an opposing wall at $x = +W$. In Figure 5.7 we plot the current profiles for the same parameters used in Figure 5.5, for both northwestward ($\theta = \pi/4$) and northeastward ($\theta = -\pi/4$) channels. In the northwestward channel, the current begins to turn as it approaches the equator, but it is only possible to compute the position of the front $x = R(y)$ to the extent of the solid lines. We

have heuristically extended the fronts such that the current widens parallel to the equator, but this is entirely speculative, and is intended to give an visual impression of what the complete solution might look like. In the northeastward channel the front turns approximately parallel to the equator, and the position of the front may be computed beyond $y = 0$. However, close to $y = 0$ the solutions in the northern and southern hemispheres are overlapping, so this section of the front is plotted simply for visual effect. The breakdown of our asymptotic solution close to the equator means that we can only speculate about the nature of the solution joining the inflow in the southern hemisphere to the outflow in the northern hemisphere. However, in general we expect the current to turn as it approaches the equator, flow along the equator as it crosses the channel, and then turn again to exit the channel. The more northwestward the orientation of the channel, the sharper these turns must be, and so the steady solution may be less stable.

The explicit x-dependence in (5.53a) also means that the solution is no longer determined completely by δ, θ and x_u, as shown in §5.3.6. To illustrate this, consider the cross-channel geostrophic balance implied by (5.53a) and (5.53b),

$$v = \frac{\left(1 + \delta^2 h \sin^2\theta\right)\dfrac{\partial h}{\partial x} - \delta h \sin\theta\,(y\cos\theta + \varepsilon\, x \sin\theta)}{y\cos\theta + \varepsilon\, x\sin\theta - 2\delta\sin\theta\dfrac{\partial h}{\partial x}}. \tag{5.56}$$

The asymptotes in the along-channel transport T occur where the across-channel average of the denominator in (5.56) at $y = -1$ approaches zero, as in §5.3.7. Thus T approaches infinity where

$$x_u\cos\theta - \varepsilon\sin\theta x_u x_m - 2\delta\sin\theta = 0, \quad x_m = \tfrac{1}{2}(R_u - W), \tag{5.57}$$

where x_m is the midpoint of the current at the upstream edge of the channel. This condition gives

$$\tan\theta = \frac{x_u}{2\delta + \varepsilon x_u x_m}. \tag{5.58}$$

The channel geometry requires that $x_m \le 0$, so the asymptote $T \to \infty$ lies in $\theta \in (0, \pi/2)$ if $\delta > \frac{1}{2}\varepsilon x_u|x_m|$, or in $\theta \in (-\pi/2, 0)$ if $\delta < \frac{1}{2}\varepsilon x_u|x_m|$. These results may all be interpreted in terms of the breakdown of cross-channel geostrophic balance (5.56), which now depends not only on the upstream width of the current x_u, but also on its absolute upstream position x_m. Otherwise, the physically relevant results for $\varepsilon \neq 0$ are broadly similar to those described in §5.3.7.

5.3.9 Implications for the AABW

We now apply this channel-crossing solution to the AABW. The channel highlighted in Figure 5.1 makes an angle of approximately 8° with the equator, and the flow is close to westwards. This corresponds to $\theta \approx 1.43\,\text{rad} \approx 82°$ in our convention of measuring θ from the eastward direction, so

the $y\cos\theta$ and $\varepsilon x\sin\theta$ terms in (5.53a) are of similar magnitude. We therefore retain the $\mathcal{O}(\varepsilon)$ x-dependent contribution to the Coriolis parameter in our solutions, as described in §5.3.8. Figures 5.1 and 5.2 suggest that the bathymetry approximately forms a channel with a half-length of $y_u = 500\,\mathrm{km}$, a half-width of $W^\star = 150\,\mathrm{km}$, and a height of $H_u = 500\,\mathrm{m}$. We use approximate Earth-like values for the planetary radius, $R_E = 6400\,\mathrm{km}$ and the rotation rate, $\Omega = 7.3\times10^{-5}\,\mathrm{rad\,s^{-1}}$. We choose a somewhat small reduced gravity, $g' = 3\times10^{-4}\,\mathrm{m\,s^{-2}}$, to avoid unrealistically large velocities in the current. Even with g' this small, the along-channel velocity and transport are an order of magnitude larger than observations suggest (see Hall et al., 1997). This may be attributed to the absence of dissipation in our idealised model.

The only remaining unspecified parameter is the width $x_u^\star$ of the current upstream, so in Figure 5.8 we plot the dimensional along-channel transport $T^\star$ as a function of $x_u^\star$. The plot is reminiscent of Figure 5.6(a), but $T^\star$ varies with $x_u^\star$ even when $\delta = 0$ because we have retained the $\mathcal{O}(\varepsilon)$ x-dependent term in (5.53a). Including the complete Coriolis force increases the cross-equatorial transport, regardless of the upstream width of the current. For $x_u^\star \gtrsim 120\,\mathrm{km}$ the current flows southward ($v < 0$) at the western wall, so the solution is no longer valid. We therefore consider this to represent the fast-flowing core of the AABW, rather than a complete description of the flow in the whole channel. In the non-traditional case ($\delta \neq 0$), cross-channel geostrophic balance (5.56) breaks down for $x_u^\star \lesssim 20\,\mathrm{km}$, as discussed in §5.3.7. However, this width is unrealistically small even for core of the AABW (see Rhein et al., 1998).

This solution suggests that the complete Coriolis force may play a substantial role in the cross-equatorial flow of the AABW, though the Figure 5.8 suggests that the transport is very sensitive to inflow conditions. Additionally, for a channel orientation close to westward ($\theta \to \pi/2$) the validity of this solution becomes questionable, as the leading-order contribution $y\cos\theta$ to the Coriolis parameter in (5.53a) vanishes. In §5.4 we address this shortcoming using an alternative asymptotic scaling in the limit $\theta \to \pm\pi/2$.

5.4 Flow through an almost-zonal channel with arbitrary topography

The orientation of the channel outlined in Figure 5.1 makes an angle of approximately 8° or 0.14 radians with the equator, corresponding to $\theta \approx 1.43\,\mathrm{rad} \approx 82°$ when we measure the angle from the northward direction. Thus the leading order contribution $y\cos\theta$ to the Coriolis parameter becomes comparable with the lengthscale ratio $R_d/y_u = \varepsilon^{1/2} \approx 0.26$ in the solutions described in §5.3.9. This motivates an alternative asymptotic scaling of the zero-potential vorticity governing equations

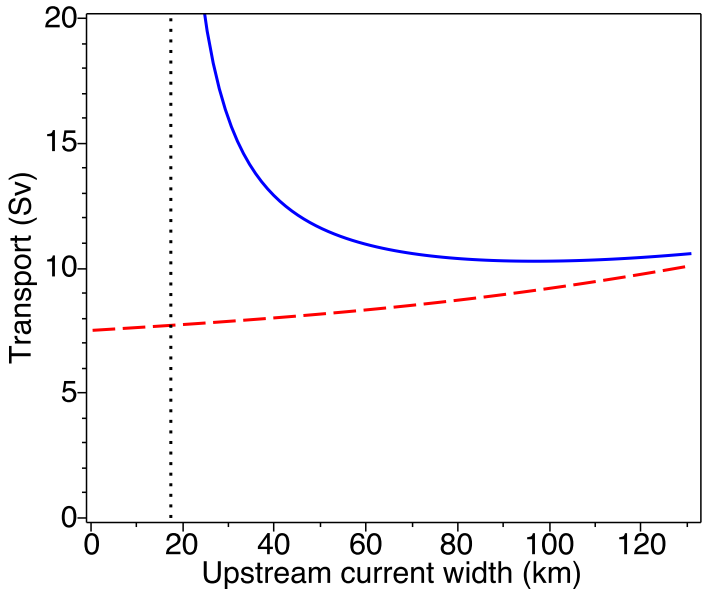

Figure 5.8: Plot of the dimensional along-channel transport against the upstream width of the current, under the traditional approximation (dashed line) and including the complete Coriolis force (solid line). The dotted line marks a vertical asymptote. The channel has similar dimensions to that plotted in Figures 5.1 and 5.2: $y_u = 500\,\mathrm{km}$, $W^\star = 150\,\mathrm{km}$, $H_u = 500\,\mathrm{m}$, and $\theta = 1.43$. We use a small reduced gravity $g' = 3 \times 10^{-4}\,\mathrm{m\,s^{-2}}$ to avoid unrealistically large velocities.

(5.13)–(5.15), in which the orientation of the channel is asymptotically close to eastward/westward. This scaling allows us to retain arbitrary variations of the bottom topography in the cross-channel direction.

Figure 5.9 illustrates this problem schematically. We consider a channel that is uniform in the y-direction, and with arbitrary variations in the x-direction, crossing the equator at an angle θ with North. The current enters from the south, leaning up against the western side of the channel, and exits to the north leaning against the eastern side, consistent with cross-channel geostrophic balance. This differs from the situation presented in Figure 5.4 in that the current now has two fronts instead of one, and both fronts may vary along the channel.

5.4.1 Scaling for an almost-zonal channel

Following §5.3.1, we seek a steady solution of the $1\frac{1}{2}$-layer shallow water equations, under the assumption of zero potential vorticity. Including arbitrary bottom topography at $z = h_b(x, y)$,

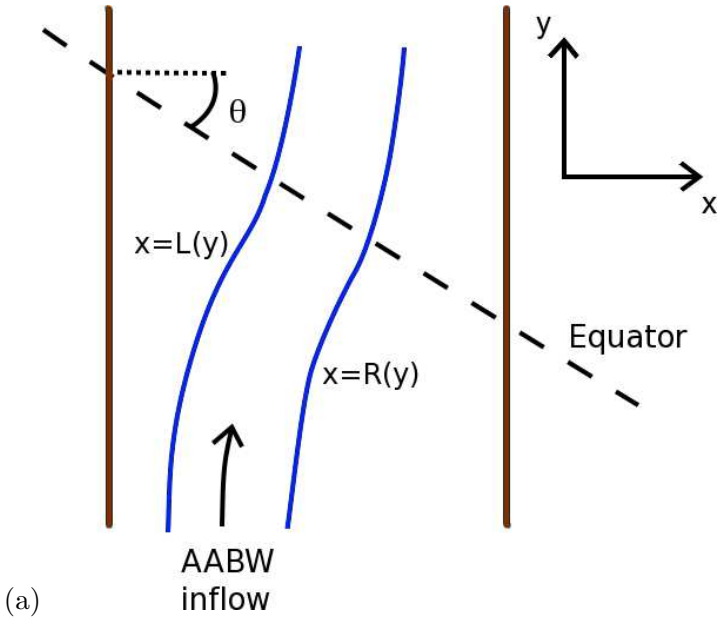

(a)

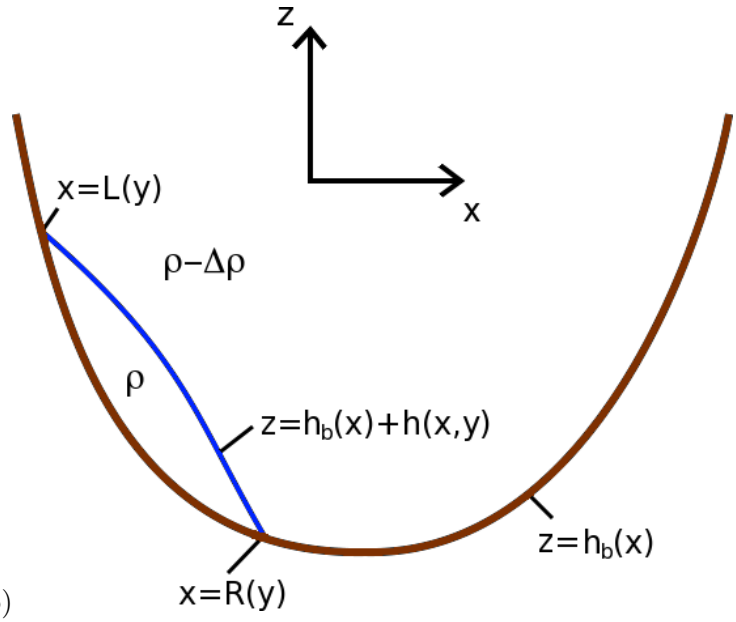

(b)

Figure 5.9: Top-down (a) and along-channel (b) schematics of the solutions presented in §5.4. The solution has a similar form to that shown in Figure 5.4, except we allow for arbitrary variations of the topography in the x-direction, and the channel is oriented arbitrarily close to eastward or westward.

equations (5.13)–(5.15) become

$$\beta(y\cos\theta + x\sin\theta) + \frac{\partial v}{\partial x} - \frac{\partial u}{\partial y}$$
$$-2\Omega\sin\theta\frac{\partial}{\partial x}\left(h_b + \tfrac{1}{2}h\right) - 2\Omega\cos\theta\frac{\partial}{\partial y}\left(h_b + \tfrac{1}{2}h\right) = 0, \tag{5.59a}$$

$$\nabla\left(\tfrac{1}{2}u^2 + \tfrac{1}{2}v^2 + g'(h_b + h) + \Omega h\left(v\sin\theta - u\cos\theta\right)\right) = 0, \tag{5.59b}$$

$$\frac{\partial}{\partial x}(hu) + \frac{\partial}{\partial y}(hv) = 0. \tag{5.59c}$$

Here we have returned to dimensional variables u, v, h, x, and y. The contribution of the topographic height h_b to the potential vorticity, and therefore to (5.59a), arises because h_b alters the distances of the fluid parcels in a column from the rotation axis, and thus alters the angular momentum of a column. The contribution to (5.59b) accounts for the gravitational pressure gradient being proportional to the gradient of the surface at $z = h_b + h$.

In §5.3.2 the upstream depth H_u served as a natural vertical lengthscale, but in the situation shown in Figure 5.9 the depth everywhere is determined by the positions of the fronts at $x = L(y)$ and $x = R(y)$. We therefore use an arbitrary vertical lengthscale H, and use this to define the gravity wave speed and radius of deformation,

$$c = \sqrt{g'H}, \quad R_d = \sqrt{\frac{c}{\beta}}. \tag{5.60}$$

We again prescribe the inflow of the current at $y = -y_u$, and assume that this distance is large compared with the radius of deformation R_d, defining the small parameter $\varepsilon = (R_d/y_u)^2 \ll 1$ as in (5.17). We alter the scaling described in §5.3.2 by assuming that the orientation of the channel is arbitrarily close to westward/eastward,

$$\theta = \pm\left(\frac{\pi}{2} - \varepsilon^{1/2}\Theta\right), \tag{5.61}$$

where $\Theta = \mathcal{O}(1)$. The '+' corresponds to an almost-westward channel, and the '−' to an almost-eastward channel. Using $\varepsilon \ll 1$, we may expand the trigonometric terms in (5.59a)–(5.59c) using Taylor series,

$$\sin\theta = \pm\left(1 - \tfrac{1}{2}\varepsilon\,\Theta^2 + \mathcal{O}\left(\varepsilon^2\right)\right), \tag{5.62a}$$

$$\cos\theta = \varepsilon^{1/2}\Theta - \tfrac{1}{6}\varepsilon^{3/2}\Theta^3 + \mathcal{O}\left(\varepsilon^{5/2}\right). \tag{5.62b}$$

Our asymptotic assumptions (5.17) and (5.61) together constrain the northward distance that the current can travel. The northward coordinate is $Y = y\cos\theta + x\sin\theta$, so upstream ($y = -y_u$) in the centre of the channel ($x = 0$), the meridional position is

$$Y(0, -y_u) = Y_u = -y_u\cos\theta \approx -y_u\varepsilon^{1/2}\Theta = -R_d\Theta. \tag{5.63}$$

Thus the current can only cover a northward distance comparable to the radius of deformation R_d. Given that typically R_d is around 150 km, this limitation is appropriate for the channel shown in Figure 5.1.

We scale (5.59a)–(5.59c) on the basis that y_u is an appropriate lengthscale in the y-direction, so the solution is slowly-varying along the channel. However, we now allow for $\mathcal{O}(1)$ variations in the

x-direction, and need only assume that the cross-channel velocity u is small to balance the mass conservation equation (5.59c) at leading order,

$$x = R_d\,\hat{x}, \quad y = \varepsilon^{-1/2} R_d\,\hat{y}, \quad u = \varepsilon^{1/2} c\hat{u}, \quad v = c\hat{v}, \quad h = H\,\hat{h}. \tag{5.64}$$

As we impose no asymptotic ordering on x, we may allow for arbitrary variations of the topography in the cross-channel direction, $h_b = H\hat{h}_b(\hat{x})$. The scaling (5.64) leaves (5.59c) unchanged in dimensionless variables, whilst (5.59a) and (5.59b) become

$$\begin{aligned} &\hat{y}\left(\Theta - \tfrac{1}{6}\varepsilon\Theta^3\right) \pm \hat{x}\left(1 - \tfrac{1}{2}\varepsilon\Theta^2\right) + \frac{\partial \hat{v}}{\partial \hat{x}} - \varepsilon\frac{\partial \hat{u}}{\partial \hat{y}} \\ &\quad \mp\delta\left(1 - \tfrac{1}{2}\varepsilon\,\Theta^2\right)\frac{\partial}{\partial \hat{x}}\left(2\hat{h}_b + \hat{h}\right) - \delta\varepsilon\Theta\frac{\partial \hat{h}}{\partial \hat{y}} = \mathcal{O}\left(\varepsilon^2\right), \end{aligned} \tag{5.65a}$$

$$\begin{aligned} &\hat{\nabla}\Big[\ \tfrac{1}{2}\varepsilon\hat{u}^2 + \tfrac{1}{2}\hat{v}^2 + \hat{h}_b + \hat{h} \\ &\qquad \pm\delta\hat{h}\hat{v}\left(1 - \tfrac{1}{2}\varepsilon\,\Theta^2\right) - \delta\varepsilon\Theta\hat{h}\hat{u}\ \Big] = \mathcal{O}\left(\varepsilon^2\right). \end{aligned} \tag{5.65b}$$

Under this scaling, the dependence of the Coriolis parameter $f = \beta Y$ on both x and y is retained at $\mathcal{O}(1)$. Meanwhile all terms involving the cross-channel velocity $\hat{u}$ appear at $\mathcal{O}(\varepsilon)$, so leading-order solution is determined entirely in terms of $\hat{v}$ and $\hat{h}$. The non-traditional parameter δ is analogous to (5.21),

$$\delta = \Omega\sqrt{\frac{H}{g'}}, \tag{5.66}$$

which is again the ratio of the non-traditional velocity scale ΩH to the internal wave speed.

We proceed by expanding the dimensionless variables as asymptotic series in ε, *e.g.* $\hat{h} = \hat{h}^{(0)} + \varepsilon\hat{h}^{(1)} + \cdots$, and solving (5.65a) and (5.65b) at each order in ε. However, here we will consider only the leading-order solution, so it is sufficient simply to neglect terms of $\mathcal{O}(\varepsilon)$ and above,

$$\Theta\hat{y} \pm \hat{x} \mp \delta\frac{\partial}{\partial \hat{x}}\left(2\hat{h}_b + \hat{h}\right) + \frac{\partial \hat{v}}{\partial \hat{x}} = 0, \tag{5.67a}$$

$$\hat{\nabla}\left(\tfrac{1}{2}\hat{v}^2 + \hat{h}_b + \hat{h} \pm \delta\hat{h}\hat{v}\right) = 0. \tag{5.67b}$$

Equations (5.67a), (5.67b) and (5.59c) must be solved subject to the thickness of the layer vanishing at the fronts $\hat{x} = \hat{L}\,(\hat{y})$ and $\hat{x} = \hat{R}\,(\hat{y})$, where the upstream positions of the fronts are prescribed,

$$\hat{h} = 0 \quad \text{at} \quad \hat{x} = \hat{L}\,(\hat{y}), \tag{5.68a}$$

$$\hat{h} = 0 \quad \text{at} \quad \hat{x} = \hat{R}\,(\hat{y}), \tag{5.68b}$$

$$\hat{L} = \hat{L}_u \quad \text{at} \quad \hat{y} = -1, \tag{5.68c}$$

$$\hat{R} = \hat{R}_u \quad \text{at} \quad \hat{y} = -1. \tag{5.68d}$$

We will show that prescribing the upstream positions of the fronts in (5.68a)–(5.68d) determines the entire leading-order solution.

5.4.2 Method of solution

We now describe an analytical solution to the leading-order equations and boundary conditions in §5.4.1. The solution is possible due to the assumption of zero potential vorticity, but the algebra still rapidly becomes unmanageably complicated. We therefore outline the steps that could be taken, in principle, to determine the complete solution for arbitrary values of the parameters.

Equations (5.67a) and (5.67b) are exact derivatives, and so may be integrated immediately to obtain

$$\Theta\hat{x}\hat{y} \pm \tfrac{1}{2}\hat{x}^2 \mp \delta\left(2\hat{h}_b + \hat{h}\right) + \hat{v} = \hat{A}\left(\hat{y}\right), \tag{5.69a}$$

$$\tfrac{1}{2}\hat{v}^2 + \hat{h}_b + \hat{h} \pm \delta\hat{h}\hat{v} = \hat{B}, \tag{5.69b}$$

where A is an arbitrary function of $\hat{y}$ and $\hat{B}$ is the Bernoulli constant. Substituting the boundary conditions (5.68a) and (5.68b) into (5.69a) and (5.69b) yields two equations for $\hat{A}\left(\hat{y}\right)$ in terms of the unknowns $\hat{L}\left(\hat{y}\right)$, $\hat{R}\left(\hat{y}\right)$ and $\hat{B}$,

$$\begin{aligned}\hat{A}\left(\hat{y}\right) &= \Theta\hat{L}\hat{y} \pm \tfrac{1}{2}\hat{L}^2 \mp 2\delta\hat{h}_b\left(\hat{L}\right) + \sqrt{2\left(\hat{B} - \hat{h}_b\left(\hat{L}\right)\right)} \\ &= \Theta\hat{R}\hat{y} \pm \tfrac{1}{2}\hat{R}^2 \mp 2\delta\hat{h}_b\left(\hat{R}\right) + \sqrt{2\left(\hat{B} - \hat{h}_b\left(\hat{R}\right)\right)}.\end{aligned} \tag{5.70}$$

These may be solved simultaneously for $\hat{B}$ in terms of the prescribed parameters Θ, δ, $\hat{L}_u$ and $\hat{R}_u$ using (5.68c) and (5.68d). Equation (5.70) then determines $\hat{A}\left(\hat{y}\right)$ in terms of $\hat{y}$, $\hat{L}\left(\hat{y}\right)$ and $\hat{R}\left(\hat{y}\right)$, and also directly relates $\hat{L}\left(\hat{y}\right)$ and $\hat{R}\left(\hat{y}\right)$. We may then solve (5.69a) and (5.69b) algebraically to determine $\hat{v}$ and $\hat{h}$ as functions of $\hat{x}$, $\hat{y}$, $\hat{L}\left(\hat{y}\right)$ and $\hat{R}\left(\hat{y}\right)$. Thus the solution is completely determined in terms of the unknown positions of the fronts, $\hat{L}\left(\hat{y}\right)$ and $\hat{R}\left(\hat{y}\right)$.

To complete the solution, we integrate the mass conservation equation (5.59c) across the current to obtain a condition analogous to (5.24),

$$\int_{\hat{L}(\hat{y})}^{\hat{R}(\hat{y})} \hat{h}\hat{v}\,\mathrm{d}\hat{x} = \hat{T}, \tag{5.71}$$

where $\hat{T}$ is the constant along-channel transport. We may determine $\hat{T}$ in terms of the prescribed parameters Θ, δ, $\hat{L}_u$ and $\hat{R}_u$ using the upstream conditions (5.68c) and (5.68d). Thus (5.70) and (5.71) constitute two equations relating $\hat{L}\left(\hat{y}\right)$ and $\hat{R}\left(\hat{y}\right)$, which may be solved simultaneously to determine the positions of the fronts everywhere. This in turn determines $\hat{v}$ and $\hat{h}$ everywhere via (5.69a) and (5.69b).

The algebraic manipulations described here are prohibitively complicated in the most general case, and the exact formulae for $\hat{v}\left(\hat{x},\hat{y}\right)$ and $\hat{h}\left(\hat{x},\hat{y}\right)$ would be much too large to interpret directly. However, the solutions presented in §5.4.3 have been obtained via exactly the procedure outlined

above, but for specific cases of the parameters Θ, δ, $\hat{L}_u$ and $\hat{R}_u$. A useful result that can be obtained directly is the equation for cross-channel geostrophic balance implied by (5.67a) and (5.67b),

$$\hat{v} = \frac{\dfrac{\partial}{\partial \hat{x}}\left(\hat{h}_b + \hat{h}\right) + \delta\hat{h}\left(\pm\Theta\hat{y} + \hat{x} - \delta\dfrac{\partial}{\partial \hat{x}}\left(2\hat{h}_b + \hat{h}\right)\right)}{\Theta\hat{y} \pm \hat{x} \mp 2\delta\dfrac{\partial}{\partial \hat{x}}\left(\hat{h}_b + \hat{h}\right)} \tag{5.72}$$

Following §5.3.7 and §5.3.8, we expect the transport $\hat{T}(\Theta, \delta, \hat{L}_u, \hat{R}_u)$ to have asymptotes when the cross-channel average of the denominator in (5.72) is zero, *i.e.* where

$$\Theta\left(\hat{R}_u - \hat{L}_u\right) \pm \tfrac{1}{2}\left(\hat{L}_u^2 - \hat{R}_u^2\right) \mp 2\delta\left(\hat{h}_b\left(\hat{L}_u\right) - \hat{h}_b\left(\hat{R}_u\right)\right) = 0. \tag{5.73}$$

Algebraic manipulation of (5.70) shows that (5.73) is exactly the condition for the denominator of the Bernoulli constant $\hat{B}$ to vanish. In §5.4.3 we consider solutions in an almost-westward channel, and we always have $R_u - L_u \geq 0$ and $L_u^2 - R_u^2 \geq 0$, so typically the transport does not approach infinity. However, we expect that equivalent solutions in an almost-eastward channel should be strongly affected by asymptotes in the transport.

5.4.3 Solutions in an AABW-like channel

The arbitrary topography $h_b(x)$ and assumption of an almost-westward or almost-eastward channel (5.61) make the solution described in §5.4.2 less general than that described in §5.3. It is therefore less useful to consider the dependence of the solution on the various dimensionless parameters, so instead we focus on dimensional solutions that are relevant to the AABW. In all of the results presented in this section the channel orientation is almost westward, and the channel shape is described by

$$h_b(x) = H\left|\frac{x}{x_0}\right|^m. \tag{5.74}$$

Here H is the maximum channel height, and serves as the vertical lengthscale, whilst x_0 is the channel half-width. We use $x_0 = 150\,\mathrm{km}$, $H = 500\,\mathrm{m}$, and $m = 4$, which yields a shape that agrees qualitatively well with the averaged bathymetry shown in Figure 5.2. In a symmetric topography such as (5.74), an antisymmetric solution with $v(x, y) = v(-x, -y)$, $h(x, y) = h(-x, -y)$, and $R(y) = -L(-y)$, satisfies the governing equations (5.69a), (5.69b), boundary conditions (5.68a)–(5.68d), and transport condition (5.71). This may be shown via a procedure similar to that described in §5.3.4. We therefore compute the solution only in one half of the channel ($y < 0$) and reflect it to obtain the solution in $y > 0$.

In Figure 5.10 we plot the positions of the fronts in a typical solution with AABW-like parameters. We have obtained this solution under the traditional approximation, as this simplifies the

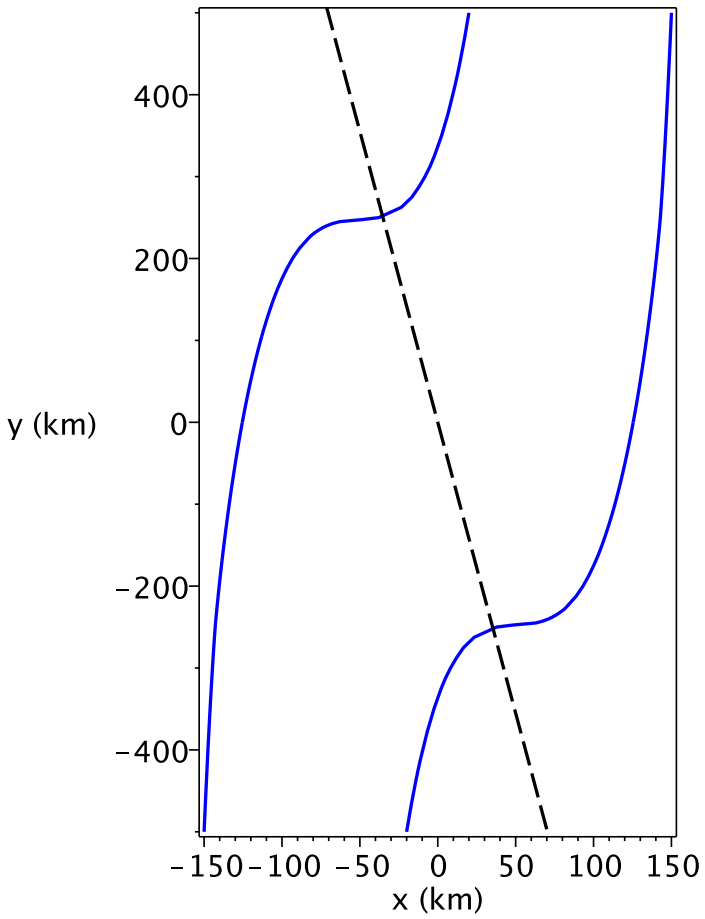

Figure 5.10: Plots of the western and eastern fronts, $x = L(y)$ and $x = R(y)$ in an AABW-like solution under the traditional approximation. The solid lines mark the positions of the fronts, and the dashed line marks the equator. In this solution $L_u = -150\,\text{km}$, $R_u = -20\,\text{km}$, $\theta = 1.43$, $y_u = 500\,\text{km}$, $g' = 10^{-3}\,\text{m}\,\text{s}^{-2}$, and the channel topography is described by (5.74).

computation greatly, yet the fronts do not differ dramatically when the complete Coriolis force is included. The behaviour of the current is broadly similar to the solutions of §5.3, in that it crosses from the western wall to the eastern wall of the channel as it crosses the equator. However, in §5.3 the solution in the southern (northern) hemisphere was constrained by the requirement that it must have non-zero depth at the western (eastern) wall, and a front to the east (west). This precluded a formal matching of these previous solutions at the equator. In the current solution both fronts are free to vary with y, so we are able to compute the solution along the entire length of the channel.

The most interesting feature of Figure 5.10 is the rapid transition to cross-channel flow at the equator, which we illustrate in Figure 5.11 with plots of the depth profile at various points on the y-axis. To understand this, consider the equation for cross-channel geostrophic balance (5.72) under

the traditional approximation ($\delta = 0$) in an almost-westward channel,

$$(\Theta\hat{y} + \hat{x})\,\hat{v} = \frac{\partial\hat{\eta}}{\partial\hat{x}}, \qquad \eta = \hat{h}_b + \hat{h}. \tag{5.75}$$

As the current approaches the equator, the scaled Coriolis parameter approaches zero, $\Theta\hat{y} + \hat{x} \to 0$. By conservation of along-channel transport (5.71), the along-channel velocity may not approach infinity ($\hat{v} \nrightarrow \infty$), so instead the gradient of the surface must approach zero ($\partial\hat{\eta}/\partial\hat{x} \to 0$). Thus, in Figure 5.10 the current leans against western wall, as in Figure 5.11 panels (a) and (b), until it can not proceed any further along the channel without crossing the equator. Around $y \approx -250\,\mathrm{km}$ the solution makes a rapid transition to a state resembling Figure 5.11(c), leaning against both sides of the channel with a minimum depth ($\partial\hat{\eta}/\partial\hat{x} = 0$) at the equator. As the current moves further along the channel, the minimum depth shifts towards the centre of the channel, following the equator, until it reaches the state shown in Figure 5.11(d) at $y = 0$. The reverse takes place as the current flows towards the northern edge of the channel.

Rapid changes in the positions of the fronts are inconsistent with out ansatz (5.64) that the solution varies slowly with y, so the validity of our asymptotic expansion is dubious at these points. If the upstream position R_u is brought closer to L_u, then the boundary $R(y)$ downstream makes a discontinuous jump from a state resembling Figure 5.11(b) to one resembling Figure 5.11(c), which certainly invalidates (5.64). If R_u is closer to the equator, the front will cross smoothly to the eastern wall of the channel, and if the current straddles the equator at the channel entrance ($\hat{L}_u < \Theta < \hat{R}_u$) the fronts need not cross the equator at all. Though the region close to the equator may require a more sophisticated analysis, this solution is a useful description of how the core of the AABW might flow steadily across the equator.

5.4.4 Effect of including the complete Coriolis force

We are principally interested in the role of the non-traditional component of the Coriolis force in transporting fluid across the equator. The along-channel transport T is determined by the conditions at the southern entrance to the channel, where the assumption of a slowly-varying solution holds well. For values of the reduced gravity g' that are realistic for the abyssal ocean, *e.g.* $g' = 10^{-3}\,\mathrm{m\,s^{-2}}$, the along-channel velocity and transport tend to be around an order of magnitude larger their measured values (*e.g.* Hall et al., 1997). This may be attributed to the absence of friction in this solution. Smaller values of g' yield more realistic velocities, but cause the transport to behave unexpectedly.

We illustrate this in Figure 5.12 using the upstream solution for the same parameters as in Figure 5.10, but with $g' = 3 \times 10^{-4}\,\mathrm{m\,s^{-2}}$. Including the complete Coriolis force leads to a substantially shallower, faster-flowing current, but the transports are almost identical. This may be understood

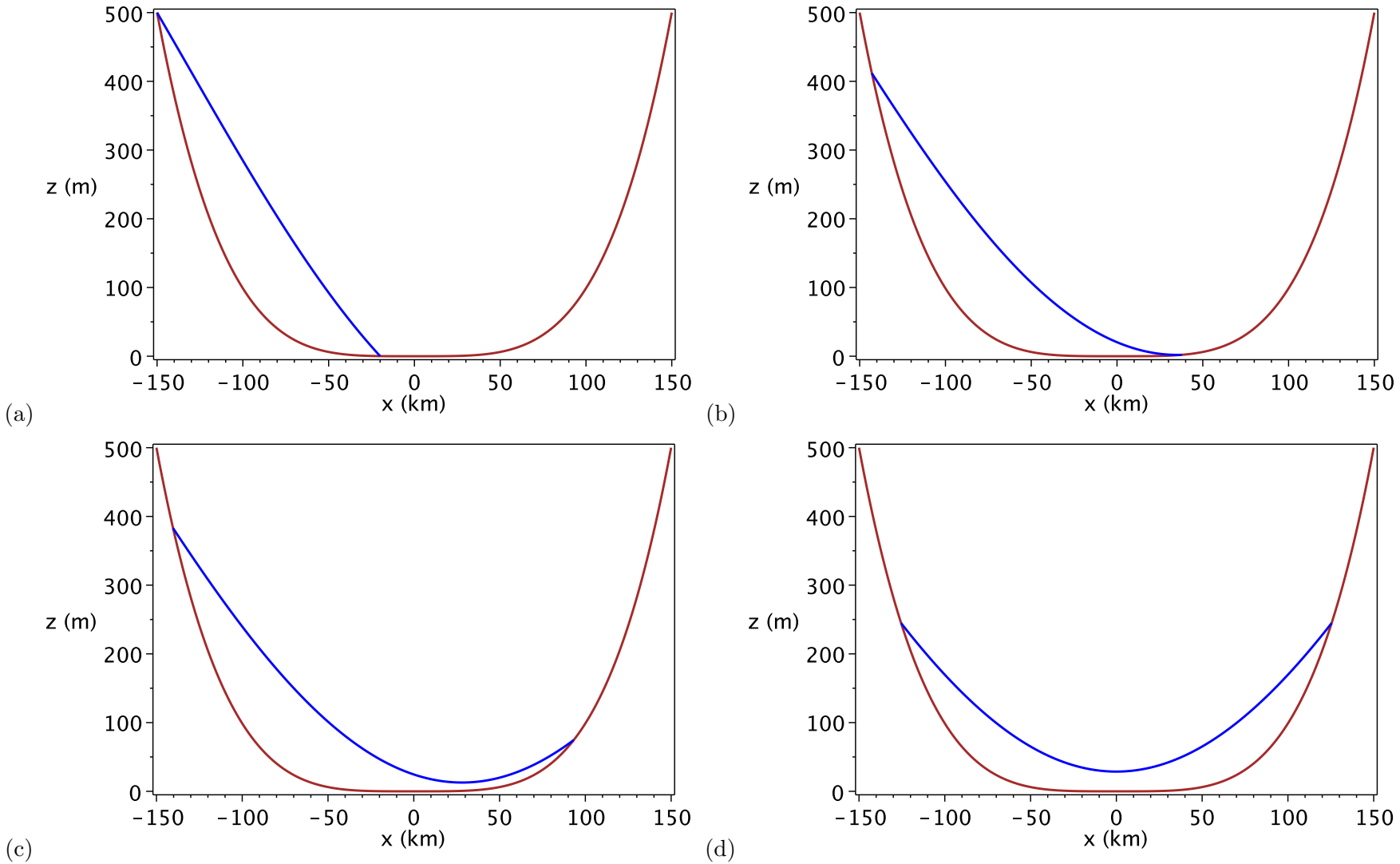

Figure 5.11: Along-channel profiles of the solution shown in Figure 5.10, at (a) $y = -500\,\mathrm{km} = -y_u$, (b) $y = -250\,\mathrm{km}$, (c) $y = -200\,\mathrm{km}$, and (d) $y = 0\,\mathrm{km}$.

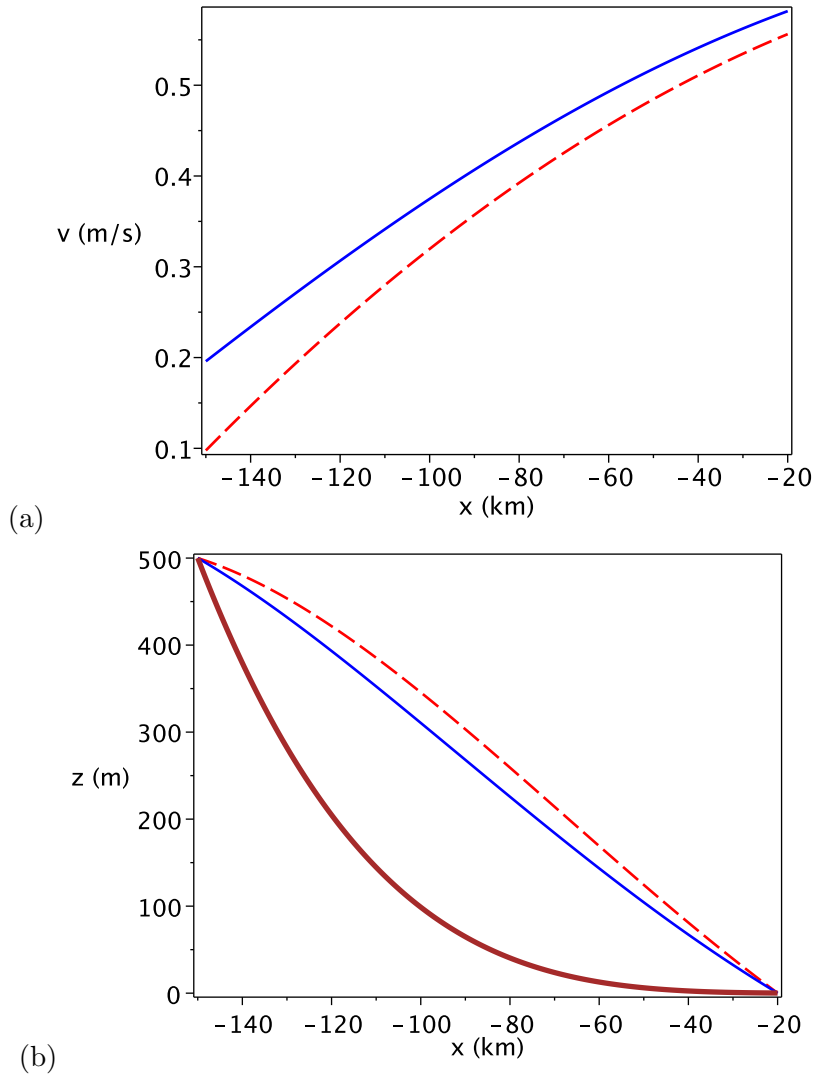

Figure 5.12: Plots of (a) the along-channel velocity and (b) the layer height at the upstream edge of the channel, both under the traditional approximation (dashed line) and with the complete Coriolis force (solid line). In (b) the thick solid line marks the bottom topography. All parameters match the solution shown in Figure 5.10, except $g' = 3 \times 10^{-4}\,\mathrm{m\,s^{-2}}$. The traditional and non-traditional along-channel transports T are 6.9 Sv and 6.8 Sv respectively.

qualitatively by redimensionalising (5.69a) and (5.69b) for an almost-westward channel,

$$\tfrac{1}{2}\beta\left(x + y\left(\tfrac{1}{2}\pi - \theta\right)\right)^2 - 2\Omega\left(h_b + \tfrac{1}{2}h\right) + v = A\left(y\right), \tag{5.76a}$$

$$\tfrac{1}{2}v^2 + g'\left(h_b + h\right) + \Omega h v = B, \tag{5.76b}$$

Here we have added an extra y-dependent term to both sides of (5.76a), without loss of generality. The left hand side is more easily recognisable as the angular momentum $\tilde{v}$ from (5.5) in an almost-westward channel, so (5.76a) states that $\tilde{v}$ is constant across the channel. This accounts for the fact that the fluid carries a planetary angular momentum that varies with the vertical av-

erage of its depth, as discussed in §5.2. Thus the fluid that lies higher up on the channel slope experiences a larger planetary angular momentum, and requires a larger along-channel velocity to balance it. Meanwhile, the large westward velocity induces a downward vertical acceleration via the non-traditional component of the Coriolis force in the three-dimensional equations. This leads to a positive contribution to the pressure in the Bernoulli equation (5.76b) via the Ωhv term. To compensate, the gravitational pressure $g(h_b + h)$ decreases, and so the current becomes shallower. These interpretations for Figure 5.12 are not robust, in that it is possible to find solutions that are counter-examples, but they provide an intuitive explanation for the effects of including the complete Coriolis force in typical solutions.

A consequence of these counteracting effects on the transport is that the non-traditional component of the Coriolis force modifies T more when g' is larger. This is counter-intuitive, because from (5.66) the non-traditional parameter δ is larger when g' is smaller, so we expect non-traditional effects to be more pronounced when the stratification is weak. In Figure 5.13 we plot the percentage change in the along-channel transport over a range of values of g', with all other parameters equal to those used in Figure 5.10. For $g' \gtrsim 10^{-3}\,\mathrm{m\,s^{-2}}$, including the complete Coriolis force leads to a clear increase in the transport. This is because g' is sufficiently large that the non-traditional contribution to the pressure is negligible compared to the gravitational terms in (5.76b), so the thickness h is almost identical in the traditional and non-traditional cases. Meanwhile the relative sizes of the terms in (5.76a) are independent of g', so there is still a substantial increase in the along-channel velocity v when the complete Coriolis force is included. For $g' \lesssim 10^{-3}\,\mathrm{m\,s^{-2}}$ the percentage change decreases rapidly, and, for $g' \lesssim 3.5 \times 10^{-4}\,\mathrm{m\,s^{-2}}$ the transport is actually slightly larger under the traditional approximation. This is because the non-traditional term in (5.76b) has become comparable in magnitude to the gravitational term, forcing the layer to become shallower (c.f. Figure 5.12) and reducing the transport. For $g \lesssim 2 \times 10^{-4}\,\mathrm{m\,s^{-2}}$ the solution fails to satisfy the boundary conditions (5.68a)–(5.68d).

Given this unusual dependence of the solution on g', it seems reasonable to analyse the effect of including the complete Coriolis force using a realistic reduced gravity for a weakly-stratified ocean, $g' = 10^{-3}\,\mathrm{m\,s^{-2}}$, and attribute the resulting unrealistically large velocities and transports to the absence of friction in the model. In Figure 5.14 we plot the transport T against the orientation of the channel θ for typical AABW-like parameters. The transport is quite sensitive to changes in θ, particularly when the complete Coriolis force is included. This is relevant to the AABW because the channel sketched in Figures 5.1 and 5.2, with $\theta \approx 1.43\,\mathrm{rad} \approx 82°$, is not an exact representation of the equatorial bathymetry. In general the cross-equatorial transport is larger when the complete Coriolis force is included, by almost 35% as $\theta \to 90°$. For $\theta \lesssim 70°$ the transports are approximately

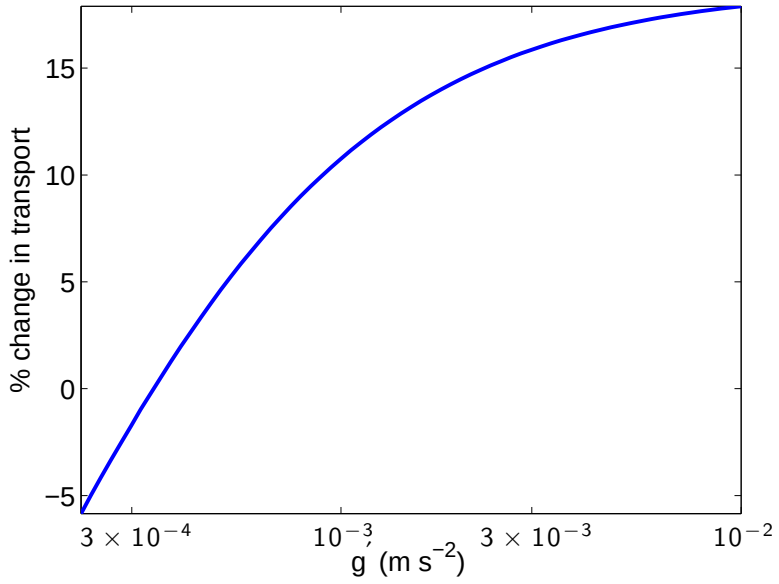

Figure 5.13: Percentage increase in the along-channel transport T when the complete Coriolis force is included, against the reduced gravity g'. In all solutions $L_u = -150\,\text{km}$, $R_u = -20\,\text{km}$, $y_u = 500\,\text{km}$, and $\theta = 1.43\,\text{rad} \approx 82°$.

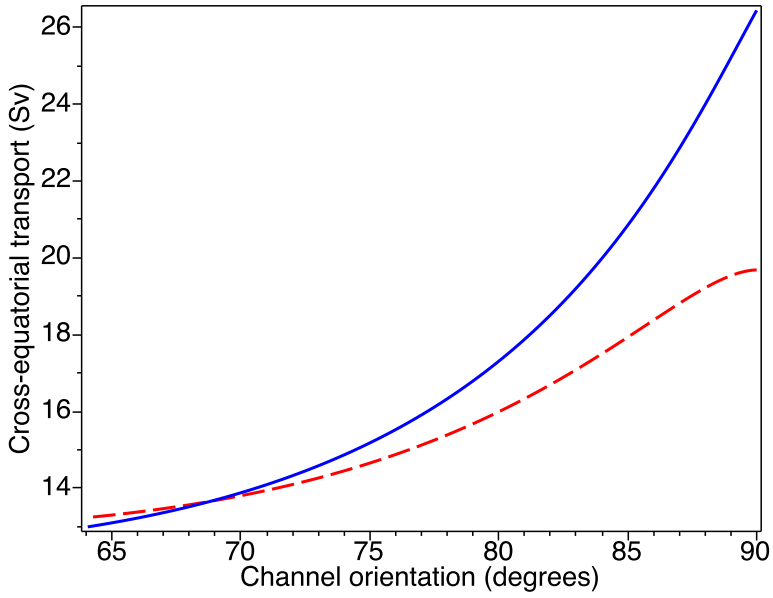

Figure 5.14: Plots of the along-channel transport T against the orientation of the channel θ, under the traditional approximation (dashed line) and including the complete Coriolis force (solid line). In all solutions $L_u = -150\,\text{km}$, $R_u = -20\,\text{km}$, $y_u = 500\,\text{km}$, and $g' = 10^{-3}\,\text{m}\,\text{s}^{-2}$.

equal, and for $\theta \lesssim 65°$ the solution breaks down, as the boundary conditions (5.68a)–(5.68d) are no longer satisfied.

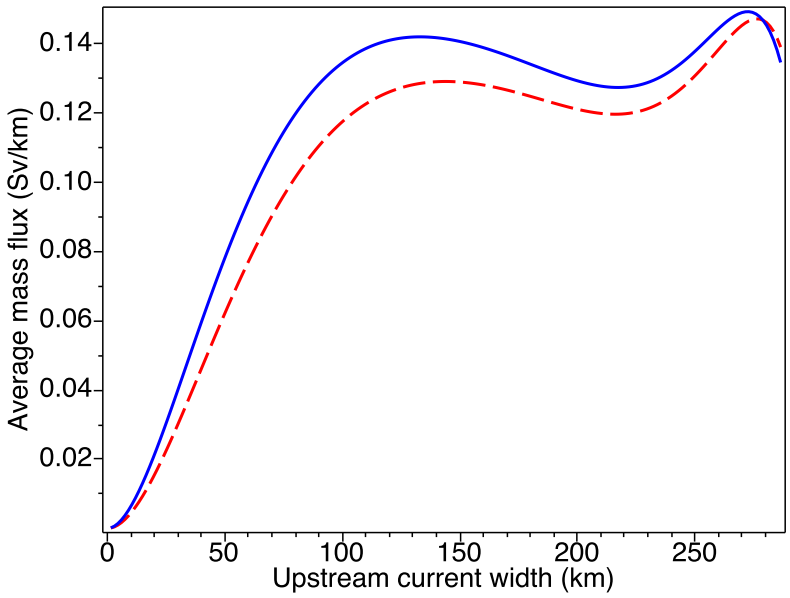

Figure 5.15: Plot of the average along-channel mass flux, T/x_u, against the upstream width, $x_u = R_u - L_u$, under the traditional approximation (dashed line) and including the complete Coriolis force (solid line). A straightforward plot of T against x_u obscures the detail in this plot. In all solutions $L_u = -150\,\mathrm{km}$, $y_u = 500\,\mathrm{km}$, $\theta = 1.43\,\mathrm{rad} \approx 82°$, and $g' = 10^{-3}\,\mathrm{m\,s^{-2}}$.

In Figure 5.15 we plot the average along-channel transport T/x_u against the upstream width $x_u = R_u - L_u$. This is perhaps the most difficult parameter to determine from observational evidence (*e.g.* Hall et al., 1997), because our solution represents only a swift core of the AABW, rather than the entire AABW water mass. In this solution T is typically proportional to x_u, except close to $x_u = 0$, so simply plotting T against x_u obscures some of the detail in Figure 5.15. This differs substantially from the solution of §5.3.6, in which the along-channel transport is independent of x_u under the traditional approximation. Again the cross-equatorial transport is typically larger when the complete Coriolis force is included, and may be as much as 30–40% larger in a narrow current. As x_u approaches the width of the channel (300 km), the solution fails to satisfy the boundary conditions (5.68a)–(5.68d).

5.5 Discussion

We have investigated the role of the "non-traditional" component of the Coriolis force in cross-equatorial flow of abyssal currents through channel-like bathymetry. Our focus, particularly in §5.4, has been on the AABW, as an unexpectedly large portion of this current crosses the equator in the western Atlantic ocean. We have used the steady $1\frac{1}{2}$-layer shallow water equations as an idealised

model of a current, or of the swift core of a larger water mass. Our analysis has been greatly simplified by the assumption the current adheres to a state of zero potential vorticity to avoid inertial instability as it crosses the equator (see Hua et al., 1997). Measurements of the deep ocean suggest that this condition is approximately satisfied within 3° of the equator (Firing, 1987).

In §5.3 we obtained asymptotic solutions for flow through a flat-bottomed channel with vertical walls, crudely approximating the along-channel average of the real equatorial bathymetry, as shown in Figure 5.2. Following Nof and Olson (1993), our fundamental asymptotic assumption (5.17) was that the deformation radius R_d be small compared with the upstream position y_u, *i.e.* $\varepsilon^{1/2} = R_d/y_u \ll 1$. Furthermore, we assumed in (5.18) that y_u was the relevant along-channel lengthscale, and that εR_d was the relevant cross-channel lengthscale. Applying these scalings, which describe a long, narrow current, yields leading-order equations (5.22a)–(5.22b) that may be integrated exactly, and that are independent of the cross-channel velocity u. The solution may be calculated explicitly, at least in principle, everywhere except close to $y = 0$, where the asymptotic assumptions are violated. We therefore connected the solutions in $y < 0$ and $y > 0$ via conservation of mass and Bernoulli energy. The resulting solution is characterised by Figure 5.5, which shows the change in the positions of the fronts along the channel.

The validity of the solutions obtained in §5.3 becomes questionable when the orientation of the channel is close to westward or eastward. When θ is sufficiently close to $\pm\pi/2$ that $\cos\theta$ becomes $\mathcal{O}(\varepsilon)$, the dimensionless Coriolis parameter $\hat{f} = \hat{y}\cos\theta + \varepsilon\hat{x}\sin\theta$ becomes asymptotically small. Maintaining the leading-order cross-channel geostrophic balance (5.51) thus requires an $\mathcal{O}(\varepsilon^{-1})$ along-channel velocity v. This motivates the alternative scaling in §5.4, in which the channel is almost-eastward or almost-westward, and in which the $\hat{x}$-dependent part of $\hat{f}$ is retained at leading order. This scaling permits arbitrary cross-channel variations of the bottom topography $z = h_b(x)$, allowing us to bring our idealised topography into better agreement with the averaged bathymetry shown in Figure 5.2. The method of solution is similar to that described in §5.3, though the arbitrary topography quickly leads to algebra that is too complicated to interpret directly.

The most obvious difference between the results of §5.3 and §5.4 is that the solutions in an almost-westward channel no longer break down close to $y = 0$, as shown in Figures 5.10 and 5.11. Instead, they undergo a rapid transition to cross-channel flow as they cross the equator. This transition is smooth when the current is sufficiently wide, but forms a discontinuity if the current is too narrow upstream. A complete description of the channel-crossing flow is possible because the positions of the fronts, $x = L(y)$ and $x = R(y)$, are unconstrained. In §5.3 the current enters from the south with a finite depth at the western wall, and no mechanism is provided for it to detach from the wall and cross the channel, so the breakdown of the solution is inevitable.

In both solutions the paths of the fronts are minimally affected by the inclusion of the complete Coriolis force, whilst the along-channel velocity v, and therefore the along-channel transport, is much more strongly affected. As discussed in §5.3.7, this is a direct consequence of cross-channel geostrophic balance, and leads to a larger transport in a westward channel and a smaller transport in an eastward channel. The difference is particularly pronounced if the current is narrower, which corresponds to larger gradients in the surface height and larger accelerations due to the non-traditional component of the Coriolis force. An alternative interpretation is that equations (5.26a), (5.54a) and (5.69a) are statements of cross-channel conservation of along-channel angular momentum $\tilde{v}$, as defined in (5.5). When the complete Coriolis force is included, the fluid acquires an additional westward velocity to balance the additional planetary angular momentum it acquires when its half-layer depth $\overline{z} = h_b + \frac{1}{2}h$ is larger. This increases the transport through a westward channel and reduces the transport through an eastward channel. The results of §5.4.3 confirm that the effect of including the complete Coriolis force is most pronounced when the channel is almost westward, as shown in Figure 5.14. The effect is also more pronounced when the current is narrower, though this is difficult to discern from Figure 5.15.

The solutions obtained in this chapter suggest that the non-traditional component of the Coriolis force may account for 10–30% of the cross-equatorial transport of the AABW. We might expect to see a similar increase in the cross-equatorial transport in more sophisticated models, or even in the real ocean, as long as the current remains in near-geostrophic balance close to the equator. However, an idealised model such as this omits many potentially important features of the abyssal dynamics. Our solutions overpredict the along-channel velocity and transport, due to the absence of frictional effects. These may be expected to be particularly important for an abyssal current flowing over highly variable bathymetry. We also do not account for mixing of the AABW with the less dense overlying layers. Possibly the most important omission is time dependence, as there is no guarantee that the steady states calculated here would be stable solutions of the time-dependent equations. For example, the numerical solutions of Nof and Borisov (1998) and Choboter and Swaters (2000) for shallow water flow in an idealised channel suggest that unsteady solutions could completely diverge from those presented here. In Chapter 6 we use unsteady numerical solutions of the non-traditional shallow water equations (5.1)–(5.2) to study the role of the complete Coriolis force in transporting fluid through a cross-equatorial channel.

Chapter 6

A numerical study of cross-equatorial flow through channel-like bathymetry

6.1 Introduction

In this chapter we use time-dependent numerical solutions of the shallow water equations derived in Chapter 2 to study the flow of cross-equatorial currents through abyssal channels. We first obtain a numerical scheme for the single-layer shallow water equations that exactly conserves total energy and potential enstrophy, in the absence of explicit dissipation. We then apply this scheme to flow through an idealised channel, and through realistic equatorial bathymetry for the AABW.

Cross-equatorial flow through abyssal channels presents a challenging problem. Such currents are difficult to observe directly, and their interaction with the highly variable ocean bathymetry makes them difficult to analyse theoretically. As a result, many of the previous studies in this area have relied heavily on numerical modelling. Killworth (1991) performed one- and two-dimensional simulations of cross-equatorial geostrophic adjustment, and showed that fluid can not penetrate beyond around two deformation radii beyond the equator via adjustment alone. Later Edwards and Pedlosky (1998) showed that dissipation by eddies allows modification of the fluid's potential vorticity, which allows fluid to travel far beyond the equator in the real ocean. Nof and Borisov (1998) solved compared the traditional shallow water equations with a "solid-balls" model, which describes the paths of a number of particles moving freely over topography (see Ripa, 1997; Borisov and Nof, 1998), in a northward cross-equatorial channel. They found that the resulting dynamics were sensitive to the steepness of the channel and the upstream width of the current, which allowed the solution to vary from a completely cross-equatorial flow and an entirely retroflecting flow.

Stephens and Marshall (2000) modelled AABW flow throughout the Atlantic ocean using the

frictional-geostrophic shallow water equations, which allow friction to balance pressure gradients at the equator. Their results agree qualitatively well with the measured path of the AABW, though the resolution of their numerical grid does not permit a detailed description of the cross-equatorial flow. Choboter and Swaters (2000) compared the traditional shallow water equations with the frictional-geostrophic equations in an idealised cross-equatorial channel. They found that the frictional-geostrophic equations struggle to model the strongly-inertial channel flow (Nof and Borisov, 1998), but capture some features of the solution well. Choboter and Swaters (2004) performed a similar comparison with realistic equatorial bathymetry, and were able to bring their model into good agreement with the measured cross-equatorial transport for the AABW.

Shallow water equations feature frequently in the previous literature on abyssal cross-equatorial flow, so using our non-traditional equations allows us to compare directly with much of the previous work on the AABW and other currents. The equations' two-dimensional description of the three-dimensional flow simplifies computation considerably, and they are an intuitive model of a current whose density differs sharply from the surrounding water mass. Additionally, the shallow water equations isolate the interaction between the principle effects of rotation, stratification and friction, with no influence from other physical processes. This elucidates the role of the complete Coriolis force, which may be obscured by the myriad of physical parametrisations present in general circulation models (*e.g.* Cullen, 1993).

In §6.2 we derive a numerical scheme for the non-traditional shallow water equations that exactly conserves total discrete energy and potential enstrophy. This is based on Salmon's (2004) reformulation of the Arakawa-Lamb scheme (Arakawa and Lamb, 1981). In §6.3 we apply this scheme to cross-equatorial flow through a channel oriented at various angles to the equator. We show that the non-traditional component of the Coriolis force is most prominent when the channel is almost-westward, as it is in the case of the AABW.

6.2 A numerical scheme for the non-traditional shallow water equations

Arakawa and Lamb (1981) derived a finite-difference discretisation of the inviscid shallow water equations that exactly conserves total mass, energy, and potential enstrophy. Long-term integrations using non-conservative finite-difference schemes are prone to a spurious cascade of energy towards the scale of the grid spacing, where the spatial truncation error is largest (see *e.g.* Arakawa, 1966). Conserving the discrete analogue of total energy alone does not prevent the cascade of energy to small scales, and leads to an increase in potential enstrophy (Arakawa and Lamb, 1977). Thus

long-time integrations require a scheme that conserves both energy and potential enstrophy. These are the conservation properties that determine the inverse cascade of energy to large scales, and the forward cascade of enstrophy to small scales, in two-dimensional turbulence. Enforcing these conservation properties also guards against nonlinear instabilities. For example, Fornberg (1973) showed that the only stable member of a class of centred finite difference schemes for the inviscid Burgers equation is the scheme with a discrete energy conservation property.

Ideally our shallow water scheme should materially conserve potential vorticity, as this is a crucial dynamical variable in large-scale geophysical flows (Muller, 1995), but on an Eulerian grid the best we can achieve is conservation of total potential enstrophy. It is possible to enforce material conservation of potential vorticity via Lagrangian schemes such as the particle-mesh method (*e.g.* Frank et al., 2002) or the contour-advective semi-Lagrangian method (*e.g.* Dritschel et al., 1999). However, our numerical scheme is motivated by cross-equatorial flow of abyssal ocean currents, discussed in Chapters 4 and 5, and in later sections of this chapter. Such flows invariably require grounding lines, where the surface of the fluid layer intersects the bottom topography. Salmon (1983) derived a Lagrangian scheme, via a Hamiltonian formulation, that describes the time-evolution of discrete blobs of fluid, and so incorporates grounding lines by definition. The main drawback of the Lagrangian approach is that inflow and outflow boundary conditions are required in a non-periodic domain, and these are much more difficult to prescribe in terms of potential vorticity contours or discrete blobs than they are on an Eulerian grid.

Arakawa and Lamb (1981) originally obtained their scheme via direct algebraic manipulation of arbitrary discretisations of the shallow water equations. Salmon (2004) later showed that this scheme, and others like it, could be represented using the methods of Hamiltonian mechanics. A Hamiltonian formulation is a natural approach to the development of conservative schemes because symmetries of the Hamiltonian system correspond directly to conservation laws in the dynamical equations, via Noether's theorem. Salmon (1988, 1998), Shepherd (1990), and Morrison (1998) review the application of Hamiltonian methods to the broader field of fluid mechanics. In this section we extend Salmon's (2004) approach to single-layer shallow water equations that include the complete Coriolis force.

6.2.1 Hamiltonian–Poisson bracket formulation

We have previously discussed the Hamiltonian–Poisson bracket formulation of the shallow water equations in Chapter 2, for the case of the multi-layer shallow water equations. This formulation permits a concise derivation of an energy- and potential enstrophy-conserving scheme for the non-traditional shallow water equations, which would otherwise present an enormous task. First, we

restate here the Hamiltonian–Poisson bracket formulation of the single-layer shallow water equations. It is convenient to use slightly modified canonical variables,

$$\tilde{\boldsymbol{u}} = (\tilde{u}, \tilde{v}), \qquad \tilde{u} = u + 2\Omega_y \left(h_b + \tfrac{1}{2}h\right), \qquad \tilde{v} = v - 2\Omega_x \left(h_b + \tfrac{1}{2}h\right). \tag{6.1}$$

We retain arbitrary orientation of the x and y axes, and allow for arbitrary spatial variation of the components of the rotation vector, $\Omega_x(x, y)$, $\Omega_y(x, y)$, and $\Omega_z(x, y)$. This definition of $\tilde{\boldsymbol{u}}$ differs from the canonical momenta $\boldsymbol{p}$ in Chapter 2, equations (2.69) and (2.75), as the F and G terms that constitute the potential for the vertical component of the Coriolis parameter, $f = 2\Omega_z$, are omitted. Thus $\boldsymbol{u}$ no longer corresponds to the components of the fluid's absolute angular momentum, given in Chapter 5, equation (5.5). It will be necessary to transform between $\boldsymbol{u}$ and $\tilde{\boldsymbol{u}}$ frequently during numerical integration, and this choice of $\tilde{\boldsymbol{u}}$ eliminates some superfluous computation and simplifies the derivation of the numerical scheme.

The definition (6.1) allows us to rewrite the non-traditional single-layer shallow water equations of Dellar and Salmon (2005) in the vector-invariant form (*c.f.* Arakawa and Hsu, 1990),

$$\frac{\partial \tilde{u}}{\partial t} - hqu + \frac{\partial \Phi}{\partial x} = 0, \tag{6.2a}$$

$$\frac{\partial \tilde{v}}{\partial t} + hqv + \frac{\partial \Phi}{\partial y} = 0, \tag{6.2b}$$

$$\frac{\partial h}{\partial t} + \frac{\partial}{\partial x}(hu) + \frac{\partial}{\partial y}(hv) = 0, \tag{6.2c}$$

where q is the potential vorticity

$$q = \frac{1}{h}\left(2\Omega_z + \frac{\partial \tilde{v}}{\partial x} - \frac{\partial \tilde{u}}{\partial y}\right), \tag{6.3}$$

and Φ is the Bernoulli potential,

$$\Phi = \tfrac{1}{2}u^2 + \tfrac{1}{2}v^2 + g(h_b + h) + h\left(\Omega_x v - \Omega_y u\right). \tag{6.4}$$

Here we have mixed our use of the velocity $\boldsymbol{u}$ and the canonical variables $\tilde{\boldsymbol{u}}$ to present the equations in a familiar form. However, the velocity will be treated as an explicit function of the canonical variables and the layer thickness via (6.1), $\boldsymbol{u} = \boldsymbol{u}(\tilde{\boldsymbol{u}}, h)$. The Hamiltonian for equations (6.2a)–(6.2c) is simply the total energy, which is independent of the Coriolis force,

$$\mathcal{H} = \iint \mathrm{d}\boldsymbol{x} \left\{ \tfrac{1}{2}h\left(u^2 + v^2\right) + gh\left(h_b + \tfrac{1}{2}h\right) \right\}, \tag{6.5}$$

although $\mathcal{H} = \mathcal{H}\left[\boldsymbol{u}(\tilde{\boldsymbol{u}}, h), h\right]$ is treated as a functional of the canonical variables. We do not specify a domain of integration for this functional, but assume that the boundaries of the domain are periodic,

or permit no normal flux, to allow us to integrate by parts as necessary below without acquiring boundary terms. Following Salmon (1988), the time-evolution of any functional $\mathcal{F}$ is given by

$$\frac{\mathrm{d}\mathcal{F}}{\mathrm{d}t} = \{\mathcal{F}, \mathcal{H}\}\,. \tag{6.6}$$

where the Poisson bracket (*c.f.* Salmon, 1988) is defined as

$$\{\mathcal{A}, \mathcal{B}\} = \iint \mathrm{d}\boldsymbol{x} \left\{ q \left(\frac{\delta \mathcal{A}}{\delta \tilde{u}} \frac{\delta \mathcal{B}}{\delta \tilde{v}} - \frac{\delta \mathcal{B}}{\delta \tilde{u}} \frac{\delta \mathcal{A}}{\delta \tilde{v}} \right) - \frac{\delta \mathcal{A}}{\delta \tilde{\boldsymbol{u}}} \cdot \nabla \frac{\delta \mathcal{B}}{\delta h} + \frac{\delta \mathcal{B}}{\delta \tilde{\boldsymbol{u}}} \cdot \nabla \frac{\delta \mathcal{A}}{\delta h} \right\}, \tag{6.7}$$

for any pair of functionals $\mathcal{A}$ and $\mathcal{B}$. Note that the functional derivatives in (6.7) are defined with respect to the canonical variables $\tilde{\boldsymbol{u}}$ and h, so this bracket reduces to the traditional Poisson bracket of Salmon (2004) when $\Omega_x = \Omega_y = 0$, since $\tilde{\boldsymbol{u}} \to \boldsymbol{u}$. Setting $\mathcal{F} = \tilde{u}(\boldsymbol{x}_0, t)$, $\mathcal{F} = \tilde{v}(\boldsymbol{x}_0, t)$ and $\mathcal{F} = h(\boldsymbol{x}_0, t)$, where $\boldsymbol{x}_0$ is a specified fixed location, in (6.6) yields equations (6.2a), (6.2b) and (6.2c) respectively.

For example, let $h_0 = h(\boldsymbol{x}_0, t)$, and set $\mathcal{F} = h_0$ in (6.6) to obtain

$$\frac{\mathrm{d}h_0}{\mathrm{d}t} = \{h_0, \mathcal{H}\} = \iint \mathrm{d}\boldsymbol{x} \left\{ q \left(\frac{\delta h_0}{\delta \tilde{u}} \frac{\delta \mathcal{H}}{\delta \tilde{v}} - \frac{\delta \mathcal{H}}{\delta \tilde{u}} \frac{\delta h_0}{\delta \tilde{v}} \right) - \frac{\delta h_0}{\delta \tilde{\boldsymbol{u}}} \cdot \nabla \frac{\delta \mathcal{H}}{\delta h} + \frac{\delta \mathcal{H}}{\delta \tilde{\boldsymbol{u}}} \cdot \nabla \frac{\delta h_0}{\delta h} \right\}.$$

For the purpose of taking variational derivatives, $\tilde{\boldsymbol{u}}$ and h are treated as independent variables so $\delta h_0 / \delta \tilde{\boldsymbol{u}} = 0$. Meanwhile $\boldsymbol{u}$ is treated as an explicit function of $\tilde{\boldsymbol{u}}$ and h, so by the variational chain rule

$$\frac{\delta \mathcal{H}}{\delta \tilde{\boldsymbol{u}}} = \left.\frac{\delta \mathcal{H}}{\delta \tilde{\boldsymbol{u}}}\right|_{\boldsymbol{u}} + \left(\frac{\delta \mathcal{H}}{\delta \boldsymbol{u}} \cdot \frac{\partial \boldsymbol{u}}{\partial \tilde{u}}, \frac{\delta \mathcal{H}}{\delta \boldsymbol{u}} \cdot \frac{\partial \boldsymbol{u}}{\partial \tilde{v}} \right) = \left(\frac{\delta \mathcal{H}}{\delta u}, \frac{\delta \mathcal{H}}{\delta v} \right) = \frac{\delta \mathcal{H}}{\delta \boldsymbol{u}} = h\boldsymbol{u}, \tag{6.8}$$

where the $|_{\boldsymbol{u}}$ indicates that $\boldsymbol{u}$ is held constant while the variational derivative with respect to $\tilde{\boldsymbol{u}}$ is taken. Now $\delta h_0 / \delta h$ is nonzero only at $\boldsymbol{x} = \boldsymbol{x}_0$, so

$$\frac{\mathrm{d}h_0}{\mathrm{d}t} = \iint \mathrm{d}\boldsymbol{x} \left\{ \frac{\delta \mathcal{H}}{\delta \boldsymbol{u}} \cdot \nabla \frac{\delta h(\boldsymbol{x}_0, t)}{\delta h(\boldsymbol{x}, t)} \right\} = \iint \mathrm{d}\boldsymbol{x} \left\{ h\boldsymbol{u} \cdot \nabla\, \delta(\boldsymbol{x} - \boldsymbol{x}_0) \right\} \tag{6.9}$$

Finally, we integrate by parts and use the divergence theorem with the periodic or no-flux boundary conditions to obtain

$$\frac{\mathrm{d}}{\mathrm{d}t} h(\boldsymbol{x}_0, t) = \iint \mathrm{d}\boldsymbol{x} \left\{ -\nabla \cdot (h\boldsymbol{u})\, \delta(\boldsymbol{x} - \boldsymbol{x}_0) \right\} = -\nabla \cdot (h\boldsymbol{u}) \Big|_{\boldsymbol{x} = \boldsymbol{x}_0} \tag{6.10}$$

Thus we recover the mass conservation equation (6.2c). Written in the form (6.2a)–(6.4), the only qualitative modification of the shallow water equations is in the Bernoulli potential $\Phi = \delta H / \delta h$. This is due to the dependence of the physical velocity $\boldsymbol{u}$ on the layer thickness h. Applying the variational chain rule,

$$\Phi = \left.\frac{\delta}{\delta h}\right|_{\tilde{\boldsymbol{u}}} H\left[\boldsymbol{u}(\tilde{\boldsymbol{u}}, h), h\right] = \left.\frac{\delta H}{\delta h}\right|_{\boldsymbol{u}} + \left.\frac{\delta H}{\delta \boldsymbol{u}}\right|_{h} \cdot \left.\frac{\partial \boldsymbol{u}}{\partial h}\right|_{\tilde{\boldsymbol{u}}} = \left.\frac{\delta H}{\delta h}\right|_{\boldsymbol{u}} - \Omega_y \left.\frac{\delta H}{\delta u}\right|_{v,h} + \Omega_x \left.\frac{\delta H}{\delta v}\right|_{u,h}, \tag{6.11}$$

leads to (6.4) on evaluating the remaining variational derivatives.

The conservation properties of the shallow water equations (6.2a)–(6.2c) correspond directly to symmetries of the Hamiltonian and Poisson bracket. Conservation of energy is an immediate consequence of the antisymmetry of the Poisson bracket, $\{\mathcal{F},\mathcal{F}\}=0$ for any functional $\mathcal{F}$. From (6.6), the rate of change of the total energy $\mathcal{H}$ is

$$\frac{\mathrm{d}\mathcal{H}}{\mathrm{d}t}=\{\mathcal{H},\mathcal{H}\}=0, \tag{6.12}$$

so energy is conserved. The other two quantities of interest are the potential enstrophy $\mathcal{P}$ and the mass $\mathcal{M}$, where

$$\mathcal{P}=\iint \mathrm{d}\boldsymbol{x}\left\{\tfrac{1}{2}hq^2\right\},\qquad \mathcal{M}=\iint \mathrm{d}\boldsymbol{x}\left\{h\right\}. \tag{6.13}$$

Both $\mathcal{P}$ and $\mathcal{M}$ are Casimirs of the Poisson bracket, meaning that the bracket of $\mathcal{P}$ or $\mathcal{M}$ with any functional $\mathcal{F}$ is zero,

$$\{\mathcal{P},\mathcal{F}\}=\{\mathcal{M},\mathcal{F}\}=0. \tag{6.14}$$

Again, setting $\mathcal{F}=\mathcal{P}$ and $\mathcal{F}=\mathcal{M}$ in (6.6) immediately leads to $\mathrm{d}\mathcal{P}/\mathrm{d}t=0$ and $\mathrm{d}\mathcal{M}/\mathrm{d}t=0$ using (6.14), so total potential enstrophy and mass are also conserved. In fact, the shallow water equations conserve an infinite class of Casimirs $\mathcal{C}$ of the form

$$\mathcal{C}=\iint \mathrm{d}\boldsymbol{x}\left\{h\,G(q)\right\}, \tag{6.15}$$

where $G(q)$ is an arbitrary function of the potential vorticity. By the chain rule, it is sufficient to show that

$$\{\tilde{\boldsymbol{u}},\mathcal{C}\}=\{h,\mathcal{C}\}=0 \tag{6.16}$$

to prove that $\mathcal{C}$ is a Casimir, as any functional $\mathcal{F}$ must be defined in terms of $\tilde{\boldsymbol{u}}$ and h. The non-traditional shallow water equations conserve Casimirs of exactly the same form (6.15) as the traditional equations, but with a different q, because making the traditional approximation amounts to replacing $\tilde{\boldsymbol{u}}$ by $\boldsymbol{u}$ everywhere in (6.3), (6.7) and (6.16).

6.2.2 Hamiltonian interpretation of the Arakawa-Lamb scheme

Arakawa and Lamb (1981) discretised the traditional shallow water equations on the Arakawa C-grid (see Arakawa and Lamb, 1977), in which the variables u, v, h and q are staggered over different gridpoints. This arrangement is illustrated in Figure 6.1. The layer thickness $h_{i+1/2,j+1/2}$ may be thought of as defining the volume of the cell bounded by the points (i,j), $(i+1,j)$, $(i,j+1)$ and $(i+1,j+1)$, with the flow between cells defined by $u_{i,j+1/2}$, $u_{i+1,j+1/2}$, $v_{i+1/2,j}$ and $v_{i+1/2,j+1}$. The potential vorticities $q_{i,j}$ are calculated from quantities defined on the other gridpoints, but are sufficiently distinguished in the numerical scheme to merit a separate definition on the corners of the cells. The spacing between adjacent gridpoints of the same variable is d.

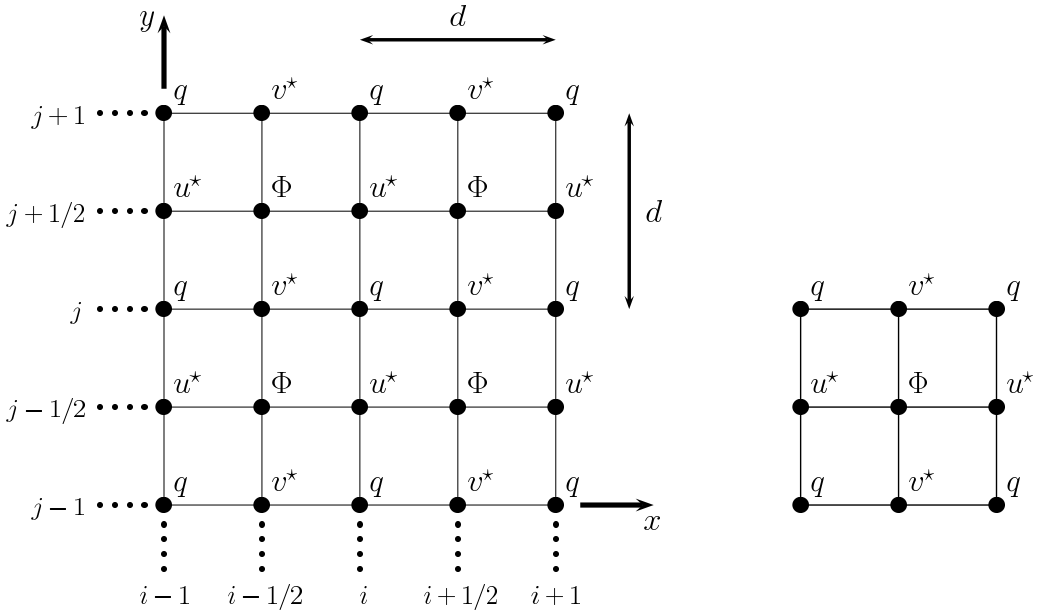

Figure 6.1: Staggered layout of the variables on the Arakawa C-grid (left), showing the indices of the computational grid and its alignment with the coordinate axes, and (right) a schematic showing the layout of the variables in an individual computational cell.

The spurious energy cascades observed in non-conservative long-time integrations are due to errors introduced in the spatial, rather than temporal, discretisation (Arakawa and Lamb, 1977). The Arakawa and Lamb (1981) scheme therefore discretises only the spatial derivatives of the traditional shallow water equations, yielding ordinary differential equations for the time derivatives of $u_{i,j+1/2}(t)$, $v_{i+1/2,j}(t)$, $h_{i+1/2,j+1/2}(t)$ at all grid points. This approach is also more general and more straightforward than considering a particular time-integration scheme, such as the Adams-Bashforth 3^{rd}-order scheme used in §6.3.

Arakawa and Lamb (1981) pose a somewhat arbitrary spatial discretisation of the shallow water equations that includes unphysical Coriolis terms that vanish in the limit $d \to 0$. They obtain a scheme that conserves discrete energy and potential enstrophy via direct algebraic manipulation of the discrete equations. Salmon (2004) illuminates this somewhat obscure derivation by framing it in terms of a discrete Hamiltonian and Poisson bracket, whose symmetries correspond to the desired conservation laws. This is a much more general approach to the construction of numerical schemes that preserve conservation laws, as symmetries of the discrete Hamiltonian and Poisson bracket correspond directly to conservation properties of the discrete evolution equations via Noether's theorem.

Following Salmon (2004), we discretise the Hamiltonian for the traditional shallow water equa-

tions as

$$H = \sum_{i,j} \tfrac{1}{2} h_{i+1/2,j+1/2} \left(\overline{u^2}^{i}_{i+1/2,j+1/2} + \overline{v^2}^{j}_{i+1/2,j+1/2} \right) + g h_{i+1/2,j+1/2} (h_b + \tfrac{1}{2} h)_{i+1/2,j+1/2}, \quad (6.17)$$

which is a natural discretisation of the total energy (6.5) on the C-grid. For convenience, we drop the factor of d^2 that would be required to make (6.17) a discrete representation of the integral $\iint \mathrm{d}\boldsymbol{x}$, as constants multiplying H make no contribution to the dynamics. The overbars on $\overline{u^2}^{i}$ and $\overline{v^2}^{j}$ denote averages over the two adjacent gridpoints in the i- and j-directions respectively,

$$\overline{u^2}^{i}_{i+1/2,j+1/2} = \tfrac{1}{2} \left(u^2_{i,j+1/2} + u^2_{i+1,j+1/2} \right), \qquad \overline{v^2}^{j}_{i+1/2,j+1/2} = \tfrac{1}{2} \left(v^2_{i+1/2,j} + v^2_{i+1/2,j+1} \right) \quad (6.18)$$

The discrete Poisson bracket is considerably more complicated. We follow Salmon's (2004) notation, and split the bracket into a potential vorticity-dependent part and a remaining part,

$$\{A, B\} = \{A, B\}_Q + \{A, B\}_R \,, \quad (6.19)$$

where A and B are algebraic functions of $u_{i,j+1/2}$, $v_{i+1/2,j}$, and $h_{i+1/2,j+1/2}$ for all i and j. The q-dependent part is

$$\{A, B\}_Q = \sum_{i,j} q_{i,j} \sum_{\boldsymbol{n},\boldsymbol{m}} \left\{ \alpha_{\boldsymbol{n},\boldsymbol{m}} \frac{\partial(A,B)}{\partial \left(u_{(i,j+1/2)+\boldsymbol{n}}, v_{(i+1/2,j)+\boldsymbol{m}} \right)} \right.$$
$$\left. + \beta_{\boldsymbol{n},\boldsymbol{m}} \frac{\partial(A,B)}{\partial \left(u_{(i,j+1/2)+\boldsymbol{n}}, u_{(i,j+1/2)+\boldsymbol{m}} \right)} + \gamma_{\boldsymbol{n},\boldsymbol{m}} \frac{\partial(A,B)}{\partial \left(v_{(i+1/2,j)+\boldsymbol{n}}, v_{(i+1/2,j)+\boldsymbol{m}} \right)} \right\}, \quad (6.20)$$

where

$$\frac{\partial(A,B)}{\partial(u,v)} = \frac{\partial A}{\partial u}\frac{\partial B}{\partial v} - \frac{\partial B}{\partial u}\frac{\partial A}{\partial v} \quad (6.21)$$

is the Jacobian of A and B with respect to u and v. The variational derivatives from (6.7) have reduced to partial derivatives in (6.20), as in Hamiltonian particle mechanics. The indices $\boldsymbol{n} = (n_x, n_y)$ and $\boldsymbol{m} = (m_x, m_y)$ are integers and the coefficients $\alpha_{\boldsymbol{m},\boldsymbol{n}}$, $\beta_{\boldsymbol{m},\boldsymbol{n}}$, and $\gamma_{\boldsymbol{m},\boldsymbol{n}}$ are only nonzero within a stencil of M gridpoints, *i.e.* for $|n_x|, |n_y|, |m_x|, |m_y| < M$. The Jacobians of the form $\partial(A,B)/\partial(u,u)$ and $\partial(A,B)/\partial(v,v)$ lead to the unphysical Coriolis terms in the Arakawa–Lamb scheme (which vanish in the limit $d \to 0$). However, these terms are necessary to conserve potential enstrophy on a staggered grid (Salmon, 2004), and they are consistent with the overall second-order accuracy of the scheme, since they introduce only an $\mathcal{O}(d^2)$ error. The residual part of the bracket is

$$\{A, B\}_R = \frac{1}{d} \sum_{i,j} \left\{ \frac{\partial B}{\partial u_{i,j+1/2}} \left(\frac{\partial A}{\partial h_{i+1/2,j+1/2}} - \frac{\partial A}{\partial h_{i-1/2,j+1/2}} \right) \right.$$
$$\left. + \frac{\partial B}{\partial v_{i+1/2,j}} \left(\frac{\partial A}{\partial h_{i+1/2,j+1/2}} - \frac{\partial A}{\partial h_{i+1/2,j-1/2}} \right) - (A \longleftrightarrow B) \right\} \quad (6.22)$$

where $(A \longleftrightarrow B)$ indicates that the terms in (6.22) should be repeated with A and B exchanged. We have discretised the gradient ∇ in the continuous Poisson bracket (6.7) using second-order central finite differences. In (6.17), (6.20) and (6.22) we employ indices that are specific to the Arakawa–Lamb scheme, whilst Salmon (2004) used integer indices for all gridpoints because this is more practical when considering several grid systems. As a result, the coefficients $\alpha_{\boldsymbol{n},\boldsymbol{m}}$, $\beta_{\boldsymbol{n},\boldsymbol{m}}$, and $\gamma_{\boldsymbol{n},\boldsymbol{m}}$ correspond to those given by Salmon (2004) for the Arakawa–Lamb scheme, but the indices must be shifted accordingly.

The dynamics of the discrete system are analogous to (6.6),

$$\frac{\mathrm{d}F}{\mathrm{d}t} = \{F, H\}\,, \tag{6.23}$$

for any algebraic function F of the variables $u_{i,j+1/2}$, $v_{i+1/2,j}$ and $h_{i+1/2,j+1/2}$. Substituting $F = u_{i,j+1/2}$, $F = v_{i+1/2,j}$, and $F = h_{i+1/2,j+1/2}$ into (6.23) yields exactly the scheme described by Arakawa and Lamb (1981). Conservation of energy is again an immediate consequence of the antisymmetry of the Poisson bracket,

$$\frac{\mathrm{d}H}{\mathrm{d}t} = \{H, H\} = 0, \tag{6.24}$$

so the discrete system exactly conserves total energy. The Arakawa–Lamb scheme also conserves discrete potential enstrophy and mass, defined respectively as

$$P = \sum_{i,j} h^{(q)}_{i,j} q^2_{i,j}, \qquad M = \sum_{i,j} h_{i+1/2,j+1/2}, \tag{6.25}$$

where

$$q_{i,j} = \frac{1}{h^{(q)}_{i,j}} \left(2\Omega^{(z)}_{i,j} + \zeta_{i,j}\right) \tag{6.26}$$

are the potential vorticities,

$$\zeta_{i,j} = \frac{1}{d} \left(v_{i+1/2,j} - v_{i-1/2,j} - u_{i,j+1/2} + u_{i,j-1/2}\right) \tag{6.27}$$

are the relative vorticities, and

$$h^{(q)}_{i,j} = \tfrac{1}{4} \left(h_{i+1/2,j+1/2} + h_{i-1/2,j+1/2} + h_{i+1/2,j-1/2} + h_{i-1/2,j-1/2}\right). \tag{6.28}$$

is the appropriate average of h on the q-gridpoints. To clarify our notation we will write the components of the rotation vector as $\left(\Omega^{(x)}, \Omega^{(y)}, \Omega^{(z)}\right)$ throughout this section. As in the continuous case, conservation of P and M is guaranteed if they are Casimirs of the discrete Poisson bracket, *i.e.*

$$\{F, P\} = \{F, M\} = 0 \qquad \text{for any } F(u, v, h). \tag{6.29}$$

Following Salmon (2004), the coefficients $\{\alpha_{\boldsymbol{n},\boldsymbol{m}}, \beta_{\boldsymbol{n},\boldsymbol{m}}, \gamma_{\boldsymbol{n},\boldsymbol{m}}\}$ may be chosen such that

$$\left\{u_{i,j+1/2}, P\right\} = \left\{v_{i+1/2,j}, P\right\} = \left\{h_{i+1/2,j+1/2}, P\right\} = 0 \qquad \text{for all } i, j, \tag{6.30}$$

so P also satisfies (6.29) by the chain rule. The mass M satisfies condition (6.29) for any choice of the coefficients in (6.20) because $\partial M/\partial u_{i,j+1/2} = \partial M/\partial v_{i+1/2,j} = 0$ and $\partial M/\partial h_{i+1/2,j+1/2} = 1$.

6.2.3 Discrete schemes for the non-traditional equations

The discrete Hamiltonian and Poisson bracket allow us to obtain an energy- and potential enstrophy-conserving finite-difference scheme for the non-traditional shallow water equations (6.2a)–(6.2c) via minor modifications of the traditional scheme. We first replace the velocities $u_{i,j+1/2}$ and $v_{i+1/2,j}$ on the gridpoints with the canonical variables $\tilde{u}_{i,j+1/2}$ and $\tilde{v}_{i+1/2,j}$, and use these as our prognostic variables, as shown in Figure 6.2. We must then determine an appropriate means of computing the physical velocities. For now, we define $u_{i,j+1/2}$ and $v_{i+1/2,j}$ using an arbitrarily-weighted average over the h-gridpoints,

$$u_{i,j+1/2} = \tilde{u}_{i,j+1/2} - \sum_{r,s} \mu_{r,s} \left[2\Omega^{(y)} \left(h_b + \tfrac{1}{2}h\right)\right]_{i+1/2+r,j+1/2+s}, \tag{6.31a}$$

$$v_{i+1/2,j} = \tilde{v}_{i+1/2,j} + \sum_{r,s} \xi_{r,s} \left[2\Omega^{(x)} \left(h_b + \tfrac{1}{2}h\right)\right]_{i+1/2+r,j+1/2+s}, \tag{6.31b}$$

where the summations are taken over all integers r and s. The weights $\mu_{r,s}, \xi_{r,s}$ must be chosen so that the right hand sides of (6.31a)–(6.31a) approximate (6.1) on the $\tilde{u}$ and $\tilde{v}$ gridpoints to at least second order in d. Thus in practice $\mu_{r,s} = \xi_{r,s} = 0$ for $|r|, |s| \geq N$, where N is the stencil size of the average. We also redefine the discrete potential and relative vorticity variables as

$$q_{i,j} = \frac{1}{h^{(q)}_{i,j}} \left(2\Omega^{(z)}_{i,j} + \tilde{\zeta}_{i,j}\right), \qquad \tilde{\zeta}_{i,j} = \frac{1}{d}\left(\tilde{v}_{i+1/2,j} - \tilde{v}_{i-1/2,j} - \tilde{u}_{i,j+1/2} + \tilde{u}_{i,j-1/2}\right) \tag{6.32}$$

Thus $\tilde{\zeta}$ is no longer the physical relative vorticity, but rather the two-dimensional curl of the canonical variables $\tilde{\boldsymbol{u}}$. It is implicit in (6.31a)–(6.31b) and (6.32) that the horizontal components of the rotation vector $\Omega^{(x)}, \Omega^{(y)}$ are defined on the h-gridpoints, in contrast to the vertical component $\Omega^{(z)}$, which is defined on the q-gridpoints. This choice has been made for convenience in deriving the discrete evolution equations.

As discussed in §2.5.1 of Chapter 2, the total energy is not changed when the complete Coriolis force is included. We therefore use exactly the same discrete Hamiltonian (6.17) for the non-traditional equations, but treat u and v as explicit functions of $\tilde{u}_{i,j+1/2}, \tilde{v}_{i+1/2,j}, h_{i+1/2,j+1/2}$ via

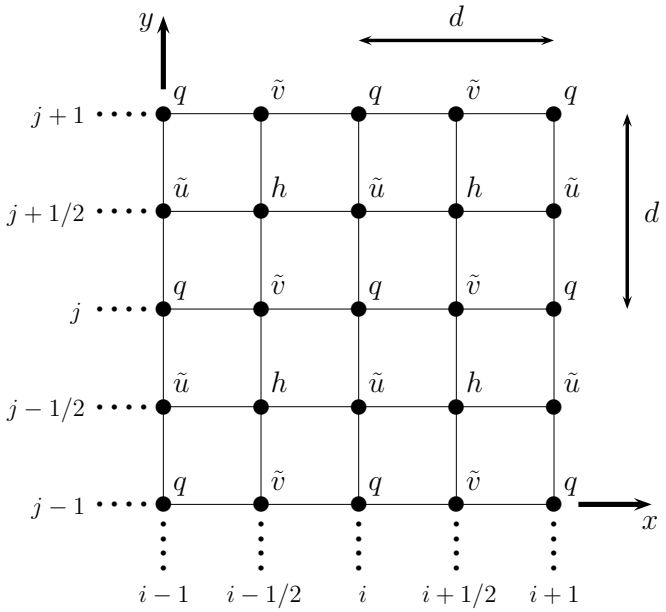

Figure 6.2: Layout of the non-traditional variables on the Arakawa C-grid

(6.31a)–(6.31b). The Poisson bracket is also identical to (6.19), but with $\boldsymbol{u}$ replaced by $\tilde{\boldsymbol{u}}$ throughout,

$$\{A,B\}_Q = \sum_{i,j} q_{i,j} \sum_{\boldsymbol{n},\boldsymbol{m}} \left\{ \alpha_{\boldsymbol{n},\boldsymbol{m}} \frac{\partial(A,B)}{\partial\left(\tilde{u}_{(i,j+1/2)+\boldsymbol{n}}, \tilde{v}_{(i+1/2,j)+\boldsymbol{m}}\right)} + \beta_{\boldsymbol{n},\boldsymbol{m}} \frac{\partial(A,B)}{\partial\left(\tilde{u}_{(i,j+1/2)+\boldsymbol{n}}, \tilde{u}_{(i,j+1/2)+\boldsymbol{m}}\right)} + \gamma_{\boldsymbol{n},\boldsymbol{m}} \frac{\partial(A,B)}{\partial\left(\tilde{v}_{(i+1/2,j)+\boldsymbol{n}}, \tilde{v}_{(i+1/2,j)+\boldsymbol{m}}\right)} \right\}, \tag{6.33a}$$

$$\{A,B\}_R = \frac{1}{d} \sum_{i,j} \left\{ \frac{\partial B}{\partial \tilde{u}_{i,j+1/2}} \left(\frac{\partial A}{\partial h_{i+1/2,j+1/2}} - \frac{\partial A}{\partial h_{i-1/2,j+1/2}} \right) + \frac{\partial B}{\partial \tilde{v}_{i+1/2,j}} \left(\frac{\partial A}{\partial h_{i+1/2,j+1/2}} - \frac{\partial A}{\partial h_{i+1/2,j-1/2}} \right) - (A \longleftrightarrow B) \right\}. \tag{6.33b}$$

The dynamics are still given by (6.23), so it follows from the antisymmetry of the Poisson bracket (6.33a)–(6.33b) that (6.24) still holds, and so total energy H is conserved. The total potential enstrophy P and mass M are given by (6.25), with the alternative definition (6.32) of the potential vorticity $q_{i,j}$. To prove that P and M are exactly conserved in the non-traditional scheme, we must show that they are both Casimirs of the non-traditional bracket (6.33a)–(6.33b). However, P, M and the bracket are identical in both the traditional and non-traditional schemes, except for the switch between $\boldsymbol{u}$ and $\tilde{\boldsymbol{u}}$. Thus, exactly the same choices for $\alpha_{\boldsymbol{n},\boldsymbol{m}}$, $\beta_{\boldsymbol{n},\boldsymbol{m}}$, and $\gamma_{\boldsymbol{n},\boldsymbol{m}}$ conserve potential enstrophy and mass in both the traditional and non-traditional schemes. This argument may be extended to all of the schemes described in Salmon (2004), but here we will consider only the non-traditional version of the Arakawa–Lamb scheme.

It now remains only to obtain explicit evolution equations for $\tilde{u}_{i,j+1/2}$, $\tilde{v}_{i+1/2,j}$ and $h_{i+1/2,j+1/2}$ from the discrete Hamiltonian (6.17) and Poisson bracket (6.33a)–(6.33b), using (6.23). For example,

for integers k and l,

$$\frac{\mathrm{d}}{\mathrm{d}t}\tilde{u}_{k,l+1/2} = \left\{\tilde{u}_{k,l+1/2}, H\right\} = \left\{\tilde{u}_{k,l+1/2}, H\right\}_Q + \left\{\tilde{u}_{k,l+1/2}, H\right\}_R. \tag{6.34}$$

The Hamiltonian H depends on $\tilde{\boldsymbol{u}}$ only through $\boldsymbol{u}$, so by the chain rule

$$\frac{\partial H}{\partial \tilde{u}_{k,l+1/2}} = \frac{\partial H}{\partial u_{k,l+1/2}}\frac{\partial u_{k,l+1/2}}{\partial \tilde{u}_{k,l+1/2}} = \frac{\partial H}{\partial u_{k,l+1/2}}, \tag{6.35a}$$

$$\frac{\partial H}{\partial \tilde{v}_{k+1/2,l}} = \frac{\partial H}{\partial v_{k+1/2,l}}\frac{\partial v_{k+1/2,l}}{\partial \tilde{v}_{k+1/2,l}} = \frac{\partial H}{\partial v_{k+1/2,l}}. \tag{6.35b}$$

Thus the contribution of $\left\{\tilde{u}_{k,l+1/2}, H\right\}_Q$ to the non-traditional discrete equations is identical to the contribution of $\left\{u_{k,l+1/2}, H\right\}_Q$ to the traditional discrete equations. This is also true of $\left\{\tilde{u}_{k,l+1/2}, H\right\}_Q$, $\left\{\tilde{v}_{k+1/2,l}, H\right\}_Q$, $\{\tilde{h}_{k+1/2,l+1/2}, H\}_Q$, and $\{\tilde{h}_{k+1/2,l+1/2}, H\}_R$. The only major modification of the Arakawa-Lamb scheme comes from the residual parts of the Poisson bracket $\left\{\tilde{u}_{k,l+1/2}, H\right\}_R$ and $\left\{\tilde{v}_{k+1/2,l}, H\right\}_R$. This is because the Hamiltonian H contains additional dependences on h through u and v,

$$\left.\frac{\partial H}{\partial h_{k+1/2,l+1/2}}\right|_{\tilde{\boldsymbol{u}}} = \left.\frac{\partial H}{\partial h_{k+1/2,l+1/2}}\right|_{\boldsymbol{u}} + \sum_{i,j}\left\{\frac{\partial H}{\partial u_{i,j+1/2}}\frac{\partial u_{i,j+1/2}}{\partial h_{k+1/2,l+1/2}} + \frac{\partial H}{\partial v_{i+1/2,j}}\frac{\partial v_{i+1/2,j}}{\partial h_{k+1/2,l+1/2}}\right\}, \tag{6.36}$$

where the subscript $|_{\boldsymbol{u}}$ indicates that u and v should be held constant in the derivative. This is the discrete analogue of (6.11). Equation (6.36) defines the discrete Bernoulli potential $\Phi_{k+1/2,l+1/2} = \partial H/\partial h_{k+1/2,l+1/2}$. From (6.17), the derivatives of H with respect to $\boldsymbol{u}$ yield the mass fluxes,

$$\frac{\partial H}{\partial u_{i,j+1/2}} = u^\star_{i,j+1/2} = \overline{h}^{\,i}_{i,j+1/2}u_{i,j+1/2}, \qquad \frac{\partial H}{\partial v_{i+1/2,j}} = v^\star_{i+1/2,j} = \overline{h}^{\,j}_{i+1/2,j}v_{i+1/2,j}, \tag{6.37}$$

so $u^\star_{i,j+1/2}$ and $v^\star_{i+1/2,j}$ are dimensionally momenta, rather than velocities. The overbars on $\overline{h}^{\,i}$ and $\overline{h}^{\,j}$ again denote averages over the two adjacent gridpoints in the i- and j-directions respectively. Evaluating the derivatives of $\boldsymbol{u}$ with respect to h in (6.36) using (6.31a)–(6.31b) yields

$$\frac{\partial u_{i,j+1/2}}{\partial h_{k+1/2,l+1/2}} = -\Omega^{(y)}_{i+1/2,j+1/2}\,\mu_{i-k,j-l}, \qquad \frac{\partial v_{i+1/2,j}}{\partial h_{k+1/2,l+1/2}} = \Omega^{(x)}_{i+1/2,j+1/2}\,\xi_{i-k,j-l}. \tag{6.38}$$

The discrete Bernoulli potential may therefore be written as

$$\begin{aligned}\Phi_{i+1/2,j+1/2} =& \tfrac{1}{2}\overline{u^2}^{\,i}_{i+1/2,j+1/2} + \tfrac{1}{2}\overline{v^2}^{\,j}_{i+1/2,j+1/2} + g(h_b+h)_{i+1/2,j+1/2}\\ &+\ \Omega^{(x)}_{i+1/2,j+1/2}\sum_{r,s}\xi_{-r,-s}\,v^\star_{i+1/2+r,j+s}\\ &-\ \Omega^{(y)}_{i+1/2,j+1/2}\sum_{r,s}\mu_{-r,-s}\,u^\star_{i+r,j+1/2+s},\end{aligned} \tag{6.39}$$

so Φ acquires discrete non-traditional terms proportional to a weighted average of $u^\star$ and $v^\star$ over the nearby $\tilde{u}$- and $\tilde{v}$-gridpoints. Comparison with (6.31a)–(6.31b) shows that this is symmetric to the weighted average over h-gridpoints in the definition of the discrete velocities $u_{i,j+1/2}, v_{i+1/2,j}$. Thus (6.39) is guaranteed to be a second-order approximation to the continuous Bernoulli potential (6.4), as long as the discrete velocities (6.31a)–(6.31b) are at least a second-order approximation to (6.1). The choice of the weights $\mu_{r,s}$ and $\xi_{r,s}$ is otherwise irrelevant to the conservation properties (and evolution equations) of the numerical scheme.

For simplicity, we use a second-order two-gridpoint average in (6.31a)–(6.31b), which corresponds to $\mu_{0,0} = \mu_{-1,0} = \frac{1}{2}$, $\xi_{0,0} = \xi_{0,-1} = \frac{1}{2}$, and $\mu_{r,s} = \xi_{r,s} = 0$ for all other r and s. The discrete velocities are then defined as

$$u_{i,j+1/2} = \tilde{u}_{i,j+1/2} - \overline{2\Omega^{(y)}\left(h_b + \tfrac{1}{2}h\right)}^{i}_{i,j+1/2}, \tag{6.40a}$$

$$v_{i+1/2,j} = \tilde{v}_{i+1/2,j} + \overline{2\Omega^{(x)}\left(h_b + \tfrac{1}{2}h\right)}^{j}_{i+1/2,j}, \tag{6.40b}$$

while the discrete Bernoulli potential becomes

$$\begin{aligned}\Phi_{i+1/2,j+1/2} = {} & \tfrac{1}{2}\overline{u^2}^{i}_{i+1/2,j+1/2} + \tfrac{1}{2}\overline{v^2}^{j}_{i+1/2,j+1/2} + g(h_b+h)_{i+1/2,j+1/2} \\ & + \Omega^{(x)}_{i+1/2,j+1/2}\overline{v^\star}^{j}_{i+1/2,j+1/2} - \Omega^{(y)}_{i+1/2,j+1/2}\overline{u^\star}^{i}_{i+1/2,j+1/2}.\end{aligned} \tag{6.41}$$

These equations may be understood more easily with the aid of Figure 6.3, which shows the locations of the computed quantities $u^\star_{i,j+1/2}$, $v^\star_{i+1/2,j}$, $\Phi_{i+1/2,j+1/2}$ and $q_{i,j}$ on the C-grid. The discrete dynamics may therefore be written as ordinary differential equations for the evolution of the discrete layer thicknesses,

$$\frac{\mathrm{d}}{\mathrm{d}t}h_{i+1/2,j+1/2} = -\frac{1}{d}\left(u^\star_{i+1,j+1/2} - u^\star_{i,j+1/2} + v^\star_{i+1/2,j+1} - v^\star_{i+1/2,j}\right), \tag{6.42}$$

and canonical variables,

$$\begin{aligned}\frac{\mathrm{d}}{\mathrm{d}t}\tilde{u}_{i,j+1/2} = {} & \alpha_{i,j+1/2}v^\star_{i+1/2,j+1} + \beta_{i,j+1/2}v^\star_{i-1/2,j+1} + \gamma_{i,j+1/2}v^\star_{i-1/2,j} \\ & + \delta_{i,j+1/2}v^\star_{i+1/2,j} - \epsilon_{i+1/2,j+1/2}u^\star_{i+1,j+1/2} + \epsilon_{i-1/2,j+1/2}u^\star_{i-1,j+1/2} \\ & - \frac{1}{d}\left(\Phi_{i+1/2,j+1/2} - \Phi_{i-1/2,j+1/2}\right),\end{aligned} \tag{6.43a}$$

$$\begin{aligned}\frac{\mathrm{d}}{\mathrm{d}t}\tilde{v}_{i+1/2,j} = {} & -\gamma_{i+1,j+1/2}u^\star_{i+1,j+1/2} - \delta_{i,j+1/2}u^\star_{i,j+1/2} - \alpha_{i,j-1/2}u^\star_{i,j-1/2} \\ & - \beta_{i+1,j-1/2}u^\star_{i+1,j-1/2} - \phi_{i+1,j+1/2}v^\star_{i+1/2,j+1} + \phi_{i+1,j-1/2}v^\star_{i+1/2,j-1} \\ & - \frac{1}{d}\left(\Phi_{i+1/2,j+1/2} - \Phi_{i+1/2,j-1/2}\right),\end{aligned} \tag{6.43b}$$

where α, β, γ, δ, ϵ and ϕ are functions of the potential vorticity (6.32), and are defined in Arakawa and Lamb (1981). The traditional and non-traditional schemes are almost identical except for the

change in prognostic variables to $\tilde{\boldsymbol{u}}$, the additional calculation of $\boldsymbol{u}$ from $\tilde{\boldsymbol{u}}$ at each time step via (6.31a)–(6.31b), and the modification of the Bernoulli potential (6.39). This ready adaptation of the Arakawa and Lamb (1981) scheme to our non-traditional shallow water equations was made possible by the Hamiltonian interpretation in Salmon (2004).

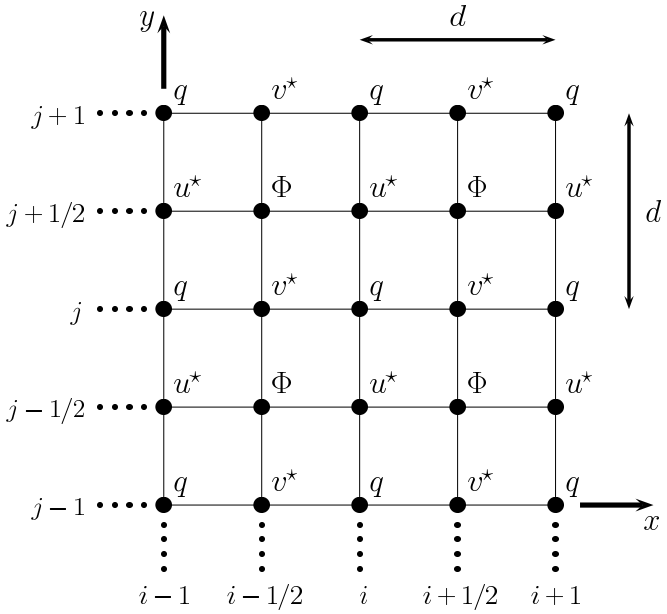

Figure 6.3: Locations of the computed mass fluxes $\boldsymbol{u}^\star$, Bernoulli potential Φ, and potential vorticity q on the Arakawa C-grid.

We may compute solutions to the shallow water equations in a periodic domain using only the discrete equations (6.42), (6.43a), and (6.43b). No dissipation is needed unless the fluid surface intersects the bottom topography during the computation. Using standard schemes for time-integration, for example the third-order Adams-Bashforth or fourth-order Runge-Kutta schemes, it is straightforward to reduce the error in the conserved mass, energy and potential enstrophy down to the precision of machine round-off error.

6.3 Cross-equatorial flow through an idealised channel

The numerical scheme derived in §6.2 allows us to explore physically relevant solutions of the non-traditional shallow water equations that are not accessible via analytical methods. The theoretical studies presented in Chapters 4 and 5 suggest that cross-equatorial flow through channel-like bathymetry may be strongly affected by the inclusion of the complete Coriolis force, particularly when the channel is almost-eastward or almost-westward. We will now investigate the role of the complete Coriolis force in the dynamics of abyssal flow across the equator via numerical integra-

tion of the traditional and non-traditional shallow water equations. However, our numerical scheme requires some modifications to handle outcropping of the fluid surface from the steep channel topography, described in §6.3.1. In §6.3.2 we verify our numerical scheme by performing a test of convergence under grid refinement, and show that it maintains second-order accuracy in the grid spacing over long time-integrations. In §6.3.3 we perform a limited sweep of the numerical parameters, and consider the effect of including the complete Coriolis force in different scenarios.

6.3.1 Numerical approach

We represent the flow of an abyssal current using the $1\frac{1}{2}$-layer, or reduced-gravity, shallow water equations, which describe the flow of a denser active layer beneath a deep, quiescent upper layer. The upper layer is assumed to react passively to the motions below, such that the pressure at the internal surface $z = h_b + h$ is approximately constant. This model is discussed in §5.2 of Chapter 5 and illustrated in Figure 6.4. The $1\frac{1}{2}$-layer equations may be obtained from the single-layer shallow-water equations (6.2a)–(6.2c) by replacing g with the reduced gravity $g' = g\Delta\rho/\rho$, where ρ is the density of the active layer and $\Delta\rho$ is the density difference between the layers. In the following subsections we detail the various aspects of our approach to computing solutions of the $1\frac{1}{2}$-layer shallow water equations in a cross-equatorial channel.

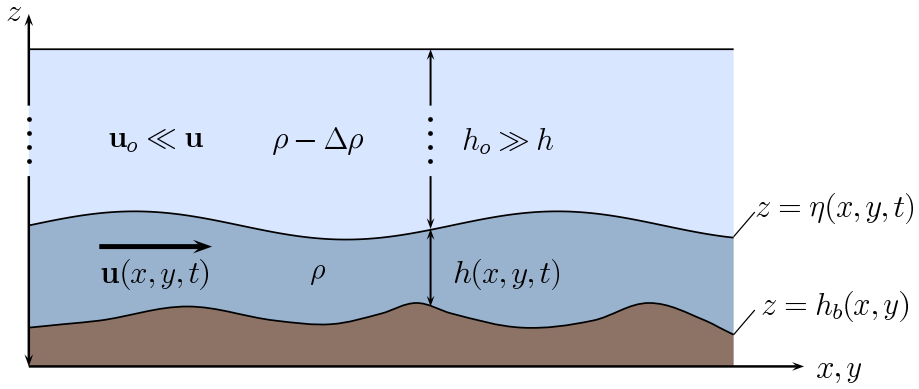

Figure 6.4: An illustration of the $1\frac{1}{2}$-layer shallow water model. A dense, active lower layer flows beneath a deep quiescent upper layer that reacts passively to motions of the internal surface.

6.3.1.1 The Salmon layer

We will compute solutions to the $1\frac{1}{2}$-layer shallow water equations in a steep-sided channel, whose shape is shown in Figure 6.6 and discussed in §6.3.1.3 below. We must therefore accommodate grounding lines, where the fluid surface intersects the bottom topography. This necessitates a modification of the numerical scheme described in §6.2, which can not tolerate a layer of zero thickness, as

$q_{i,j} \to \infty$ as $h_{i,j}^{(q)} \to 0$ from (6.32). Following Salmon (2002), we modify the shallow water equations so that they preserve a very shallow layer of fluid in 'dry' regions of the computational domain, which we will refer to to as the "Salmon layer". To prevent the thickness of the layer approaching zero, we modify the potential energy in the shallow water Hamiltonian (6.5),

$$\mathcal{H} = \iint \mathrm{d}\boldsymbol{x} \left\{ \tfrac{1}{2} h \left(u^2 + v^2\right) + g' h \left(h_b + \tfrac{1}{2} h\right) + \frac{g'}{n-2} h^2 \left(\frac{h_s}{h}\right)^n \right\}, \tag{6.44}$$

where $n > 2$ is a positive integer for computational efficiency. We have replaced g by g' to reflect the fact that we are using the $1\frac{1}{2}$-layer equations. The additional term in (6.44) approaches infinity as h approaches zero, and vanishes as h approaches infinity. This prevents the layer thickness from becoming much smaller than h_s, which we will refer to as the "Salmon thickness", without modifying the dynamics where $h \gg h_s$. Salmon (2002) successfully used this method for one- and two-dimensional calculations of shallow water flows, and chose $n = 4$ as a suitable compromise between the efficacy of the Salmon layer and the numerical stiffness. In the shallow water equations (6.2a)–(6.2c), this modification of the potential energy affects only the Bernoulli potential (6.4),

$$\Phi = \tfrac{1}{2} u^2 + \tfrac{1}{2} v^2 + g'(h_b + h) - g' h \left(\frac{h_s}{h}\right)^n + h \left(\Omega_x v - \Omega_y u\right). \tag{6.45}$$

This may be included in our discrete evolution equations (6.43a)–(6.43b) via a straightforward modification of the discrete Hamiltonian (6.17) and the discrete Bernoulli potential (6.41),

$$\Phi_{i+1/2,j+1/2} = \cdots - g' h_{i+1/2,j+1/2} \left(\frac{h_s}{h_{i+1/2,j+1/2}}\right)^n, \tag{6.46}$$

where $\cdots$ indicates the expression in (6.41). This modification does not destroy conservation of discrete energy or potential enstrophy conservation, but the numerical scheme now conserves the discrete analogue of the modified energy (6.44).

6.3.1.2 Explicit dissipation

Although in principle it is possible to obtain energy- and potential enstrophy-conserving numerical solutions using the modified Bernoulli potential (6.46), in practice the Salmon layer necessitates the inclusion of explicit dissipation in the shallow water momentum equations,

$$\frac{\partial \tilde{\boldsymbol{u}}}{\partial t} + q h\, \hat{\boldsymbol{z}} \times \boldsymbol{u} + \nabla \Phi = A_h \frac{1}{h} \nabla \cdot \boldsymbol{\sigma} - A_v \left(\frac{h_s}{h}\right)^m \boldsymbol{u}. \tag{6.47}$$

The term proportional to A_v, which we will refer to as the vertical dissipation, prevents the Salmon layer from being accelerated to unphysically large velocities. This dissipation is proportional to the physical velocity $\boldsymbol{u}$, rather than the canonical variables $\tilde{\boldsymbol{u}}$, as one would expect for a linear drag.

We restrict $m \geq 2$ to positive integer values for computational efficiency. Where the layer thickness is small, $h \ll h_s$, the dominant accelerations present in the fluid are

$$\frac{\partial \boldsymbol{u}}{\partial t} \approx -\, g'(n-1) \left(\frac{h_s}{h}\right)^n \nabla h - A_v \left(\frac{h_s}{h}\right)^m \boldsymbol{u}. \tag{6.48}$$

This force balance is illustrated in Figure 6.5. The artificial pressure gradient, due to the modification of the potential energy in (6.44), does not accelerate the fluid in 'dry' regions, where the layer thickness is approximately constant, $|\nabla h| \approx 0$. However, at the grounding line, where the fluid thickness falls below the Salmon thickness $h < h_s$, the artificial pressure gradient exerts a large acceleration into the Salmon layer. Including the vertical dissipation limits the velocity that the fluid in the Salmon layer can attain. The accelerations on the right hand side of (6.48) balance approximately when

$$\boldsymbol{u} \approx -\frac{g'(n-1)}{A_v} \left(\frac{h_s}{h}\right)^{n-m} \nabla h. \tag{6.49}$$

As a consequence, it is necessary to have a small mass 'leak' into the Salmon layer in order to preserve a stationary grounding line. This effect may be minimised by using a larger m, but there is again a trade-off with the numerical stiffness of the equations. In all of the simulations described below we use $m = n = 4$. To incorporate the vertical dissipation term into our discrete evolution equations, we need only compute appropriate approximations to h on the $\tilde{u}$- and $\tilde{v}$-gridpoints,

$$\frac{\partial}{\partial t}\tilde{u}_{i,j+1/2} = \cdots - A_v \left(\frac{h_s}{\overline{h}^i_{i,j+1/2}}\right)^m u_{i,j+1/2}, \tag{6.50a}$$

$$\frac{\partial}{\partial t}\tilde{v}_{i+1/2,j} = \cdots - A_v \left(\frac{h_s}{\overline{h}^j_{i+1/2,j}}\right)^m v_{i+1/2,j}. \tag{6.50b}$$

Although the fluid is subject to the action of these friction-type terms throughout the domain, in the bulk of the fluid the layer thickness is much larger than the Salmon thickness, $h \gg h_s$, and so the effect of this dissipation is negligible.

We will refer to the other dissipative term in (6.47), proportional to A_h, as the horizontal dissipation. This term is necessary for numerical stability, as sufficiently shallow water waves of sufficiently large amplitude steepen to form discontinuous shocks that cannot be resolved on the discrete grid, and which generate spurious oscillations in the solution. This might occur in a situation resembling Figure 6.5, where a deep body of fluid flows towards 'dry' topography, represented by a Salmon layer. Additionally, when the horizontal dissipation parameter A_h is small, the solution becomes turbulent, and large-amplitude breaking waves may form through random nonlinear wave interactions. We use the physically consistent lateral friction advocated by Shchepetkin and O'Brien (1996),

$$\boldsymbol{\sigma} = \begin{bmatrix} U & V \\ V & -U \end{bmatrix}, \quad \text{where} \quad U = h\left(\frac{\partial u}{\partial x} - \frac{\partial v}{\partial y}\right), \quad V = h\left(\frac{\partial u}{\partial y} + \frac{\partial v}{\partial x}\right). \tag{6.51}$$

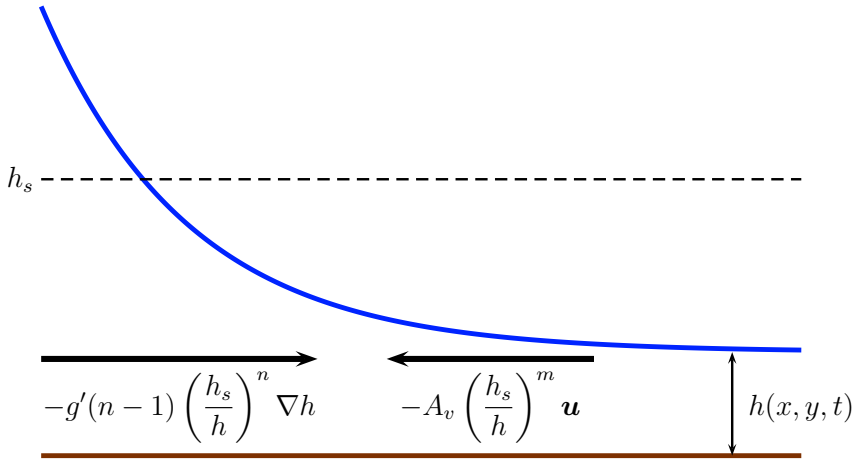

Figure 6.5: An illustration of the dominant acceleration balance at the contact line, where the layer thickness falls below the Salmon thickness, $h < h_s$. To balance the artificial pressure gradient due to the modified potential energy in (6.44), we include a friction that becomes large only when $h < h_s$.

This corresponds to $A_1 = A_h$ and $A_2 = 0$ in the notation of Shchepetkin and O'Brien (1996). This form of the stress tensor $\boldsymbol{\sigma}$ is physically consistent, in that it conserves momentum and angular momentum, dissipates energy, and is invariant under coordinate transformations. We have written $\boldsymbol{\sigma}$ in the form (6.51) because it has a convenient discretisation on the C-grid, but it may be written more generally as

$$\boldsymbol{\sigma} = h\left[(\nabla \boldsymbol{u}) + (\nabla \boldsymbol{u})^T - \mathbf{I}\,\nabla \cdot \boldsymbol{u}\right], \tag{6.52}$$

as in the compressible Navier-Stokes equations (see Batchelor, 2000). Shchepetkin and O'Brien (1996) showed that using a physically consistent stress tensor avoids the creation of artificial vorticity sources in flow over topography. On the C-grid shown in Figure 6.1, U and V have natural definitions on the h- and q-gridpoints respectively,

$$U_{i+1/2,j+1/2} = \frac{1}{d}\, h_{i+1/2,j+1/2}\left(u_{i+1,j+1/2} - u_{i,j+1/2} - v_{i+1/2,j+1} + v_{i+1/2,j}\right), \tag{6.53a}$$

$$V_{i,j} = \frac{1}{d}\, h^{(q)}_{i,j}\left(u_{i,j+1/2} - u_{i,j-1/2} + v_{i+1/2,j} - v_{i-1/2,j}\right). \tag{6.53b}$$

We may then incorporate the horizontal dissipation in our discrete evolution equations as

$$\frac{\partial}{\partial t}\tilde{u}_{i,j+1/2} = \cdots + \frac{A_h}{d}\left(\frac{U_{i+1/2,j+1/2} - U_{i-1/2,j+1/2} + V_{i,j+1} - V_{i,j}}{\overline{h}^{\,i}_{i,j+1/2}}\right), \tag{6.54a}$$

$$\frac{\partial}{\partial t}\tilde{v}_{i+1/2,j} = \cdots + \frac{A_h}{d}\left(\frac{V_{i+1,j} - V_{i,j} - U_{i+1/2,j+1/2} + U_{i+1/2,j-1/2}}{\overline{h}^{\,j}_{i+1/2,j}}\right). \tag{6.54b}$$

This differs from the discretisation of Shchepetkin and O'Brien (1996), who also use a C-grid in their computations, but solve the shallow water equations in momentum-conserving form. This form is obtained by multiplying (6.47) by h and rearranging using the mass conservation equation (6.2c).

Including the dissipative terms on the right hand side of (6.47) destroys the discrete conservation laws for energy and potential enstrophy. However, this does not render obsolete the energy- and potential enstrophy-conserving scheme derived in §6.2. It is still useful to be able to calculate the exact rate of energy dissipation in the solution, which is guaranteed to be due entirely to the explicit horizontal and vertical dissipative terms. Additionally, we ensure that there are no spurious energy sources due to errors associated with the spatial discretisation (*c.f.* Fornberg's (1973) study of Burger's equation). Thus, although the physics of the channel flow preclude a numerical integration that exactly preserves desirable conservation laws, such as those for energy, potential enstrophy, and indeed potential vorticity, we may at least include the necessary dissipation in a physically consistent manner.

6.3.1.3 Channel geometry

We found in Chapter 5 that abyssal cross-equatorial flow depend strongly on the orientation of the channel. We have specified the channel orientation by the angle θ, which measures the positive angle from North to the y-axis. We align the x-axis with the cross-channel direction, and the y-axis with the along-channel direction. We position the axes such that $(0, 0)$ lies on the equator, which is described by the line $y\cos\theta + x\sin\theta = 0$. Changing θ modifies the shallow water equations only through the components of the rotation vector, Ω_x, Ω_y and Ω_z. Following Grimshaw (1975), on an equatorial β-plane these components are approximately

$$\Omega_x = \Omega\sin\theta, \qquad \Omega_y = \Omega\cos\theta, \qquad \Omega_z = \beta\left(y\cos\theta + x\sin\theta\right), \tag{6.55}$$

where $\Omega \approx 7.29\times10^{-5}\,\mathrm{rad\,s^{-1}}$ is the absolute rate of rotation, $\beta = 2\Omega/R_E$, and $R_E \approx 6384\,\mathrm{km}$ is the equatorial radius of the Earth. Dellar (2011) later derived this "non-traditional β-plane" rigorously under a Hamiltonian formulation. We will restrict our attention to three channel orientations: a northward channel ($\theta = 0$), a northwestward channel ($\theta = \pi/4$), and an almost-westward channel ($\theta = 1.4$).

Nof and Borisov (1998) studied cross-equatorial flow through a northward parabolic channel, and considered the effect of the steepness of the channel and the upstream width of the current on the dynamics of a cross-equatorial current. We are most interested in the dynamical effects of the channel orientation, the non-traditional component of the Coriolis force, and the modification of potential vorticity via dissipation. We therefore fix the channel shape and length such that they are relevant to the AABW. Choboter and Swaters (2000) studied frictional-geostrophic and shallow water flow through a hyperbolic channel of fixed shape, which resembles a parabola close to its centre and approaches a constant gradient far from its centre. Similarly, we prescribe a channel

that resembles a polynomial of power p close to its centre at $x = 0$, and approaches a linear slope as $|x| \to \infty$,

$$h_b(x) = H \frac{(1+\alpha)\left|\frac{x}{W}\right|^p}{\alpha + \left|\frac{x}{W}\right|^{p-1}}. \tag{6.56}$$

Here H and W are the channel height and width respectively, and the form of (6.56) has been chosen such that $h_b(\pm W) = H$. For $|x/W| \ll \alpha$ the channel resembles a polynomial of power p, and for $|x/W| \gg \alpha$ the slope is approximately linear. Equivalently, as $\alpha \to \infty$ the channel approaches a polynomial of power p, $h_b/H \to |x/W|^p$, and as $\alpha \to 0$ the channel approaches two linear slopes connected by a discontinuity at $x = 0$, $h_b/H \to |x/W|$.

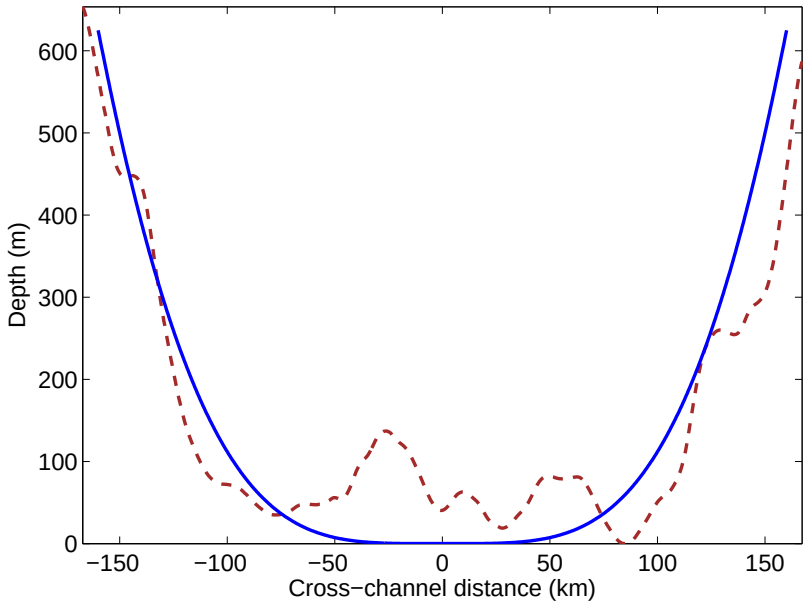

Figure 6.6: Comparison of the along-channel average of the real equatorial bathymetry from Figure 5.2 with the numerical topography (6.56) for $\alpha = 5$, $p = 4$, $W = 150\,\text{km}$ and $H = 500\,\text{m}$. The topography extends up to over 600 m at $x = \pm 160\,\text{km}$ to accommodate the sponge layers at the sides of the domain, as described in §6.3.1.4.

In all of the simulations discussed here we use $\alpha = 5$, $p = 4$, $W = 150\,\text{km}$ and $H = 500\,\text{m}$. We plot the corresponding channel profile in Figure 6.6, where it is compared with the along-channel average of the bathymetry shown in Figure 5.2. The channel extends 10 km beyond $x = \pm W$ to accommodate the sponge layers at the boundaries, described in §6.3.1.4 below. This shape captures the main characteristics of the bathymetry that the real AABW flows through, but omits small-scale features and along-channel variations. The particular choice (6.56) is motivated by the numerical stiffness of the Salmon layer. It would be more straightforward to prescribe topography of quartic form $h_b = H(x/W)^4$, corresponding to $p = 4$ and $\alpha \to \infty$ in (6.56), as we did in Chapter 5.

Ideally we would use the same channel shape for the purpose of comparison, but the slope at the edges of the quartic channel is very steep compared to the grid spacing. Salmon (2002) found that one-dimensional computations on a slope became unstable when the Salmon thickness h_s became smaller than Δh_b, the change in topographic height between adjacent gridpoints. We find that including vertical dissipation in (6.47) restores stability, but steep topographic gradients necessitate prohibitively small numerical time steps. Using (6.56) limits the steepness of the topography towards the edges of the channel, whilst retaining an approximately quartic shape in the centre.

6.3.1.4 Initial and boundary conditions

We consider the flow of an abyssal current into an initially dry channel, so the initial state for our computations must describe only the Salmon layer lying over the channel topography. It is desirable that this should be a steady solution of the shallow water equations with the modified Bernoulli potential (6.45), as otherwise the incoming current may encounter a spurious flow within the Salmon layer. Setting $\boldsymbol{u} \equiv \mathbf{0}$ in (6.47) yields $\nabla\Phi = \mathbf{0}$, or

$$h_b + h - h\left(\frac{h_s}{h}\right)^n = \Phi_0 \quad \Longrightarrow \quad \left(\frac{h}{h_s}\right)^n + \left(\frac{h_b - \Phi_0}{h_s}\right)\left(\frac{h}{h_s}\right)^{n-1} - 1 = 0, \tag{6.57}$$

where Φ_0 is determined by choosing $h(x_0)$ at an arbitrary location x_0. The solution to this n^{th}-order polynomial determines the appropriate height of the Salmon layer everywhere in the channel. In all of the simulations described in §6.3.3 we use $h_s = 25\text{m}$ and $h(0) = h_s/2 = 12.5\,\text{m}$, which we have found to be sufficiently shallow that the flow of the current is not disrupted, without imposing an excessively small time step on the numerical integration. In Figure 6.7 we plot the thickness of the Salmon layer across the channel. There is considerable variation in the thickness of the layer, as a larger contribution from the artificial part of the pressure gradient is required at the edges of the channel to balance the physical pressure due to gravity. If a Salmon layer of uniform thickness is used, the solution rapidly generates a flow towards the channel centre that interferes with the current, and in some cases develops into breaking waves that destabilise the computation.

Ideally, as the current approaches the end of the channel, it should be allowed to exit, and thereafter it should not affect the flow in the interior. This is also true of the side boundaries, for although one might consider a no-flux boundary condition here, from §6.3.1.1 we know that typically a small flow into the Salmon layer is required to sustain a steady grounding line. This flow must be allowed to exit the domain through the side boundaries to permit the possibility of a steady solution. We therefore employ sponge layers (*e.g.* Israeli and Orszag, 1981) at all of the domain boundaries. Nof and Borisov (1998) and Choboter and Swaters (2004) used this technique in their studies of abyssal cross-equatorial flow using numerical integrations of the traditional shallow water

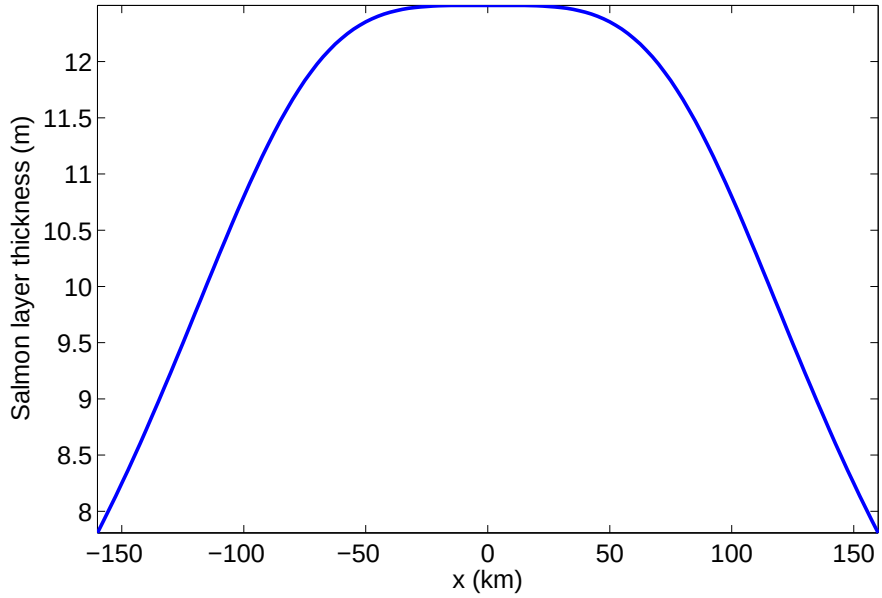

Figure 6.7: Plot of the thickness of the Salmon layer that is initially prescribed in the channel.

equations. In each of the prognostic variables $\tilde{u}$, $\tilde{v}$ and h, the sponge layers cover the S_x gridpoints closest to the boundaries in the x direction, and the S_y gridpoints closest to the boundaries in the y direction. At each time step, all gridpoints in these regions are relaxed towards their values at $t = 0$. This means that the *physical* velocity $\boldsymbol{u}$ is relaxed towards zero, whilst h is relaxed towards the Salmon layer thickness. The relaxation factors at the i^{th} gridpoint from the x-boundary, and at the j^{th} gridpoint from the y-boundary, are

$$s_i^{(x)} = \left(\frac{i-1}{S_x}\right)^{\Delta t/T_s}, \qquad s_j^{(y)} = \left(\frac{j-1}{S_y}\right)^{\Delta t/T_s}, \tag{6.58}$$

where Δt is the time step and T_s is the sponge timescale. In all of the simulations described here we use $T_s = 1/(2\Omega)$, equivalent to approximately 0.08 days or one dimensionless time unit under our nondimensionalisation (6.62). The forms of the relaxation factors in (6.58) have been chosen such that they vary linearly from 0 to 1 over $i = 1, \ldots, S_x$ and $j = 1, \ldots, S_y$ on a timescale T_s. So, for example, after each time step each discrete layer thickness $h_{i+1/2,j+1/2}(t)$ with $i < S_x$ is relaxed as follows,

$$h_{i+1/2,j+1/2}(t) \to h_{i+1/2,j+1/2}(0) + s_i^{(x)}\left[h_{i+1/2,j+1/2}(t) - h_{i+1/2,j+1/2}(0)\right]. \tag{6.59}$$

There is an exception over part of the southern boundary, where $\boldsymbol{u}$ and h are instead relaxed towards the inflow condition.

As in Chapter 5 we prescribe the inflow of the current at the southern edge of the channel, leaning up against the western wall. However, we do not impose the assumption of zero potential vorticity as it is somewhat restrictive, and because it prescribes different inflow conditions when

the complete Coriolis force is included. Instead we choose a shape for the layer thickness h, and calculate the along-channel velocity v from *traditional* cross-channel geostrophic balance,

$$v = \frac{g'}{2\Omega_z}\frac{\partial}{\partial x}\left(h_b + h\right). \tag{6.60}$$

The across-channel velocity u of the inflow is set to zero. For simplicity we prescribe a quadratic depth profile whose shape is determined by the positions of the grounding lines and the gradient of the surface at the western side of the channel,

$$h = 0 \;\text{ at }\; x = L_u, \qquad h = 0 \;\text{ at }\; x = R_u, \qquad \frac{\partial}{\partial x}(h_b + h) = \lambda \;\text{ at }\; x = L_u. \tag{6.61}$$

Of course, we cannot prescribe $h = 0$ as this creates a singularity in the discrete potential vorticity (6.32), so we only prescribe the inflow according to (6.61) and (6.60) where h exceeds the thickness of the Salmon layer. In all of our simulations we use $R_u = -145\,\text{km}$, $L_u = 0$, and $\lambda = -0.002$. This configuration is plotted in Figure 6.8. This inflow represents the core of the AABW (*c.f.* Nof and Borisov, 1998; Durrieu de Madron and Weatherly, 1994), rather than the entire water mass, which occupies all depths below 4000 m (Hall et al., 1997).

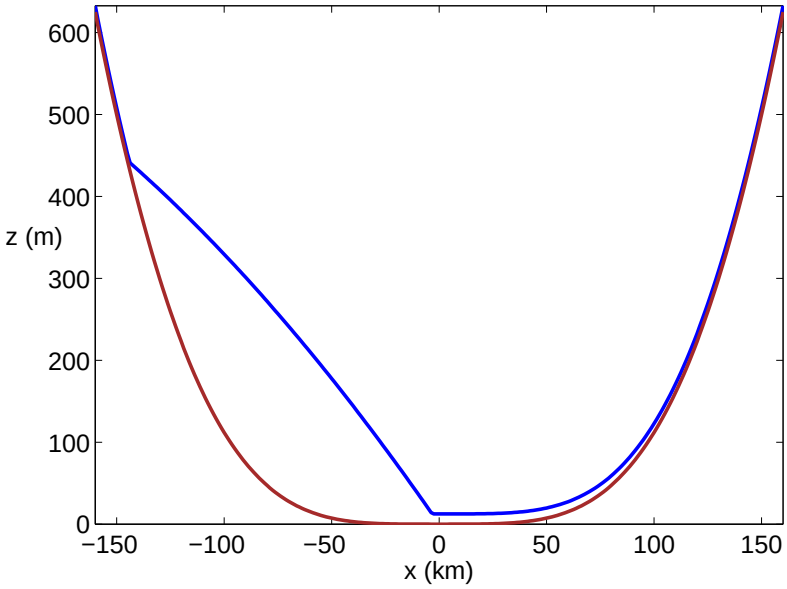

Figure 6.8: Plot of the upstream depth profile prescribed by (6.61). The layer surface is quadratic in x, and the along-channel velocity is determined via cross-channel geostrophic balance (6.60). The solution is relaxed towards this shape in the sponge layer at the southern end of the channel.

6.3.1.5 Nondimensionalisation

As is conventional in the treatment of systems of partial differential equations, we compute our numerical solutions in dimensionless variables. We nondimensionalise the $1\frac{1}{2}$-layer shallow water

equations using

$$\boldsymbol{x} = R_d\hat{\boldsymbol{x}}, \quad \boldsymbol{u} = c\hat{\boldsymbol{u}}, \quad h = H\hat{h}, \quad h_b = H\hat{h}_b, \quad (\Omega_x, \Omega_y, \Omega_z) = \Omega\left(\hat{\Omega}_x, \hat{\Omega}_y, \hat{\Omega}_z\right), \tag{6.62}$$

where $H = 1000\,\mathrm{m}$ is a convenient characteristic vertical lengthscale, and we define

$$c = \sqrt{g'H}, \qquad R_d = \frac{c}{2\Omega}, \qquad \delta = 2\Omega\sqrt{\frac{H}{g'}}, \tag{6.63}$$

the internal gravity wave speed, internal radius of deformation, and non-traditional parameter respectively. We could also have used the internal equatorial radius of deformation, $R_{eq} = \sqrt{c/\beta}$, but this would restrict our numerical approach to near-equatorial flows. Under this nondimensionalisation the $1\frac{1}{2}$-layer shallow water momentum equation becomes

$$\frac{\partial\hat{\tilde{\boldsymbol{u}}}}{\partial\hat{t}} + \hat{q}\hat{h}\,\hat{\boldsymbol{z}}\times\hat{\boldsymbol{u}} + \hat{\nabla}\hat{\Phi} = \hat{A}_h\frac{1}{\hat{h}}\hat{\nabla}\cdot\hat{\boldsymbol{\sigma}} - \hat{A}_v\left(\frac{\hat{h}_s}{\hat{h}}\right)^m\hat{\boldsymbol{u}}, \tag{6.64}$$

where

$$\hat{\tilde{u}} = \hat{u} + \delta\hat{\Omega}_y\left(h_b + \tfrac{1}{2}h\right), \qquad \hat{\tilde{v}} = \hat{v} - \delta\hat{\Omega}_x\left(h_b + \tfrac{1}{2}h\right), \tag{6.65}$$

are the dimensionless canonical variables, and

$$\hat{A}_h = \frac{A_h}{c\,R_d} = \frac{2\Omega A_h}{g'H}, \qquad \hat{A}_v = \frac{A_v}{2\Omega}, \qquad \hat{h}_s = \frac{h_s}{H}, \tag{6.66}$$

are the dimensionless horizontal and vertical dissipation parameters, and dimensionless Salmon thickness. In the simulations described below we define the dissipation via the dimensionless parameters $\hat{A}_h$ and $\hat{A}_v$, as they define the rates of dissipation relative to the dynamical scales, instead of in absolute terms.

6.3.2 Convergence under grid refinement

The fundamental numerical scheme derived in §6.2 has been substantially extended to describe the flow of a current through a cross-equatorial channel, as described at length in §6.3.1. These extensions are necessary to accommodate grounding lines, which are inevitable when the topography is as steep as that shown in Figure 6.6. It is difficult to validate this scheme against known exact solutions of the non-traditional shallow water equations, as no such exact solutions have yet been found. However, it is still possible to verify the self-consistent convergence of our scheme under refinement of the spatial grid.

We define three test cases for verification, all of which follow the set-up described in §6.3.1. The physical parameters associated with each test case are listed in Table 6.1. In test cases 1 and 2 We use a channel of length 1000 km and width 320 km, where the cross-channel profile is shown in

Figure 6.6, because this matches the approximate dimensions of the bathymetry where the AABW crosses the equator. In order to test the most general configuration of the scheme, we orient the channel at $\theta = \pi/4$ rad and include the complete Coriolis force. In test case 3 we use $\theta = 1.4$ rad, which is more realistic for the AABW. However, in a 1000 km-long channel the upstream position of the current shown in Figure 6.8 is very close to the equator, and so cross-channel geostrophic balance prescribes an unreasonably large velocity. We therefore extend the channel to a length of 2000 km. As we shall see, the most interesting dynamics arise where the current crosses the equator, and our extension of the channel simply provides a realistic inflow.

Test case	L_x (km)	L_y (km)	θ (rad)	$\hat{A}_h$	$\hat{A}_v$	g' (m s^{-2})
1	320	1000	$\pi/4$	0.1	0.08	10^{-4}
2	320	1000	$\pi/4$	0.04	0.08	10^{-4}
3	320	2000	1.4	0.05	0.08	10^{-4}

Table 6.1: Physical parameters used in the three convergence test cases.

In test case 1 we use a relatively large horizontal dissipation $\hat{A}_h = 0.1$, anticipating that the solution should approach a steady state as a result. In test cases 2 and 3 we use somewhat smaller values of $\hat{A}_h = 0.04$, and $\hat{A}_h = 0.05$ respectively, anticipating more variable solutions that may or may not approach a steady state, and which might not converge as well as a more dissipative solution. Ideally the dimensionless vertical dissipation parameter $\hat{A}_v$ should be as large as possible to minimise the fluid escaping through the Salmon layer. However, increasing $\hat{A}_v$ requires a smaller time step, as discussed below, so we have chosen $\hat{A}_v = 0.08$ as a suitable compromise. We have chosen a somewhat small reduced gravity of $g' = 10^{-4}$ m s^{-2} to avoid unrealistically large velocities in the solutions, and to represent the very weak stratification in the abyssal ocean (Hall et al., 1997; Rhein et al., 1998).

In each test case we integrate from $\hat{t} = 0$ to $\hat{t} = 20000$, equivalent to a dimensional time of approximately 1587, days or 4.4 years, at five different grid sizes. We use the Adams-Bashforth 3$^{\text{rd}}$-order scheme to step the solution forward in time. The range of numerical parameters in each test case is listed in Table 6.2. At each successive resolution we halve the grid spacing d, which ranges from 10 km to 0.625 km. In a hyperbolic system such as this, one might expect the numerical solution to be stable if the CFL condition were satisfied, *i.e.* $\Delta t < d/c_{\max}$, where $c_{\max}$ is the maximum wave speed. We may estimate $c_{\max}$ using the linear wave speed for the shallow water equations, including

the modification of the potential energy (6.44), but excluding the effect of rotation and topography,

$$c_{\max} \approx \max_{u,v,h} \left| |\boldsymbol{u}| \pm \sqrt{g'h \left(1 + (n-1)\left(\frac{h_s}{h}\right)^n\right)} \right| \tag{6.67}$$

However, the vertical dissipation term in (6.47) also imposes a restriction on the time step size, when the layer thickness h is small, which is not dependent on the grid spacing. This is why the number of time steps N_t is identical for $N_x = 33$, $N_x = 64$, $N_x = 129$ and $N_x = 257$. At $N_x = 513$ the CFL condition becomes more restrictive than the vertical dissipation, so we have reduced the time step in proportion with the grid spacing.

N_x	d (km)	N_t	S_x	S_y
33	10	320001	1	5
64	5	320001	2	10
129	2.5	320001	4	20
257	1.25	320001	8	40
513	0.625	640001	16	80

Table 6.2: Numerical parameters that vary in all convergence test cases.

In each test case, we measure the convergence of our scheme towards the numerical solution of highest resolution, $N_x = 513$. We use the layer thickness h for the purpose of this measurement, though we could equally have used any other discrete variable. We measure the closeness of two solutions h and $h^\star$ using an ℓ^2-norm of the h-gridpoints in the interior of the domain, excluding the sponge layers at the edges,

$$||h - h^\star||_2 = \sqrt{\frac{1}{(N_x - 2S_x)(N_y - 2S_y)} \sum_{i=S_x+1}^{N_x - Sx} \sum_{j=S_y+1}^{N_y - S_y} \left(h_{i+1/2,j+1/2} - h^\star_{i+1/2,j+1/2}\right)^2}. \tag{6.68}$$

This norm may be applied only to solutions on identical spatial grids, so we interpolate all of the computed solutions onto the coarsest grid, $N_x = 33$, before applying (6.68).

6.3.2.1 Test case 1

In Figures 6.9 and 6.10 we illustrate the time-evolution of the solution in test case 1, at the highest resolution $N_x = 513$. The current enters in the southwest corner of the channel and flows north as a western boundary current. As the current approaches the equator, it crosses the channel, and then forms a strong return flow on the eastern side of the channel. By $t = 317$ days, the return flow has started to exit back out of the southern side of the channel. In the northern hemisphere eddies

pinch off from the retroflecting flow, visible at $t = 476$ days, but the point of retroflection is pushed steadily further north, and the solution reaches a steady state around $t = 800$ days. In the steady state, shown at $\hat{t} = 1587$ days in Figure 6.10, a large, almost-stationary body of fluid has collected along the Eastern side of the channel, and both the northward flow and the southward return flow follow a path around the side of this body. In this state the solution is visibly influenced by the sponge layers at the ends of the channel, particularly at the northern end. Numerical integrations in a longer channel reach a very similar steady state, which suggests that the sponge layers do not influence the flow in the interior.

In Figure 6.11 we plot convergence of the solutions under grid refinement at various times in the integration. Overall the scheme appears to converge with the square of the grid spacing. Where the solution varies most rapidly in time (between $t = 300$ days and $t = 600$ days), small phase differences between resolutions lead to an exaggerated difference in the ℓ^2 norm, which measures only the pointwise difference between solutions. Hence the convergence at $t = 317$ days and $t = 635$ days is actually somewhat better than this plot suggests. In the steady state at $t = 1587$ days the convergence is almost exactly second-order. This verifies the steady state, but also suggests that the steady solution may be an attractor of the discrete system, which might skew the results in favour of second-order convergence at long times. Thus, while this test case confirms the second-order convergence of our scheme, it also motivates test cases 2 and 3, in which the solution does not approach a steady state during the integration.

6.3.2.2 Test case 2

In test case 2 we use identical parameters to test case 1, but we reduce the horizontal dissipation parameter to $\hat{A}_h = 0.04$. This solution also reaches a steady state beyond $t = 1587$ days, but the smaller dissipation leads to turbulent behaviour as the solution approaches this state. In Figures 6.12 and 6.13 we illustrate the evolution of the current over time. The initial behaviour is similar to that of test case 1, in that the current flows northward as a western boundary current and crosses the channel at the equator. At $t = 119$ days the current is almost entirely retroflecting back across the equator, demonstrating the strong influence of the Coriolis force and potential vorticity conservation. From this point on the flow exhibits rapid temporal variation, and irregularly pinches off eddies that exit to the north, visible at $t = 278$ days and $t = 397$ days. However, the northward transport due to these eddies is insufficient to prevent the eastern side of the channel slowly filling with almost-stationary fluid. By $t = 1349$ days the eddy pinch-off point has visibly moved further north, and soon after $t = 1587$ days the solution reaches a steady state resembling that in Figure 6.10.

Figure 6.14 shows the convergence of this solution under grid refinement. At $t = 397$ days the

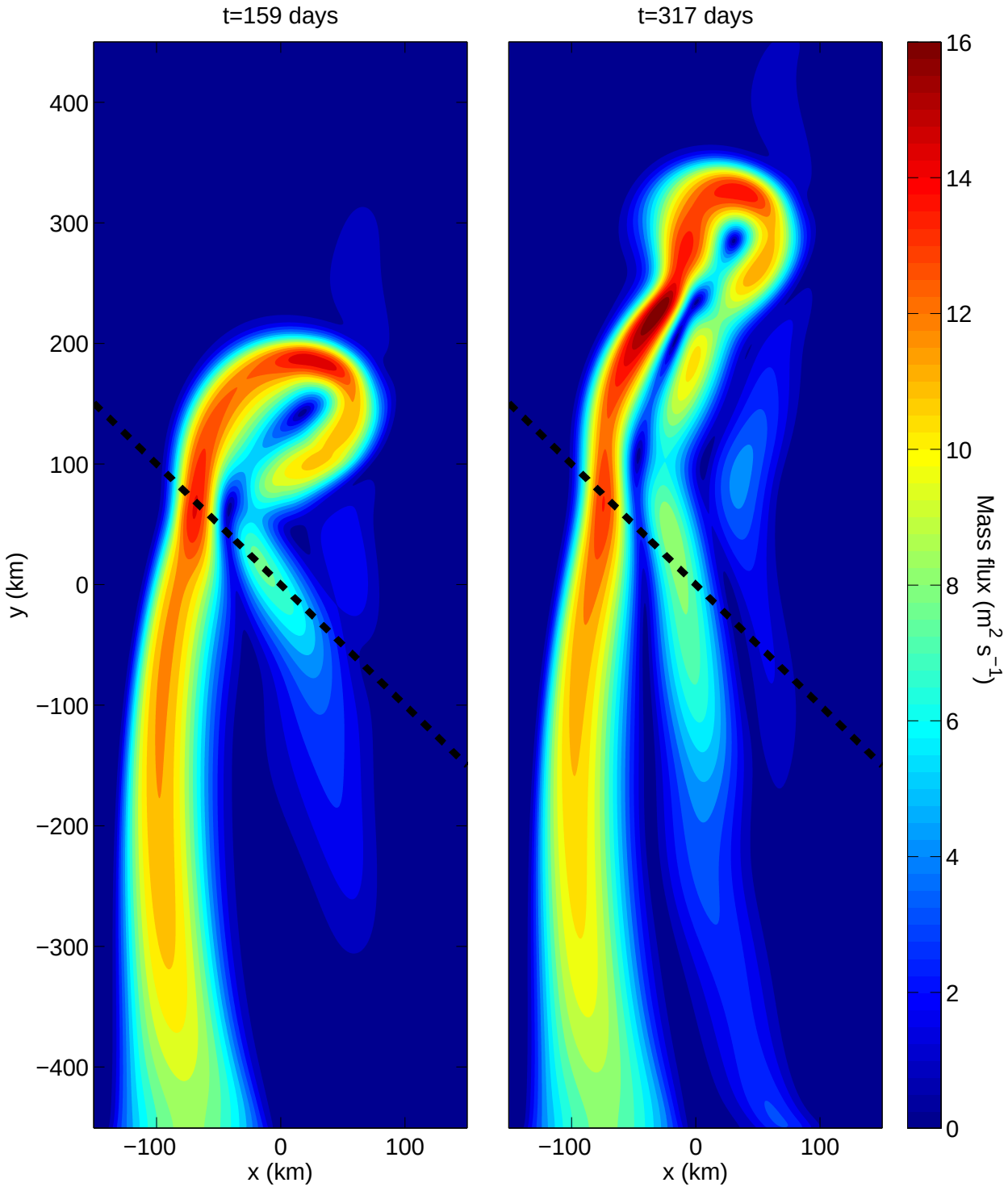

Figure 6.9: Snapshots of the absolute mass flux $|h\boldsymbol{u}|$ in test case 1, computed on a spatial grid of 513×1601 points. The dashed line marks the equator. We omit the sponge layers at the edges of the domain.

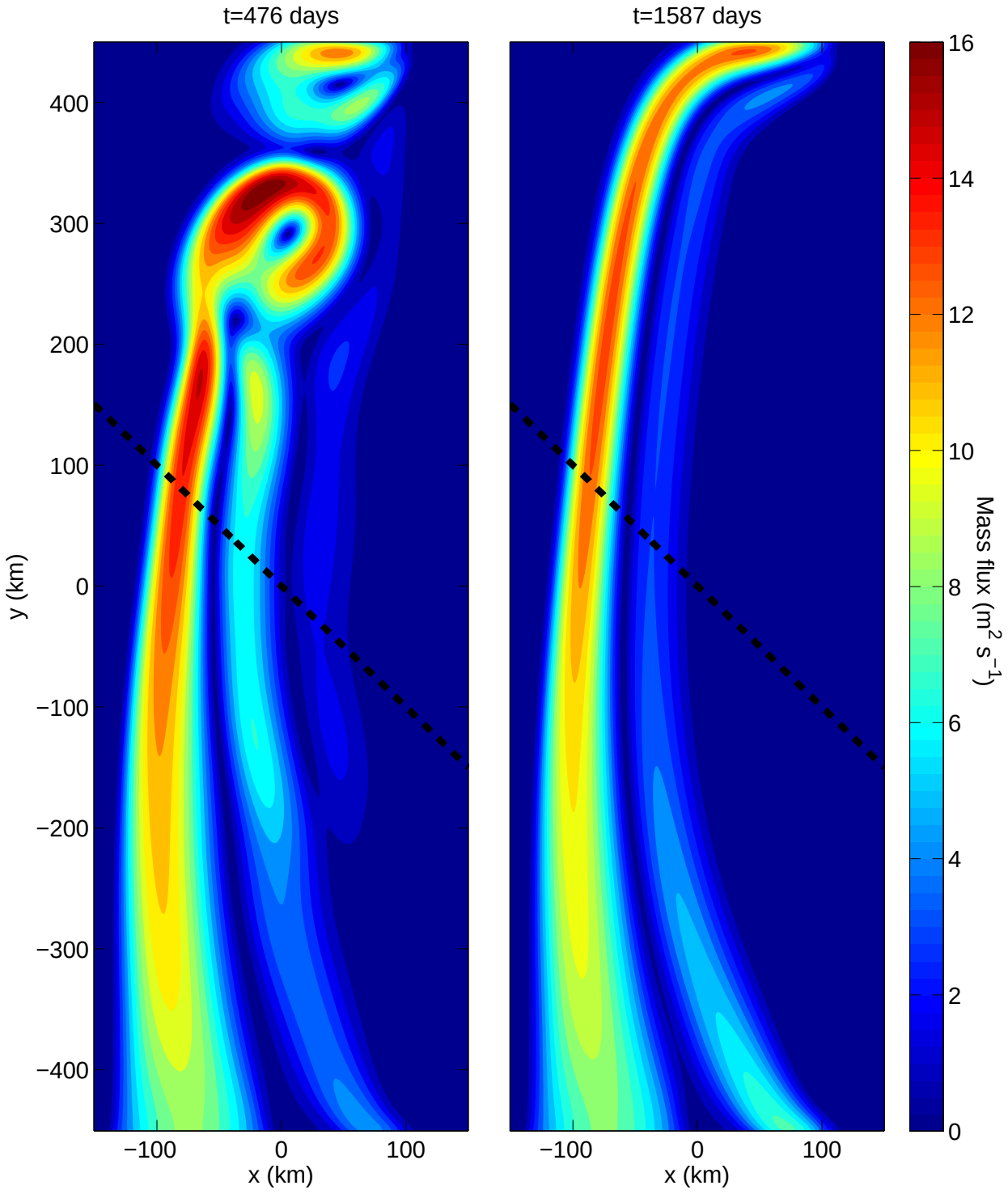

Figure 6.10: Snapshots of the absolute mass flux $|h\boldsymbol{u}|$ in test case 1, computed on a spatial grid of 513×1601 points. The dashed line marks the equator. We omit the sponge layers at the edges of the domain.

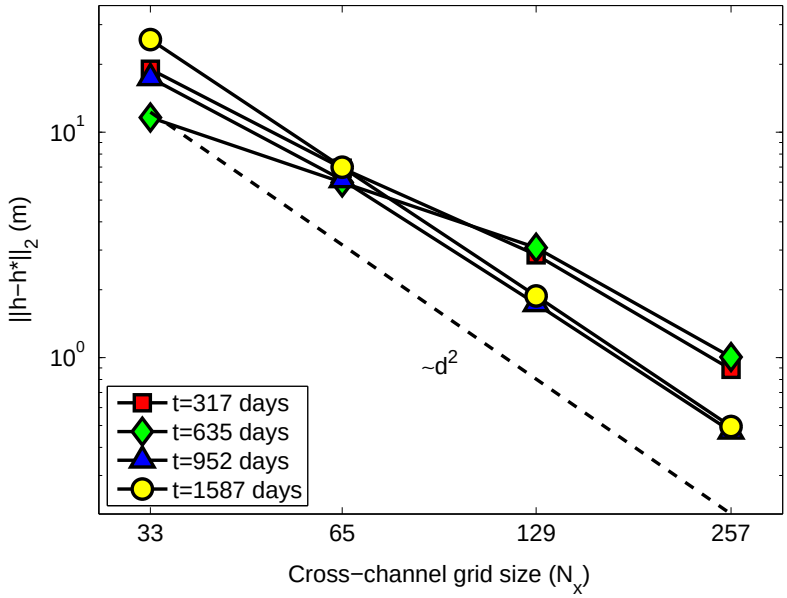

Figure 6.11: Convergence of the solution in test case 1 under grid refinement. The convergence is calculated using an ℓ^2-norm of the discrete layer thicknesses $h_{i+1/2,j+1/2}$, defined by (6.68). The grid spacing is $d = L_x/(N_x - 1)$.

solution converges slowly, but beyond this there is no evidence of pointwise convergence whatsoever. We know from test case 1 that the scheme is convergent, so this result indicates that the solution is chaotic at small $\hat{A}_h$. That is, small differences in the solutions, due to truncation errors arising from the spatial discretisation, are magnified over time. However, we still expect that statistical properties of the solution should exhibit convergence under grid refinement. As an example, we consider the transport out of the northern end of the channel, which is an important diagnostic quantity in our analysis in §6.3.3. We denote this as

$$T(t) = \left[\int_{x_w}^{x_e} hv \, \mathrm{d}x \right]_{y=y_n}, \tag{6.69}$$

where x_w and x_e are the positions of the western and eastern sponge layers on the x-axis, respectively, and y_n is the position of the northern sponge layer on the y-axis. In Figure 6.15 we plot the convergence of the time-averaged transport $\overline{T}$, where

$$\overline{T} = \frac{2}{t_{\max}} \int_{t_{\max/2}}^{t_{\max}} T \, \mathrm{d}t. \tag{6.70}$$

We average over the latter half of our time interval to avoid the initial development of the flow, during which the solution exhibits weak pointwise convergence but has not reached the northern end of the channel. The time-averaged transport exhibits convincing second-order convergence under grid refinement. We conclude that in chaotic cases such as this, the numerical solution provides a

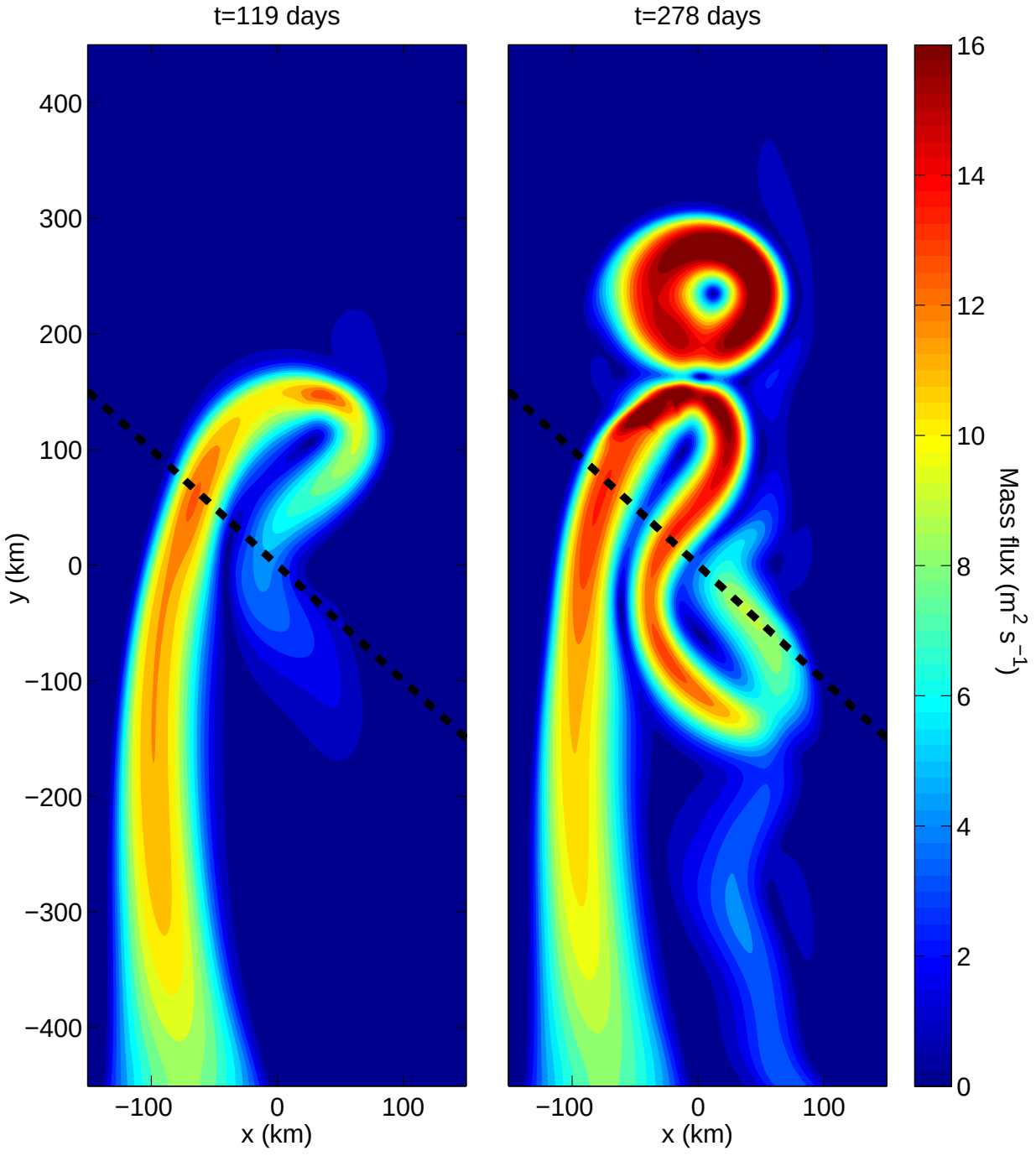

Figure 6.12: Snapshots of the absolute mass flux $|h\boldsymbol{u}|$ in test case 2, computed on a spatial grid of 513×1601 points. The dashed line marks the equator. We omit the sponge layers at the edges of the domain.

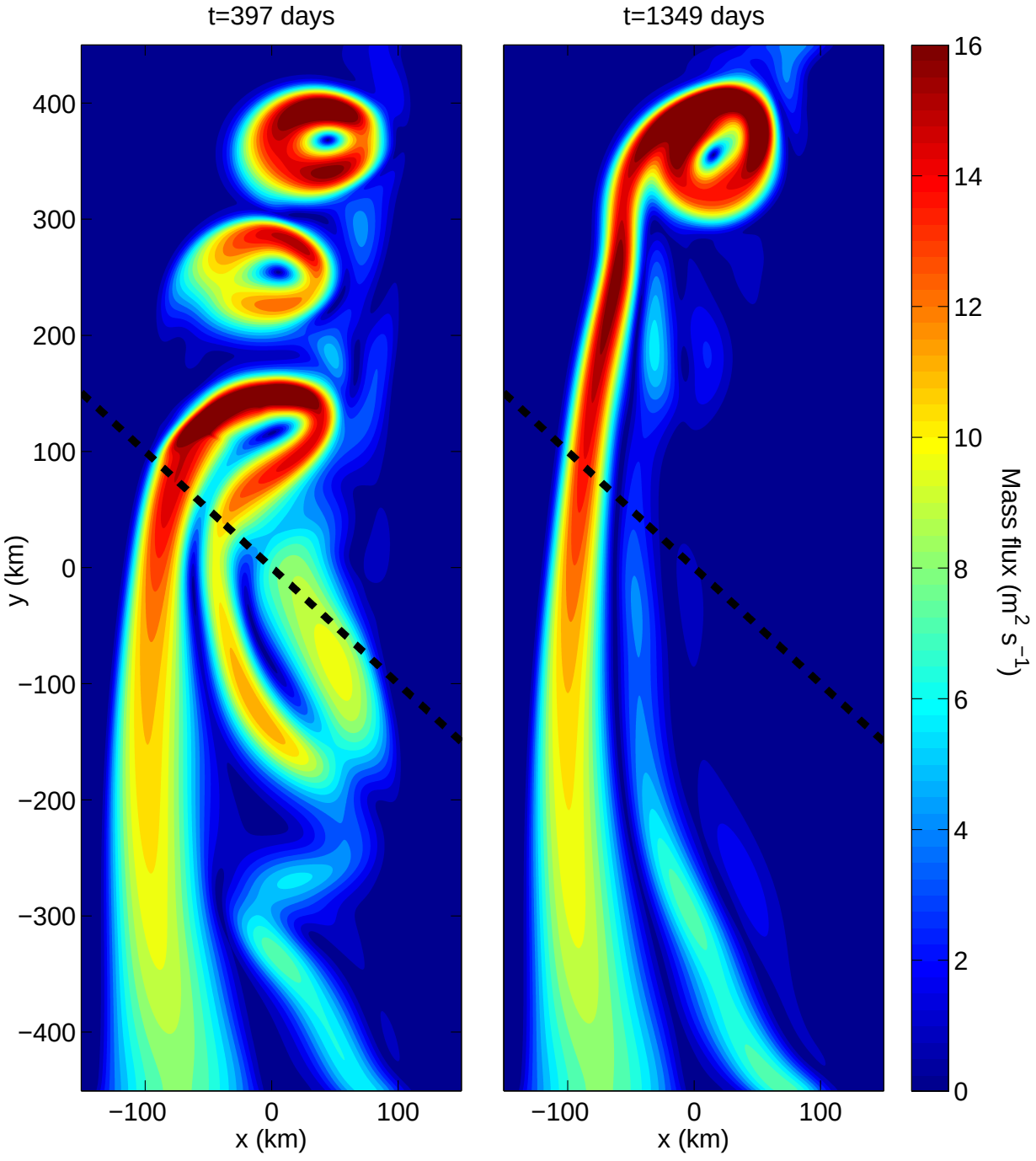

Figure 6.13: Snapshots of the absolute mass flux $|h\boldsymbol{u}|$ in test case 2, computed on a spatial grid of 513×1601 points. The dashed line marks the equator. We omit the sponge layers at the edges of the domain.

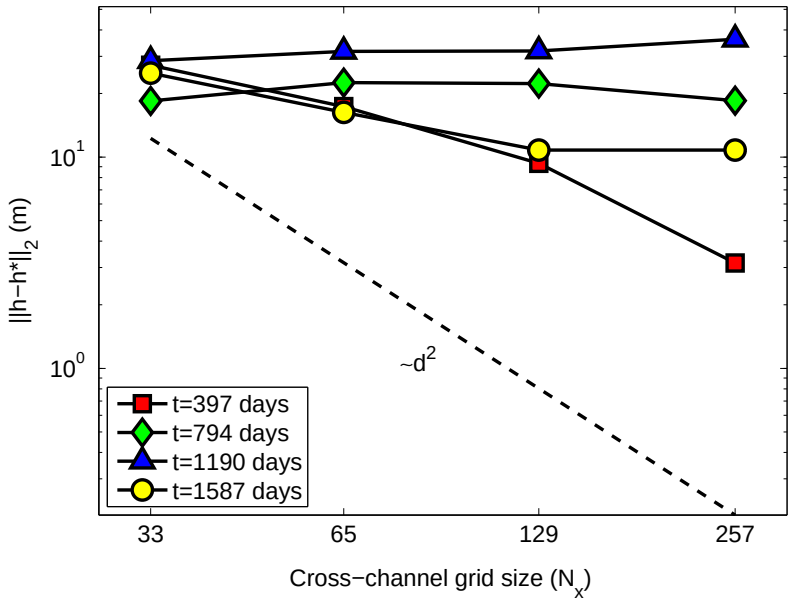

Figure 6.14: Convergence of the solution in test case 2 under grid refinement. The convergence is calculated using an ℓ^2-norm of the discrete layer thicknesses $h_{i+1/2,j+1/2}$, defined by (6.68). The grid spacing is $d = L_x/(N_x - 1)$.

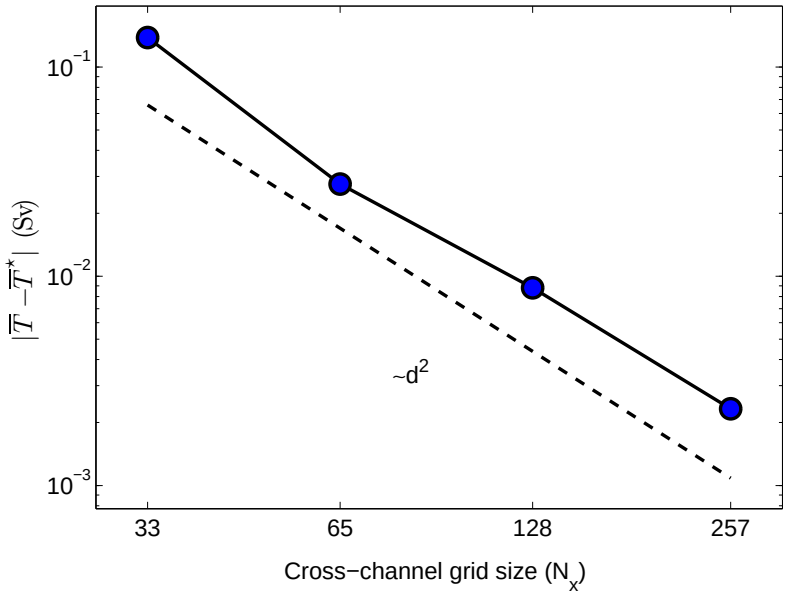

Figure 6.15: Convergence of the time-averaged northern transport in test case 2, defined by (6.70), under grid refinement. We measure the transport in Sverdrups, where $1\,\mathrm{Sv} = 10^6\,\mathrm{m}^3\,\mathrm{s}^{-1}$. The grid spacing is $d = L_x/(N_x - 1)$.

consistent description of the time-averaged behaviour of the flow, though not of the instantaneous solution at any given time.

6.3.2.3 Test case 3

Our final test case is the most relevant to the AABW, which crosses the equator through an almost-westward channel whose profile is shown in Figure 6.6. The solution is summarised in Figure 6.16. In this case the flow takes longer to reach the equator because it must traverse a longer channel, and because the orientation of the equator means that the current can exist as a western boundary current for longer. The current crosses the equator at such a shallow angle that it no longer retroflects completely, as in Figure 6.12. Instead a steady return flow forms to the southeast, whilst eddies pinch off and travel northwest. These eddies carry sufficient mass to prevent an accumulation of fluid in the channel, so the solution does not approach a steady state, and eddies form at a consistent frequency for as long as we have been able to perform the numerical integration. In Figure 6.17 we plot the convergence of this solution under grid refinement. Despite rapid temporal variations throughout the solution, the scheme achieves approximately second-order convergence under the ℓ^2-norm.

This convergence study also provides a practical means of determining a sufficient spatial resolution for the purpose of our parameter studies in §6.3.3. In Figure 6.18 we plot the total mass flux out of the northern end of the channel during the latter half of our time integration, for each of the grid sizes in Table 6.2. At $N_x = 33$ the solution substantially under-predicts the transport, and the transport signature of the eddies is barely visible. The eddies are poorly resolved, and their circulation weakens noticeably as they travel northward in the channel. At $N_x = 65$ the solution provides a qualitatively accurate description of the eddy formation and transport, but the small-scale structure of the eddies is not sufficiently resolved to capture the sharp peaks in transport. The transports at $N_x = 129$, $N_x = 257$ and $N_x = 513$ are almost indistinguishable on this plot. The northern transport serves as a key point of comparison in our parameter studies in §6.3.3. Using $N_x = 129$ has been deemed to provide sufficient resolution the structure of the eddies and other features of the flow, without demanding excessively long computations. However, at low $\hat{A}_h$ we must increase the grid size to $N_x = 257$ to preserve numerical stability.

6.3.3 Effect of including the complete Coriolis force

In §6.3.2 we verified our numerical scheme and discussed solutions for some typical parameter configurations. We now investigate the role of the complete Coriolis force in cross-equatorial flow in different parameter regimes. We are principally interested in the dependence of the cross-equatorial

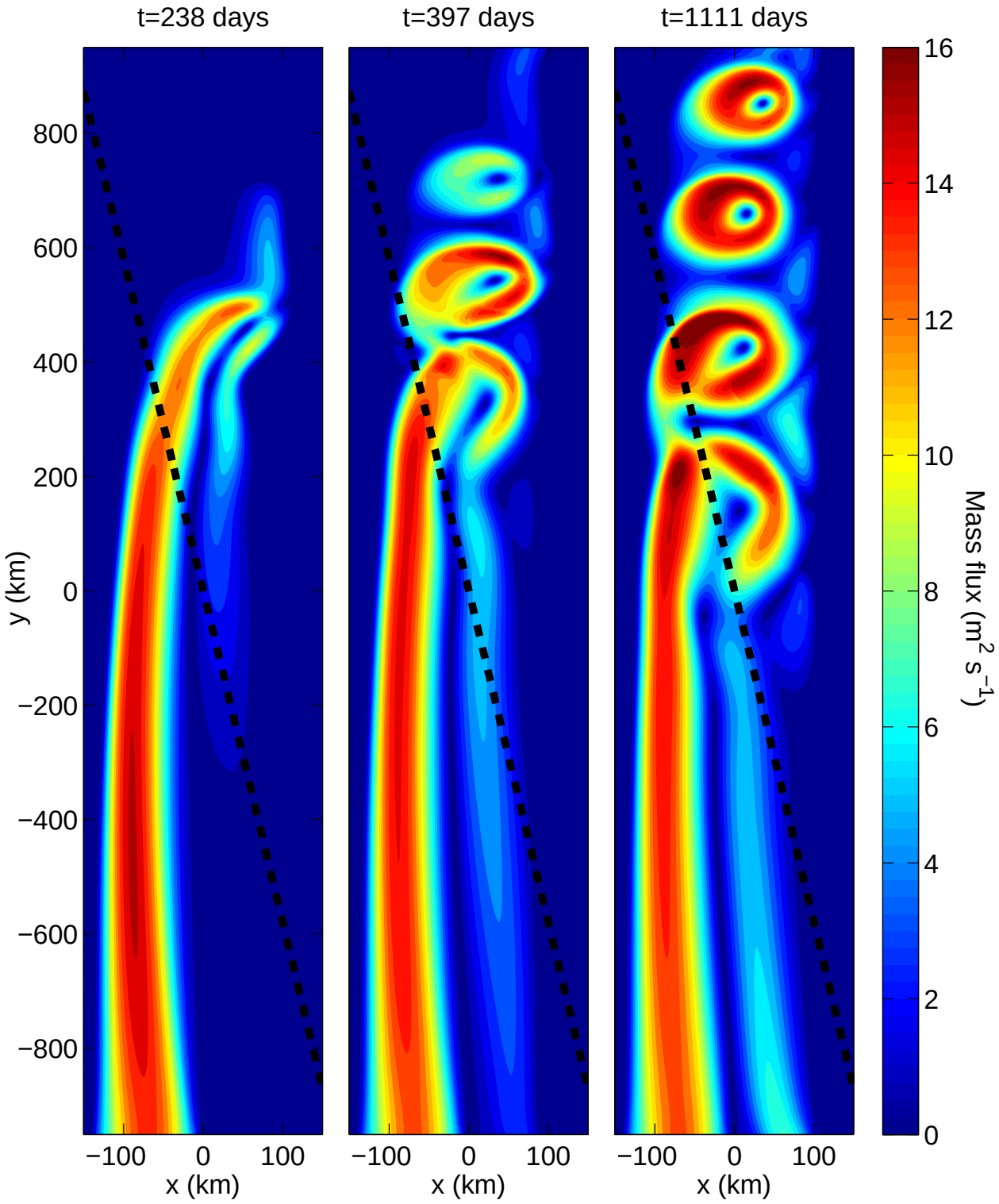

Figure 6.16: Snapshots of the absolute mass flux $|h\boldsymbol{u}|$ in test case 3, computed on a spatial grid of 513×3201 points. The dashed line marks the equator. We omit the sponge layers at the edges of the domain.

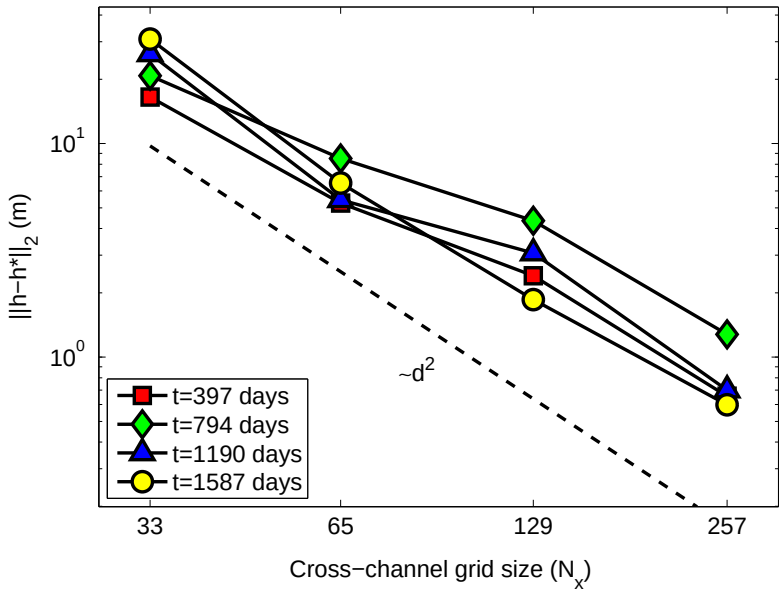

Figure 6.17: Convergence of the solution in test case 3 under grid refinement. The convergence is calculated using an ℓ^2-norm of the discrete layer thicknesses $h_{i+1/2,j+1/2}$, defined by (6.68). The grid spacing is $d = L_x/(N_x - 1)$.

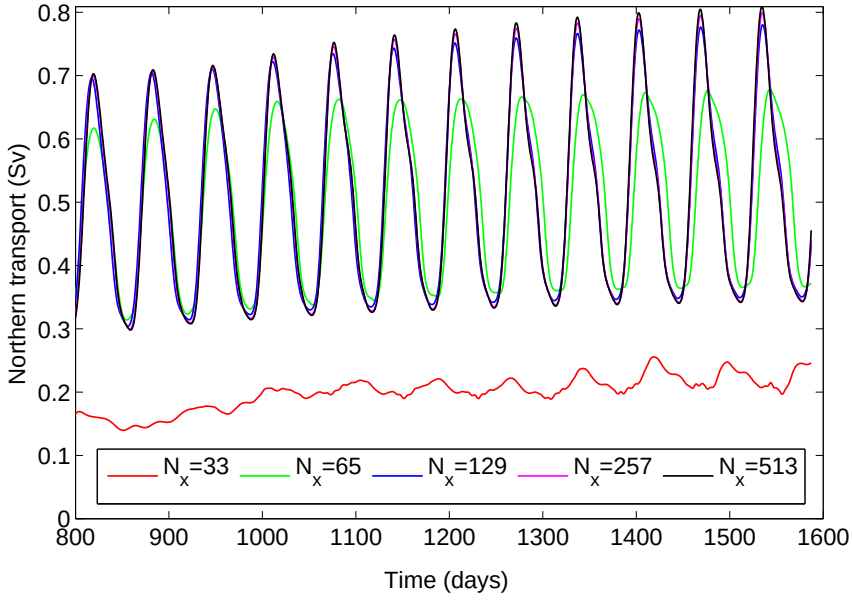

Figure 6.18: Northern transport T from (6.69) between $t = t_{\max}/2$ and $t = t_{\max}$ in test case 3, for each of the grid sizes given in Table 6.2.

transport on the horizontal dissipation $\hat{A}_h$, channel orientation θ, reduced gravity g', and of course the non-traditional component of the Coriolis force. In the following we will hold all other parameters fixed and vary the dimensionless horizontal dissipation parameter $\hat{A}_h$ from (6.66), rather than its dimensional counterpart A_h, because $\hat{A}_h$ defines a horizontal Ekman number for the flow (*e.g.* Pedlosky, 1987). We therefore expect that transitions in the behaviour of the solution should take place at fixed $\hat{A}_h$, rather than A_h, and indeed this is evident in the results below.

We use the topography and upstream depth profile shown in Figure 6.8 in all of our numerical integrations. This defines a different upstream along-channel velocity profile via (6.60) at different channel orientations, due to the dependence of Ω_z on latitude. We therefore discuss separately our results for a northward channel ($\theta = 0$), a northwestward channel ($\theta = \pi/4$), and an almost-westward channel ($\theta = 1.4$) in §6.3.3.1, §6.3.3.2 and §6.3.3.3 respectively. In each case we consider $g' = 10^{-4}\,\mathrm{m\,s^{-2}}$ and $g' = 2 \times 10^{-4}\,\mathrm{m\,s^{-2}}$, which yield inflow velocities on the order of centimetres per second, in agreement with the observations of Hall et al. (1994). For each θ and g', we have obtained numerical solutions with dissipation parameters in the range $\hat{A}_h \in [0.01, 0.12]$, which covers the most dynamically interesting range of solutions that are numerically stable. For smaller values of the dissipation parameter, $\hat{A}_h < 0.01$, we require a grid size of at least $N_x = 513$, which is prohibitively large for long-term numerical integrations.

For $\theta = 0$ and $\theta = \pi/4$ we use a channel of length 1000 km, centred on the equator, as this agrees approximately with the equatorial bathymetry traversed by the AABW. For $\theta = 1.4$ we use a channel of length 2000 km so that cross-channel geostrophic balance (6.60) prescribes a realistic inflow velocity, as described in §6.3.2. For $\hat{A}_h > 0.02$ we use a grid of width $N_x = 129$ points, and for $\hat{A}_h \leq 0.02$ we use $N_x = 257$ to improve resolution of small-scale features and preserve numerical stability. Where it has been possible to obtain solutions at both $N_x = 257$ and $N_x = 129$, the results show excellent agreement. For each set of parameters we integrate numerically from $\hat{t} = 0$ to $\hat{t} = \hat{t}_{\max} = 10^5$, corresponding to a dimensional time of approximately 22 years. Time integration is performed using the third-order Adams-Bashforth scheme with 1.6×10^6 time steps of size 0.0625, or approximately 7.2 minutes.

As in §6.3.2, we use a vertical dissipation $\hat{A}_v = 0.08$ as a suitable compromise between numerical stiffness and minimising mass loss through the Salmon layer. Typically around 15–20% of the fluid that enters at the southern end of the channel will ultimately escape via the sides of the channel because a small flow into the Salmon layer is required to sustain the grounding lines, as discussed in §6.3.1.1. This is exaggerated by the long, thin channel: 80–85% of the inflow exits through the ends of the channel, which constitute only 25% of the sponge boundary in the 1000 km channel, and 14% in the 2000 km channel. For the simulations described in §6.3.2, with $g = 10^{-4}\,\mathrm{m\,s^{-2}}$, the average

mass flux out of the channel sides is 0.1–0.15 $\mathrm{m^2\,s^{-1}}$, which is negligible compared a typical mass flux of 10 $\mathrm{m^2\,s^{-1}}$ in the interior. We conclude that although a substantial proportion of the inflow exits unphysically through the sides of the channel, the dynamical effect of this mass leak is very small.

6.3.3.1 Northward channel, $\theta = 0$

Our solutions in a northward channel somewhat resemble those described for a northwestward channel in §6.3.2.1 and §6.3.2.2. The current crosses the channel when it reaches the equator, and then develops eddies and other chaotic flow patterns. The eastern side of the channel gradually fills with almost-stationary fluid, pushing eddy formation further and further north until the solution reaches a steady state. In Figures 6.19 and 6.20 we plot the time-averaged mass flux through the northern end of the channel, which we use as a measure of the cross-equatorial transport, for a range of values of the horizontal dissipation parameter $\hat{A}_h$. As we reduce $\hat{A}_h$, the solution takes an increasingly long time to approach the steady state. This is because energy dissipation is slower at smaller $\hat{A}_h$, so it takes longer for almost-stationary fluid to settle in the channel. When $g = 10^{-4}\,\mathrm{m\,s^{-2}}$ and $\hat{A}_h = 0.01$, the solution does not reach a steady state within 7936 days under the traditional approximation, but does when the complete Coriolis force is included. This accounts for the relatively large difference between the transports at $\hat{A}_h = 0.01$ in Figure 6.19.

The averaged cross-equatorial transport plotted in Figures 6.19 and 6.20 varies little with $\hat{A}_h$. This is surprising, as stronger dissipation should allow greater modification of the fluid's potential vorticity, and therefore permit a stronger cross-equatorial flow (Edwards and Pedlosky, 1998). However, we showed with our asymptotic solutions in Chapter 5, even inviscid fluid can pass completely through a cross-equatorial channel, so potential vorticity modification is not essential for near-equatorial flows. In this case the build-up of fluid along the eastern side of the channel dictates the form of the steady solution. The fluid does acquire relative vorticity as it crosses the equator, in order to conserve potential vorticity, but manifests this relative vorticity as additional shear, rather than the formation of eddies. In Figure 6.21 we plot the steady state for $\hat{A}_h = 0.02$ and $\hat{A}_h = 0.12$ when $g' = 10^{-4}\,\mathrm{m\,s^{-2}}$. At $\hat{A}_h = 0.02$ the northward jet sharpens much more dramatically than it does when $\hat{A}_h = 0.12$, corresponding to an increase in the magnitude of the relative vorticity $\zeta = \partial v/\partial x - \partial u/\partial y \approx \partial v/\partial x$ that is required to balance the change in planetary vorticity across the equator. In these solutions the extent of the almost-stationary fluid along the eastern side of the channel is limited by the sponge layers at the edges, but numerical integrations in a 2000 km-long channel exhibit very similar behaviour.

In a northward channel the zonal flow is confined to be small, so we expect little influence from

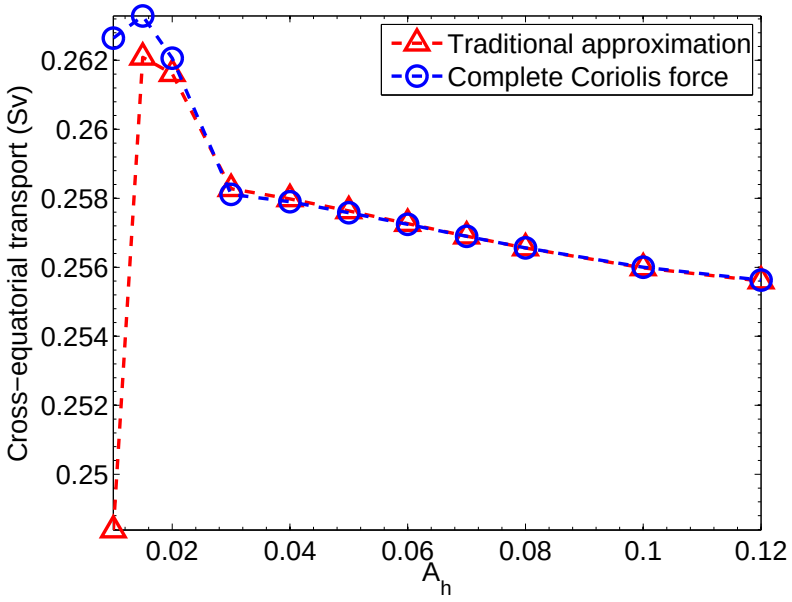

Figure 6.19: Time-averaged transport $\overline{T}$ through the northern end of the northward channel ($\theta = 0$) with $g = 10^{-4}\,\mathrm{m\,s^{-2}}$, for a range of values of the horizontal dissipation parameter $\hat{A}_h$.

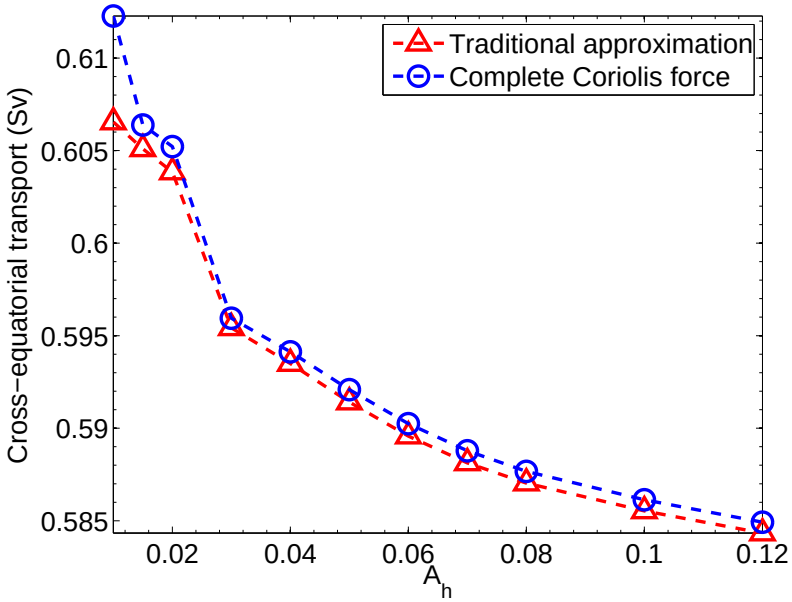

Figure 6.20: Time-averaged transport $\overline{T}$ through the northern end of the northward channel ($\theta = 0$) with $g = 2 \times 10^{-4}\,\mathrm{m\,s^{-2}}$, for a range of values of the horizontal dissipation parameter $\hat{A}_h$.

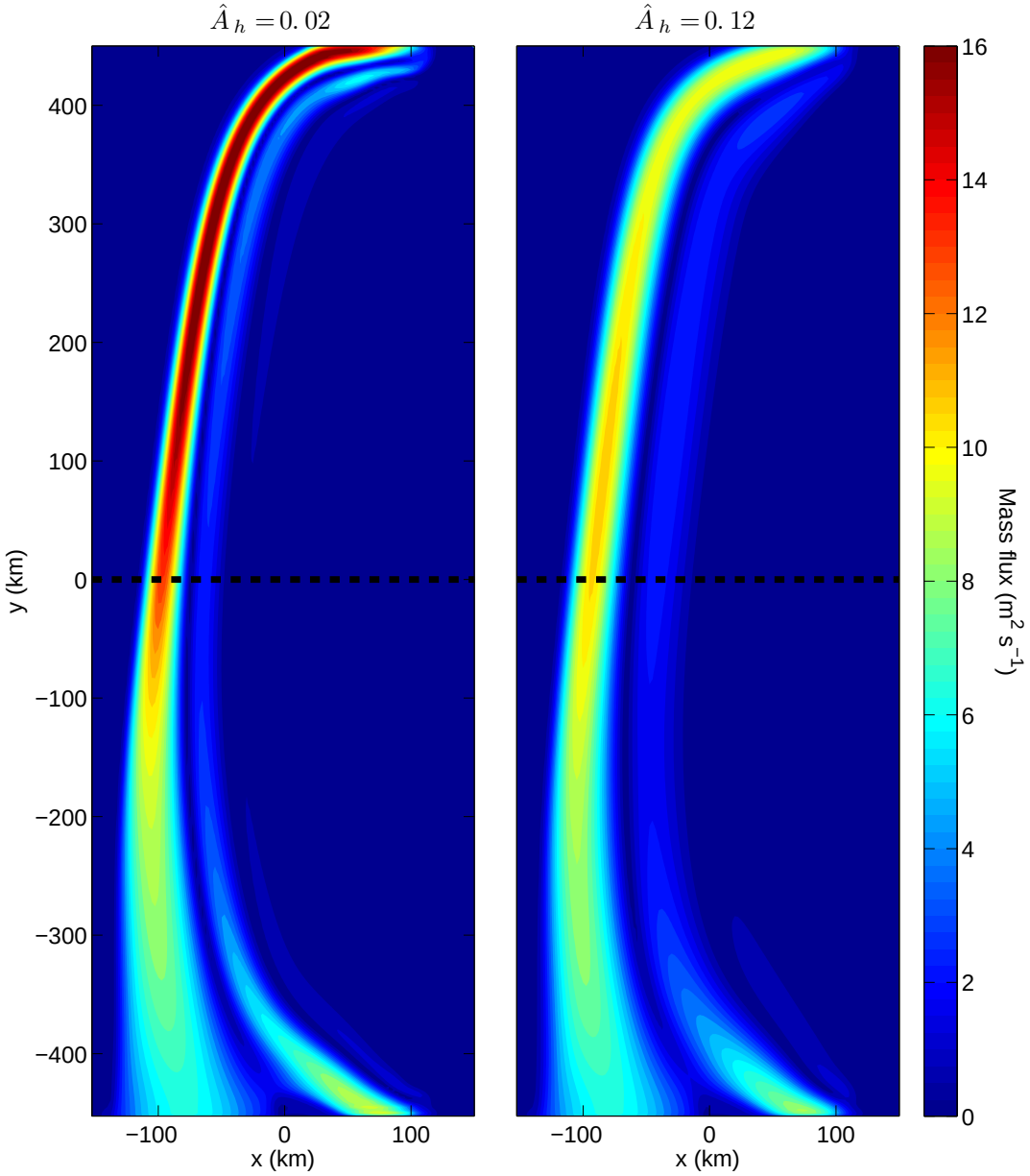

Figure 6.21: Snapshots of the steady-state absolute mass flux $|h\boldsymbol{u}|$ under weak ($\hat{A}_h = 0.02$) and strong ($\hat{A}_h = 0.12$) horizontal dissipation, in a northward channel ($\theta = 0$) with $g' = 10^{-4}\,\mathrm{m\,s^{-2}}$. Both solutions have been computed on a spatial grid of 129×401 points. The dashed line marks the equator. We omit the sponge layers at the edges of the domain.

the non-traditional component of the Coriolis force, which connects vertical and zonal motions. In Chapter 5 our asymptotic solutions for cross-equatorial flow through an idealised northward channel were completely unaffected by the inclusion of the complete Coriolis force. Our numerical solutions confirm this analysis, as in Figures 6.19 and 6.20 there is no discernible difference between making the traditional approximation and including the complete Coriolis force. There is a slightly larger difference between the cross-equatorial transports at $\hat{A}_h = 0.01$ because the traditional solution does not reach a steady state within 7936 days.

6.3.3.2 Northwestward channel, $\theta = \pi/4$

As our channel is long compared to its breadth, we might not expect to see much difference between solutions computed in a northward channel and a northwestward channel. Our idealised asymptotic solutions in Chapter 5 did not change dramatically when the equator was oriented at 45° to the channel because it was assumed that the relevant along-channel lengthscale was much larger than the cross-channel lengthscale. However, the flow structures shown in Figures 6.9–6.10 and 6.12–6.13 have comparable along-channel and across-channel lengthscales, so in fact the solution behaves quite differently in a northwestward channel. At large $\hat{A}_h$ the solution approaches a steady state within around 1000–2000 days, whilst at small $\hat{A}_h$ the solution never reaches a steady state, and instead forms a series of eddies that propagate out of the northern end of the channel. There appears to be a sharp transition between these two regimes, though we only have data for a limited number of values of $\hat{A}_h$.

In Figures 6.22 and 6.23 we plot the time-averaged transport $\overline{T}$ through the northern end of the channel for a range of values of the horizontal dissipation parameter $\hat{A}_h$. When $g = 10^{-4}\,\mathrm{m\,s^{-2}}$ the solution rapidly approaches a steady state for $\hat{A}_h \geq 0.04$, but remains unsteady for $\hat{A}_h \leq 0.03$. This transition is visible in Figure 6.22. When $g = 2 \times 10^{-4}\,\mathrm{m\,s^{-2}}$ the solution rapidly approaches a steady state for $\hat{A}_h \geq 0.05$, and remains unsteady for $\hat{A}_h \leq 0.04$. The time-averaged transport $\overline{T}$ varies little between the steady solutions, as in the northward channel, but the unsteady solutions show more variability. As we reduce $\hat{A}_h$, the solution becomes increasingly chaotic, because fluid must acquire a larger relative vorticity as it crosses the equator. The resulting eddies travel towards the northern end of the channel, but their propagation is slower when $\hat{A}_h$ is smaller, because they dissipate vorticity more slowly. Thus we expect that at even smaller $\hat{A}_h$, the time-averaged transport $\overline{T}$ should decrease further.

In Figure 6.24 we illustrate the increasingly chaotic behaviour of the solution at small $\hat{A}_h$ using the Fourier transform of the cross-equatorial transport $T(t)$. We define the k^{th} Fourier component

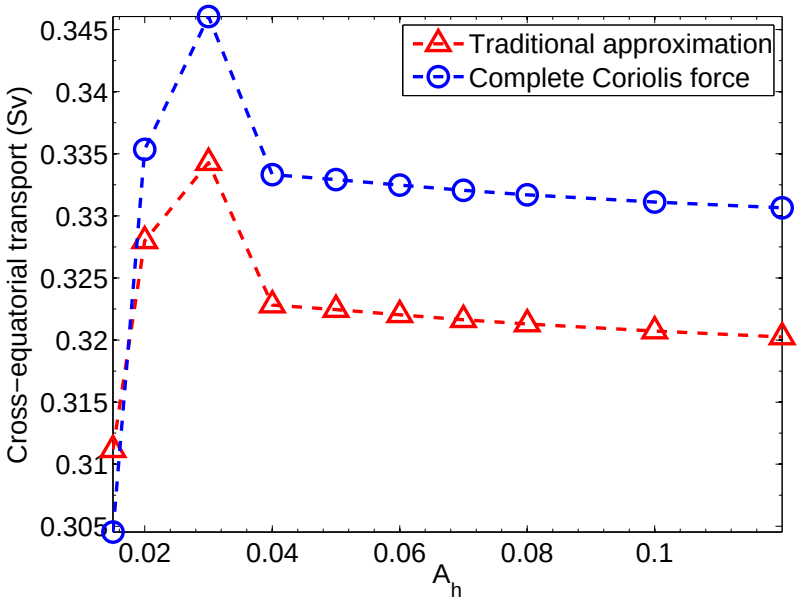

Figure 6.22: Time-averaged transport $\overline{T}$ through the northern end of the northwestward channel ($\theta = \pi/4$) with $g = 10^{-4}\,\mathrm{m\,s^{-2}}$, for a range of values of the horizontal dissipation parameter $\hat{A}_h$.

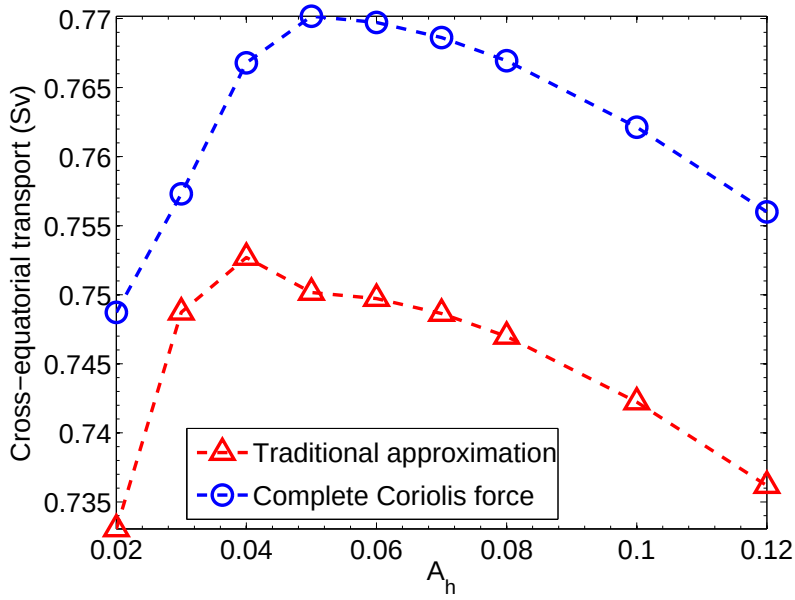

Figure 6.23: Time-averaged transport $\overline{T}$ through the northern end of the northwestward channel ($\theta = \pi/4$) with $g = 2 \times 10^{-4}\,\mathrm{m\,s^{-2}}$, for a range of values of the horizontal dissipation parameter $\hat{A}_h$.

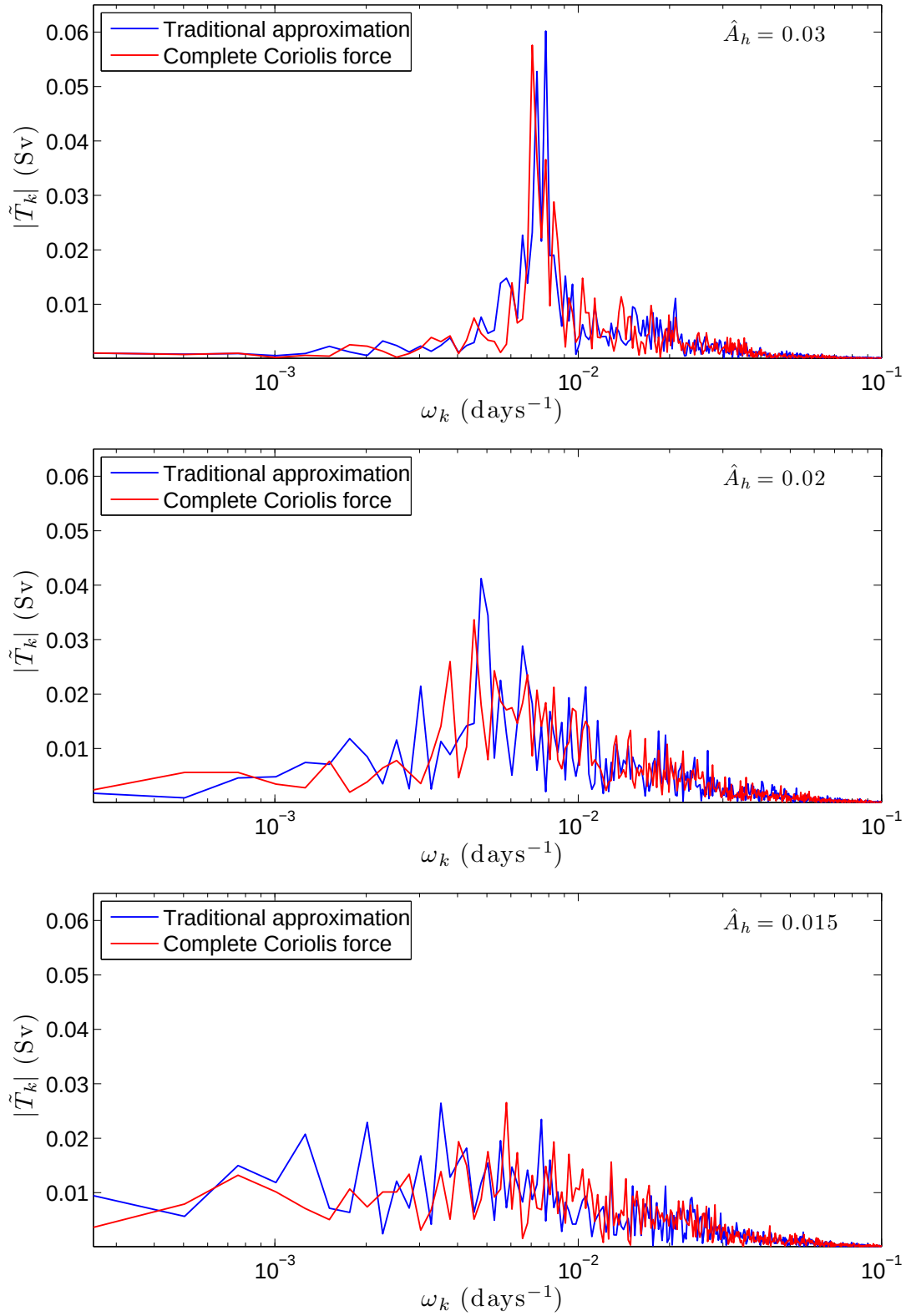

Figure 6.24: Magnitudes of the Fourier components $|\tilde{T}_k|$ of the transport through the northern end of the northwestward channel between $t = t_{\max}/2$ and $t = t_{\max}$. In all cases the reduced gravity is $g' = 10^{-4}\,\mathrm{m\,s^{-2}}$. The magnitudes of the negative frequencies are symmetric and given by $|\tilde{T}_{-k}| = |\tilde{T}_k|$.

of the transport as

$$\tilde{T}_k = \frac{2}{t_{\max}} \int_{t_{\max}/2}^{t_{\max}} \left(T(t) - \overline{T}\right) \exp\left(-2\pi \mathrm{i} \omega_k t\right) \, \mathrm{d}t, \tag{6.71}$$

where $\omega_k = 2k/t_{\max}$ is the frequency corresponding to the k^{th} component. We have subtracted the time-averaged transport $\overline{T}$ from (6.70) to eliminate the time-independent component, $\tilde{T}_0 = 0$. This highlights the contribution of the eddies, which account for a large proportion of the cross-equatorial transport, as in Figure 6.18. The transport T may then be written as

$$T(t) = \overline{T} + \sum_{k=-\infty}^{\infty} \tilde{T}_k \exp\left(2\pi \mathrm{i} \omega_k t\right). \tag{6.72}$$

We have chosen this form so that the period of the oscillation corresponding to the k^{th} Fourier component is $\tau_k = 1/\omega_k$, and the amplitude of this oscillation is $\tilde{T}_k$. This provides a more intuitive interpretation of Figure 6.24.

At $\hat{A}_h = 0.03$ there is a relatively well-defined eddy period of around $\tau_k \approx 130$ days that dominates all other Fourier components of T. This indicates that eddies form with a regular period, but are subject to small variations due to variability in the surrounding flow. At $\hat{A}_h = 0.02$ the Fourier components appear to have a maximum around $\tau_k \approx 200$ days, but it is less pronounced than at $\hat{A}_h = 0.03$. The flow exhibits a much wider range of eddy formation periods, though they are still clustered around $\tau_k \approx 200$ days. At $\hat{A}_h = 0.015$ there is no discernible dominant timescale, though the flow is largely confined to motions with periods between $\tau_k \approx 100$ days and $\tau_k \approx 1000$ days. This turbulent behaviour at low $\hat{A}_h$ has thus far limited our numerical study of the northwestward channel to $\hat{A}_h \geq 0.015$.

Including the complete Coriolis force has a modest effect on the flow in a northwestward channel, as in our asymptotic solutions of Chapter 5. Figure 6.24 shows that there may be dramatic differences between the traditional and non-traditional solutions over short lengthscales or timescales, because in a chaotic flow even a small additional force will give rise to large local variations in the solution after a sufficiently long time. However, the statistical properties of the flow do not differ greatly. For example, the time-averaged cross-equatorial transport $\overline{T}$ is consistently a few percent larger under the complete Coriolis force. This may be because a larger westward flow is possible in non-traditional cross-channel geostrophic balance, as discussed in Chapter 5, though this holds only when g' is not too small.

6.3.3.3 Almost-westward channel, $\theta = 1.4$

An almost-westward channel with $\theta = 1.4$ is most relevant for the AABW, which traverses an equatorial channel with the approximate dimensions and orientation used in this study. The behaviour of the exhibits some similarities to that in a northwestward channel ($\theta = \pi/4$), discussed in

§6.3.3.2. For both $g' = 10^{-4}\,\mathrm{m\,s^{-2}}$ and $g' = 2 \times 10^{-4}\,\mathrm{m\,s^{-2}}$, the solution approaches a steady state for $\hat{A}_h \geq 0.07$, and approaches a quasi-steady state for $\hat{A}_h \leq 0.06$. The steady state resembles those shown in Figures 6.10 and 6.21. The quasi-steady state is characterised by periodic formation of eddies, as illustrated in Figure 6.16.

In Figures 6.25 and 6.26 we plot the time-averaged cross-equatorial transport $\overline{T}$ against the horizontal dissipation $\hat{A}_h$. In both cases there is a clear transition between the steady and quasi-steady regimes. As in the northward and northwestward channels, the time-averaged transport in the steady solutions varies little with $\hat{A}_h$. However, $\overline{T}$ increases substantially as we reduce the horizontal dissipation from $\hat{A}_h = 0.06$ to $\hat{A}_h \approx 0.02$. A plausible explanation is that at $\hat{A}_h = 0.06$ the dissipation is small enough to permit the formation of eddies, but still inhibits their propagation through the channel. As we reduce $\hat{A}_h$, the eddies are less restricted by the horizontal dissipation, and may therefore transport more fluid through the channel. However, at smaller $\hat{A}_h$ the eddies are also less dissipative, and so the rate of potential vorticity modification is slower. The may explain the maximum of $\overline{T}$ at $\hat{A}_h \approx 0.02$ in Figure 6.25. We might expect to find a similar maximum if we extended Figure 6.26 to smaller values of $\hat{A}_h$.

In contrast to the northwestward channel of §6.3.3.2, the solution does not exhibit increasingly chaotic behaviour as we reduce $\hat{A}_h$ over the range shown in Figures 6.25 and 6.26. The flow develops structure at smaller scales, consistent with a reduction in effective viscosity, but the transport through the northern end of the channel remains almost perfectly periodic. In Figure 6.27 we plot the magnitudes of the Fourier components T_k, defined in (6.71), of the northern transport $T(t)$ for a typical solution. The spike in $|T_k|$ at $\omega_k \approx 2.2 \times 10^{-2}\,\mathrm{days}^{-1}$ defines an eddy formation period of $\tau_e \approx 46\,\mathrm{days}$. Spikes of progressively smaller amplitude are visible at periods of $\tau_e/2$, $\tau_e/3$, $\tau_e/4$, and $\tau_e/5$. Such a combination of modes describes an oscillation of arbitrary shape, and period τ_e. In Figure 6.28 we plot τ_e against $\hat{A}_h$ for all solutions that do not approach a steady state. At $g' = 10^{-4}\,\mathrm{m\,s^{-2}}$ the horizontal dissipation has little impact on τ_e, whereas at $g' = 2 \times 10^{-4}\,\mathrm{m\,s^{-2}}$, decreasing $\hat{A}_h$ leads to a substantially shorter eddy formation period. Thus the increase in transport $\overline{T}$ with decreasing $\hat{A}_h$ in Figure 6.26 is due to the eddies forming more rapidly. We have omitted the eddy periods at $\hat{A}_h = 0.06$ in Figure 6.28(a) because the traditional solution is on the verge of transition to a steady flow, and the formation of eddies takes place much closer to the northern end of the channel than in all other cases considered here.

Our asymptotic solutions in Chapter 5 suggest that the non-traditional component of the Coriolis force should be most prominent in the almost-westward channel because it connects vertical and zonal fluid motions. Figures 6.25 and 6.26 show that there is a consistent increase in the cross-equatorial transport when the complete Coriolis force is included, particularly when $\hat{A}_h$ is small.

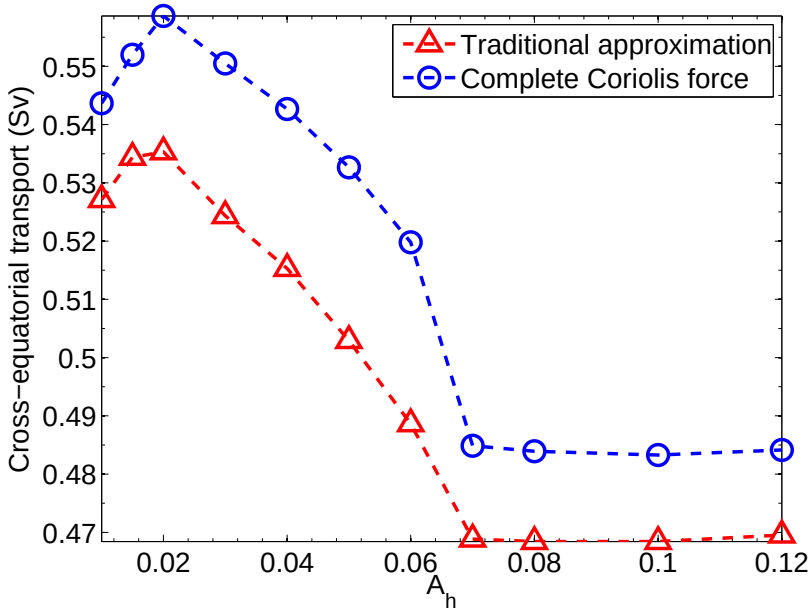

Figure 6.25: Time-averaged transport $\overline{T}$ through the northern end of the almost-westward channel ($\theta = 1.4$) with $g = 10^{-4}\,\mathrm{m\,s^{-2}}$, for a range of values of the horizontal dissipation parameter $\hat{A}_h$.

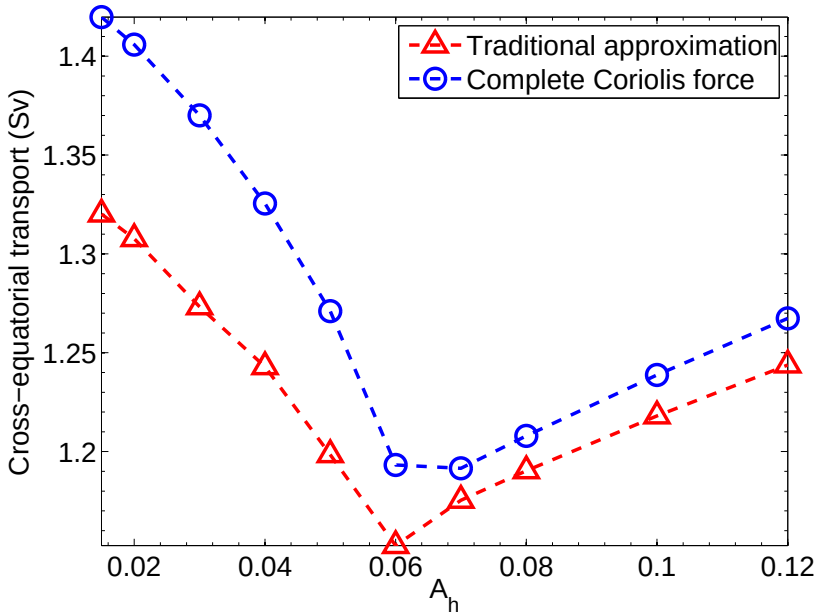

Figure 6.26: Time-averaged transport $\overline{T}$ through the northern end of the almost-westward channel ($\theta = 1.4$) with $g = 2 \times 10^{-4}\,\mathrm{m\,s^{-2}}$, for a range of values of the horizontal dissipation parameter $\hat{A}_h$.

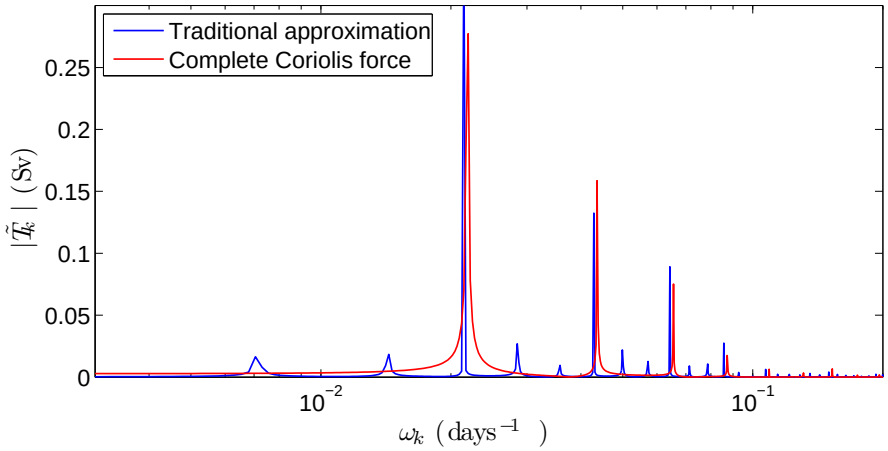

Figure 6.27: Fourier amplitudes $|\tilde{T}_k|$ in an almost-westward channel with $A_h = 0.03$ and $g' = 2\times10^{-4}\,\mathrm{m\,s^{-2}}$. This plot is typical of all non-steady solutions in the almost-westward channel.

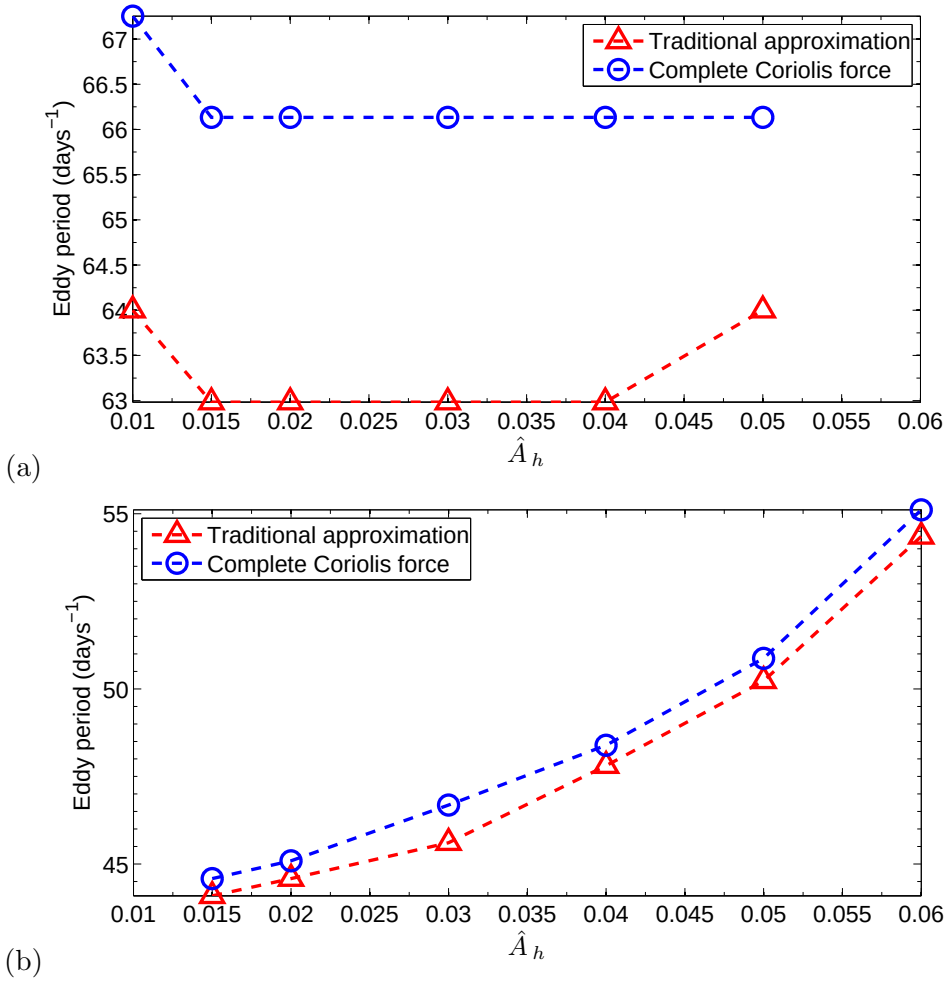

Figure 6.28: Eddy formation periods in non-steady solutions in an almost-westward channel, plotted for various values of the horizontal dissipation $\hat{A}_h$.

However, this increase is no larger than 10%. Including the complete Coriolis force also influences the character of the eddies formed in the channel. In Figure 6.27 the non-traditional Fourier components acquire additional non-zero amplitudes at frequencies scattered around the eddy formation frequency. As a result, the eddy transport may vary by as much as 20%, whereas under the traditional approximation it is typically uniform. The eddy formation period is also typically around 5% longer under the complete Coriolis force, as shown in Figure 6.28. The combination of these differences suggests that the non-traditional eddies form more slowly, but transport substantially more fluid, than their traditional counterparts, and that there is much more variability between individual eddies.

6.4 Discussion

In this chapter we have discussed computational approaches to solving the non-traditional shallow water equations derived in Chapter 2. In §6.2 we derived a non-traditional extension of the Arakawa and Lamb (1981) finite-difference scheme, which exactly conserves total discrete energy and potential enstrophy. This procedure was simplified considerably by following the approach of Salmon (2004), who showed that the traditional Arakawa and Lamb (1981) scheme may be formulated as a discrete Hamiltonian (6.17) and Poisson bracket (6.19), with discrete dynamics (6.23). We obtained our scheme for the non-traditional shallow water equations by using suitably-defined canonical variables (6.1) as our discrete prognostic variables. The canonical variables $\tilde{\boldsymbol{u}}$ are sufficiently similar to the physical velocities $\boldsymbol{u}$, which are canonical variables for the traditional shallow water equations, that the Arakawa and Lamb (1981) scheme need only be modified slightly to incorporate them. The most important decision is how to compute the discrete physical velocities $\{u_{i,j+1/2}, v_{i+1/2,j}\}$ from the surrounding prognostic variables $\{\tilde{u}_{i,j+1/2}, \tilde{v}_{i+1/2,j}, h_{i+1/2,j+1/2}\}$, posed in general form in (6.31a)–(6.31b). In §6.2.3 we showed that any second-order approximation may be chosen, as this affects only the discrete approximation of the non-traditional terms in the pressure gradient. The resulting scheme may be used to integrate the inviscid non-traditional shallow water equations over arbitrary bottom topography. Discrete time-integration introduces small errors in the energy and potential enstrophy, but it is straightforward to reduce these errors down to the level of machine precision using high-order time-stepping schemes and a small time step.

In §6.3 we obtained numerical solutions for cross-equatorial flow through a channel, a problem that we approached theoretically in Chapters 4 and 5. Our approach is complicated considerably by the presence of grounding lines, where the fluid surface intersects the bottom topography, because the Arakawa and Lamb (1981) scheme becomes unstable if the layer thickness h approaches zero

anywhere in the computational domain. We avoid this by prescribing a Salmon layer (*c.f.* Salmon, 2002) over all "dry" areas of the topography, as discussed in §6.3.1.1. However, this necessitates the inclusion of a numerical dissipation to prevent unphysical acceleration of the Salmon layer, and an effective viscosity to prevent the fluid surface steepening to a shock when it encounters the Salmon layer, as discussed in §6.3.1.2. These terms explicitly dissipate energy and potential enstrophy, but this does not render the scheme derived in §6.2 obsolete. It is still desirable that the core dynamics of the discrete shallow water equations do not have spurious sources or sinks of energy and potential enstrophy, as this is detrimental to long-term numerical stability (Arakawa, 1966). For example, Fornberg (1973) showed that a class of centred finite difference schemes for the inviscid Burgers equation are subject to short-time numerical instability unless the scheme is constructed to conserve discrete energy.

We verified our extended numerical approach in §6.3.2, showing that its convergence under grid refinement is in good agreement with the theoretical second-order accuracy of the spatial discretisation (*c.f.* §6.3.2.1 and §6.3.2.2). At low horizontal dissipation $\hat{A}_h$ the behaviour is chaotic, so even small grid-scale errors lead to $\mathcal{O}(1)$ pointwise differences in the resulting solution. In such situations (*c.f.* §6.3.2.2) the pointwise convergence of the scheme is poor, but statistical properties of the solution, such as the time-averaged cross-equatorial transport, still exhibit convincing second-order convergence. We also determined that a grid spacing of $d = 2.5\,\mathrm{km}$ would typically capture the behaviour of the solution with good accuracy, whilst simulations on coarser grids could not capture the small-scale structure of the eddies, and therefore tended to substantially under-predict the cross-equatorial transport.

In §6.3.3 we investigated the dynamics of a current flowing through a cross-equatorial channel, with particular emphasis on the AABW. We considered a range of values of the channel orientations θ, reduced gravity g', and horizontal dissipation parameter $\hat{A}_h$, both under the traditional approximation and including the complete Coriolis force. The behaviour of the solution is strongly dependent on the orientation of the channel. In general, for sufficiently large $\hat{A}_h$ the solution eventually approaches a steady state that resembles Figures 6.9 and 6.21. For sufficiently small $\hat{A}_h$ the solution approaches a periodic or quasi-periodic state in which the current crosses the equator via a series of eddies, illustrated in Figures 6.13 and 6.16. As θ varies from 0 to $\pi/2$, the transition between these states occurs at larger $\hat{A}_h$. This is because an eddy moving a distance y_e along the channel covers a northward distance of $y_e \cos\theta$, and therefore may be expected to acquire a relative vorticity proportional to $\cos\theta$. Thus, for fixed $\hat{A}_h$, which determines the rate of relative vorticity dissipation, the eddies must propagate more slowly when θ is closer to 0. Energy dissipation simultaneously leads to almost-stationary fluid building up in the channel, so it is inevitable that when

$\hat{A}_h$ is sufficiently large, the eddies will no longer form.

These numerical results suggest a somewhat less prominent role of the complete Coriolis force than in previous chapters. Our asymptotic solutions of Chapter 5 indicate that the non-traditional component of the Coriolis force may account for up to 30% of the cross-equatorial transport of the AABW, but our time-dependent solutions place this estimate below 10%. This may be due to the very small reduced gravity $g \sim 10^{-4}\,\mathrm{m\,s^{-2}}$ used in our numerical solutions. In Chapter 5 we showed that a current with zero potential vorticity in cross-channel geostrophic balance has a larger non-traditional transport at a more realistic value of $g' = 10^{-3}\,\mathrm{m\,s^{-2}}$, and a larger traditional transport at $g' = 3 \times 10^{-4}\,\mathrm{m\,s^{-2}}$. Whilst we do not expect this result to translate directly to our numerical integrations, which are subject to fewer assumptions about the solution, it is conceivable that non-traditional geostrophic balance permits more of the AABW to enter the equatorial channel and cross into the northern hemisphere. We could explore this possibility using a larger reduced gravity and an alternative inflow condition in the channel, or using the full equatorial bathymetry. Including the complete Coriolis force also has some unexpected effects on the eddies generated in the cross-equatorial channel, which experience up to 20% variation in their transport and take approximately 5% longer to form than under the traditional approximation.

Whilst we have confidence in the quality of our numerical solutions, they may benefit from an improved approach to the grounding lines. Although the dynamic effect of fluid leaking into the Salmon layer is small, it is not entirely satisfactory to lose 15–20% of the inflow through the channel sides. A straightforward remedy is to decrease the thickness of the Salmon layer. This permits a smaller vertical dissipation $\hat{A}_v$, which is in turn less restrictive on the time step. However, the current tends to steepen and form shocks more rapidly on encountering such a shallow Salmon layer, which may lead to numerical instability. We may partially offset this by including a bulk viscosity to our stress tensor, following Shchepetkin and O'Brien (1996), but ideally our solutions should be as non-dissipative as possible. The development of an effective and robust approach to grounding lines in numerical integrations of the shallow water equations is the subject of ongoing work.

Chapter 7

Conclusion

7.1 Summary of results

Our derivation in Chapter 2 of the multi-layer shallow water equations with complete Coriolis force is fundamental to all of the work in this thesis. Our derivation extends the single-layer derivation of Dellar and Salmon (2005) to arbitrarily many superposed layers, and correctly handles arbitrary spatial variations of the rotation vector $\mathbf{\Omega}$. Dellar and Salmon (2005) had in turn corrected the treatment of the the bottom topography in Bazdenkov et al. (1987). We derived the non-traditional shallow water equations by averaging vertically over each layer, and via two related Lagrangian formulations of the three-dimensional Euler equations. All of these derivations depend on the assumption of a small aspect ratio, and of approximately columnar motion within each layer. By making these approximations in the Lagrangian for the three-dimensional Euler equations, we ensured that the expected conservation laws for mass, energy, momentum and potential vorticity are preserved in the shallow water equations. Our derivation by depth-averaging yields the same set of equations, so we may be confident that our equations contain an accurate representation of the non-traditional component of the Coriolis force. These equations are practical for studying non-traditional effects in large-scale ocean flows because they do not depend on the vertical coordinate, so numerical integrations are less complicated. Similar methods may be used to include the non-traditional component of the Coriolis force in ocean circulation models that use isopycnal coordinates, like the Miami Isopycnic Coordinate Ocean Model.

In Chapter 3 we analysed hyperbolicity and linear plane waves in the non-traditional multi-layer shallow water equations. Hyperbolicity is an important requirement of the shallow water equations, as otherwise they are ill-posed for initial-value problems. We may reasonably expect the hyperbolicity of the multi-layer shallow water equations to be modified by the use of a quasi-hydrostatic pressure (*c.f.* White and Bromley, 1995), because using a fully non-hydrostatic pressure

(Green and Naghdi, 1976; Miles and Salmon, 1985) makes the two-layer equations unconditionally ill-posed (Liska and Wendroff, 1997). However, our results suggest that non-traditional effects modify the criteria for the equations to be hyperbolic by no more than 5%, so we should be able to compute solutions under roughly the same conditions as for the traditional multi-layer shallow water equations. By contrast, linear plane waves exhibit some dramatic and unexpected changes when the complete Coriolis force is included. The surface and internal wave modes connect in the limit of long wavelength, with a smooth transition over a range of "sub-inertial" wave numbers where the frequency lies below the inertial frequency. This range corresponds to a distinguished asymptotic limit $k = \mathcal{O}(\delta)$, where k is the dimensionless wavenumber relative to the deformation radius R_d, and $\delta = H/R_d$ is the ratio of vertical to horizontal lengthscales. In this limit the gravitational pressure gradient becomes comparable to the non-traditional component of the Coriolis force. The sub-inertial waves are not distinguishable as either surface or internal waves, and are characterised by oscillations on both the upper surface and the internal surfaces that are out of phase with one another. This suggests that the amplitudes of very long ocean waves may be constrained, as non-traditional waves must oscillate on both the internal density surfaces and on the upper surface of the ocean, which requires much more energy than oscillating purely on the internal surfaces.

A substantial portion of this thesis is concerned with the role of non-traditional effects in cross-equatorial flow of abyssal ocean currents like the AABW. Our shallow water equations are ideal for this purpose, as they describe the interaction of non-traditional rotation with arbitrary bottom topography, and are neither restricted to small-amplitude oscillations (*c.f.* Raymond, 2000), nor rotationally-dominated flow (*c.f.* Colin de Verdière and Schopp, 1994; Schopp and Colin de Verdière, 1997). In Chapter 4 we constructed an idealised model of the AABW using one-dimensional shallow water flow across an equatorial channel. Although a rather crude simplification of the real abyssal dynamics, this description provides an intuition for the action of the non-traditional component of the Coriolis force. Fluid crossing the equator through a zonal channel remains closer to the axis of rotation throughout its motion, as illustrated in Figure 4.3, and so conservation of angular momentum dictates that it need not acquire such a large westward velocity at the equator. The fluid only feels the contribution of the topographic contribution to its planetary angular momentum if the complete Coriolis force is included. An equivalent interpretation is that fluid crossing the equatorial channel experiences a smaller change in its relative vorticity, by conservation of potential vorticity. Our inviscid analytical results and computed solutions reflect this analysis. Including dissipation allows the fluid to modify its potential vorticity, and thereby acquire less relative vorticity as it crosses the equator. We found that for approximately the same change in relative vorticity, the cross-equatorial transport was always larger when the non-traditional component of the Coriolis

force was included. We also revisited the one-dimensional cross-equatorial geostrophic adjustment problem of Killworth (1991), and showed that including the complete Coriolis force always permits more fluid to cross further into the northern hemisphere.

A major shortcoming of the analysis in Chapter 4 was the restriction to one space dimension, so in Chapter 5 we considered steady asymptotic solutions for flow through an arbitrarily-oriented cross-equatorial channel. We restricted our attention to flows with zero potential vorticity, because Hua et al. (1997) showed that near-equatorial flows are subject to symmetric instability unless the non-traditional three-dimensional Ertel potential vorticity Q_E has the same sign as the traditional Coriolis parameter f, implying $fQ_E > 0$. Fluid within around 3° of the equator therefore tends to homogenise to a state of zero potential vorticity, which is consistent with Firing's (1987) measurements of the deep ocean. We first considered a channel with vertical walls, following the asymptotic solutions of Nof (1990) and Nof and Olson (1993) for northward/southward-flowing cross-equatorial currents. As Nof and Olson (1993) showed, the current must cross the channel as it crosses the equator, in order to preserve cross-channel geostrophic balance. Including the complete Coriolis force leads to a larger transport in a northwestward channel, and a smaller transport in a northeastward channel. The most intuitive physical interpretation for this is that the current's velocity at the grounding line is fixed by the upstream boundary conditions, and is almost identical whether or not the complete Coriolis force is included. The flow has zero potential vorticity and varies slowly along the channel, so the angular momentum is approximately constant across the channel, as expressed by (5.26a). Away from the grounding line, the non-traditional component of the Coriolis force contributes an additional positive planetary angular momentum proportional to the half-layer depth $\overline{z} = h_b + \frac{1}{2}h$, so the fluid must acquire negative relative angular momentum in the form of a westward velocity. This increases the transport through a northwestward channel, and decreases the transport through a northeastward channel. As the orientation of the channel approaches westward/eastward, geostrophic balance breaks down and the validity of this solution becomes questionable. This motivated an alternative asymptotic scaling for an almost-westward or almost-eastward channel, which also conveniently permits arbitrary cross-channel variations of the bottom topography. In an almost-westward channel whose dimensions are similar to the equatorial bathymetry traversed by the AABW, the non-traditional component of the Coriolis force may account for as much as 30% of the current's transport.

The solutions obtained in Chapter 5 omit time-dependence, which is a vital component of many geophysical flows. Although the steady solutions elucidate the role of the non-traditional component of the Coriolis force, they may not be stable or attracting in a time-dependent formulation. Two-dimensional time-dependent solutions are typically too complicated to obtain analytically, so in

Chapter 6 we derived a numerical scheme for our non-traditional single-layer shallow water equations. We generalised the Arakawa and Lamb (1981) finite-difference scheme using the discrete Hamiltonian and Poisson bracket of Salmon (2004). This scheme exactly conserves discrete energy and potential enstrophy, which avoids a spurious build-up of energy at small scales over long-term numerical integrations (Arakawa, 1966; Arakawa and Lamb, 1977). The scheme may be used as–is to compute inviscid solutions of the non-traditional shallow water equations over arbitrary topography. However, the calculation will break down if the thickness of the fluid layer approaches zero anywhere in the domain, because the potential vorticity q must be computed explicitly on each grid point at each time step.

To apply our numerical scheme to cross-equatorial flow through a channel, which necessarily involves grounding lines, we included a "Salmon layer" (Salmon, 2002) to prevent the layer thickness h decreasing much below a specified "Salmon thickness" h_s. We also included explicit vertical dissipation to avoid the Salmon layer being accelerated to unphysically large velocities, and horizontal dissipation to represent the effect of sub-gridscale eddies and prevent shock formation. The modified scheme exhibits approximate second-order convergence under refinement of the spatial grid, though only time-averaged quantities converge when the flow is chaotic. The time-dependent solutions do not resemble the steady asymptotic solutions derived in Chapter 5, as the current tends to break up into a series of eddies as it crosses the equator. When the horizontal dissipation parameter $\hat{A}_h$ is sufficiently large the channel fills with almost-stationary fluid, and approaches a steady state. When $\hat{A}_h$ is smaller the long-term behaviour depends strongly on the orientation of the channel. In a northward channel the solution approaches a steady state for all $\hat{A}_h$. In a northwestward channel the current crosses the equator as a series of eddies, but becomes increasingly chaotic with smaller $\hat{A}_h$, and exhibits variability over timescales ranging from 100 to 1000 days. In an almost-westward channel the current forms eddies with a regular period ranging from 40 to 60 days, depending on $\hat{A}_h$ and the mass flux into the channel. As our asymptotic solutions from Chapter 5 suggested, the non-traditional component of the Coriolis force is most prominent in the almost-westward channel. However, our solutions show a somewhat smaller increase in transport when the complete Coriolis force is included — typically no more than 10%. Including the complete Coriolis force also increases the eddy formation period by around 5%, and leads to up to 20% variation in the eddy transport.

7.2 Future work

A vast number of previous studies of the ocean have been conducted using the traditional shallow water equations, and in principle our non-traditional shallow water equations could be used to

determine the role of the complete Coriolis force in any of them. However, we would only expect a flow to be substantially affected by the non-traditional component of the Coriolis force if it were weakly-stratified, interacted with steep bathymetry, or exhibited motion close to or across the equator. The examples considered in this thesis are just a few of the oceanographic phenomena that satisfy these requirements. In this section we discuss our ongoing work on this topic, and potential areas of future research.

In Chapter 3 we investigated internal waves, where the weak density stratification defines a comparatively short horizontal lengthscale, and so non-traditional effects should particularly pronounced. Much of the previous literature on non-traditional effects has focused on internal waves for this reason (*e.g.* Thuburn et al., 2002a,b; Gerkema and Shrira, 2005a,b; Kasahara, 2003; Kasahara and Gary, 2010). We have shown that long linear plane waves on a mid-latitude f-plane exhibit mode reconnection and dramatic structural changes when the complete Coriolis force is included. It would be interesting to see whether long waves in a continuously-stratified fluid exhibit similar structural changes. We might also expect to find dramatic structural changes in Kelvin waves, inertia-gravity waves, and Rossby waves on an equatorial β-plane (see Gill, 1982). Dellar and Salmon (2005) found that equatorial waves in the single-layer shallow water equations were barely affected by the inclusion of the complete Coriolis force. By contrast, it may be shown that the non-traditional multi-layer shallow water equations no longer admit Kelvin wave solutions with zero meridional velocity in every layer. This appears to contradict Fruman (2009), who found that the dispersion relation for equatorial waves in a continuously-stratified fluid was not modified by the inclusion of the complete Coriolis force.

In Chapter 3 we showed that non-traditional effects are most pronounced in northward/southward propagating waves, so similarly it may be that waves propagating across the equator exhibit the most interesting deviations from the traditional theory. The non-traditional shallow water equations also provide a practical means of studying non-linear internal waves, which are difficult to approach analytically from the three-dimensional continuously-stratified equations of motion. We computed the cross-equatorial propagation of nonlinear waves as part of our geostrophic adjustment study in Chapter 4, but focused on the long-time average behaviour, rather than the waves themselves. This numerical approach may be the most straightforward way to study these waves, as the latitudinal variation of the Coriolis parameter complicates analysis via mode decomposition. Our numerical solutions also showed that certain initial conditions lead to the fluid separating into two distinct masses in the northern and southern hemispheres. It may be possible to determine an analytical solution for these cases following the method of Killworth (1991), but allowing for a discontinuity in the particle labels for the fluid columns.

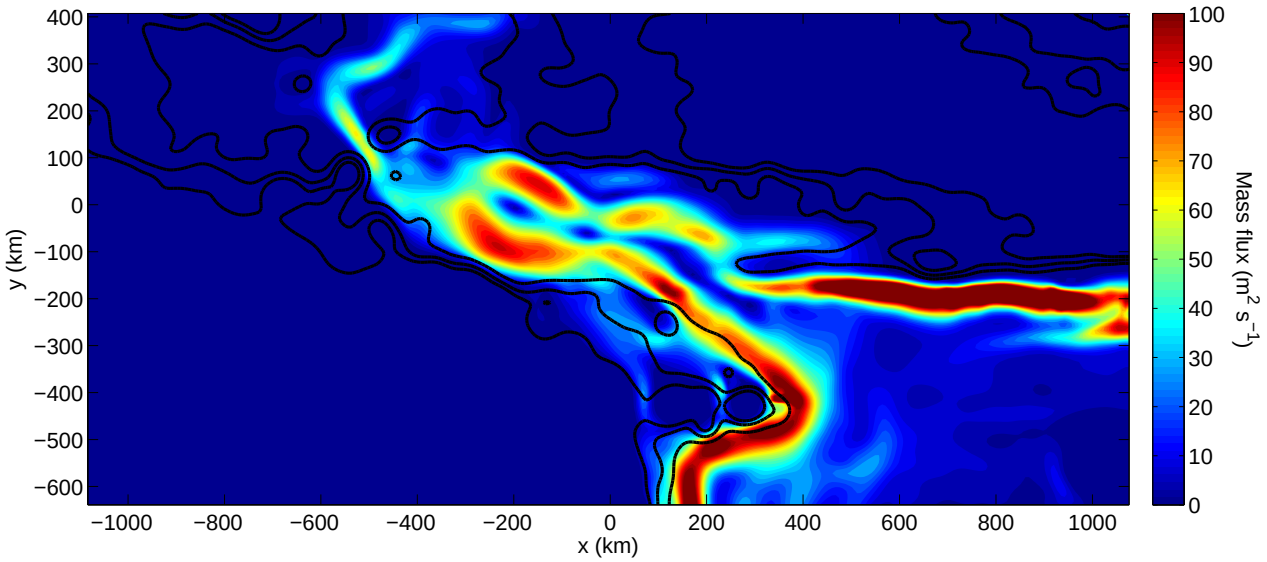

Figure 7.1: Snapshot of a numerical solution using the smoothed equatorial bathymetry shown in Figure 1.3. The black solid lines mark the −3750 m, −4000 m, and −4250 m contours. The AABW enters from the south as a western boundary current, and splits into an eastward-flowing portion in the southern hemisphere and a northward-flowing portion in the northern hemisphere. The current crosses the equatorial channel as a series of eddies, as in our idealised channel solutions in Chapter 6.

In Chapter 6 the steep-sided cross-equatorial channel meant that we had to accommodate grounding lines in our numerical solutions of the non-traditional shallow water equations. Salmon's (2002) method of modifying the potential energy to ensure a positive layer thickness is an elegant approach to this problem, but in flow over steep topography it is necessary to include explicit dissipative terms, as explained in §6.3.1. This approach is similar to the method of Arakawa and Hsu (1990) for handling vanishing layer thickness in the shallow water equations, which Choboter and Swaters (2004) used to model the AABW. It may be useful to obtain shallow water-type equations that do not require *ad-hoc* modifications to accommodate grounding lines, perhaps by tracking a density surface that can intersect the topography without invalidating the model. Such a model would not be applicable to the more general case of a fluid layer being squeezed to a vanishingly small thickness by adjacent layers, but might provide a more accurate representation of the abyssal dynamics.

Of all the work described in this thesis, the numerical simulations described in Chapter 6 offer the broadest scope for future research. We have only explored the dependence of the solution on the viscous dissipation, stratification, and channel orientation, which we have judged to be most relevant parameters to cross-equatorial flow of the AABW. We may also expect the dynamics to be sensitive to the shape of the channel and the inflow condition, as Nof and Borisov (1998) found for a northward channel. We were only able to obtain solutions for $\hat{A}_h \gtrsim 0.01$ because the flow

tends to steepen and form shocks, which in turn cause numerical instability. It may be possible to remedy this by retaining the vertical acceleration terms from the three-dimensional equations in our non-traditional shallow water equations (*c.f.* Green and Naghdi, 1976; Miles and Salmon, 1985). This introduces additional dispersive terms in the shallow water momentum equations that counteract nonlinear steepening due to advection. However, this approach could not be extended to two or more layers of fluid because the multi-layer analogues of the Green and Naghdi (1976) equations are unconditionally ill-posed (Liska and Wendroff, 1997).

We have also extended the numerical approach described in §6.3.1 to the smoothed equatorial bathymetry shown in Figure 1.3. In Figure 7.1 we plot the absolute mass flux in a snapshot of a computed solution in this bathymetry. We also plot the bathymetric contours at $-3750\,\mathrm{m}$, $-4000\,\mathrm{m}$, and $-4250\,\mathrm{m}$ to highlight the shape of the deep, cross-equatorial channel. Preliminary results show the current behaves similarly in the equatorial bathymetric channel as it does in the idealised almost-westward channel used in Chapter 6, breaking up into a series of eddies that propagate westward and transport fluid into the northern hemisphere. The flow becomes more chaotic as the lateral dissipation decreases. This differs from the results of Choboter and Swaters (2004), whose numerical solutions always approached a steady state. The inherent time dependence of the channel flow may also explain the time-variability in the measurements of Hall et al. (1997), who observed quasi-annual variations in the depth of the AABW at the equator. We have not yet carried out a full parameter survey because the realistic bathymetry has very steep slopes (on oceanographic scales) at the South American continental rise and at the mid-Atlantic ridge. The Salmon thickness and vertical dissipation must therefore be chosen carefully in order to preserve numerical stability without influencing the interior flow of the current.

Bibliography

Milton Abramowitz and Irene A. Stegun. *Handbook of Mathematical Functions with Formulas, Graphs, and Mathematical Tables*. Dover, New York, ninth Dover printing, tenth GPO printing edition, 1964.

C. Amante and B. W. Eakins. ETOPO1 1 arc-minute global relief model: procedures, data sources and analysis, NOAA technical memorandum NESDIS NGDC-24. Technical report, NOAA, 2009.

A. Arakawa. Computational design for long-term numerical integrations of the equations of atmospheric motion. *Journal of Computational Physics*, 1:119–143, 1966.

A. Arakawa and Y. J. G. Hsu. Energy conserving and potential-enstrophy dissipating schemes for the shallow water equations. *Monthly Weather Review*, 118(10):1960–1969, 1990.

A. Arakawa and V. R. Lamb. Computational design of the basic dynamical processes of the UCLA general circulation model. *Methods of computational physics*, 7:173–265, 1977.

A. Arakawa and V. R. Lamb. A potential enstrophy and energy conserving scheme for the shallow water equations. *Monthly Weather Review*, 109(1):18–36, 1981.

G. K. Batchelor. *An Introduction to Fluid Dynamics*. Cambridge University Press, 2000.

S. V. Bazdenkov, N. N. Morozov, and O. P. Pogutse. Dispersive effects in two-dimensional hydrodynamics. In *Soviet Physics Doklady*, volume 32, page 262, 1987.

S. Benzoni-Gavage and D. Serre. *Multi-Dimensional Hyperbolic Partial Differential Equations: First Order Systems and Applications*. Oxford University Press, Oxford, 2007.

R. Bleck and E. P. Chassignet. Simulating the oceanic circulation with isopycnic-coordinate models. *The Oceans: Physical-Chemical Dynamics and Human Impact*, pages 17–39, 1994.

R. Bleck, C. Rooth, H. Dingming, and L. T. Smith. Salinity-driven thermocline transients in a wind- and thermohaline-forced isopycnic coordinate model of the North Atlantic. *Journal of Physical Oceanography*, 22(12):1486–1505, 1992.

S. Borisov and D. Nof. Deep, cross-equatorial eddies. *Geophysical & Astrophysical Fluid Dynamics*, 87(3):273–310, 1998.

E. Boss, N. Paldor, and L. Thompson. Stability of a potential vorticity front: From quasi-geostrophy to shallow water. *Journal of Fluid Mechanics*, 315:65–84, 1996.

V. Botte and A. Kay. A model of the wind-driven circulation in Lake Baikal. *Dynamics of Atmospheres and Oceans*, 35:131–152, 2002.

F. P. Bretherton. Low frequency oscillations trapped near the equator. *Tellus*, 16:181–185, 1964.

R. Camassa, D. D. Holm, and C. D. Levermore. Long-time effects of bottom topography in shallow water. *Physica D. Nonlinear Phenomena*, 98:258–286, 1996.

S. Chandrasekhar. *Hydrodynamic and Hydromagnetic Stability*. Oxford University Press, Oxford, 1961.

P. F. Choboter and G. E. Swaters. Modeling equator-crossing currents on the ocean bottom. *Canadian Applied Mathematics Quarterly*, 8:367–385, 2000.

P. F. Choboter and G. E. Swaters. Shallow water modeling of Antarctic Bottom Water crossing the equator. *Journal of Geophysical Research – Oceans*, 109:C03038, 2004.

W. Choi and R. Camassa. Weakly nonlinear internal waves in a two-fluid system. *Journal of Fluid Mechanics*, 313:83–103, 1996.

A. Colin de Verdière and R. Schopp. Flows in a rotating spherical shell: the equatorial case. *Journal of Fluid Mechanics*, 276:233–260, 1994.

M. Cullen. The unified forecast/climate model. *The Meteorological Magazine*, 122:81–94, 1993.

P. J. Dellar. Variations on a beta-plane: derivation of non-traditional beta-plane equations from Hamilton's principle on a sphere. *Journal of Fluid Mechanics*, 674:174–195, 2011.

P. J. Dellar and Rick Salmon. Shallow water equations with a complete Coriolis force and topography. *Physics of Fluids*, 17:106601–19, 2005.

T. E. Dowling and A. P. Ingersoll. Jupiter's Great Red Spot as a shallow water system. *Journal of the Atmospheric Sciences*, 46(21):3256–3278, 1989.

D. G. Dritschel, L. M. Polvani, and A. R. Mohebalhojeh. The contour-advective semi-Lagrangian algorithm for the shallow water equations. *Monthly Weather Review*, 127(7):1551–1565, 1999.

X. D. Durrieu de Madron and G. Weatherly. Circulation, transport and bottom boundary layers of the deep currents in the Brazil Basin. *Journal of Marine Research*, 52(4):583–638, 1994.

C. Eckart. *Hydrodynamics of Oceans and Atmospheres*. Pergamon, Oxford, 1960.

C. A. Edwards and J. Pedlosky. Dynamics of nonlinear cross-equatorial flow. Part I: Potential vorticity transformation. *Journal of Physical Oceanography*, 28:2382–2406, 1998.

E. Firing. Deep zonal currents in the central equatorial Pacific. *Journal of Marine Research*, 45: 791–812, 1987.

B. Fornberg. On the instability of leap-frog and Crank-Nicolson approximations of a nonlinear partial differential equation. *Mathematics of Computation*, 27(121):45–57, 1973.

J. Frank, G. Gottwald, and S. Reich. A Hamiltonian particle-mesh method for the rotating shallow water equations. In M. Griebel and M. A. Schweitzer, editors, *Meshfree Methods for Partial Differential Equations*, volume 26 of *Lecture Notes in Computational Science and Engineering*, pages 131–142. Springer, 2002.

K. O. Friedrichs. Symmetric hyperbolic linear differential equations. *Communications on Pure and Applied Mathematics*, 7(2):345–392, 1954.

M. A. M. Friedrichs and M. M. Hall. Deep circulation in the tropical North Atlantic. *Journal of Marine Research*, 51(4):697–736, 1993.

M. D. Fruman. Equatorially bounded zonally propagating linear waves on a generalized β plane. *Journal of the Atmospheric Sciences*, 66(9):2937–2945, 2009.

M. D. Fruman, B. L. Hua, and R. Schopp. Equatorial zonal jet formation through the barotropic instability of low-frequency mixed Rossby-gravity waves, equilibration by inertial instability, and transition to superrotation. *Journal of the Atmospheric Sciences*, 66(9):2600–2619, 2009.

L. L. Fu. Observations and Models of Inertial Waves in the Deep Ocean. *Reviews of Geophysics*, 19:141–170, 1981.

C. Garrett and W. Munk. Space-time scales of internal waves. *Geophysical Fluid Dynamics*, 3: 225–264, 1972.

C. Garrett and W. Munk. Internal waves in the ocean. *Annual Reviews of Fluid Mechanics*, 11: 339–369, 1979.

R. Garver. On the nature of the roots of a quartic equation. *Mathematics News Letter*, 7:6–8, 1933.

T. Gerkema and V. I. Shrira. Near-inertial waves in the ocean: beyond the "traditional approximation". *Journal of Fluid Mechanics*, 529:195–219, 2005a.

T. Gerkema and V. I. Shrira. Near-inertial waves on the "nontraditional" β plane. *Journal of Geophysical Research – Oceans*, 110:C01003, 2005b.

T. Gerkema, J. T. F. Zimmerman, L. R. M. Maas, and H. van Haren. Geophysical and astrophysical fluid dynamics beyond the traditional approximation. *Reviews of Geophysics*, 46:RG2004, 2008.

A. E. Gill. *Atmosphere-Ocean Dynamics*. Academic Press, London, U.K., New York, U.S.A., 1982.

E. Godlewski and P. A. Raviart. *Numerical Approximation of Hyperbolic Systems of Conservation Laws*. Springer-Verlag, New York, 1996.

H. Goldstein. *Classical Mechanics, 2nd Edition*. Reading, Massachusetts: Addison–Wesley, 1980.

A. E. Green and P. M. Naghdi. A derivation of equations for wave propagation in water of variable depth. *Journal of Fluid Mechanics*, 78:237–246, 1976.

R. Grimshaw. A note on the beta-plane approximation. *Tellus*, 27:351–357, 1975.

M. M. Hall, M. S. McCartney, and J. A. Whitehead. Antarctic Bottom Water flux in the equatorial western Atlantic. *Journal of Physical Oceanography*, 27(9):1903–1926, 1997.

M. M. Hall, J. A. Whitehead, and M. S. McCartney. Moored measurements of Antarctic Bottom Water at the equator. *International WOCE Newsletter*, 17:5–8, 1994.

M. C. Hendershott. Long waves and ocean tides. In Bruce A. Warren and Carl Wunsch, editors, *Evolution of Physical Oceanography*, pages 292–341. Massachusetts Institute of Technology Press, 1981.

E. J. Hinch. *Perturbation Methods*. Cambridge University Press, Cambridge, 1991.

D. D. Holm, J. E. Marsden, and T. S. Ratiu. *Hamiltonian Structure and Lyapunov Stability for Ideal Continuum Dynamics*. University of Montreal Press, Montreal, 1986.

D. Houghton and E. Isaacson. Mountain winds. *Studies in Numerical Analysis*, 2:21–52, 1970.

B. L. Hua, D. W. Moore, and S. L. Gentil. Inertial nonlinear equilibration of equatorial flows. *Journal of Fluid Mechanics*, 331:345–371, 1997.

B. Hughes. Effect of rotation on internal gravity waves. *Nature*, 1964.

R. S. Irving. *Integers, Polynomials, and Rings*. Springer, 2004.

M. Israeli and S. A. Orszag. Approximation of radiation boundary conditions. *Journal of Computational Physics*, 41:115–135, 1981.

A. Kasahara. The roles of the horizontal component of the Earth's angular velocity in nonhydrostatic linear models. *Journal of the Atmospheric Sciences*, 60:1085–1095, 2003.

A. Kasahara. Initial-value approach to study the inertio-gravity waves without the 'traditional approximation'. *Journal of Computational Physics*, 225:2175–2197, 2007.

A. Kasahara and J. M. Gary. Studies of inertio-gravity waves on midlatitude beta-plane without the traditional approximation. *Quarterly Journal of the Royal Meteorological Society*, 136:517–536, 2010.

H. Kelder and H. Teitelbaum. A note on instabilities of a Kelvin-Helmholtz velocity profile in different approximations. *Il Nuovo Cimento C*, 14(2):107–118, 1991.

P. D. Killworth. Cross-equatorial geostrophic adjustment. *Journal of Physical Oceanography*, 21: 1581–1601, 1991.

W. Ku. Explicit criterion for the positive definiteness of a general quartic form. *IEEE Transactions on Automatic Control*, 10:372–373, 1965.

A. Kurganov and E. Tadmor. New high-resolution central schemes for nonlinear conservation laws and convection-diffusion equations. *Journal of Computational Physics*, 160:241–282, 2000.

H. Lamb. *Hydrodynamics*. Cambridge University Press, Cambridge, 6th edition, 1932.

G. A. Lawrence. On the hydraulics of boussinesq and non-boussinesq 2-layer flows. *Journal of Fluid Mechanics*, 215:457–480, 1990.

P. H. LeBlond and L. A. Mysak. *Waves in the Ocean*. Elsevier, 1978.

S. Leibovich and S. K. Lele. The influence of the horizontal component of Earth's angular velocity on the instability of the Ekman layer. *Journal of Fluid Mechanics Digital Archive*, 150:41–87, 1985.

M. J. Lighthill. A technique for rendering approximate solutions to physical problems uniformly valid. *Philosophical Magazine Series 7*, 40(311):1179–1201, 1949.

R. Liska, L. Margolin, and B. Wendroff. Nonhydrostatic two-layer models of incompressible flow. *Computers & Mathematics with Applications*, 29:25–37, 1995.

R. Liska and B. Wendroff. Analysis and computation with stratified fluid models. *Journal of Computational Physics*, 137:212–244, 1997.

R. R. Long. Long waves in a two-fluid system. *Journal of the Atmospheric Sciences*, 13:70–74, 1956.

J. Marshall, C. Hill, L. Perelman, and A. Adcroft. Hydrostatic, quasi-hydrostatic, and nonhydrostatic ocean modeling. *Journal of Geophysical Research*, 102(C3):5733–5752, 1997.

J. Marshall and F. Schott. Open-ocean convection: Observations, theory, and models. *Reviews of Geophysics*, 37:1–64, 1999.

M. S. McCartney and R. A. Curry. Transequatorial flow of Antarctic Bottom Water in the western Atlantic Ocean: Abyssal geostrophy at the equator. *Journal of Physical Oceanography*, 23(6): 1264–1276, 1993.

J. Miles and R. Salmon. Weakly dispersive nonlinear gravity-waves. *Journal of Fluid Mechanics*, 157:519–531, 1985.

P. J. Morrison. Hamiltonian description of the ideal fluid. *Reviews of Modern Physics*, 70(2): 467–521, 1998.

P. Muller. Ertel's potential vorticity theorem in physical oceanography. *Reviews of Geophysics*, 33: 67–97, 1995.

W. Munk. Internal waves and small-scale processes. *Evolution of Physical Oceanography*, 291, 1981.

W. Munk and N. Phillips. Coherence and band structure of inertial motion in the sea. *Reviews of Geophysics*, 6(4), 1968.

D. Nof. Why are some boundary currents blocked by the equator. *Deep Sea Research Part I: Oceanographic Research*, 37:853–873, 1990.

D. Nof and S. Borisov. Inter-hemispheric oceanic exchange. *Quarterly Journal of the Royal Meteorological Society*, 124(552), 1998.

D. Nof and D. Olson. How do western abyssal currents cross the equator? *Deep Sea Research Part I: Oceanographic Research*, 40:235–255, 1993.

J. Pedlosky. *Geophysical Fluid Dynamics*. Springer-Verlag, 1987.

A. O. Persson. The Coriolis Effect: Four centuries of conflict between common sense and mathematics, Part I: A history to 1885. *History of Meteorology*, 2:1, 2005.

N. . Phillips. Energy Transformations and Meridional Circulations associated with simple Baroclinic Waves in a two-level, Quasi-geostrophic Model1. *Tellus*, 6(3):273–286, 1954.

N. A. Phillips. Reply to Comment by Veronis. *Journal of the Atmospheric Sciences*, 25:1155–1157, 1968.

N. A. Phillips. Principles of large scale numerical weather prediction. In P. Morel, editor, *Dynamic meteorology: Lectures delivered at the Summer School of Space Physics of the Centre National d'Études Spatiales*, pages 3–96, Dordrecht, Boston, 1973. D. Reidel Publishing Company.

W. H. Raymond. Equatorial meridional flows: Rotationally induced circulations. *Pure Applied Geophysics*, 157:1767–1779, 2000.

M. Renardy and R. C. Rogers. *An Introduction to Partial Differential Equations*. Springer, New York, 2nd edition, 2004.

M. Rhein, L. Stramma, and G. Krahmann. The spreading of Antarctic bottom water in the tropical Atlantic. *Deep Sea Research Part I: Oceanographic Research Papers*, 45(4):507–528, 1998.

P. Ripa. Symmetries and conservation laws for internal gravity waves. In B. J. West, editor, *Nonlinear Properties of Internal Waves*, volume 76 of *AIP Conference Proceedings*, pages 281–306, New York, 1981. American Institute of Physics.

P. Ripa. Nonlinear wave-wave interactions in a one-layer reduced-gravity model on the equatorial beta plane. *Journal of Physical Oceanography*, 12:97–111, 1982.

P. Ripa. Conservation-laws for primitive equations models with inhomogeneous layers. *Geophysical and Astrophysical Fluid Dynamics*, 70:85–111, 1993.

P. Ripa. "Inertial" oscillations and the β-plane approximation(s). *Journal of Physical Oceanography*, 27:633–647, 1997.

B. Saint-Guily. On internal waves. Effects of the horizontal component of the earth's rotation and of a uniform current. *Deutsche Hydrographische Zeitschrift*, 23:16–23, 1970.

R. Salmon. Hamilton's principle and Ertel's theorem. In M. Tabor and Y. M. Treve, editors, *Mathematical Methods in Hydrodynamics and Integrability of Dynamical Systems*, volume 88 of *AIP Conference Proceedings*, pages 127–135, New York, 1982a. American Institute of Physics.

R. Salmon. The shape of the main thermocline. *Journal of Physical Oceanography*, 12(12):1458–1479, 1982b.

R. Salmon. Practical use of Hamilton's principle. *Journal of Fluid Mechanics*, 132:431–444, 1983.

R. Salmon. Hamiltonian Fluid Mechanics. *Annual Review of Fluid Mechanics*, 20:225–256, 1988.

R. Salmon. *Lectures on Geophysical Fluid Dynamics*. Oxford University Press, USA, 1998.

R. Salmon. Numerical solution of the two-layer shallow water equations with bottom topography. *Journal of Marine Research*, 60:605–638, 2002.

R. Salmon. Poisson-bracket approach to the construction of energy- and potential-enstrophy-conserving algorithms for the shallow-water equations. *Journal of the Atmospheric Sciences*, 61:2016–2036, 2004.

R. Schopp and A. Colin de Verdière. Taylor columns between concentric spheres. *Geophysical & Astrophysical Fluid Dynamics*, 86:43–73, 1997.

A. F. Shchepetkin and J. J. O'Brien. A physically consistent formulation of lateral friction in shallow-water equation ocean models. *Monthly Weather Review*, 124:1285–1300, 1996.

T. G. Shepherd. Symmetries, conservation laws, and Hamiltonian structure in geophysical fluid dynamics. *Advances in Geophysics*, 32:287–338, 1990.

C. W. Shu and S. Osher. Efficient implementation of essentially non-oscillatory shock-capturing schemes, II. *Journal of Computational Physics*, 83:32–78, 1989.

J. C. Stephens and D. P. Marshall. Dynamical pathways of Antarctic Bottom Water in the Atlantic. *Journal of Physical Oceanography*, 30:622–640, 2000.

M. E. Stern. Trapping of low frequency oscillations in an equatorial "boundary layer". *Tellus*, 15: 246–250, 1963.

A. L. Stewart and P. J. Dellar. Multilayer shallow water equations with complete Coriolis force. Part I. Derivation on a non-traditional beta-plane. *Journal of Fluid Mechanics*, 651:387–413, 2010.

A. L. Stewart and P. J. Dellar. Cross-equatorial flow through an abyssal channel under the complete Coriolis force: two-dimensional solutions. Submitted to *Ocean Modelling*, 2011a.

A. L. Stewart and P. J. Dellar. Multi-layer shallow water equations with complete Coriolis force. Part II. Hyperbolicity and linear plane waves. Revised manuscript submitted to *Journal of Fluid Mechanics*, 2011b.

A.L. Stewart and P.J. Dellar. The rôle of the complete Coriolis force in cross-equatorial flow of abyssal ocean currents. *Ocean Modelling*, 38:187–202, 2011c.

H. Stommel and A. B. Arons. On the abyssal circulation of the world ocean — 1. Stationary planetary flow patterns on a sphere. *Deep-Sea Research*, 6(2):140–154, 1960a.

H. Stommel and A.B. Arons. On The abyssal circulation of the world ocean — 2. An idealized model of the circulation pattern and amplitude in oceanic basins. *Deep-Sea Research*, 6(3):217–233, 1960b.

C. H. Su and C. S. Gardner. Korteweg-de Vries equation and generalizations. III. Derivation of Korteweg-de Vries equation and Burgers' equation. *Journal of Mathematical Physics*, 10:536–539, 1969.

J. Thuburn, N. Wood, and A. Staniforth. Normal modes of deep atmospheres. I: Spherical geometry. *Quarterly Journal of the Royal Meteorological Society*, 128:1771–1792, 2002a.

J. Thuburn, N. Wood, and A. Staniforth. Normal modes of deep atmospheres. II: f-F-plane geometry. *Quarterly Journal of the Royal Meteorological Society*, 128:1793–1806, 2002b.

G. K. Vallis. *Atmospheric and Oceanic Fluid Dynamics: Fundamentals and Large-Scale Circulation*. Cambridge University Press, Cambridge, U.K., New York, U.S.A., 2006.

H. van Haren and C. Millot. Rectilinear and circular inertial motions in the Western Mediterranean Sea. *Deep-Sea Research Part I: Oceanographic Rsearch Papers*, 51(11):1441–1455, 2004.

H. van Haren and C. Millot. Gyroscopic waves in the Mediterranean Sea. *Geophysical Research Letters*, 32:L24614, 2005.

G. Veronis. On the approximations involved in transforming the equations of motion from a spherical surface to the β-plane. I. Barotropic systems. *Journal of Marine Research*, 21:110–124, 1963.

G. Veronis. Dynamics of large-scale ocean circulation. In Bruce A. Warren and Carl Wunsch, editors, *Evolution of Physical Oceanography*, pages 140–183. Massachusetts Institute of Technology Press, 1981.

F. Wang and L. Qi. Comments on "Explicit criterion for the positive definiteness of a general quartic form". *IEEE Transactions on Automatic Control*, 50:416–418, 2005.

A. A. White. A view of the equations of meteorological dynamics and various approximations. In John Norbury and Ian Roulstone, editors, *Large-Scale Atmosphere-Ocean Dynamics 1: Analytical Methods and Numerical Models*, pages 1–100, Cambridge, 2002. Cambridge University Press.

A. A. White and R. A. Bromley. Dynamically consistent, quasi-hydrostatic equations for global models with a complete representation of the Coriolis force. *Quarterly Journal of the Royal Meteorological Society*, 121:399–418, 1995.

A. A. White, B. J. Hoskins, I. Roulstone, and A. Staniforth. Consistent approximate models of the global atmosphere: shallow, deep, hydrostatic, quasi-hydrostatic and non-hydrostatic. *Quarterly Journal of the Royal Meteorological Society*, 131:2081–2107, 2005.

G. B. Whitham. *Linear and Nonlinear Waves*. Wiley New York, 1974.

T. Y. Wu. Long waves in ocean and coastal waters. *Journal of Engineering Mechanics, ASCE*, 107: 501–522, 1981.

V. Zeitlin. *Nonlinear Dynamics of Rotating Shallow Water: Methods and Advances*. Elsevier Science, 2007.